Contribution to the development of Brillouin optical time-domain analysis sensors

Javier Urricelqui

Department of Electrical and Electronic Engineering
Public University of Navarre

This dissertation is submitted for the degree of
Doctor of Philosophy

Supervisors:
Alayn Loayssa
Mikel Sagues

June 2016

Agradecimientos/Acknowledgements

Pensando en cómo comenzar los agradecimientos de esta tésis, me remonto al instante en el que estando todavía en Viena, escribí mi primer email a Alayn para preguntarle en qué tema andaba trabajando por aquel año 2011. Tras recibir una típica contestación de mi director, es decir, con *extensa* información de los sensores BOTDA y del efecto de dispersión Brillouin estimulada y sin todavía saber muy bien en qué y dónde me estaba metiendo, decidí probar durante unos meses si me gustaba el tema del laboratorio y los sensores distribuidos de la mano de su compañero Mikel. Desde aquel instante, ambos me habéis aportado el conocimiento, ideas y consejos que han permitido convertir este proyecto de investigación en la actual tésis que tenéis entre manos. Muchas gracias de todo corazón a ambos, a día de hoy contáis con mi mayor respeto y admiración.

Mis agradecimientos al grupo de "Brillouineros" no estarían al completo si no mencionase a mis compañeros y amigos, Jon, Juanjo y Haritz. Hemos pasado excelentes momentos en el laboratorio que sin duda alguna nos ha ayudado a sobrellevar las crisis que sufríamos cuando misteriosamente "algo" dejaba de funcionar correctamente en nuestros montajes. Espero que podamos seguir planificando viajes en nuestros congresos más exóticos, Brasil fue épico con el Amazonas y espero que Corea sea aún mejor con el grupo al completo. Tampoco puedo olvidarme en mencionar al resto de compañeros que han trabajado en el grupo de comunicaciones ópticas: Dani, Santi, Rosana, Mikel, Sergio, Manolo, Ander, Felipe, Jairo, Aitor, Verónica, César, Montse y Paola; asi como los compañeros que han estado en mi despacho: Ángel, Adrián, Fernando, Aitor, Magda, Nerea y Aintzane.

Además, me gustaría recordar en estas líneas a todas aquellas personas de otros grupos de investigación que he ido encontrando en el desarrollo de mi tésis. A los integrantes del grupo de la Universidad de Cantabria, en especial a Rubén y Jesús, con los que he tenido el gran placer de trabajar codo con codo y supieron cómo conquistarme desde el primer minuto con sus deliciosos productos de la tierruca. Al grupo de la Universidad de Alcalá de Henares, en especial a Xabi con el que he coincidido en multitud de ocasiones a lo largo de nuestras carreras, pero también a Alejandro y Alexia por los buenos momentos que hemos pasado en los diferentes congresos, asi como en escuelas de verano. I would like to thank Avi Motil,

Yair Peled and Arik Bergman from Tel Aviv University for the conversations and dinners that we have enjoyed during the conferences.

Four months of this thesis dissertation are from the group for fibre optics at EPFL, where I carried out my stay research: Mehdi, Kenny, Andrey, Xin, Desmond, Alexandra and specially Luc, for his extraordinary suggestions on BOTDA sensors and his excellent personal treatment. He made me feel as another PhD student of his wonderful group during this short time at his laboratory. No me gustaría pasar por alto a uno de sus integrantes, Marcelo, un excelente investigador y compañero; gracias por todo el trabajo que realizaste conmigo a lo largo de toda la estancia, discusiones fundamentales en el laboratorio y en nuestros trayectos de metro hacia casa que estoy seguro no olvidaré, pero también por las risas y demás ratos que hemos pasado juntos, hiciste que mi estancia en Lausana fuese muy agradable. Furthermore, during this time, I met Zhisheng from Beijing University of Posts and Telecommunications and Zhiyong from Huazhong University of Science and Technology, who showed me the genuine culture and gratitude from China.

I would also like to thank the members of the thesis committee for the evaluation and reading of this thesis dissertation: Dr. José Miguel López Higuera from Universidad de Cantabria, Dr. Miguel González Herráez from Universidad de Alcalá and Dr. Sébastien Le Floch from University of Applied Sciences Western Switzerland.

Además, quiero trasladar mi agradecimiento a las instituciones que han permitido que esta tésis se pudiese desarrollar: Universidad Pública de Navarra a través del programa de ayudas para la formación de personal investigador, ayudas al personal investigador y ayudas a la movilidad; Comisión Interministerial de Ciencia y Tecnología a través de los proyectos TEC2010-20224-C02-01, IPT-2011-1212-920000 y TEC2013-47264-C2-2-R; marco COST TD1001 a través de la ayuda aportada para la realización de estancias de investigación a jóvenes investigadores.

No podría terminar estos agradecimientos sin escribir de las personas que más me importan en la vida y a las que dedico esta tésis, mi familia. Mis padres, María y José Ramón, quienes me han dado todo el amor, fuerza y apoyo incondicional para que día a día fuese consiguiendo cada uno de mis objetivos. Mi hermana Lorena, una excelente persona tanto a nivel personal como profesional y modelo a seguir que, sin duda alguna, es responsable de muchas de mis elecciones en mi vida profesional. Mi pareja Amagoia, una de las personas que mejor me complementan, compañera de viaje, alegrías y aventuras, además de una fiel animadora que me incentiva a seguir consiguiendo todos mis propósitos. Gracias por toda vuestra ayuda, sin vosotros no sería la persona que conocéis.

Abstract

Infrastructures are key elements in our everyday lifestyle. They provide cities and towns the quality of life that human being requires. Nevertheless, the vast majority are deaf, dumb and blind since there is no a proper way to evaluate its integrity and state. In this context, fiber-optics sensors can be an interesting solution since they can be embedded within the structure and provide information of the stress, strain, temperature or deformation suffered by the structure. Furthermore, the properties of the optical fiber such as immunity to electromagnetic interference, chemical passive, light weigh, small size, mechanical compatibility with different materials or passive nature, make fiber-optics sensors an interesting technology, and sometimes the only feasible solution for a wide range of applications. Just to mention some of them, there is interest in monitoring structures such as roads, railways, bridges, tunnels, damns, power lines or pipelines. Depending on the sensing application, it is possible to use point sensors in which the measurand can only be retrieved at specific locations within the infrastructure. However, these structures have in common large dimensions and may need to monitor all the points of the structure since there is not way to predict the exact location to install the point sensor. In this case, distributed optical fiber sensors present as a disruptive technology in which, each point of the optical fiber becomes itself the sensing element. Embedding it within materials and structures allows to create a nerve system that monitor all the points of the structure. This feature makes this technology unique in the world with no real competitors.

Distributed fiber sensors based on stimulated Brillouin scattering (SBS), particularly, the configuration known as Brillouin optical time-domain analysis (BOTDA) sensors, are the central object of this thesis dissertation. This configuration is the most promising technology since it is able to resolve different scenarios such as long-range monitoring distances with hundreds of kilometers using sub-meter spatial resolution or short-distances around a few kilometers with centimeters spatial resolution. Furthermore, the technique can be also applied to dynamic measurements being able to monitor vibrations of hundreds of kHz for relative short distances.

The BOTDA technique is based on the counter-propagation of two optical signals, a pulsed signal and a probe wave. When both waves have a frequency difference around the

Brillouin frequency shift (BFS) of the fiber, they interact through SBS. This interaction only occurs whenever the pulsed signal meets the probe wave, so that the power of the probe wave is locally modified obtaining a distributed measurement. The variation of the optical probe power is maximum, when the frequency difference between both waves matches with the BFS. Therefore, in order to determine the BFS at each location of the fiber, the BOTDA technique requires to sweep the frequency difference between both waves obtaining for each location of the fiber, a power distribution known as the Brillouin amplitude spectrum. The peak of the Brillouin spectrum provides the BFS measurement, which provides the temperature or strain information of the scanned points.

Although the BOTDA technique has been thoroughly studied, there still exist some limitations in these sensors. The uncertainty on the determination of the BFS basically depends on the signal-to-noise ratio (SNR) of the measurements. This key parameter has a linear relationship to the detected power of the probe wave, which must be limited at the input of the fiber due to a detrimental effect known as non-local effects. As mentioned before, when the frequency difference between the probe signal and the pump wave matches the BFS, the interaction is maximum. In case that the BFS is uniform along the sensing fiber, the energy given by the pulsed signal is considerably higher for that frequency difference than for others. The non-local effects induce a distortion of the measured spectrum and impairs the BFS measurement. Moreover, if non-local effects are negligible, there still exist a probe power limitation given by the amplification of spontaneous Brillouin scattering components, which results in noise added to the probe wave and hence, it impairs the SNR of the measurement. Furthermore, another parameter directly related with the SNR is the peak power of the pulsed signal. The input peak power is also limited by another effect called modulation instability, which depletes the power of the pulsed signal along its propagation reducing the interaction with the probe wave at certain locations of the sensing fiber.

In addition to these power limitations, the sensing range and the spatial resolution (given by the number of points resolved by the sensor) also limit the available SNR of the measurements. The first one is limited by the optical attenuation of the fiber, which turn to be doubled in these systems due to the counter-propagation of the probe wave and the pulsed signal. The second one is given by the temporal duration of the pulsed signal, which reduces the effective interaction between both waves and broadens the measured Brillouin spectrum for pulse durations lower than 10 ns.

This thesis dissertation concentrates on solving some of the limitations described by proposing novel techniques. The first technique is based on using a phase-modulated probe wave with self-heteroyne detection and RF demodulation in BOTDA sensors. The self-heterodyne detection along with the RF demodulation allows to increase the SNR of

the detected signal and to recover the amplitude of the Brillouin interaction as well as the phase-shift. The phase modulation allows to measure a phase-shift spectrum that obviously depends on the BFS measurement but also it is tolerant to changes of the pulse power and the attenuation of the fiber. This technique is interesting for dynamic BOTDA sensors, i.e. real-time monitoring sensors, in which attenuation of the optical fiber is a usual issue due to the losses caused by mechanical stress. Furthermore, as the technique is tolerant to changes of the peak power of the pulsed signal, it can tolerate non-local effects. This allows to increase the SNR by the increment of the probe power.

Furthemore, this BOTDA sensor has been combined with a well-known technique, called differential pulse-width pair technique. It allows to enhance the spatial resolution without broadening the measured spectrum. In this case, the technique was applied to amplitude and phase-shift measurements. In addition to it, new approaches of this sensor based on the deployment of multiple pulsed signals with special features have been deployed to mitigate the effect of modulation instability and to reduce the measurement time in dynamic BOTDA sensors.

A second technique proposed during this thesis dissertation is the BOTDA sensor using a probe wave whose optical frequency is modulated along the distance of the fiber. As mentioned before, if the BFS of the fiber is uniform, the effect induced by non-local effects is more detrimental. Consequently, if the probe wave changes along the fiber, the Brillouin interaction is not longer uniform and the probe power can be increased. Moreover, this technique also allows to reduce the noised added to the probe wave due to amplification of spontaneous Brillouin scattering components overcoming both limitations of the probe wave. Consequently, the proposed technique allows to considerably increase the precision of the sensor.

In addition to it, the second technique is also useful to generate distributed Brillouin amplifiers (DBA). Combining the DBA with a standard BOTDA sensor, the DBA can transfer energy to the pulsed signal at the final kilometers of the fiber, i.e. the fiber section in which the pulsed signal has a low power due to the suffered attenuation. Therefore, the system allows to increase the detected SNR of the measurement.

Finally, the thesis presents a study of the different noise sources that could affect to BOTDA sensors. Different noises sources such as double Rayleigh scattering generated by the probe wave or phase-to-intensity noise conversion in the SBS process are theoretically and experimentally analyzed. The study points out some guidelines of the importance of each noise for the different distance ranges in BOTDA sensors.

Contents

List of figures

List of tables

Nomenclature

Symbols

A_{eff}	Effective area
α	Attenuation coefficient of the medium
α_B	Brillouin scattering coefficient
α_P	Attenuation coefficient at the pump wavelength
α_s	Sound absorption coefficient
α_S	Attenuation coefficient at the Stokes wavelength
β	Propagation constant
β_2	Group-velocity dispersion coefficient
c	Speed of light in vacuum
C	Compressibility of the material
C_s	Adiabatic compressibility
d	Depletion/gain factor of pump wave
D	Fiber dispersion parameter
δ	Frequency step
$\Delta\chi$	Fluctuation of the dielectric suceptibility
$\Delta\varepsilon$	Fluctuation of the dielectric constant
$\delta\varepsilon$	Strain variation

Δf	Effective noise bandwidth
$\Delta \nu$	Frequency detuning of probe wave from the Brillouin peak frequency
$\delta \nu$	Frequency difference between the maximum depletion frequency of the pump wave and the BFS
$\Delta \nu_B$	Brillouin linewidth
$\Delta \nu_{LS}$	Laser source linewidth
$\Delta \nu_{mod}$	Frequency deviation
$\Delta \omega$	Instantaneous frequency
ΔP	Variation of optical power
ΔP_S	BOTDA sensor response
$\Delta \rho$	Density variations
$\Delta \tau_P$	Relative temporal delay between pulse and probe wave
Δz	Spatial resolution
$\mathbf{E}$	Electric field
E_{DRS}	Electric field of double Rayleigh scattering
E_P	Electric field of the pump wave
E_{Pi}	Input electric field of the pump wave
ε_0	Dielectric permittivity in vacuum
E_S	Electric field of the Stokes wave
E_{0i}	Input electric field of the local oscillator
E_{SBi}	Input electric field of the sideband
E_{Si}	Input electric field of the Stokes wave
η	Mixing efficency
f_μ	Microwave frequency

f_{RF}	Frequency modulation
g_0	Brillouin peak coefficient
Γ	Damping rate of acoustic wave
γ	Nonlinear coefficient
Γ_B	Phonon decay rate
γ_e	Electrostrictive constant
G_{MI}	Modulation instability spectrum
G_{SBS}	Exponential form of Brillouin magnitude spectrum
g_{SBS}	Magnitude of Brillouin spectrum
h	Planck constant
H_{rx}	Receiver spectral response
H_{SBS}	Complex Brillouin spectrum
I_{DRS}	Intensity of the DRS components
I_P	Intensity of the pump wave
I_S	Intensity of the Stokes wave
i_s	Shot noise
i_T	Thermal noise
K	Bulk modulus
$\mathbf{k}$	Wave vector
k_B	Boltzmann constant
L	Length of the optical fiber
λ	Wavelength
L_{eff}	Effective length
μ_0	Magnetic permittivity in vacuum

n	Refractive index of medium
n_o	Ordinary refractive index
N_{AV}	Number of averages
N_{BFS}	Number of cycles of BFS
n_e	Extraordinary refractive index
ν	Optical frequency
ν_0	Optical frequency of the local oscillator
ν_B	Brillouin frequency shift
ν_{B0}	Brillouin frequency shift at room temperature and loose-state
$\nu_{B,e}$	Brillouin frequency shift accuracy
ν_L	Optical frequency of the DBA pump wave
ν_P	Optical frequency of the pump wave
$\nu_{SL,0}$	Average optical frequency of the Stokes wave
ν_S	Optical frequency of the Stokes wave
Ω	Frecuency of acoustic wave
ω	Angular frequency
Ω_B	Angular Brillouin frequency shift
Ω_c	Cut-off frequency
Ω_P	Pump frequency detuning
$\mathbf{P}$	Polarization field
p	Pressure wave
P_{0i}	Input optical power of local oscillator
$\bar{P}$	Average optical power
P_{DRS}	DRS noise power spectral density

ϕ	Cromatic dispersion phase-shift
ϕ_{NL}	Nonlinear phase-shift
ϕ_S	Phase of probe wave
ϕ_{SpBS}	Phase of SpBS wave
P_L	Optical power of DBA pump
P_P	Optical power of pump wave
P_{Pi}	Input optical power of pump wave
P_{ref}	Reflected optical power
P_{rx}	Optical power at the receiver
P_S	Optical power of Stokes wave
P_{SBi}	Input optical power of the sideband
P_{Si}	Input optical power of Stokes wave
p_{st}	Strictive pressure
$\mathbf{q}$	Acoustic wave vector
Q	Acoustic wave field
q	Electron charge
R	Reflectivity FBG spectrum
R_D	Responsivity of the photoreceiver
$R_{D,MI}$	Depletion ratio of modulaion instability
ρ	Density of medium
ρ_{DRS}	Rayleigh backscattering coefficient
R_L	Load resistor
R_{Rb}	Rayleigh backscattering coefficient
$\hat{S}_P$	Normalized pump vector representing SOP

$\hat{S}_S$	Normalized Stokes vector representing SOP
σ_{BFS}	Brillouin frequency shift precision
σ_{crit}	Critical gain of modulation instability
$\sigma^2_{\Delta\nu}$	Variance of the frequency detuning
$\sigma_{\Delta\nu_P}$	Instantaneous frequency deviation of pump signal
$\sigma_{\Delta\nu_S}$	Instantaneous frequency deviation of probe signal
$\sigma^2_{\Delta P_S}$	Variance of the sensor response
σ^2_{DRS}	Double Rayleigh scattering noise variance
σ^2_{FBG}	Phase-to-intensity noise variance generated at the SBS process
σ^2_I	Relative intentisy noise variance of the laser source
σ^2_S	Shot noise variance
σ^2_{SBS}	Phase-to-intensity noise variance generated at the FBG
$\sigma^2_{SpBS-Probe}$	SPBS-probe beating noise variance
σ^2_T	Thermal noise variance
S_n	Noise power spectral density
S_s	Shot noise power spectral density
S_T	Thermal noise power spectral density
T	Temperature
T_0	Room temperature
τ_p	Phonon lifetime
θ_{RF}	RF phase-shift
T_P	Temporal pulse duration
υ_a	Acoustic velocity
φ_{SBS}	Brillouin phase-shift spectrum

ζ	Fraction of peak level

Acronyms / Abbreviations

ASE	Amplified spontaneous emission
AWG	Arbitrary waveform generator
BFS	Brillouin frequency shift
BGS	Brillouin gain spectrum
BOCDA	Brillouin optical correlation-domain analysis
BOFDA	Brillouin optical frequency-domain analysis
BOTDA	Brillouin optical time-domain analysis
c.c.	Complex conjugate
CW	Continuos wave
DBA	Distributed Brillouin amplifier
DCM	Dispersion compensating module
DFB	Distributed feedback
DGD	Differential group delay
DPP	Differential pulse-width pair
DRA	Distributed Raman amplifier
DRS	Double Rayleigh scattering
EC	External cavity
EDFA	Erbium-doped fiber amplifier
ESA	Electrical spectrum analyzer
FBG	Fiber Bragg grating
FM	Frequency modulation
FWM	Four-wave mixing

GVD	Group-velocity dispersion
MI	Modulation instability
MZ-EOM	Mach-Zehnder electro-optic modulator
NLE	Non-local effects
NLSE	Nonlinear Schrödinger equation
ODSB-SC	Optical double sideband with suppressed-carrier
OSA	Optical spectrum analizer
OSSB	Optical single sideband
PBS	Polarization beam splitter
PC	Polarization controller
PDPP	Phasorial differential pulse-width pair
PM	Phase modulation
POF	Programmable optical filter
PSD	Power spectral density
PS	Polarization scrambler
RF	Radio frequency
RIN	Relative intensity noise
SA	Slope-assisted
SBS	Stimulated Brillouin scattering
SMF	Single-mode fiber
SNR	Signal-to-noise ratio
SOA	Semiconductor optical amplifier
SOP	State of polarization
SpBS	Spontaenous Brillouin scattering

SPM	Self-phase modulation
SRS	Stimulated Raman scattering
VNLSE	Vector nonlinear Schrödinger equation

Introduction to the thesis

Motivation

The development of telecommunications based on optical fibers has actually allowed a virtual world to emerge, one in which distance no longer represents a barrier to communicate broadband signals. Since the decade of 1960, years of the invention of the laser and the modern low-loss optical fibers, the available market has significant growth favoring not only the development of telecommunications, but also the sensing based on fiber technology. From that time, the field of optical fiber sensing has enormously developed, being able to monitor parameters such as temperature, strain, gas concentration, acceleration or fluid level among other solutions. Compared with other technologies, such as electric sensors, optical fiber sensors offer a number of advantages, such as small size, immunity to electromagnetic interference, a very wide operating range, chemical passivity or multiplexing capabilities. These aspects make optical sensors an attractive and competitive solution for different applications in which other technologies can not be installed.

Among the different optical sensors available in the market, there are point sensors, such as fiber Bragg gratings or interferometric sensors, and distributed sensors, based on phenomena such as Raman, Rayleigh or Brillouin scattering. The main difference between both categories resides on the use given to the optical fiber, while the point sensors employ the optical fiber as the link to propagate the signals between the intrinsic or extrinsic point sensor and the interrogator, the distributed sensors transform the optical fiber in the sensing element, i.e. it is the transducer. Consequently, the measurement is distributed along the optical fiber. This may be considerably interesting, when many points of a structure need to be monitored. In this case, a single distributed fiber sensor can replace many point sensors, which reduces the cost per sensing point when monitoring large structures. This is the reason behind the success of distributed sensors.

Consequently, distributed sensors have become a disruptive technology in the field of structural health monitoring due to the ability to monitor long ranges with high spatial resolutions. Among the different phenomena used in distributed sensors, stimulated Brillouin

scattering has no competence, since measurements over more than 100 km have been done with sub-meter spatial resolution. These features provide excellent results in many practical fields such as in civil and structural engineering to monitor bridges, damns, pipelines or tunnels, in harsh environments like nuclear power plants or oil and gas industries. Moreover, Brillouin distributed sensors can also be useful in the energy sector to monitor the power grid dynamically evaluating the local current load or the degradation of the line. In addition to the long range applications, distributed Brillouin sensors also provide the possibility to dynamically assess the state of short structures (from 100 meters length). This is the case of wind turbine blades in which this technology can determine the correct operation of it during the test of the prototype or in railway traffic monitoring to determine useful information, such as train identification, axle counting, speed detection, and dynamic load calculation.

The numerous applications described above and the interest of other industries are the main motivation to further improve the performance of these sensors.

Objectives of the thesis

This thesis dissertation concentrates on improving the performance of Brillouin optical time-domain analysis (BOTDA) sensors, one of the most studied and developed Brillouin distributed sensor. In particular, the thesis presents advanced techniques for improving different aspects of dynamic and static BOTDA sensors. These approaches basically try to improve the signal-to-noise ratio (SNR) of the detected Brillouin signal, which is the key parameter determining the features of the sensor.

The factors limiting the ultimate signal-to-noise ratio achieved by BOTDA sensors are:

- The maximum optical power of the waves deployed in BOTDA sensors, i.e. the pump and probe waves.
  - The pump power is limited by modulation instability, an effect that depletes the pump power along its propagation through the fiber and consequently, it reduces the maximum sensing range of the sensor.
  - The probe wave power is limited by the so-called non-local effects (NLE). This effect induces an error of the estimated temperature or strain value determined by the sensor, worsening its accuracy. In case that NLE are negligible, then Brillouin induced noise in the detected probe signal limits the ultimate probe power used in BOTDA sensors.
- The monitoring range of the BOTDA sensor sets the available amplitude signal at the end of the fiber. The longer is the optical attenuation experienced by pump and

probe waves, the smaller is the detected amplitude signal. Consequently, it reduces the available SNR at the end of the fiber. Moreover, the effect of the optical attenuation turns to be double since both waves counter-propagate along the fiber.

- The spatial resolution sets the number of points resolved by the sensor but it also determines the temporal duration that probe and pump interact. For short pulse durations, the obtained amplitude signal is lower than for longer pulse durations. Consequently, it reduces the SNR of the measurement at the expense of increasing the resolved number of points.

- The intensity of the noise sources of BOTDA sensors. The higher is the intensity of the noise sources, the lower will be the SNR of the measurement.

Structure of the thesis

The content of this thesis dissertation is divided in five chapters:

The first chapter is an introduction to the different scattering phenomena and, in particular, to Brillouin scattering, in order to understand the physical underpinnings of this effect. The details of Brillouin scattering, such as the conservation of momentum and energy, the Brillouin spectrum or the theoretical model in stimulated Brillouin scattering have been described to later introduce the different techniques used to implement distributed optical fiber sensors. Among the different configurations, special interest is devoted to the Brillouin optical time-domain analysis sensor in which the theoretical model is presented to provide a better understanding of the sensor behaviour. After that, the different factors limiting the performance of BOTDA sensors are discussed along with the solutions proposed at the current state of the art.

The second chapter is devoted to a novel BOTDA sensor that deploys a phase-modulated probe wave and self-heterodyne detection. First, the theoretical model of the detected signal affected by Brillouin scattering is described to find out that the detected phase-shift is tolerant to variations of the local Brillouin gain suffered by the probe wave. This feature is particularly important for dynamic and static BOTDA sensors. In the first case, the technique benefits from measurements tolerant to variations of the attenuation of the optical fiber, which are highly probable in a structure with dynamic deformation. While in static BOTDA sensor, which comprises long monitoring distances, this feature allows to tolerate non-local effects and hence, the probe power can be safely increased.

Secondly, this technique is combined with well-known procedures to enhance the spatial resolution of the sensor but, in this case, using the detected phase-shift signal without loosing the tolerance to variations of the local Brillouin gain.

Finally, the sensor is used with multiple pump waves, instead of a single pump as it is conventionally done, to decrease the measurement time of dynamic BOTDA sensors. Furthermore, the deployment of multiple pump waves allows to increase the injected pump power and hence, mitigating the effect of modulation instability.

In the third chapter, a novel technique based on frequency modulation of the probe wave is proposed for BOTDA sensors. Since the Brillouin interaction depends on the frequency difference between probe and pump waves, the frequency modulation of the probe wave allows to reduce the Brillouin interaction experienced by the pump wave along the fiber. Consequently, the technique allows to increase the injected probe power overcoming non-local effects. Moreover, the same principle is used to mitigate the Brillouin induced noise when the probe power is higher than the Brillouin threshold of the fiber. Consequently, the probe wave reaches the optical receiver with a high enough optical power to enhance the SNR of the measurements.

In the fourth chapter, a BOTDA sensor using a distributed Brillouin amplifier is introduced and demonstrated. The technique is based on the deployment of an additional pump wave to generate a distributed Brillouin amplifier (DBA), whose properties are controlled to properly amplify the desired signal. Specifically, the DBA provides amplification to the pump wave typically used in BOTDA sensor, so that, at the last kilometers of the fiber, i.e. where the optical pump pulses have suffered a greater attenuation, the pulsed signal is amplified obtaining (if it is desired) the same Brillouin gain than at the first kilometers of the fiber.

In the fifth chapter, a study of the different noise sources affecting the conventional BOTDA sensor is presented. The study identifies the noise sources caused by the propagation of the probe wave along the fiber and by the Brillouin interaction between probe and pump waves. This study allows to update the signal-to-noise ratio parameter of BOTDA sensors taking into account the additional noise sources considered in this thesis together with the typical noise sources coming from the receiver stage, such as thermal and shot noises or the relative intensity noise coming from the laser source.

Finally, the sixth chapter summarizes the conclusions obtained from the work done in previous chapters and presents the open lines of this thesis.

Chapter 1

Distributed optical fiber sensors based on Brillouin scattering

Distributed optical fiber sensors occupy an essential place in many monitoring applications. Using an optical fiber as the sensing element, they are able to provide information about the quantity to be measured at each location of an optical fiber. These sensors are based on scattering phenomena caused by fluctuations in the optical properties of the medium, which may be associated with local or temporal changes of the refractive index. Depending on the scattering process, the sensor allows to measure a different measurands. In this thesis dissertation, the different contributions focus on the distributed measurement of temperature and strain using the Brillouin scattering nonlinear effect. Consequently, this chapter will describe the working principles of distributed fiber sensors based on Brillouin scattering to provide a deep understanding of this technique.

This chapter briefly introduces the different types of light scattering, to later present the physics behind the Brillouin scattering for both process, the spontaneous and stimulated regimes. All the relevant parameters such as the Brillouin frequency shift (BFS) or the Brillouin linewidth are also defined during this chapter providing a complete theoretical background. Then, the most common configurations based on stimulated Brillouin scattering (SBS) are introduced, to finally focus on the Brillouin optical time-domain analysis (BOTDA) sensor, as the improvement of these sensors is the main target of this thesis. The classical model of stimulated Brillouin scattering based on three coupled differential equations is solved to obtain the basic theoretical response of BOTDA sensors. Finally, the limitations and state of the art are reviewed to provide the big-picture of BOTDA sensors.

1.1 Scattering effects in optical fibers

An incident light beam may generate different types of scattering when it propagates in matter. Depending on the intensity of the incident light beam, it is possible to differentiate between spontaneous or stimulated scattering effects. Spontaneous light scattering occurs when low intensities are injected into the media and hence, the light scattering occurs without modifying the optical properties of the material system by the presence of this incident light beam [1, 2]. Therefore, the spontaneous scattering effect is caused by the mechanical and thermal excitation of the medium with an intensity that is proportional to the intensity of the incident light beam. However, whenever the intensity of the incident light is sufficiently larger than a certain threshold, the optical properties of the material are modified, becoming a nonlinear process. In this case, the scattering effect becomes stimulated. This process will be described in detail in forthcoming sections (1.3).

If the media is inhomogeneous, e.g. an optical fiber, the scattering process removes some photons of the incident light generating scattered photons that might be shifted in direction, frequency and phase. There are different scattering mechanisms depending on the energy transfer of the medium to the scattered photon, existing two main types:

- **Elastic scattering:** the scattered photons maintain the same energy and hence, they have the same frequency that the incident light.

- **Inelastic scattering:** as a result of an energy transfer between the photons and the medium, the scattered photons have a different energy and consequently, they are frequency-shifted. If the energy is taken by the media, then the scattered photons are down-shifted in frequency and are called Stokes components. On the contrary, if the energy is given from the medium, the scattered photons are up-shifted being called anti-Stokes components.

Figure 1.1 depicts the various types of light scattering when a monochromatic wave of frequency ν_0 propagates through an optical fiber [1]. Four types of scattering effects are shown:

- **Rayleigh scattering:** results from fixed density fluctuations of the medium, i.e. from variations of the molecular organization state. The scattered light has no frequency-shift, being an elastic phenomenon.

- **Rayleigh-wing scattering**: is caused by fluctuations in the orientation of the anisotropic molecules in the medium.

- **Brillouin scattering:** is caused by the propagation of density fluctuations of the medium resulting from propagating pressure waves. It is an inelastic scattering, where the light is scattered by acoustic phonons with a frequency-shift resulting from the Doppler effect and hence, determined by the acoustic velocity in the medium. Depending on the propagation direction of the acoustic wave, the frequency of the scattered light is down-shifted (Stokes component) when the acoustic wave is moving away from the incident light, while the frequency is up-shifted for the other case.
- **Raman scattering:** results from the interaction between light and molecular vibrations modes. The incident photons exchange energy with optical phonons, which have considerably more energy than the acoustic waves involved in Brillouin scattering. This makes Raman scattering a highly inelastic process characterized by a frequency shift three orders of magnitude higher than in Brillouin scattering.

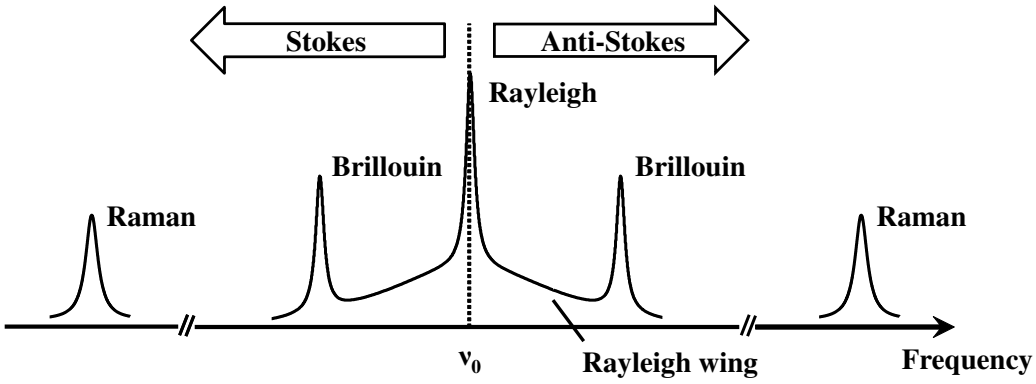

Fig. 1.1. Spectral components resulting from light scattering in inhomogeneous medium.

In the following sections, the spontaneous and stimulated Brillouin scattering will be described, omitting the rest of scattering effects as the main contribution of this thesis dissertation is based on Brillouin scattering.

1.2 Spontaneous Brillouin scattering: a linear regime

Spontaneous Brillouin scattering (SpBS) can be described by the analysis of the pressure waves that induce fluctuations in the dielectric permittivity. The equation of motion for a pressure wave is well known from the field of acoustics and is given by [1]:

$$\frac{\partial^2 \Delta p}{\partial t^2} - \Gamma \nabla^2 \frac{\partial \Delta p}{\partial t} - \upsilon_a \nabla^2 \Delta p = 0 \tag{1.1}$$

where Γ is the damping rate and v_a is the acoustic velocity in the medium expressed in terms of thermodynamic variables as:

$$v_a = \sqrt{\frac{K_s}{\rho}} = \sqrt{\frac{1}{C_s \rho}} \tag{1.2}$$

where ρ is the density of the medium, K_s is the bulk modulus and C_s is the adiabatic compressibility. As an illustration of the nature of the acoustic wave equation (1.1), the following propagation wave can be considered [1]:

$$\Delta p = \Delta p_0 \exp\left[i\left(\mathbf{q}\cdot\mathbf{r} - \Omega t\right)\right] + \text{c.c.} \tag{1.3}$$

where $\Omega = v_a|\mathbf{q}|$ is the frequency of the acoustic wave and $\mathbf{q}$ its wave vector. In order to study the interaction between the incident beam light and the acoustic wave, a monochromatic wave is assumed and given by [1]:

$$\mathbf{E} = E_0 \exp\left[i\left(\mathbf{k}\cdot\mathbf{r} - \omega t\right)\right] + \text{c.c.} \tag{1.4}$$

where ω is its frequency and $\mathbf{k}$ is the wave vector. The scattered light can be described by the use of the perturbed wave equation derived from the Maxwell's equation [1]:

$$\nabla^2\mathbf{E} - \frac{n^2}{c^2}\frac{\partial^2\mathbf{E}}{\partial t^2} = \mu_0 \frac{\partial^2\mathbf{P}}{\partial t^2} \tag{1.5}$$

where n is the refractive index of the medium, c is the speed of light in vacuum, μ_0 is the magnetic permittivity in vacuum, $\mathbf{E}$ is the electric field of the wave, $\mathbf{P}$ is the polarization field induced by electric dipoles. In the case of linear optics, the induced polarization depends linearly on the electric field [1]:

$$\mathbf{P} = \Delta\chi\mathbf{E} = \Delta\varepsilon\mathbf{E} \tag{1.6}$$

where $\Delta\chi$ is the fluctuation of the dielectric susceptibility and $\Delta\varepsilon$ is the fluctuation of the dielectric constant, which both affect the refractive index of the medium $n = \sqrt{\varepsilon/\varepsilon_0} = \sqrt{1+\chi}$. Assuming that the variations of the density are given by adiabatic density fluctuations i.e. acoustic waves, then Eq. (1.6) yields [1]:

$$\mathbf{P} = \varepsilon_0 \left(\frac{\partial\varepsilon}{\partial\rho}\right)\left(\frac{\partial\rho}{\partial p}\right)\Delta p\,\mathbf{E} = \varepsilon_0 \gamma_e C_s \Delta p\,\mathbf{E} \tag{1.7}$$

where γ_e is the electrostrictive constant and ε_0 is the dielectric permittivity in the vacuum.

By combining Eq. (1.3) through Eq.(1.5) and Eq. (1.7), the scattered light is given by [1]:

$$\nabla^2\mathbf{E}-\frac{n^2}{c^2}\frac{\partial^2\mathbf{E}}{\partial t^2}=-\frac{\gamma_e C_s}{c^2}\Big[(\omega-\Omega)^2 E_0\Delta p_0^*\exp\left[i(\mathbf{k}-\mathbf{q})\cdot\mathbf{r}-i(\omega-\Omega)t\right] + (\omega+\Omega)^2 E_0\Delta p_0\exp\left[i(\mathbf{k}+\mathbf{q})\cdot\mathbf{r}-i(\omega+\Omega)t\right]+\text{c.c.}\Big] \tag{1.8}$$

The first term in Eq. (1.8) is the Brillouin Stokes component with frequency $\omega'=\omega-\Omega$ and wave vector $\mathbf{k}'=\mathbf{k}-\mathbf{q}$. The second term is the Brillouin anti-Stokes component with frequency $\omega'=\omega+\Omega$ and wave vector $\mathbf{k}'=\mathbf{k}+\mathbf{q}$.

1.2.1 Conservation of momentum and energy

The acoustic phonons of Brillouin scattering carry a momentum that grows proportionally to the phonon frequency, the proportionally factor being given by the acoustic velocity of the medium. The energy and the momentum must be conserved during the interaction, consequently the observation of Brillouin scattering is subject to very strict phase-mismatch condition due to the large momentum involved in the interaction. Simultaneously applying energy and momentum conservation to the 3 interacting waves in the Stokes case (see Table 1.1) is obtained [3]:

Energy conservation:

$$\frac{h}{2\pi}\omega=\frac{h}{2\pi}\left(\omega'+\Omega\right) \tag{1.9}$$

Momentum conservation:

$$h\mathbf{k}=h\left(\mathbf{k}'+\mathbf{q}\right) \tag{1.10}$$

This translates into a set of coupled equations by making explicit each component of Fig. 1.2 [3]:

$$\begin{cases}|\mathbf{k}'|\sin\theta=|\mathbf{k}'|\sin\theta'\\ |\mathbf{k}|=|\mathbf{k}'|\cos\theta+|\mathbf{q}|\cos\theta'\end{cases}$$

After squaring and summing these coupled equations and using the relationships between frequencies and wave vectors, the following relation is obtained considering that the acoustic velocity is much smaller than the light velocity [3]:

$$\Omega=\frac{2n\omega v_a}{c}\sin\left(\frac{\theta}{2}\right) \tag{1.11}$$

Note that the acoustic frequency depends on the angle of the scattered light, being zero for forward scattering ($\theta=0$). On the other hand, the maximum frequency shift, known as

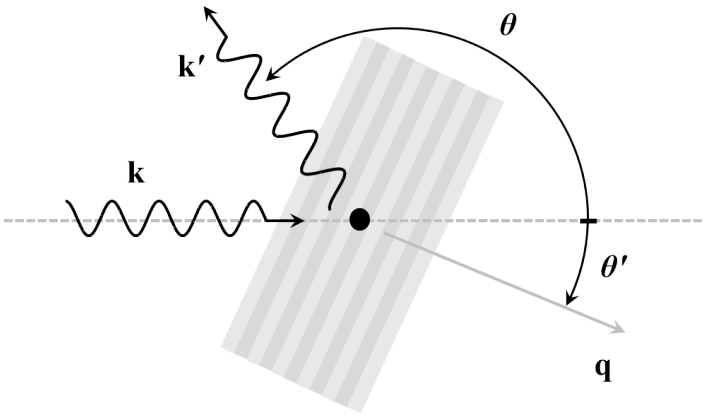

Fig. 1.2. Relation between the wave vectors of the acoustic, incident and scattered waves. The scattered light is considered a Stokes component as the acoustic wave propagates in the same direction of the incident light.

Brillouin frequency shift, occurs for backward scattering ($\theta = \pi$):

$$\Omega_B = \frac{2n\omega v_a}{c} \tag{1.12}$$

Note that in single-mode fibers (SMF), there are only two possible propagation directions for the scattered light, the forward or backward. Consequently, Brillouin scattering signal is a backscattered light, exhibiting the maximum frequency shift ($\nu_B = \Omega_B/2\pi$) around 10.8 GHz at 1550 nm.

	Frequency	Wavevector	Relation
Incident wave	ω	$\mathbf{k}$	$\omega = \lvert\mathbf{k}\rvert\,(c/n)$
Scattered Stokes wave	$\omega' = \omega - \Omega$	$\mathbf{k}' = \mathbf{k} - \mathbf{q}$	$\omega' = \lvert\mathbf{k}'\rvert\,(c/n)$
Acoustic wave	Ω	$\mathbf{q}$	$\Omega = \lvert\mathbf{q}\rvert v_a$

Table 1.1 Frequencies and wave vectors of the 3 waves involved in Brillouin scattering process and the relation between the frequency and the wavevector.

1.2.2 Brillouin spectrum and linewidth

The Brillouin scattered light of a monochromatic incident light has a certain linewidth due to the attenuation of the acoustic wave presented in Eq. (1.3). Substituting the acoustic wave that is considered to propagate along the axis of the fiber in Eq. (1.1), then q and Ω must

satisfy the following dispersion relation:

$$\Omega^2 = q^2\left(\upsilon_a^2 - i\Omega\Gamma\right) \tag{1.13}$$

This relation can be expressed as [2]:

$$q \simeq \frac{\Omega}{\upsilon_a} + \frac{i\Gamma_B}{2\upsilon_a} \tag{1.14}$$

where $\Gamma_B = \Gamma q^2$ is the phonon decay rate. Substituting the latter expression in Eq. (1.3), it can be demonstrated that the intensity of the acoustic wave varies spatially as [2]:

$$|\Delta p\,(z)\,|^2 = |\Delta p_0|^2 \exp\left(-\alpha_s z\right) \tag{1.15}$$

being α_s the sound absorption coefficient given by [2]:

$$\alpha_s = \frac{\Gamma_B}{\upsilon_a} \tag{1.16}$$

and hence, the phonon lifetime is defined as:

$$\tau_p = \frac{1}{\Gamma_B} \tag{1.17}$$

As a consequence of exponential damping shape of Eq. (1.15), it can be found that, in the frequency domain, the Brillouin components are not monochromatic and exhibit a Lorentzian spectral profile given by [2]:

$$g_{SBS}\left(\nu\right) = g_0 \frac{\left(\Delta\nu_B/2\right)^2}{\left(\nu - \nu_B\right)^2 + \left(\Delta\nu_B/2\right)^2} \tag{1.18}$$

where $\Delta\nu_B = \Gamma_B/2\pi$ is the full-width half-maximum (FWHM) Brillouin linewidth and g_0 is the Brillouin peak at resonance $\nu = \nu_B$.

1.3 Stimulated Brillouin scattering: a nonlinear regime

In the previous section, the analysis focused on the spontaneous Brillouin scattering caused by a polarization field that has a linear proportional relation with the applied electric field (see Eq. (1.6)). This effect is observed under low intensity conditions, where the incident light is scattered by fluctuations of optical properties of a material induced by thermal or quantum-mechanical zero-point effects. During this section, the analysis will study the effect

caused when a high intensity is injected in the medium. It alters the optical properties of the medium, becoming in a stimulated process, which are typically much more efficient than the spontaneous scattering effects.

As a result of the high intensities used to stimulate the process, the polarization field induced by the electric dipoles is now a nonlinear function of the electrical field given by:

$$\mathbf{P_{NL}} = \chi_3 \vdots \mathbf{EEE} \tag{1.19}$$

where χ_3 is the third-order susceptibility responsible of the stimulated scattering effects. Taking into account the attenuation coefficient α and the non-linear polarization field, the perturbed wave equation shown in Eq. 1.5 is now expressed as [4]:

$$\nabla^2\mathbf{E} - \frac{n^2}{c^2}\frac{\partial^2\mathbf{E}}{\partial t^2} - \frac{\alpha n}{c}\frac{\partial \mathbf{E}}{\partial t} = \mu_0 \frac{\partial^2 \mathbf{P^{NL}}}{\partial t^2} \tag{1.20}$$

During the following sections, the details of nonlinear scattering resulting from induced density variations of a material system will be described focusing on the most important example of such processes: stimulated Brillouin scattering. This process can be stimulated thanks to two different physical mechanisms that drive the acoustic wave: electrostriction and optical absorption. The first mechanism will be described in detail in the following section. The second is based on the heat induced by absorption in regions of high optical intensity, which tends to cause the material to expand in those regions. The density variation excites and acoustic disturbance generating SBS. However, absorptive SBS is less commonly used than electrostrictive SBS, since it can occur only in lossy optical media. For this reason the electrostrictive case will only be studied in this chapter.

1.3.1 Electrostriction

The tendency of materials to compress in the presence of an electric field is described as electrostriction [2]. Electrostriction is of interest both as a mechanism leading to a third-order nonlinear optical response and as a coupling mechanism that leads to stimulated Brillouin scattering. The origin of the electrostrictive force can be described from a global point of view as a consequence of the maximization of stored energy [2]. This force acts on each individual molecule placed in the electric field, developing a dipole moment. Considering this force and the energy stored in the polarization of each molecule, the strictive pressure is obtained:

$$p_{st} = -\frac{1}{2}\varepsilon_0 \rho \left(\frac{\partial \varepsilon}{\partial \rho}\right) \langle \mathbf{E}\cdot\mathbf{E}\rangle = -\frac{1}{2}\varepsilon_0 \gamma_e \langle \mathbf{E}\cdot\mathbf{E}\rangle \tag{1.21}$$

where the angular brackets denote a time average over an optical period. Since p_{st} is negative, the total pressure is reduced in regions of high field strength inducing variations of the density, which can be written (considering Eq. (1.21)) as:

$$\Delta\rho = -\rho\left(\frac{1}{\rho}\frac{\partial\rho}{\partial p}\right)p_{st} = -\rho C p_{st} \tag{1.22}$$

where $C = \rho^{-1}(\partial\rho/\partial p)$ is the compressibility of the material. Substituting Eq. (1.21) in Eq. (1.22), it is found:

$$\Delta\rho = \frac{1}{2}\varepsilon_0\rho C\gamma_e\langle\mathbf{E}\cdot\mathbf{E}\rangle \tag{1.23}$$

If the changes in the susceptibility in the presence of an optical field are represented as $\Delta\chi = \Delta\varepsilon$, where $\Delta\varepsilon = (\partial\varepsilon/\partial\rho)\Delta\rho$ and $\Delta\rho$ is given by Eq. (1.23), then it yields:

$$\Delta\chi = \varepsilon_0 C_T \chi_e^2 |\mathbf{E}|^2 \tag{1.24}$$

where two monochromatic waves that differ by approximately the Brillouin frequency shift have been assumed. Consequently, the complex amplitude of the nonlinear polarization fields is given by [1]:

$$\mathbf{P_{NL}} = \varepsilon_0 C_T \chi_e^2 |\mathbf{E}|^2 \mathbf{E} \tag{1.25}$$

By inserting Eq. 1.25 into the perturbed wave equation presented in Eq. 1.20 for the two optical waves involved in SBS and considering the acoustic wave, it is possible to obtain the coupled-wave equations for SBS presented in the following section.

1.3.2 Stimulated Brillouin scattering induced by electrostriction

As shown in section 1.3.1, electrostriction is one of the necessary mechanism to generate SBS in optical fibers. The effect is exploited by the interference generated between two signals, a pump and a probe wave that counter-propagate in a section of an optical fiber. When the interference frequency between both waves is approximately the Brillouin frequency shift of the fiber, an acoustic wave is generated through electrostriction. This acoustic wave modulates the refractive index of the fiber generating a moving Bragg grating that scatters the pump signal. Due to the Doppler effect, the scattered light is down-shifted by the Brillouin frequency shift when the acoustic wave propagates in the same direction than the pump signal, or it is up-shifted on the contrary case. In the first case, the Stokes signal adds constructively to the probe signal, reinforcing the acoustic wave. In the second case, the anti-Stokes signal is depleted due to the energy transfer to the pump signal.

1.3.3 Theoretical model of SBS (steady-state solution)

The complete process described above between the probe wave $E_S(z,t)$, the pump signal $E_P(z,t)$ and the acoustic wave $Q(z,t)$ can be modeled (under the assumption of plane-wave interaction) by the following system of coupled equations [1]:

$$\left[\frac{\partial}{\partial z}+\frac{n}{c}\frac{\partial}{\partial t}+\alpha_P\right]E_P(z,t)=\frac{i\omega_P\gamma_e}{2nc\rho_0}QE_S(z,t) \tag{1.26a}$$

$$\left[-\frac{\partial}{\partial z}+\frac{n}{c}\frac{\partial}{\partial t}+\alpha_S\right]E_S(z,t)=\frac{i\omega_S\gamma_e}{2nc\rho_0}Q^*E_P(z,t) \tag{1.26b}$$

$$\left[-2iq\upsilon_a^2\frac{\partial}{\partial z}-2i\Omega\frac{\partial}{\partial t}+\left(\Omega_B^2-\Omega-i\Omega\Gamma_B\right)\right]Q(z,t)=\varepsilon_0\gamma_e q^2E_P(z,t)E_S^*(z,t) \tag{1.26c}$$

In order to obtain the evolution of $E_S(z,t)$, the previous system of equations can be solved either directly, through numerical integration or analytically with some preliminary simplifications. For instance, solving the three wave equations is only meaningful, whenever the interaction is shorter than the acoustic lifetime (τ_p), while if the interaction is longer, the steady state is reached and all time derivatives can be neglected [3]. Moreover, the acoustic velocity is assumed to be much smaller than the light velocity, so that the acoustic wave is taken as static and in addition, it vanishes after propagation over a few optical wavelengths (distance over which any change of the optical field is negligible [3]). Consequently the spatial derivative in Eq. (1.26c) is set equal to zero. After considering all these approximations, Eq. (1.26c) can be directly solved, yielding [3]:

$$Q(z)=\varepsilon_0\gamma_e q^2\frac{E_P(z)E_S^*(z)}{\Omega_B^2-\Omega^2-i\Omega\Gamma_B} \tag{1.27}$$

Assuming that the frequency difference between pump and probe is very close ($\omega=\omega_S\approx\omega_P$), so that the attenuation is considered approximately equal for both optical frequencies ($\alpha=\alpha_S\approx\alpha_P$), then Eq. (1.26a) and (1.26b) become, after substitution of Eq. (1.27), in:

$$\frac{d}{dz}E_P(z)=\frac{i\varepsilon_0\omega\gamma_e^2q^2}{2nc\rho_0}\frac{|E_S(z)|^2E_P(z)}{\Omega_B^2-\Omega^2-i\Omega\Gamma_B}-\alpha E_P(z) \tag{1.28a}$$

$$\frac{d}{dz}E_S(z)=-\frac{i\varepsilon_0\omega\gamma_e^2q^2}{2nc\rho_0}\frac{|E_P(z)|^2E_S(z)}{\Omega_B^2-\Omega^2+i\Omega\Gamma_B}+\alpha E_P(z) \tag{1.28b}$$

Note that Eq. (1.28b) shows that SBS is a pure gain process, whose gain depends basically on the pump or probe intensities. Defining the intensity as $I(z)=2n\varepsilon_0c|E(z)|^2$, it is possible

to write the coupled intensity equations as:

$$\frac{d}{dz}I_P(z) = -g_{SBS}(\nu)\, I_P(z)\, I_S(z) - \alpha I_P(z) \tag{1.29a}$$

$$\frac{d}{dz}I_S(z) = -g_{SBS}(\nu)\, I_P(z)\, I_S(z) + \alpha I_S(z) \tag{1.29b}$$

where I_P and I_S are the intensities of pump and probe, respectively and g_B is the Brillouin gain transfer given by Eq. (1.18). Assuming that no depletion is observed on the pump wave, the pump intensity exponentially decays along the fiber ($I_P(z) = I_P(0)\,\mathrm{e}^{-\alpha z}$), being $I_P(0)$ the intensity at the input of the fiber ($z = 0$). Substituting the previous expression in Eq. (1.29b), the following solution for the Stokes wave is obtained:

$$\begin{aligned} I_S(z) = {} & I_S(L)\exp\left[-\alpha(L-z)\right]\cdot \\ & \cdot\exp\left[g_{SBS}(\nu)\, I_P(0)\exp(-\alpha z)\,\frac{1-\exp\left[-\alpha(L-z)\right]}{\alpha}\right] \end{aligned} \tag{1.30}$$

where $I_S(L)$ is the Stokes signal at the input of the fiber ($z = L$) and the expression in brackets of the second exponential term represents the whole interaction length of I_S to the location z. This expression is the known parameter of the effective length of the fiber, which is conventionally defined from $z = 0$ obtaining:

$$L_{eff} \equiv \frac{1-\exp(-\alpha L)}{\alpha} \tag{1.31}$$

Note that Eq. (1.30) shows that the Stokes signal exponentially grows due to SBS along its propagation and logically, it is also attenuated due to the absorption coefficient of the optical fiber. While this solution has been obtained for a gain-based BOTDA configuration, the system of equations in (1.29) could be also valid for a loss-based BOTDA sensor. This can be modelled by simply changing the sign for the Brillouin interaction term in both equations.

1.3.4 SBS threshold

As shown in Eq. (1.30), the injected signal grows in the backward direction because of Brillouin amplification occurring as a result of SBS [2]. However, when this signal is not used, the Stokes wave grows from spontaneous Brillouin scattering that is initiated by phonons resulting from thermal agitation in the fiber. This effect can be modelled by injecting a fictitious photon per mode at a distance where the gain exactly equals the fiber loss, i.e. the power of the Stokes components at the input of the pump wave is equal to the pump power at the output of the fiber. This is defined as the SBS threshold, which occurs for a critical pump

power [2]:

$$P_{th}^{SBS} \approx 21 \frac{A_{eff}}{g_0 L_{eff}} \tag{1.32}$$

where A_{eff} is the effective area. Using the typical values for fibers in 1550 nm optical communication systems, A_{eff} =80 μm^2, L_{eff} ≈20 km and g_0 =1.5·10^{-11} m/W, the critical power is approximately 5.6 mW, what makes SBS a dominant nonlinear process.

1.4 Distributed fiber sensors based on Brillouin scattering

Stimulated Brillouin scattering can be employed for making distributed fiber sensors capable of sensing temperature or strain changes. The basic idea of using this phenomenon relies on the linear dependence of the Brillouin frequency shift with the acoustic velocity and the refractive index of the optical fiber (see Eq. (1.12)). These quantities vary with the temperature or the strain, and hence, the BFS value is modified. Moreover, the BFS variations have been demonstrated to shown an excellent linearity for both measurands over a wide range. This relationship can be described with the following expression [5]:

$$\nu_B(T, \delta\varepsilon) - \nu_{B0} = A \cdot \delta\varepsilon + B \cdot (T - T_0) \tag{1.33}$$

where ν_{B0} is the BFS measured at room temperature (T_0=25°C) and in loose state of the fiber, $\delta\varepsilon$ is the strain difference and T is the temperature. The constants A and B are given by [5]:

$$A' = \frac{A}{\nu_{B0}} = \frac{\partial n}{n\partial\varepsilon} - \frac{\partial\rho}{2\rho\partial\varepsilon} + \frac{\partial E_1}{2E_1\partial\varepsilon} \tag{1.34a}$$

$$B' = \frac{B}{\nu_{B0}} = \frac{\partial n}{n\partial T} - \frac{\partial\rho}{2\rho\partial T} + \frac{\partial E_1}{2E_1\partial T} \tag{1.34b}$$

where E_1 is the second-order nonlinear coefficient of Young's module. In addition to the BFS parameter, there exist another relation between the Brillouin gain and linewidth with the temperature or strain that could be useful to monitor or distinguish the quantities of these variables [6]. However, the Brillouin frequency shift is the parameter measured with highest resolution and hence, the most convenient for distributed Brillouin fiber sensors.

1.4.1 Types of Brillouin distributed sensors

There are different kinds of distributed fiber sensors based on stimulated Brillouin scattering. They are classified depending on the principle used to retrieve the Brillouin spectrum distribution along the fiber. Basically, there are analysis based on: correlation domain, denominated

Brillouin optical correlation-domain analysis (BOCDA) sensor, frequency domain, named Brillouin optical frequency-domain analysis (BOFDA) and time domain, called Brillouin optical time-domain analysis (BOTDA) sensor.

During the following subsections, the BOFDA and BOCDA will be described to finally focus in the BOTDA sensor, which is the technique studied and developed during the development of this thesis.

1.4.2 Brillouin optical correlation-domain analysis

Brillouin optical correlation-domain analysis sensor was proposed for the first time in 2000 as a very attractive solution to achieve high spatial resolution (around 40 cm) over short distances [7]. Since then, this technique has been improved being able to detect variations of temperature or strain with a length of a few milimeters [8].

The BOCDA technique is based on the counter-propagation of quasi-CW pump and probe waves that are identically frequency-modulated by a sinusoidal function. When both waves counter-propagate through the fiber, the frequency difference stays constant for some points of the fiber (called nodes), while it continuously varies for the other positions as shown in Fig. 1.3. Considering that both waves are frequency-shifted by the BFS of the fiber, the SBS occurs exclusively at these nodes denominated here as correlation peak positions. In the rest of the fiber, the frequency difference varies much more rapidly than the time required to excite the acoustic wave and hence, the Brillouin transfer is negligible. Therefore, only at the correlation peaks positions, the acoustic wave is properly created transferring the gain between the pump and probe waves. Then, sweeping the frequency difference between both signals, the Brillouin spectrum is scanned. It must be remarked that the frequency of the sinusoidal function and the delay induced by one of the branches must be carefully selected to scan only one point of the fiber. Otherwise, the technique would be scanning different points at the same time being impossible to determine the Brillouin spectrum of each location. Once there is a correlation peak along the fiber, the location of this point can be adjusted to scan other positions by simply varying the modulation frequency and repeating again the frequency swept. In this way, the whole length of the fiber is scanned.

This technique has remarkable performance regarding the achieved spatial resolution. This parameter is given by the modulation depth and the Brillouin intrinsic linewidth and consequently, as it has been mentioned before, it can reach higher spatial resolutions than other techniques. Moreover, the measured linewidth of the Brillouin spectrum does not broaden since the acoustic wave is continuously excited. However, each point of the sensing fiber must be individually scanned before continuing with the next point. Consequently, the

measurement time is lineal proportional to the number of points resolved by the system being excessively high compared to BOTDA sensors.

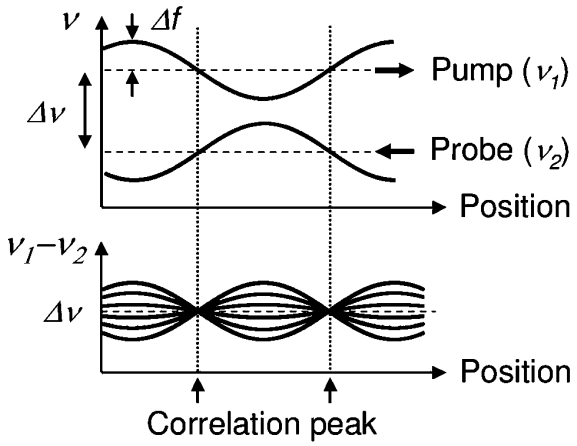

Fig. 1.3. Operation principle of BOCDA; ν represents optical frequency ©2008, IEEE [9].

1.4.3 Brillouin optical frequency-domain analysis

Brillouin optical frequency-domain analysis sensors were firstly presented in 1996 [10]. The technique relies on the measurement of the complex transfer function of the fiber given by the relation between the amplitudes of the pump and probe waves. The technique deploys two counter-propagating signals, a CW pump signal and a probe wave frequency-shifted by the BFS that is amplitude-modulated by a sine function. The resulting interaction of both signals is detected by two separate photoreceivers that fed a network analyzer. The procedure is repeated by changing the frequency modulation of the sinusoidal function. Once the frequency modulation is swept, the network analyzer provides the transfer function of the fiber, which is inverse Fourier transformed to retrieve the Brillouin response for each section of the fiber.

This technique can provide measurements with high spatial resolution, which depends on the frequency range swept. However, in contrast to the BOCDA technique, the spatial resolution is limited by the lifetime of the acoustic phonon and hence, by the Brillouin gain spectrum (BGS) linewidth. Consequently, the interaction results very weak leading to a low signal-to-noise ratio (SNR). Furthermore, if long distances and high spatial resolutions are required, the number of frequencies needed to measure the transfer function of the fiber is larger, and hence it considerably increases the measurement time. Finally, the performance of this sensor has been worse than other Brillouin distributed fiber sensors, although recently,

a post-processing method has allowed to monitor 5.5 km with 3 cm of spatial resolution, proving them as a valid solution [11].

1.4.4 Brillouin optical time-domain analysis

Brillouin optical time-domain analysis sensors were first demonstrated in 1990 for temperature [12] and strain [13] monitoring. Since then, BOTDA technology has been the most widely used Brillouin distributed sensor with applications in numerous fields [14–16]. The principles of the technique are depicted in Fig. 1.4. It is based on the Brillouin interaction

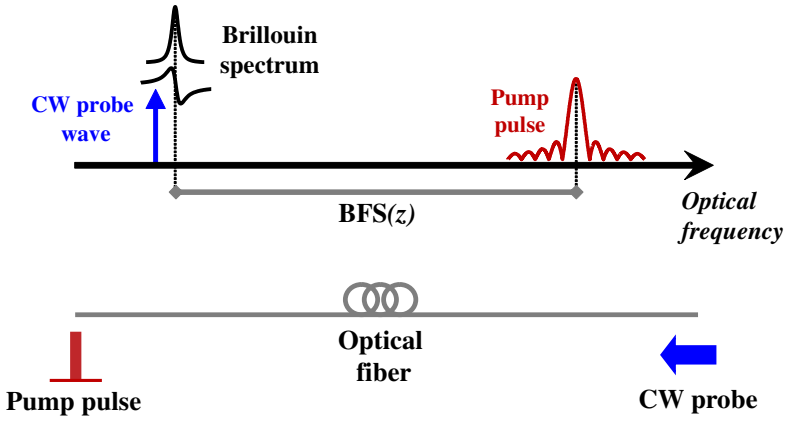

Fig. 1.4. Operation principle of BOTDA: a pulsed signal and a CW signal counter-propagates through an optical fiber with a frequency difference around the BFS.

between two counter-propagating signals: a pulsed pump and a CW probe signal with a frequency difference around the BFS of the fiber. During the propagation of the pulsed signal, an acoustic wave is locally generated, whose characteristics depend on the fiber section where both signals meet. This acoustic wave couples energy between both signals; depending on the relative frequency of the probe wave regarding the pulsed signal, the probe wave suffers amplification ($\nu_P - \nu_S \approx \nu_B$) or depletion ($\nu_S - \nu_P \approx \nu_B$) at each location of the fiber. The time-dependent information retained by the probe signal serves as reference to measure the Brillouin gain/loss for a given frequency detuning (see Fig. 1.5). This temporal evolution of the probe wave can be directly translated to a position-dependent information using the round-trip time relation:

$$z = \frac{c}{2n} t \tag{1.35}$$

where t is the measured time since the pulse signal enters the fiber and z the location where pulse and probe waves meet. In order to measure the BFS, it is necessary to determine the frequency difference at which the gain is maximum for each location of the fiber. Therefore,

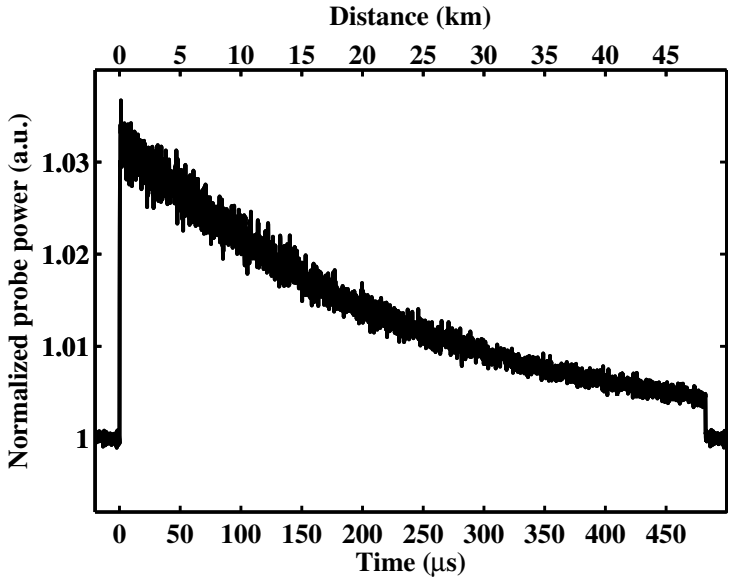

Fig. 1.5. Evolution of the probe signal in BOTDA sensors along the fiber for a given frequency difference between probe and pump waves.

a frequency swept of the frequency difference between pump and probe wave must be done and each time-domain trace saved. Sorting the different traces with the frequency difference, the Brillouin spectrum distribution is reconstructed (see Fig. 1.6). The accurate BFS of the fiber is then obtained by fitting these measurement spectra to the theoretical model for the Brillouin gain presented in Eq. (1.18).

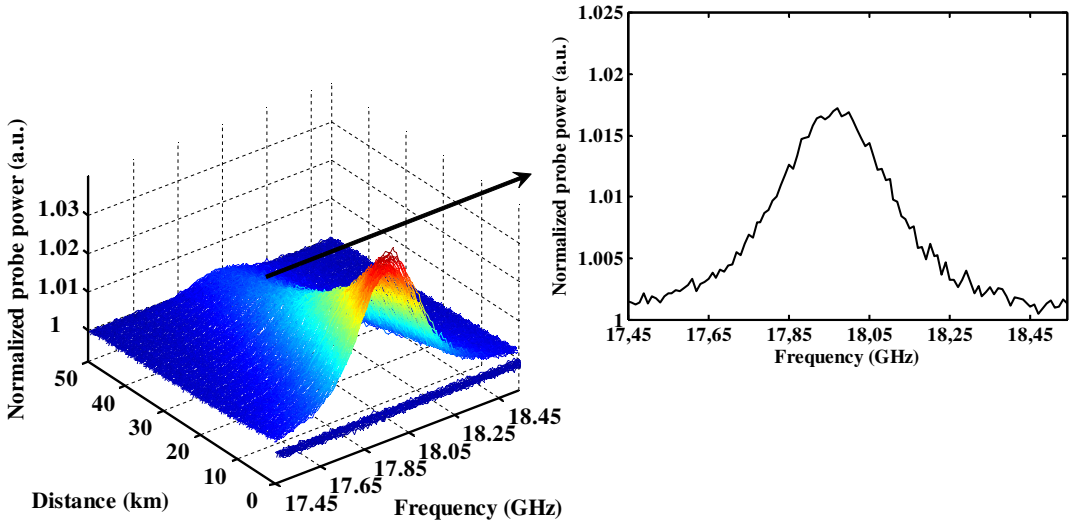

Fig. 1.6. Reconstructed Brillouin distribution spectra along the fiber.

Theoretical model for BOTDA sensors

As it was previously mentioned, while the pulsed signal propagates through the fiber, it transfers energy to the probe wave being amplified at each location. The amplification of the probe wave shown in Fig. 1.5 can be modeled by solving the steady-state equation system shown in Eq. 1.28 and repeated here for clarity using the notation for BOTDA sensors used in [17]:

$$\frac{d}{dz}E_P(z) = \left[-\frac{g_0}{2}\frac{i\Delta\nu_B}{i\Delta\nu_B + 2\Delta\nu}|E_S|^2 - \frac{\alpha}{2}\right]E_P \tag{1.36a}$$

$$\frac{d}{dz}E_S(z) = \left[-\frac{g_0}{2}\frac{i\Delta\nu_B}{i\Delta\nu_B - 2\Delta\nu}|E_P|^2 + \frac{\alpha}{2}\right]E_S \tag{1.36b}$$

where E_P and E_S are the optical field of pump and probe waves, respectively, g_0 is the Brillouin gain coefficient, $\Delta\nu = \nu_S - \nu_P + \nu_B$ is the frequency detuning of the probe signal regarding the Brillouin peak frequency, ν_S and ν_P are the optical frequencies of probe and pump signals, respectively, being $\nu_S < \nu_P$. The pump pulse propagates to $z = L$ and the probe wave to $z = 0$. Assuming that the pulsed signal only experiences the fiber attenuation through its propagation, i.e. the Brillouin interaction is negligible, then Eq. (1.36a) can be directly solved obtaining:

$$E_P(z) = E_{Pi}\exp\left[-\frac{\alpha}{2}z\right] \tag{1.37}$$

where E_{Pi} is the input pump optical field. This result can be directly used in Eq. (1.36b) to calculate the Brillouin interaction suffered by the probe wave at a given location z when both waves interact.

$$E_S(z-\Delta z) = E_S(z)\exp\left[\frac{g_0}{2}\frac{(\Delta\nu_B/2)^2 - i(\Delta\nu\Delta\nu_B/2)}{(\Delta\nu_B/2)^2 + \Delta\nu^2}|E_P(z)|^2\Delta z\right] \tag{1.38}$$

where $\Delta z = T_P \cdot c/(2n)$ is the spatial resolution of the system and T_P is the temporal pulse duration. Note that in Eq. (1.38), it has been assumed that the attenuation of the pump pulse during the Brillouin interaction is negligible due to the short interaction length between both waves, and hence the pulsed signal maintains its amplitude. Note also that Eq. (1.38) shows that at a given location z, the probe field changes in amplitude and phase due to SBS process, but until that location, the probe wave only attenuates and after Brillouin interaction, it continues attenuating until it reaches the receiver, yielding:

$$E_S(z)\Big|_{rx} = E_{Si}\exp\left(-\frac{\alpha}{2}L\right)\exp\left(\frac{g_0}{2}\frac{(\Delta\nu_B/2)^2 - i(\Delta\nu\Delta\nu_B/2)}{(\Delta\nu_B/2)^2 + \Delta\nu^2}|E_P(z)|^2\Delta z\right) \tag{1.39}$$

where E_{Si} is the input probe optical field at the input of the fiber ($z = L$). Substituting Eq. (1.37) in Eq. (1.39) and calculating the detected optical power at the output of the receiver, the following expression is obtained:

$$P_S(z)\Big|_{rx} = P_{Si}\exp(-\alpha L)\exp\left(\frac{g_0}{A_{eff}}\frac{(\Delta\nu_B/2)^2}{(\Delta\nu_B/2)^2+\Delta\nu^2}P_{Pi}\exp(-\alpha z)\Delta z\right) \tag{1.40}$$

where P_{Pi} and P_{Si} are the input optical powers of the pump and probe waves, respectively, and A_{eff} is the effective area of the fiber. Note that Eq. (1.40) shows the measured response of the BOTDA sensor for any location of the fiber, which can be further simplified assuming that the BOTDA sensor operates in a small signal regime, yielding:

$$P_S(z)\Big|_{rx} \approx P_{Si}\exp(-\alpha L)\left[1+\frac{g_0}{A_{eff}}\frac{(\Delta\nu_B/2)^2}{(\Delta\nu_B/2)^2+\Delta\nu^2}P_{Pi}\exp(-\alpha z)\Delta z\right] \tag{1.41}$$

where the second term in the bracket represents the Brillouin gain of the sensor. Note that the Brillouin gain is proportional to the gain coefficient, the local pump power and the pulse duration [18]. Moreover, if the Brillouin frequency is uniform along the fiber, then the trace shows an exponential decrease as a function of the distance of the fiber. However, if the Brillouin gain is not uniform, then the position dependence of $\Delta\nu_B(z)$ will determine a gain profile different from the exponential decay. This will also be the case if the pump is subject to distributed amplification or any type of nonlinear interaction [18]. Considering that both waves only suffer the attenuation along the fiber, it is evident that the larger the sensing fiber, the smaller is the Brillouin interaction at the end of the fiber ($z = L$). Consequently, under standard BOTDA conditions, the worst-case sensor precision must be demonstrated with measurements performed at the end of the fiber, where the sensor response is [18]:

$$P_S(L)\Big|_{rx} \approx P_{Si}\exp(-\alpha L)+\frac{g_0}{A_{eff}}\frac{(\Delta\nu_B/2)^2}{(\Delta\nu_B/2)^2+\Delta\nu^2}P_{Pi}P_{Si}\exp(-2\alpha L)\Delta z \tag{1.42}$$

Note that in Eq. (1.41) the Brillouin gain at a distant L is scaled by a factor $\exp(-\alpha L)$. However, this signal must propagate back to the receiver and hence the effect of the fiber attenuation turns out to be doubled ($\exp(-2\alpha L)$) as shown in Eq. (1.42). This fact is essential to grasp how the sensing distance impacts on the detected signal of BOTDA traces at the far end of the fiber [18].

Once the theoretical model of BOTDA sensors has been explained, the following section discusses the fundamental limitations of the technique.

1.5 State of the art and limitations of BOTDA sensors

The objective of BOTDA sensors is to retrieve the Brillouin frequency shift distribution profile of the fiber, i.e. the temperature and strain profiles, with the higher precision and the larger number of points along the fiber. Recently, the relation between the standard deviation of the BFS, which is defined as the precision of the sensor, and the parameters of the measured Brillouin spectrum has been established by calculating the propagation of errors on the parameters obtained from a least-square parabolic fit [18]:

$$\sigma_{BFS}(z) = \sqrt{\frac{1}{SNR(z)} \frac{3 \cdot \delta \cdot \Delta\nu_B}{8\sqrt{2}(1-\zeta)^{3/2}}} \tag{1.43}$$

where δ is the frequency step, ζ is the fraction of the peak level over which the quadratic least-square fitting is carried out and SNR is defined as the quadratic relation between the measured response of the Brillouin spectrum (see the second term of Eq. (1.41)) and the total noise power of the system. As shown in Eq. (1.43), the accuracy of the sensor basically depends on the signal-to-noise parameter, the Brillouin linewidth and the data used for the parabolic fit. Therefore, the standard deviation of the BFS can be improved by:

- Increasing the probe power: firstly limited by the apparition of non-local effects and secondly by the onset of intense amplified spontaneous Brillouin scattering.
- Increasing the pump power: limited by depletion induced by modulation instability or Raman effect.
- Incrementing the number of points scanned of the Brillouin spectrum: limited by the measurement time.

During the following subsections, each different issue will be further explained and the solutions proposed to solve or alleviate them will be reviewed.

1.5.1 Probe power limitations: non-local effects and spontaneous Brillouin scattering

When a pump pulse and a probe wave counter-propagate through an optical fiber, the pump pulse provides amplification to the probe wave as shown in section 1.4.4. Simultaneously, the Brillouin interaction slightly depletes the amplitude of the pump signal at each section of the fiber (as conveyed by Eq. (1.36a)). Due to the continuous interaction of the pulse with the probe wave, the impact becomes much higher on the pump pulse than on the probe wave,

which, for each time-resolved interval, only interacts once with the pump over a restricted length of the fiber determined by the pulse duration. As a consequence, in order to calculate the effect of the Brillouin interaction over the pulsed signal, it can be assumed that the probe signal only attenuates through the optical fiber. This assumption allows to directly solve Eq. (1.36a), yielding:

$$E_P(L) = E_{Pi} \exp\left(-\frac{\alpha}{2}L\right) \exp\left(-\frac{g_0}{2}\frac{(\Delta\nu_B/2)^2 - i(\Delta\nu\Delta\nu_B/2)}{(\Delta\nu_B/2)^2 + \Delta\nu^2}|E_{Si}|^2 L_{eff}\right) \tag{1.44}$$

Note that this equation shows the amplitude variation and phase-shift of the pump field induced by the Brillouin interaction. Calculating the optical power from Eq. (1.44), the pump power at the output of the fiber is:

$$P_P(L) = P_{Pi} \exp(-\alpha L) \exp\left(-\frac{g_0}{A_{eff}}\frac{(\Delta\nu_B/2)^2}{(\Delta\nu_B/2)^2 + \Delta\nu^2}P_{Si}L_{eff}\right) \tag{1.45}$$

Note that the previous expression assumes that the BFS of the fiber is uniform. As shown in Eq. (1.45), the power of the pulsed signal attenuates by the fiber losses but also due to the Brillouin interaction, which displays a frequency dependence given by the natural response of the Brillouin interaction. Due to the fact that Brillouin interaction is distributed along the fiber and is cumulative for the pump pulse, the effect is more severe at the far end of the fiber [19]. Consequently, the Brillouin spectra at those locations will be scanned with a pump pulsed signal that has a power dependent on the pump and probe frequency detuning, δ_{nu}. Due to the Brillouin gain dependence with the pulse power, non-local effects may distort the retrieved Brillouin gain spectrum at a section whose BFS differs from the uniform BFS section of the fiber. This would induce a bias of the peak frequency and hence, an error on the estimated BFS as shown in Fig. 1.7. It must be pointed out that both configurations, loss and gain, lead to a distorted Brillouin spectrum and hence, none of these configurations offers a decisive advantage [19]. The only difference resides on the biasing direction of the peak: while a gain configuration biases the peak to higher BFS values in Fig. 1.7, a loss configuration biases it to lower values. Analyzing the gain configuration, then the amount of depletion (d) suffered by the pulsed signal can be characterized by a dimensionless coefficient:

$$d = \frac{P_{P0} - P_P(L)}{P_{P0}} \tag{1.46}$$

where P_{P0} and $P_P(L)$ is the pump power in the absence and presence of Brillouin interaction at the output of the fiber, respectively. Using Eq. (1.45), this factor can be analytically

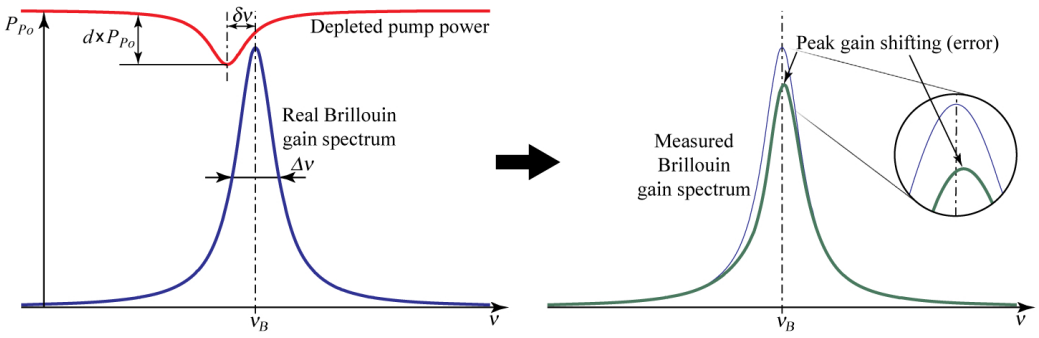

Fig. 1.7. Effect of pump depletion at the measured Brillouin gain spectrum, when the pump power is reduced by a fraction d at a frequency difference between both signals and the BFS given by $\delta\nu$. P_{P0} represents the pump power affected only by attenuation of the fiber. ©2013 Optical Society of America [19].

calculated as a function of the input probe power and the effective length of the fiber [19]:

$$1-d=\frac{P_P(L)}{P_{Po}(L)}=\exp\left(-\frac{g_0}{A_{eff}}P_S(L)L_{eff}\right) \tag{1.47}$$

Note that the previous expression considers the maximum depletion of the pump signal, which occurs at the peak frequency of the Brillouin spectrum. Using Eq. (1.47), the maximum input probe power for a given depletion factor is given by [19]:

$$P_S(L)<-\ln(1-d)\frac{A_{eff}}{g_0 L_{eff}} \tag{1.48}$$

This equation shows that the maximum probe power for a given depletion factor has no dependence with the pulse power or pulse duration, and it only depends on the properties of the optical fiber. Moreover, the error induced by a given depletion factor can be calculated using the following relation [19]:

$$\nu_{B,e}\cong\frac{d\delta\nu}{\left(1+4\left(\frac{\delta\nu}{\Delta\nu_B}\right)^2\right)^2-2d\left(1+2\left(\frac{\delta\nu}{\Delta\nu_B}\right)^2\right)} \tag{1.49}$$

where $\delta\nu$ represents the frequency difference between the maximum depletion frequency of the pump pulse and the BFS of the scanned fiber section. Note that to obtain Eq. (1.49), it has been assumed that the error is much smaller than the Brillouin linewidth and the minus sign reflects that the Brillouin gain peak is biased to higher frequencies when the depletion peak of the pump pulse is situated at lower frequencies [19].

Fig. 1.8 shows the error induced by non-local effects at the estimation of the BFS for the worst-case scenario, which occurs when $\delta\nu = \Delta\nu_B/3$ [19]. Note that for a 1-MHz error in the BFS value, the depletion factor must not exceed 0.17, which means an input probe power of -14 dBm for a long sensing fiber ($L > L_{eff} = 22km$).

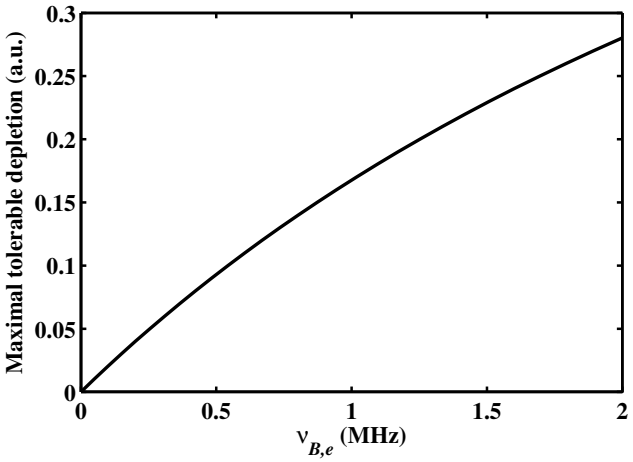

Fig. 1.8. Relation between the depletion factor and the error induced on the determination of the BFS for the worst-case scenario.

The first model capable of estimating the BFS error induced by non-local effects was presented in 1995 [20]. This effect has been thoroughly studied to reduce or even eliminate its influence on the measurements. Different methods have been introduced in the literature:

- An algorithm for temperature/strain profile reconstruction [21]: this numerical technique is based on a multidimensional minimization that allows to reconstruct the BFS profile through its expansion in harmonic functions. This method has demonstrated to be able to monitor long fibers under the previous knowledge of some characteristic of the sensing fiber and it has been experimentally demonstrated on a 7-km sensing fiber. Unfortunately, the post-processing time of this technique grows with the number of harmonics and in addition to it, the needed number of harmonics depends on the BFS profile. Therefore, the required time may substantially change from one fiber to the next.

- Pulsing the probe wave [22]: this technique is based on pulsing both waves, the pump and the probe waves. In this case, both waves only interact at a given section of the fiber instead of the whole fiber length. Consequently, the Brillouin interaction accumulated by the pump pulse is lower and hence, the resulting probe power can be increased.

Although the technique is very useful, it increases the measurement time, depending on the number of sections in which the fiber is divided.

- Optimizing the system parameters [23]: this technique experimentally checks the influence of non-local effects on a temperature-controlled hot-spot by swapping the fiber inputs of probe and pump waves. This defines the maximum probe power injected to the fiber, which, for a particular case, was experimentally demonstrated to be -10 dBm for a 25 km fiber length. This value is relatively close to the proposed theoretical model, which limits the probe power to -14 dBm for fibers much longer than 22 km. This technique is very useful to observe the influence of non-local effects, if the hot-spot is exactly located at the correct position where the impact of non-local effects is higher i.e., the end of the fiber.

- Balanced interaction between the pulsed wave and a Stokes and anti-Stokes components [24]: this technique was proposed for a BOFDA sensor but it is equally applied and is valid for BOTDA sensors. It is based on the generation of two complementary Brillouin interactions over the pulsed wave, so that the pulsed wave is not affected by the Brillouin interaction. Further research has shown that an unbalanced double sideband probe wave allows to better improve the tolerance to non-local effects [25].

Among the different techniques presented above, the balanced double-sideband probe wave has been the most exploited since it allows to inject a high probe power limited by the Brillouin threshold (around 5-6 dBm for long fibers) [19] and it does not increase the measurement time. However, it has been recently demonstrated that a second order non-local effect that occurs with this configuration limits the probe power to around -3 dBm for an induced error of about 1 MHz. The limitation is given by a spectral distortion of the pump pulse, when the frequency difference between both probe waves does not match the BFS of the fiber. For this frequency detuning, the net interaction between both Brillouin interactions is not further compensated and hence, the pulsed spectrum is distorted, turning into an assymetrical and spectrally shifted upwards or downwards depending if the frequency difference between the probe and pump signals is higher or lower than the BFS [26]. This problem has been solved using two different methods. One is based on setting the frequency difference given by the average BFS of the fiber and modify the frequency of both probe waves in the same direction instead of opposite direction to scan the Brillouin spectrum. This allows to tolerate the non-local effects for uniform BFS allowing to inject a high probe power limited by SpBS. The other method is also based on a double-sideband probe wave, whose sidebands are frequency modulated along the fiber. This generates two net Brillouin interactions that are complementary and flat over the pulse spectrum. Consequently, it does

not induce amplitude or frequency distortion of the pump pulse. Thanks to the frequency modulation of both probe waves, the probe power injected is higher than in the previous cases and more important, the method overcomes the typical Brillouin threshold of the fiber. This method will be further explained in chapter 3 since it is a contribution of this thesis dissertation.

1.5.2 Pump power limitations: modulation instability, Raman effect and self-phase modulation

In BOTDA sensors, a high pump power must be launched into the sensing fiber to compensate the fiber attenuation and hence, increase the detected Brillouin gain. However, modulation instability (MI) appears in optical fibers when the pump pulses are very powerful. This effect induces depletion on the pump power [27, 28] and it can distort the sensor response [29]. This effect is the consequence of the interplay between anomalous dispersion and the Kerr effect in fiber [30]. It generates two symmetric sidebands around the frequency of the pump pulse, whose spectrum can be expressed as [30]:

$$G_{MI}(\Omega_P) = 1 + \frac{\sinh^2\left(2\gamma P_{Pi} L \sqrt{\left(\frac{\Omega_P}{\Omega_c}\right)^2 \left(1 - \left(\frac{\Omega_P}{\Omega_c}\right)^2\right)}\right)}{2\left(\frac{\Omega_P}{\Omega_c}\right)^2 \left(1 - \left(\frac{\Omega_P}{\Omega_c}\right)^2\right)} \tag{1.50}$$

where γ is the nonlinear coefficient of the fiber, P_{Pi} is the input pump power, Ω_P is the frequency detuning around the pump frequency and Ω_c is the cutoff frequency. During the propagation of the pump signal along the fiber, there is a power exchange between the sidebands and the pump pulse leading to power fluctuations of the pump pulse, which are directly translated into the BOTDA trace as shown in Fig. 1.9. Consequently, some sections of the fiber are not correctly monitored due to the low SNR.

Furthermore, in a BOTDA, the pump pulse is typically amplified by an erbium-doped fiber amplifier (EDFA), which may increase considerably the amplified spontaneous emission (ASE) co-propagating with the pulsed signal. This background noise seeds the apparition of MI as shown in Fig. 1.10. Therefore, a suitable filter before launching the pump pulse into the fiber may reduce this effect [31].

The limitation on the pump power induced by MI can be calculated using the following expression, which gives the critical power, P_{crit}, for the onset of this effect [30]:

$$P_{crit} = \frac{\sigma_{crit}}{2\gamma L_{eff}} \tag{1.51}$$

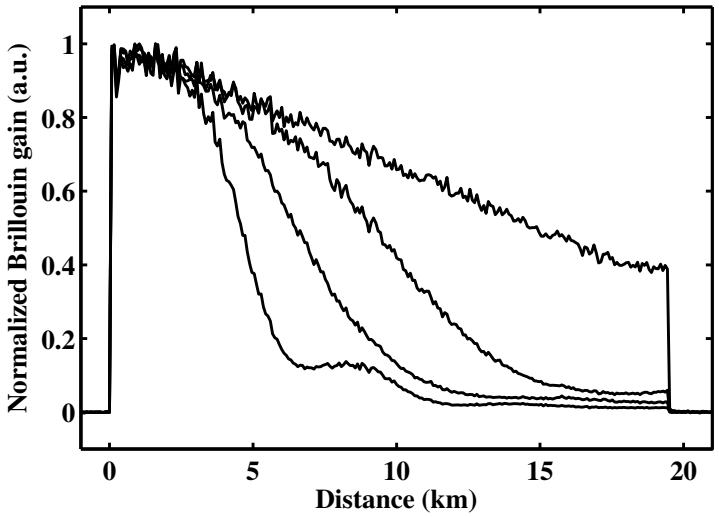

Fig. 1.9. Evolution of the Brillouin gain signal affected by modulation instability when increasing the peak pump power.

where σ_{crit} is the critical gain that can be calculated as a function of the noise power spectral density (S_n) and the depletion ratio ($R_{D,MI}$) [30]:

$$\sigma_{crit} - \ln(\sigma_{crit}) = \ln(R_{D,MI}) - \left(\frac{S_n}{10} + 9\right)\ln(10) + \frac{\ln(2)}{2} \tag{1.52}$$

The limitation imposed by MI determines the maximum pump power injected into a fiber around 22 dBm. This power limitation can be overcome by utilizing dispersion shifted fibers (DSF) with normal dispersion [32]. However, the reduced effective area and lower dispersion of DSF favours the apparition of other nonlinear effects at higher power thresholds, such as Raman scattering [28]. In this case, a rapid pump depletion is observed when Raman scattering occurs, severely limiting the distance range. This effect is caused by the less strict phase matching condition in Raman scattering that makes possible forward scattering. Consequently, the Raman signal co-propagates with the pump pulse and may interact over long fibers or even the whole fiber length. For very long fibers, the maximum value of the pump pulse that avoids spontaneous Raman scattering is around 30 dBm [28].

Another limitation related, in this case, to the power of the pump pulse and also to the temporal shape of the pump pulse, is self-phase modulation. This nonlinear effect induces a phase-shift on the transmitted signal caused by the intensity dependence of the refractive index that leads to spectral broadening of the pump pulse [2]. In order to study this effect, the nonlinear Schrödinger equation (NLSE) must be solved after assuming some simplifications.

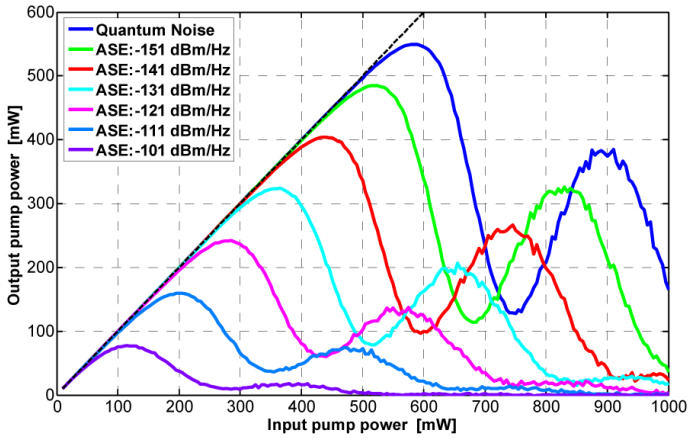

Fig. 1.10. Output pump power as a function of the inpup pump power for different values of ASE noise. ©2015 Optical Society of America [30].

For instance, it is considered a time-scale with a reference point that travels at the same velocity as the envelope wave of the pulse signal. This time-scale is also normalized by the pulse duration (T_P) leading to the following relation for the pulsed signal [2]:

$$A(z,\tau) = P_{Pi}\,U(z,\tau) \tag{1.53}$$

where P_{Pi} is input optical power, $U(z,\tau)$ is the normalized pulsed signal and $\tau = (t - z\cdot n/c)/T_P$ is the normalized time-scale. Neglecting the dispersion of the group velocity, then the NLSE yields:

$$\frac{\partial U}{\partial z} = i\gamma P_{Pi}\exp^{-\alpha z}|U(z,\tau)|^2 U(z,\tau) \tag{1.54}$$

At the output of the fiber, the solution of Eq. (1.54) is expressed as:

$$U(L,\tau) = U(0,\tau)\exp(i\phi_{NL}) \tag{1.55}$$

where ϕ_{NL} is the nonlinear phase introduced by SPM and expressed as [2]:

$$\phi_{NL}(L,\tau) = \gamma P_{Pi}|U(0,\tau)|^2 L_{eff} \tag{1.56}$$

Note that SPM does not affect the pulse shape as shown in Eq. (1.55) but it gives rise to an intensity dependence phase-shift that takes its maximum value at the center of the pulsed signal ($\tau = 0$) as shown in Eq. (1.56). However, the temporal dependence of the phase induced by SPM gives rise to a spectra broadening. This can be understood by considering that any temporal variation of the phase implies a variation of the instantaneous frequency across the pulse from its central value ω_P. This difference of the instantaneous frequency is

given by:

$$\Delta\omega(\tau) = -\frac{\partial\phi_{NL}}{\partial\tau} = -\gamma P_{Pi} L_{eff} \frac{\partial}{\partial\tau}|U(0,\tau)|^2 \tag{1.57}$$

This time dependence is equivalent to a chirp, whose magnitude increases with the distance, i.e. new frequency components appear during the propagation of the pulsed signal. This effect depends on the shape of the deployed pulsed. For example, using a super-Gaussian pulse pulse, the SPM-induced chirp comes determined by:

$$\Delta\omega(\tau) = \gamma P_{Pi} L_{eff} \frac{2m}{T_P} \left(\frac{\tau}{T_P}\right)^{2m-1} \exp\left[-\left(\frac{\tau}{T_P}\right)^{2m}\right] \tag{1.58}$$

where m =1 for a Gaussian pulse and for higher values becomes a rectangular pulse shape. As shown in Eq. (1.58), the SPM-induced chirp is reduced when m tends to higher values [33]. Consequently, this effect can be easily solved by using perfectly shaped rectangular pump pulses with sharp rising and falling edges.

1.5.3 Number of resolved points: the spatial resolution

The spatial resolution (Δz) and hence the number of points resolved for a certain length of fiber is determined by the temporal pulse duration (T_P), which are related by:

$$\Delta z = T_P \cdot c/(2n) \tag{1.59}$$

The previous expression, which is valid for any reflectometry technique, shows that the shorter the pulse duration, the better the spatial resolution obtained. For instance, for a given pulse duration of 10 ns, which occupies 2 m at the optical fiber, the spatial resolution of the system is 1 m since the scattered signal counter-propagates the pulsed wave, halving the effective interaction length of the pulse.

However, the use of short pulses has two serious problems. One of them is the shorter Brillouin interaction and hence, the reduced Brillouin gain detected as shown in Eq. (1.41). On the other hand, when the duration of the pulsed signal is shorter than the phonon lifetime, the linewidth of the Brillouin spectrum considerably broadens from 30 MHz to more than 100 MHz, since the measured Brillouin spectrum is given by the convolution of the pulse spectrum with the natural Brillouin spectrum presented in Eq. (1.18) [34, 35]. Consequently, the broadening of the Brillouin linewidth leads to a reduction in the accuracy of the BFS evaluation. For these reasons, the spatial resolution of conventional BOTDA sensors is typically limited to 1-meter spatial resolution.

During the last years, this issue has been analyzed and different methods have been proposed to obtain high-spatial resolution. The vast majority are based on a pre-excitation of the acoustic wave, which allows to reach an steady-state response and a reduced linewidth of the Brillouin spectrum.

- Bright pulse [36]: this technique is based on counter-propagating a CW probe signal with a pulse combined with a small CW component. The latter pre-pumps the phonon field before the arrival of the pulse, resulting in an increased Brillouin interaction for the duration of the pulse and a lower linewidth of the Brillouin spectrum.

- Dark pulse [37]: this technique benefits from the immediate interruption of the Brillouin scattering when one of the waves, either the pump or the probe wave, is switched off. It employs two CW signals that continuously excite the acoustic wave and hence, interact over all the fiber. Then, one of the optical waves, e.g. the Stokes wave is briefly turned off, ceasing the depletion over the pump pulse. After this brief interruption of the Stokes wave, which is called darked pulse, the probe wave is turned on again and the the Brillouin transfer continues without significantly modifying the acoustic wave due to the short dark pulse duration. Measuring the absence of Brillouin interaction, it is possible to reconstruct the Brillouin spectrum with the natural Brillouin linewidth and with higher Brillouin amplitude than in the conventional technique.

- Pulse pre-pump [38]: the technique is very similar to the bright pulse but instead of using a CW, it uses a pulse of low intensity to pre-activate the acoustic wave before a stronger interrogating pulse arrives. Consequently, the system allows to enhance the spatial resolution while reaching a narrow Brillouin spectrum.

- Brillouin echoes [39]: this technique deploys two continuous waves but the phase of one of them is abruptly and briefly shifted by a π value during a time-frame shorter than the phonon lifetime. During this π phase-shifted pulse, the pump wave is completely reflected and generates a destructive interference on the signal. This is observed as a small apparent loss on the signal waveform.

- Differential pulse-width pair [35]: this technique is based on the subtraction of two different Brillouin spectra, which are measured using pulses with a slightly different duration. The temporal duration of both pulses is set to be wide enough to measure a narrow Brillouin linewidth. Meanwhile, the subtraction of both spectra removes the fraction of the response that is common to both pulses and hence, it only retains the differential part, which contributes to measure the differential Brillouin spec-

trum. Therefore, the temporal difference between both pulses defines the new spatial resolution of the system.

1.5.4 Sensing range

As shown in section 1.4.4, specifically in Eq. (1.42), the fiber losses affect twice the measured Brillouin response at the far end of the fiber: once due to the attenuation of the probe wave and other by the attenuation of the pump power, which also reduces the amplification of the probe wave. This double attenuation suffered by the detected Brillouin signal considerably reduces the detected SNR at the end of the fiber, leading to a poor performance of the sensor as shown in Eq. (1.43).

As mentioned at the previous sections 1.5.1 and 1.5.2, the fiber attenuation can not be compensated by indefinitely increasing the probe or pump power. Consequently, the SNR can only improve by increasing the number of averages, which also increases the measurement time, not being at all the perfect solution.

During the last years, great effort has been done to further improve the sensing range of BOTDA sensors, reaching sensing distances around 150 km in fiber loop configuration [40] or 200 km using a leading fiber to monitor the the farthest point at 100 km [41]. Among the different configurations, it is possible to find the following methods in the literature.

- First-order Raman amplification [42]: the technique is based on the distributed gain amplification generated by stimulated Raman scattering that amplifies separately or simultaneously the probe or pump power. Therefore, the probe and/or pump powers are increased along the fiber, which allows to enhance the sensor response.

- Second order Raman amplification [43]: this method is based on injecting a Raman pump at 1365 nm in both inputs of the fiber and generate a cavity at the fiber so that, it starts to lase at 1455 nm, where gain overcomes losses in the cavity. This produces a stable Raman pump along the fiber at 1455 nm that will be used to amplify the signals involved in the SBS process at 1550 nm. Consequently, the level of the different waves is maintained along the fiber so that the Brillouin transfer does not decrease with the fiber length reaching a virtual transparency in the sensing fiber.

- Coding techniques [44]: the method is based on launching into the fiber pulse sequences with some particular properties, which allow to obtain the impulse response of the fiber using a particular decoding process.

- Discrete amplification [40]: the BOTDA sensor deploys EDFAs at a given location of the sensing fiber to amplify both signals. Consequently, the fiber losses are compensated at this point and the measurement distance is increased.

- Self-heterodyne detection [45]: the method is based on co-propagating a probe wave with a powerful local oscillator, so that he probe interacts with the pulsed signal but not with the local oscillator. The latter is used to amplify the probe wave when both signals beat at the receiver, consequently, the SNR is enhanced.

The previous techniques could be combined to further enhance the SNR of the system. This is the case of the proposed solution based on Raman amplification and pulse coding [46].

Another point of view to enhance the SNR and hence, increase the sensing distance, is to reduce the noise level of the system. Some numerical simulations suggest that the response of the BOTDA sensor is limited by relative to intensity noise (RIN) and point out that the sensing distance could be considerably increased when this noise is reduced [47]. Recently, it has been identified that Raman-assisted BOTDA sensors are limited by RIN transfer of the Raman laser [48]. Since then, two different solutions have been proposed to reduce this noise. One of them is based on the deployment of a balanced receiver that detects and subtracts both probe waves deployed in a balanced BOTDA sensor [49]. Consequently, the common noise suffered by both probe waves, such as RIN transfer from the Raman pump, is considerably reduced. The other one is based on transferring the detected probe wave from baseband, where the RIN transfer is maximum, to a higher electric frequency. In this way the noise affected by the probe signal is reduced around 20 dB [50]. In chapter 5, the different contributions to the noise level of a conventional system will be described, analyzing the dominant noise source for different fiber lengths.

1.5.5 Measurement time

As mentioned in section 1.4.4, the process to measure the Brillouin spectra distribution requires to sweep the frequency difference between probe and pulse waves. This is a time consuming procedure that restricts the use of BOTDA sensors to static measurements.

During the last years, the possibility to extend this technique to dynamic measurements has been thoroughly studied due to the growing interest to monitor vibrations in different structures. Consequently, different solutions were proposed:

- Slope-assisted (SA) BOTDA sensor with constant probe frequency [51]: the technique is based on setting the probe frequency to the skirt of the Brillouin spectrum and detect the amplitude variations of the Brillouin signal along time. Any amplitude variation

is interpreted as a change of the Brillouin frequency shift. The relation between both parameters is given by the shape of the Brillouin gain spectrum. Consequently, the system needs a calibration measurement, i.e. a standard measurement of the Brillouin spectra distribution, before being able to dynamically monitor the BFS variations.

- Slope-assisted BOTDA sensor with tailored probe wave [52]: the previously described technique is valid when the BFS of the fiber is uniform. However, there are fibers with different BFS sections along its length. If the BFS of a fiber's section is larger than the available measurement range of the previous technique, then that section will not be monitored. The proposed method solves this problem, since the frequency of the probe wave varies along the fiber, so that the probe frequency is set at the skirt of the Brillouin spectrum even if the BFS changes along the fiber.

- Slope-assisted BOTDA sensor with comb probe wave [53]: the measurement range of the SA-BOTDA is bounded by the linear section of one of the Brillouin spectrum slopes. This range is approximately half of the measured Brillouin linewidth, being very limited to properly monitor large variations of the BFS. The method proposes to use three probe waves (multiplexed in time) with a different and constant frequency, so that the Brillouin skirt is scanned at three different points. This allows to increase the measurement range of this sensor by scanning different frequency points.

- Double slope-assisted BOTDA sensor [54]: the previous methods translate amplitude variations into changes of the BFS. However, all the amplitudes changes may not be related to changes of the BFS. For example, if the attenuation of the sensing fiber changes due to deformation of the monitored structure, then the pulse power and the detected Brillouin gain is modified. The variation of the detected amplitude will be misinterpreted as a BFS variation. This method proposes to use the information of two measurements: one taken from the positive slope and the other from the negative, so that the difference between the two measurements divided by their sum is immune to variations of the detected amplitude.

- Fast BOTDA sensor [55]: the technique is based on the fast switching that provides an arbitrary waveform generator (AWG) compared to a slow sweeping electronic synthesizer, when the frequency difference between probe and pump is swept. Each frequency of the probe wave is launched one after the other with a period given by the round-trip time. Consequently, the measurement time is only given by the product of the round-trip time, the number of frequencies used to scan the Brillouin spectrum and the number of averages.

- Swept-free BOTDA sensor [56]: the technique counter-propagates a comb probe and pump waves. Each pair of probe and pump waves scan a different point of the Brillouin spectrum, so that the acquisition of the Brillouin distribution is only limited by the round-trip time (without including the post-processing).

Chapter 2

BOTDA sensors using heterodyne detection

Direct detection is the most common technique deployed in Brillouin optical time-domain analysis (BOTDA) sensors to recover the Brillouin gain or loss information contained at the probe wave. The detection is made in base-band converting the optical signal directly to the electrical domain tipically using a high-transimpedance receiver to enhance the system response. However, even using this kind of receiver, the gain or loss generated by stimulated Brillouin scattering (SBS) is rather limited (typically less than 1% in BOTDA sensors using long monitoring distances and high spatial resolutions) being the detected signal very close to the noise floor of the system. This makes it very challenging to obtain clean measurements, hence, the accuracy of the sensor worsens. Furthermore, the use of direct detection only allows to detect the magnitude of the optical field but not the phase-shift response, limiting the available options.

During this chapter, the benefits of applying self-heterodyne detection and radio frequency (RF) demodulation in BOTDA sensors are introduced, not only to improve the signal-to-noise ratio (SNR) of the system, but to exploit the possibility to measure either the magnitude or the phase-shift of a different spectral shape affected by SBS with special features. Furthermore, a novel BOTDA sensor based on phase-modulated (PM) probe wave and self-heterodyne detection is presented. The technique measures the interference generated at the optical receiver between the beating of the first sidebands with the carrier, which provides a RF phase-shift spectrum with tolerance to variations of the local gain suffered by the phase-modulated probe wave. As it will be discussed later, the tolerance to variations of the local gain has major implications for research fields such as dynamic sensing or long-range systems limited by non-local effects (NLE). Moreover, making use of both sidebands of the phase-modulated probe wave, it is possible to enhance the detected signal by a 3 dB factor, deploy a new

polarization diversity technique that does not need from any average at the oscilloscope to avoid polarization fluctuations or mitigate the apparition of modulation instability.

2.1 Introduction

Figure 2.1 schematically represents the Brillouin interaction at a given location of the fiber between a probe wave and a pump pulse and the typical detection technique used in conventional direct-detection BOTDA sensors.

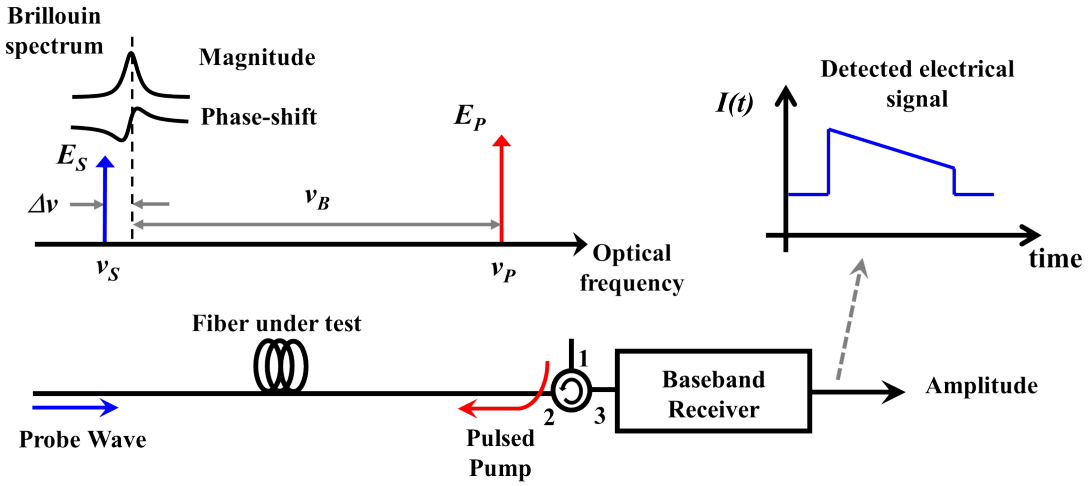

Fig. 2.1. Schematic of the conventional BOTDA interaction and detection using direct detection.

As mentioned previously in section 1.4.4 and repeated here for clarity, the probe wave reaches the receiver once it has interacted with the pulsed signal, being its detected optical power:

$$\begin{aligned} P_S(z,\Delta\nu) &= P_{Si}\exp(-\alpha L)\exp\left(\frac{g_0}{A_{eff}}\frac{\Delta\nu_B^2}{\Delta\nu_B^2+4\Delta\nu^2}P_{Pi}\exp(-\alpha z)\Delta z\right) \\ &\approx P_{Si}\exp(-\alpha L)+\frac{g_0}{A_{eff}}\frac{\Delta\nu_B^2}{\Delta\nu_B^2+4\Delta\nu^2}P_{Si}\exp(-\alpha L)P_{Pi}\exp(-\alpha z)\Delta z \end{aligned} \tag{2.1}$$

where P_{Si} and P_{Pi} are the input probe and pump power, respectively, α is the attenuation of the optical fiber, L is the length of the fiber, A_{eff} is the effective area of the fiber, g_0 is the Brillouin coefficient, $\Delta\nu_B$ is the Brillouin linewidth, $\Delta\nu$ is the frequency detuning from the center of the Brillouin spectrum with reference to the probe's frequency and Δz is the spatial resolution. The approximation in the second term is obtained assuming a small gain, which

is the case for BOTDA sensors. Note also that pump pulses longer than the acoustic lifetime have been assumed and hence, the spectrum is Lorentzian. However, for pump pulses shorter than the acoustic lifetime, the effective interaction spectrum is given by the convolution of the natural Brillouin spectrum with the pulse spectrum [57]. As shown by the approximation of Eq. (2.1), the second component of the right-hand side reflects that the Brillouin energy transfer to the probe wave is directly proportional to the detected probe power. Accordingly, with a stronger probe power, the detected Brillouin gain increases but at the expense of the apparition of non-local effects, which can be noticeable with powers as low as -14 dBm in long-range measurements, as shown in section 1.5.1 [19]. Therefore, the maximum probe power launched to the fiber in long range BOTDA measurements must be kept at this level, limiting significantly the performance of these systems.

Another configuration, proposed by our research group, is the BOTDA sensor depicted in Fig. 2.2, which deploys a self-heterodyne detection [45]. Instead of a single probe signal,

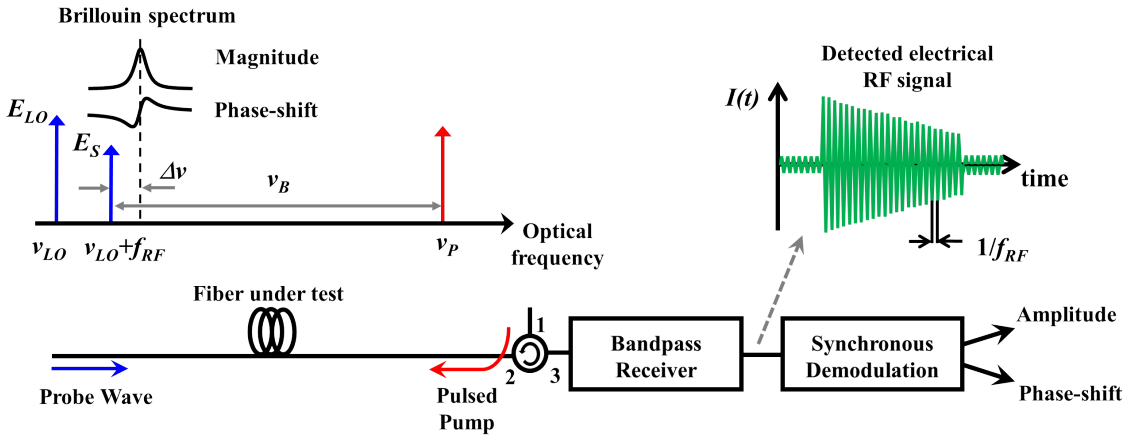

Fig. 2.2. Schematic of the BOTDA interaction and self-heterodyne detection with synchronous demodulation.

two signals arrive to the receiver: a local oscillator and the probe wave. Both signals have a different frequency, so that the probe wave is the only one to interact with the pulse wave via SBS and the local oscillator propagates along the fiber together with the probe wave until they reach the receiver. In this case, the optical field at the input of the photodetector coming from the interaction between pump and probe at a particular location, z, can be expressed as [45]:

$$\begin{aligned} E(t)\big|_{rx} = {} & E_{0i}\exp(i2\pi\nu_0 t)\exp\left(-\alpha\frac{L}{2}\right) \\ & + E_{Si}\exp(i2\pi(\nu_0+f_{RF})t)\,H_{SBS}(z,\Delta\nu)\exp\left(-\alpha\frac{L}{2}\right) \end{aligned} \tag{2.2}$$

where E_{0i} and ESi are the complex optical fields of the local oscillator and the probe wave, respectively, ν_0 is the optical frequency of the local oscillator and f_{RF} is the frequency difference of the probe wave from the local oscillator and H_{SBS} is the complex Brillouin spectrum given by:

$$H_{SBS}(z,\Delta\nu) = \exp\left(\frac{g_0}{A_{eff}}\frac{\Delta\nu_B}{\Delta\nu_B + 2i\Delta\nu}P_P(z)\Delta z\right) = G_{SBS}\exp(i\varphi_{SBS}) \tag{2.3}$$

$$G_{SBS}(z,\Delta\nu) = \exp\left(\frac{g_0}{A_{eff}}\frac{\Delta\nu_B^2}{\Delta\nu_B^2 + 4\Delta\nu^2}P_P(z)\Delta z\right) \tag{2.4}$$

$$\varphi_{SBS}(z,\Delta\nu) = -\frac{g_0}{A_{eff}}\frac{2\Delta\nu_B\Delta\nu}{\Delta\nu_B^2 + 4\Delta\nu^2}P_P(z)\Delta z \tag{2.5}$$

being $P_P(z) = P_{Pi}\exp(-\alpha z)$ the evolution of the pump power assuming that there is no pump depletion. Note that, depending on the BOTDA configuration, the equation above can represent a Brilloguin gain spectrum ($g_0 > 0$) but also a Brillouin loss spectrum ($g_0 < 0$). The detected optical power at the heterodyne frequency is given by [45]:

$$\begin{aligned} P(t)\big|_{f_{RF}} &= 2\sqrt{P_{0i}P_{Si}}\exp(-\alpha L)\, G_{SBS}\cos(2\pi f_{RF}\, t + \varphi_{SBS}) \\ &= 2\sqrt{P_{0i}P_{Si}}\exp(-\alpha L)\exp\left(\frac{g_0}{A_{eff}}\frac{\Delta\nu_B^2}{\Delta\nu_B^2 + 4\Delta\nu^2}P_P(z)\Delta z\right) \\ &\cdot\cos\left(2\pi f_{RF}\, t - \frac{g_0}{A_{eff}}\frac{2\Delta\nu_B\Delta\nu}{\Delta\nu_B^2 + 4\Delta\nu^2}P_P(z)\Delta z\right) \end{aligned} \tag{2.6}$$

As shown in Eq. (2.6), the detected optical power is given by the product of the power of both optical signals, the probe wave and the local oscillator. In the case that the local oscillator has the same power that the probe wave, then the signal power is double than the base-band detection. However, if the local oscillator power is even higher, the detected signal is much greater than in the base-band detection. This is the reason behind the improvement of the sensitivity of the detector obtained in a coherent detection, because the lower power signal of the probe wave is amplified considerably by the local oscillator. Therefore, the maximum performance of the system is obtained by setting the probe power to the limit defined by the non-local effects and the local oscillator power to the Brillouin threshold of the fiber. This maximizes the product of the power between both signals offering an improved performance regarding the conventional technique [45].

Furthermore, we can see that the signal expressed in Eq. (2.6) is not only an amplitude-modulated signal but also a phase-modulated signal, since the phase-shift contribution is not lost in the optical to electrical conversion. This allows to recover the Brillouin gain spectrum

(BGS) as well as the Brillouin phase-shift distribution as shown in Fig. 2.3. Note that for this particular case, i.e. using a local oscillator and a probe wave, the detected magnitude and phase-shift are directly related to the Brillouin gain and phase-shift spectra, exactly following the same spectral shape.

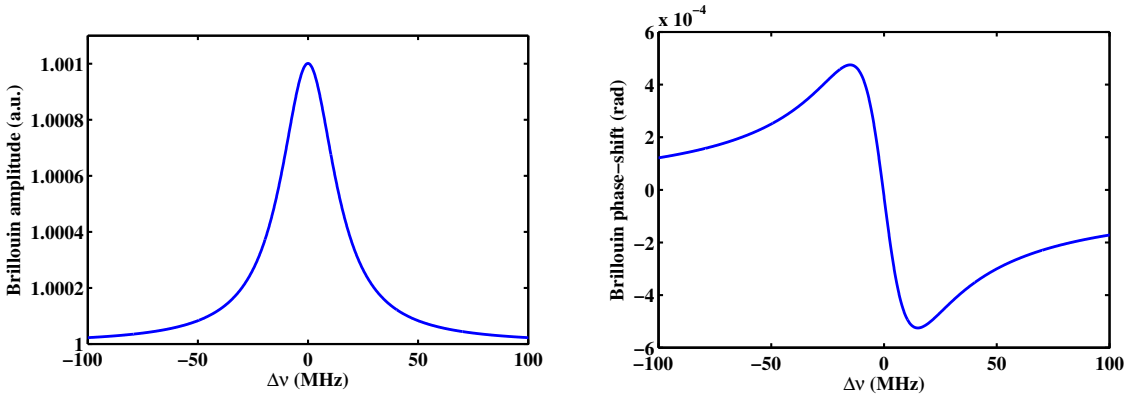

(a) (b)

Fig. 2.3. Brillouin (a) amplitude and (b) phase-shift measured with the self-heterodyne detection technique using a OSSB probe.

2.2 BOTDA sensors using a phase-modulated probe wave and heterodyne detection

In the previous section, we have observed that heterodyne detection shows a better performance compared to typical baseband detection techniques due to the amplification of the probe signal when it beats with a powerful local oscillator. In this case, the technique is able to retrieve both the Brillouin gain and phase-shift spectra. However, the self-heterodyne technique can also be applied to other probe modulation techniques, such as phase modulation, where the recovered RF phase-shift has a different spectral shape than the Brillouin phase-shift. This spectrum presents different features that makes it interesting for dynamic and long-range BOTDA sensors as it is shown below.

In Fig. 2.4, the fundamentals of the BOTDA sensor using a phase-modulated probe wave are depicted. As shown, a narrow band phase-modulated probe wave is injected into one end of the optical fiber under test, while a pump pulse is introduced at the other end. The first upper-sideband of the phase modulation acts as a probe wave interacting with the pump pulse along the fiber via stimulated Brillouin scattering and is finally directed to the receiver using a circulator. Considering that SBS interaction only affects one component of the modulation,

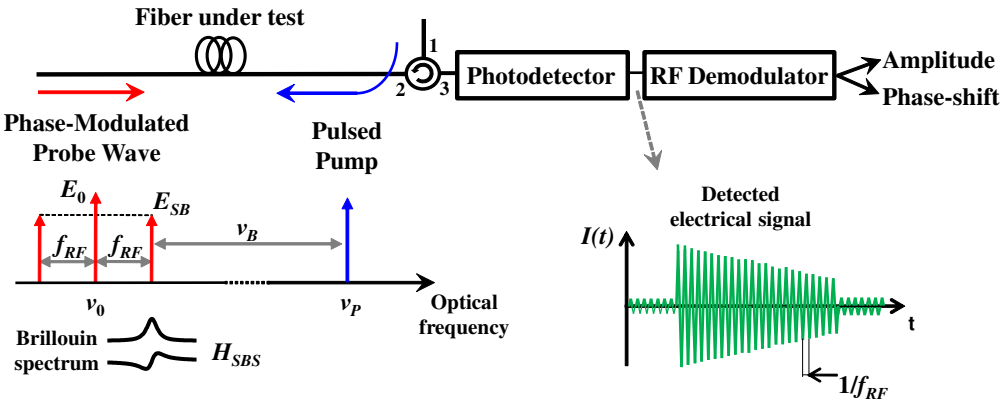

Fig. 2.4. Schematic representation of SBS interaction and the received signal.

then the optical field at the input of the photodetector coming from the interaction of pump and probe at a particular location in the fiber, z, is given by the following expression:

$$\begin{aligned} E_T(t)\big|_{rx} = &-E_{SBi}\exp\left(i2\pi\left(\nu_0 - f_{RF}\right)t\right)\exp\left(-\frac{\alpha}{2}L\right) \\ &+ E_{0i}\exp\left(i2\pi\nu_0 t\right)\exp\left(-\frac{\alpha}{2}L\right) \\ &+ E_{SBi}\exp\left(i2\pi\left(\nu_0 + f_{RF}\right)t\right)H_{SBS}(z,\Delta\nu)\exp\left(-\frac{\alpha}{2}L\right) \end{aligned} \tag{2.7}$$

where E_{0i} and E_{SBi} are the amplitudes of the input optical fields of the carrier and first sidebands of the phase-modulated probe wave, ν_0 is the optical frequency of the carrier, f_{RF} is the frequency modulation and $\Delta\nu = \nu_0 + f_{RF} - \nu_P + \nu_B(z)$, is the frequency detuning of the Brillouin spectrum from the probe wave and ν_P is the pump frequency. The detected optical power is the square of the received optical field presented in Eq. (2.7). For this case, three components are obtained at the output of the receiver: a base-band component and two RF tones. Among them, the RF signal interesting for this study is the one at the frequency modulation f_{RF}, which can be expressed:

$$\begin{aligned} P(t)\big|_{f_{RF}} = &\,2\sqrt{P_{0i}P_{SBi}}\exp(-\alpha L)\,G_{SBS}(z,\Delta\nu)\cos\left(2\pi f_{RF}t + \varphi_{SBS}(z,\Delta\nu)\right) \\ &-2\sqrt{P_{0i}P_{SBi}}\exp(-\alpha L)\cos\left(2\pi f_{RF}t\right) \end{aligned} \tag{2.8}$$

where P_{0i} and P_{SBi} are the input powers of the carrier and sidebands, respectively. Note that Eq. (2.8) represents the subtraction of two sinusoidal signals coming from the beating between each sideband and the carrier. In case that there is not SBS interaction, the result of this equation will be zero as corresponds to a phase-modulated signal. If Eq. (2.8) is written

in phasorial form to easily operate, then the resultant signal is:

$$\overline{P}\big|_{f_{RF}} = 2\sqrt{P_{0i}P_{SBi}}\exp\left(-\alpha L\right)\left[H_{SBS}\left(z,\Delta\nu\right)-1\right] \tag{2.9}$$

Assuming small signal in Eq. (2.3) and substituting in Eq. 2.9, then it yields:

$$\begin{aligned}\overline{P}\big|_{f_{RF}} &= 2\sqrt{P_{0i}P_{SBi}}\exp\left(-\alpha L\right)\\ &\cdot\left[\frac{g_0}{A_{eff}}\frac{\Delta\nu_B^2}{\Delta\nu_B^2+4\Delta\nu^2}P_P\left(z\right)\Delta z - i\frac{g_0}{A_{eff}}\frac{2\Delta\nu_B\Delta\nu}{\Delta\nu_B^2+4\Delta\nu^2}P_P\left(z\right)\Delta z\right]\end{aligned} \tag{2.10}$$

Calculating the amplitude and the phase-shift of Eq. (2.10) and writing it again in the temporal form, it is obtained:

$$\begin{aligned}P\left(t\right)\big|_{f_{RF}} &= 2\sqrt{P_{0i}P_{SBi}}\exp\left(-\alpha L\right)\frac{g_0\Delta\nu_B}{\sqrt{\Delta\nu_B^2+4\Delta\nu^2}}\\ &\cdot\cos\left(2\pi f_{RF}\,t-\arctan\left(2\frac{\Delta\nu}{\Delta\nu_B}\right)\right)\end{aligned} \tag{2.11}$$

Note that in contrast to the baseband signal or the detected RF signal detailed in section 2.1, the RF signal in Eq. (2.11) does not present a constant baseline. This effect is caused by the intrinsic phase properties of the modulation, whose result in the absence of Brillouin intercation is zero as shown in Eq. (2.11). Thanks to this feature, the detected Brillouin signal using the phase-modulated probe wave can be measured using the maximum resolution of the analog-to-digital converter following the demodulator.

In addition, note that Eq. (2.11) also displays the same multiplication factor of the probe signal with the local oscillator demonstrated in section 2.1 but using a phase-modulated probe wave, whose carrier is the local oscillator. For this particular case, the index of the phase modulation is kept low enough to generate a narrow band phase modulation, whose carrier is powerful enough to amplify the low probe sideband limited by non-local effects [45].

Furthermore, another significant difference is the resultant spectral shape measured using a phase-modulated probe wave. The amplitude follows a Lorentzian profile as shown in Fig. 2.5(a). However, the RF phase-shift spectrum recovered from a phase-modulated probe wave clearly differs from the typical Brillouin phase-shift (see Fig. 2.5(b)). While the Brillouin phase-shift starts and finishes at zero value, the RF phase-shift spectrum goes from $-\pi/2$ rad to $\pi/2$ rad. This difference between both phase-shift spectra can be further clarified representing Eq. 2.8 in the form of a phasor diagram (see Fig. 2.6). It depicts the interference between the two beat terms that results from the phase-modulated probe wave affected by SBS interaction. Assuming small gain approximations, such as the amplitude of Brillouin gain is

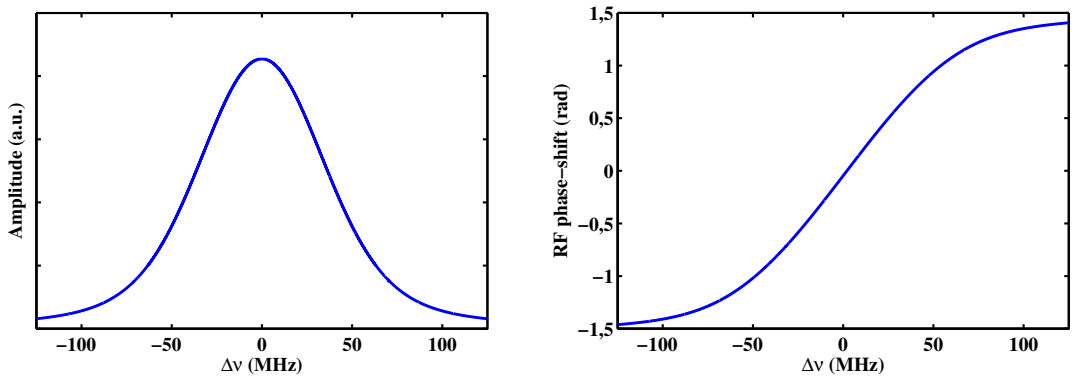

(a) (b)

Fig. 2.5. Detected RF (a) amplitude and (b) phase-shift measured with the self-heterodyne detection technique using a phase-modulated probe

small ($G_{SBS} << 1$) and the small-angle approximations of the basic trigonometric functions, then the real and imaginary parts of the phasor represent the Brillouin gain and phase-shift, respectively. Taking into account that the tails of the Brillouin phase-shift spectrum are much longer than the Brillouin gain spectrum, which drops at the nearby of the Brillouin resonance due to its Lorentzian shape (see Fig. 2.3), then the resultant phasor tends to $\pm\pi/2$ depending on the sign of the Brillouin phase-shift. In addition, the RF phase-shift spectrum exhibit an almost linear behaviour near the Brillouin frequency shift (BFS) and hence, it can be very interesting to be exploited in dynamic measurements. However, even more interesting is the absence of the local Brillouin gain/loss parameter in the detected RF phase-shift. This peculiar result is only true for small gain scenarios, which are the typical case for BOTDA sensors.

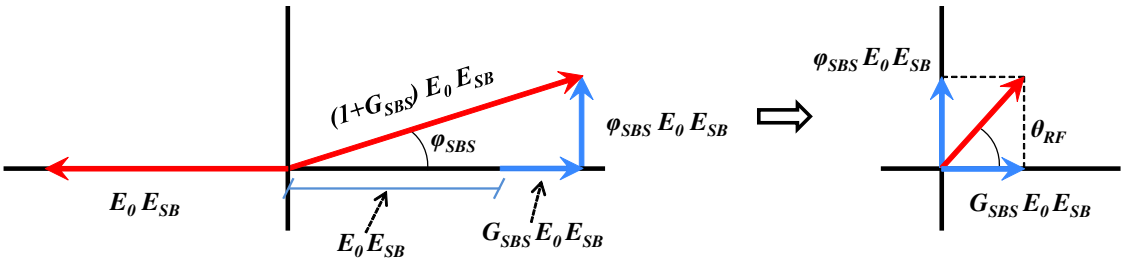

Fig. 2.6. Phasor diagram of the detected RF signal.

Furthermore, it is interesting to remark that Fig. 2.4 only represents one of the possible Brillouin interactions produced between a phase-modulated probe wave and a pulse wave. However, other components of the phase modulation could be employed to generate the SBS

interaction, for example, using the lower sideband as the probe wave and the same gain-based BOTDA configuration, the resultant RF signal is equal to the one shown in Eq. (2.11) but with an offset added to the detected phase-shift. However, more interesting is to analyze the loss-based BOTDA configuration, i.e. when the pulsed wave interacts with the lower sideband of the phase-modulated probe wave. Following the same calculation steps described along this section, it is possible to obtain exactly the same RF signal shown in Eq. (2.11). As it is described in section 2.3.2, the RF signal for both Brillouin interaction is identical because the Brillouin loss transfer is compensated by the π phase difference between both sidebands of the phase modulation and besides, the Brillouin phase-shift experienced for each sideband is also equal. This feature allows to generate two Brillouin interactions with the phase-modulated probe wave, a loss and a gain Brillouin transfer with the lower and upper sideband, respectively, yielding to a 3-dB improvement as the same RF signal is measured twice (see section 2.3.1).

In this thesis, we have worked in solutions using the presented technique for two different fields: dynamic and long-range BOTDA sensors. For dynamic sensors based on the slope-assisted technique, we have proposed:

1. **Dynamic sensing based on the slope-assisted technique using the RF phase-shift spectrum.** In contrast to the techniques based on the detected amplitude, this system benefits from the tolerance to variations of the attenuation of the fiber or the local Brillouin gain to provide dynamic measurements without error induced by these factors.

2. **Polarization diversity technique using orthogonal pump pulses.** The technique is based on the use of two orthogonal pump pulses which simultaneously interact with the phase-modulated probe wave. The orthogonallity of the two pump pulses guarantees that two complementary Brillouin interactions take place at each position of the fiber, so that polarization independent measurements are performed throughout the fiber.

While for long-range BOTDA sensors, we have proposed:

- **BOTDA sensor tolerant to non-local effects.** The system benefits from the tolerance to changes of the Brillouin local gain, but in this case the variations of the pump pulse are caused by the continuous Brillouin interaction of the pump with the probe wave.

- **Phasorial subtraction to enhance the spatial resolution and long-range measurements using the RF phase-shift spectrum.** The application of differential pulse-width pair is deployed in this kind of sensor showing not only an improved spatial resolution but also tolerance to non-local effects of the resultant differential RF signal.

- **Mitigation of modulation instability by using orthogonal pump pulses.** The use of orthogonally-polarized pulses at different wavelengths not only mitigates the impact of modulation instability, but also the four-wave mixing occurring in systems using pumps with parallel polarization; thus, providing an important sensing range enhancement with a reduced pump depletion

During the following sections, each research topic is put in context, briefly explaining the difficulties of each technique and the solutions proposed by other researchers. Then, the fundamentals of the proposed technique are explained to finally present the experimental demonstration.

2.3 Dynamic measurements using BOTDA sensors

In Brillouin optical time-domain analysis sensors, the Brillouin spectra distribution is determined by measuring the probe power variation as a function of the time-of-flight of the pulse for successive frequency detuning between probe and pump waves. After the completion of the frequency sweep, the different measurements are arranged as a function of the frequency detuning. This allows to reconstruct the Brillouin spectrum at each location of the fiber in order to finally obtain the Brillouin frequency shift using a curve fitting procedure. The complete process is a time-consuming procedure, mainly caused by the need for scanning the probe frequency to recover the Brillouin gain spectrum. Consequently, the BOTDA technique is traditionally limited to static measurements. However, the possibility of using distributed fiber sensor to perform dynamic measurements could be of great interest for some application fields, such as the measurement of vibrations in civil or aeronautic structures [51].

During the last few years, a great effort has been done to extend the use of Brillouin distributed sensors to perform dynamic measurements [55, 58–62]. Among them, the first to be introduced was a simple technique known as the slope-assisted BOTDA (SA-BOTDA) technique [55, 59], which does not require to modify the experimental setup but changes the measurement process to obtain the Brillouin frequency shift measurement. The technique is based on tuning the probe wave to the skirt of the BGS, so that variations of the BFS are translated to changes of the amplitude of the detected probe wave, as shown in Fig. 2.7. In order to perform this calculation, the technique requires a first calibration measurement to retrieve the complete Brillouin gain distribution. Then, one of the skirts of the BGS is fitted using a polynomial function. The coefficients of this fitting are used to calculate the variation of the BFS induced by a change of the detected amplitude. Consequently, the BFS distribution can be obtained using a fixed frequency of the probe wave reducing the acquisition time from minutes to seconds or less.

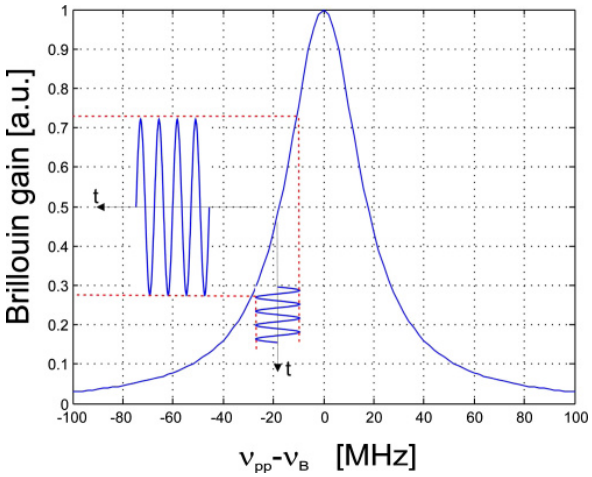

Fig. 2.7. Principle of operation of the slope-assisted technique ©2009 Optical Society of America [51].

2.3.1 Benefits of phase-modulated probe wave in SA-BOTDA technique

The slope-assisted technique is one of the simplest procedures to perform dynamic measurements using Brillouin distributed sensors. However, it faces some key challenges when making measurements tolerant to variations of the detected probe wave amplitude that are unrelated to strain changes, such as changes of the attenuation along the sensing fiber or of the pump power. Any variation of the attenuation caused by bending of the optical fiber modifies the detected amplitude of the probe wave, being directly interpreted by the system as a variation of the BFS. This issue has been thoroughly studied reaching smart solutions that simultaneously [63] or periodically [54] probe both slopes of the BGS, so that using the ratio between both readings, it is possible to tolerate pump power variations as large as 6 dB [54].

Another issue with SA-BOTDA sensors is its limited dynamic measurement range, i.e. the maximum temperature/strain variations that the system can measured dynamically. As the technique uses one of the skirts of the BGS to translate variations of the BFS to changes of the detected amplitude, any variation of the BFS larger than the effective Brillouin linewidth can not be properly measured. This problem has been alleviated by broadening the measured Brillouin gain spectrum using shorter pump pulses [64]. However, the reduction of the pump pulse also reduces the detected amplitude of the Brillouin gain spectrum, which in turn decreases the precision of the sensor. Therefore, in order to keep the same sensor performance, this effect must be compensated by increasing the pulse amplitude. However, this is again limited by modulation instability or small variations of the measured Brillouin linewidth [39, 65].

Finally, other key challenges faced by this dynamic SA-BOTDA sensors are the ability to handle longitudinally inhomogeneous BFS fibers, since there are always differences due to different concentration of dopants, to pre-strain applied while embedding or gluing the fiber to the structure, or to temperature differences in different sections. Assuming that the sensing fiber has two sections with a different BFS, then it may not be possible to simultaneously scan the skirt of the Brillouin gain spectra of both sections due to the fixed frequency difference between probe and pump waves in SA-BOTDA sensors. Consequently, it is necessary to change the probe frequency doubling the measurement time to scan the whole fiber. An intelligent solution to avoid this reduction is to generate a probe wave comprised by different optical frequencies, as many as different BFS sections can be found along the fiber, so that all sections are properly scanned [52].

In the following section, the benefits of using a SA-BOTDA based on a phase-modulated probe wave and RF demodulation are explained. The system is independent of the Brillouin peak gain experienced by the probe wave and of the optical power detected. Therefore, BFS measurements based on the RF phase-shift are immune to attenuation variations in the fiber or changes in the power level of the pump pulses. Furthermore, the optical detection deployed can lead to an enhanced precision, to the broadening of the measurement range and to the enhancement of the measurement time.

Fundamentals

Figure 2.8 schematically depicts the fundamentals of the proposed system.

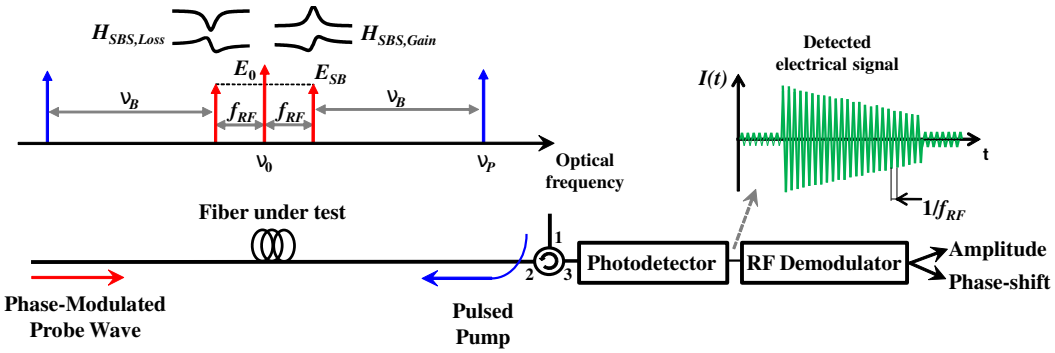

Fig. 2.8. Schematic representation of double SBS interaction with a phase-modulated probe wave and detected RF signal.

A phase-modulated probe wave is injected in one end of the optical fiber under test, while two symmetrical pump pulses are introduced at the other end. Each sideband of the phase modulation interact with its respective pump pulse along the fiber via stimulated Brillouin scattering and the signal is directed to the receiver. The optical field at the input of the

photodetector coming from the interaction of pump and probe at a particular location in the fiber, z, is given by the following expression:

$$\begin{aligned} E(t)\big|_{rx} = &-E_{SBi}\exp\left(-\frac{\alpha}{2}L\right)\exp\left(i2\pi\left(\nu_0 - f_{RF}\right)t\right)H_{SBS,Loss}(z,\Delta\nu) \\ &+E_0\exp\left(-\frac{\alpha}{2}L\right)\exp\left(i2\pi\nu_0 t\right) \\ &+E_{SB}\exp\left(-\frac{\alpha}{2}L\right)\exp\left(i2\pi\left(\nu_0 + f_{RF}\right)t\right)H_{SBS,Gain}(z,\Delta\nu) \end{aligned} \tag{2.12}$$

where $H_{SBS,Gain}$ and $H_{SBS,Loss}$ are the Brillouin gain and loss spectrum defined in Eq. 2.3. Then, the resultant RF signal for a certain location of the fiber z can be obtained following the same procedure explained in section 2.2 yielding:

$$\begin{aligned} P(t)\big|_{f_{RF}} = &\,4\sqrt{P_{0i}P_{SBi}}\exp\left(-\alpha L\right)\frac{g_0\Delta\nu_B}{\sqrt{\Delta\nu_B^2+4\Delta\nu^2}} \\ &\cdot\cos\left(2\pi f_{RF}\,t - \arctan\left(2\frac{\Delta\nu}{\Delta\nu_B}\right)\right) \end{aligned} \tag{2.13}$$

Notice that the detected optical power is doubled compared to Eq. (2.11) due to the double Brillouin interaction generated by the second pump pulse. Furthermore, as it is shown in Eq. (2.13), the detected RF phase-shift is independent of the particular Brillouin gain peak experienced by the probe wave and of the received optical power. This effect is highlighted in Fig. 2.9, where the RF phase-shift in our system and the amplitude in a conventional gain-based BOTDA are calculated and represented for different values of g_0. As it is shown, the RF phase-shift traces are identical for the different values of g_0. This fact has major implications for dynamic sensing. The strain measurements of conventional dynamic BOTDA are based on setting the probe wave to a wavelength on the slope of the amplitude spectrum and translating changes in the detected probe amplitude to variations in BFS. The amplitude spectrum is sensitive to variations in pump power or attenuation in the fiber. Therefore, these measurements are susceptible to errors, which are highly probable in a structure with dynamic deformation, where they would be misinterpreted as strain changes. In the method proposed in this paper, these errors are avoided by employing the phase-shift spectrum of the detected RF signal, instead of the amplitude spectrum. As it is schematically depicted in Fig.2.9(b), the probe wave is set to the slope of the detected phase-shift, obtaining a measurement that is immune to variations of the pump power (via g_0) and of the received probe power.

This tolerance of the RF phase-shift to changes of the Brilloin gain can be further clarified by representing the RF signal in the phasor diagram. As shown previously in Eq. 2.10, the real and the imaginary axis of the phasor representing the resultant RF signal are proportional

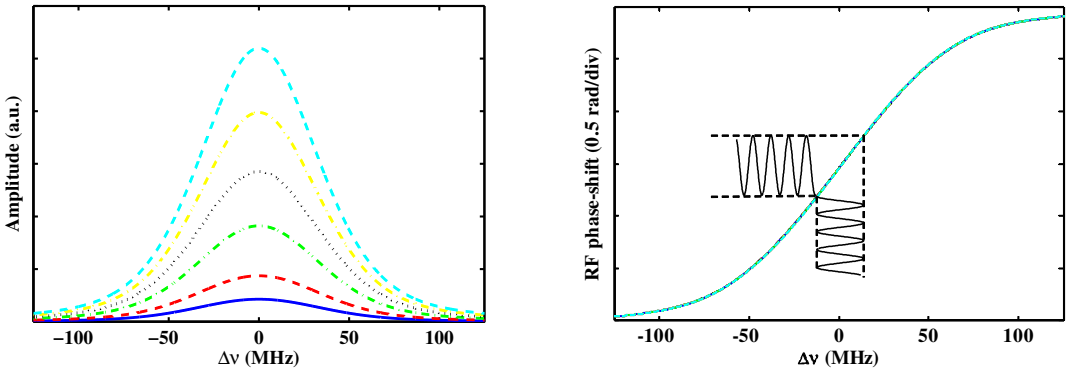

(a) (b)

Fig. 2.9. Calculated (a) amplitude at conventional BOTDA and (b) RF phase-shift of the proposed technique for different values of g_0. In (b) the effect of a variation in BFS on the detected RF phase-shift is schematically depicted (black sinusoids) to highlight the dynamic measurement principle.

to the Brillouin gain and phase-shift, respectively, which in turn are both directly proportional to the Brillouin peak gain or pump/probe power as it is shown in Eq. (2.3). Therefore, any change in these parameters will just modify the detected RF amplitude, but not its phase-shift, as it is depicted in Fig. 2.10. This is found to be valid for Lorentzian interaction as well as for other Brillouin spectra resulting from the use of narrow pump pulses.

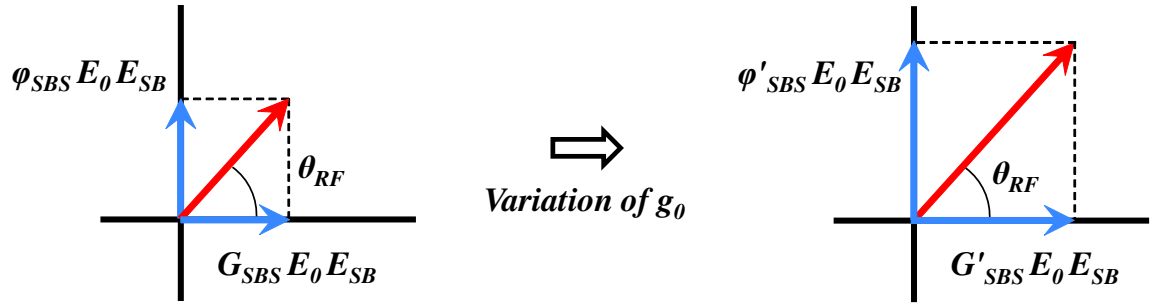

Fig. 2.10. Tolerance of RF phase-shift (θ_{RF}) to variations of the Brillouin gain.

Another important issue to consider in dynamic sensing is the precision of the measurement. According to the measurement principle explained above, this can be calculated taking into account the received noise and the slope of the function used to translate BFS variations into amplitude (in conventional BOTDA) or phase-shift changes (in our scheme). Fig. 2.11 compares the precision of our technique to that of the conventional BOTDA. This error has been calculated at each frequency as the standard deviation of repeated measurements. These simulations were performed calculating the error in phase and in amplitude produced by a

given Gaussian noise at each point of the spectral profile, and translating this noise, using the slope of the employed spectral shape, into errors of the BFS measurement. Moreover, Gaussian pulses of short duration has been used, whose effective interaction spectrum can be approximated to a Faddeeva function [66]. It is possible to observe that the maximum accuracy is better when using phase measurements, and it is because we can center the measurement in the maximum value of the Brillouin gain spectrum, unlike in amplitude measurements. In addition, just one of the two possible sides of the amplitude spectrum for conventional BOTDA is depicted in Fig. 2.11.

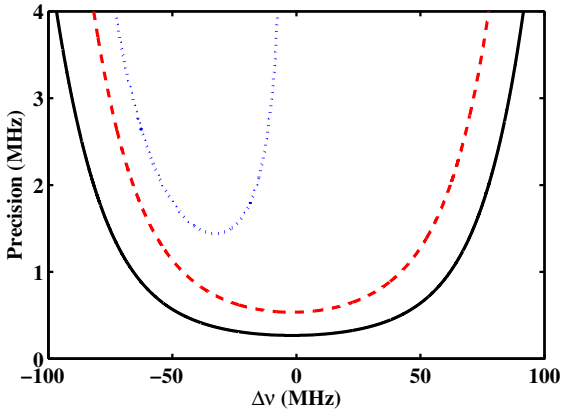

Fig. 2.11. Calculated BFS precision for the conventional SA-BOTDA (dotted line) and phase-shift technique (dashed line), both with an equal SNR of 44dB, and for the phase-shift technique with 6-dB SNR enhancement (solid line).

As it is shown in the figure, the phase-shift technique obtains greater measurement range for a given precision than that of the conventional BOTDA. Note that the measurement range has been defined as the total measurable span within a maximum error. For instance, for a precision of at least 1 MHz (around 20 $\mu\varepsilon$ for standard single mode fiber) the measurement range would be 88 MHz (1760 $\mu\varepsilon$) for the phase-shift technique, while the conventional SA-BOTDA cannot even reach this precision for the same conditions. Furthermore, note that Eq. (2.13) shows that the detected signal and its SNR can be enhanced simply by increasing the carrier power, while keeping the sidebands power low enough to avoid non-local effects [45]. For example, if this feature is exploited to achieve a 6-dB SNR improvement, this would result in a enhanced measurement range of 127 MHz (2540 $\mu\varepsilon$) with 1-MHz precision, as it is highlighted in Fig. 2.11. Furthermore, according to the measurement principle followed in dynamic BOTDA sensors, there is a direct dependence of the measurement range on the spectral shape employed to translate variations of BFS into amplitude or phase-shift changes. Therefore, the use of shorter pump pulses broadens the

interaction spectrum and hence increases the measurement range. Fig. 2.12 illustrates this procedure by comparing the RF phase-shift spectrum and BFS measurement precision for two pump pulses of different temporal duration. As it is shown, the measurement range of the sensor is enlarged from 74 MHz (1480 $\mu\varepsilon$) to 88 MHz (1760 $\mu\varepsilon$) for a 1 MHz (20 $\mu\varepsilon$) target precision. However, this assumes constant SNR, which in practice requires additional averaging.

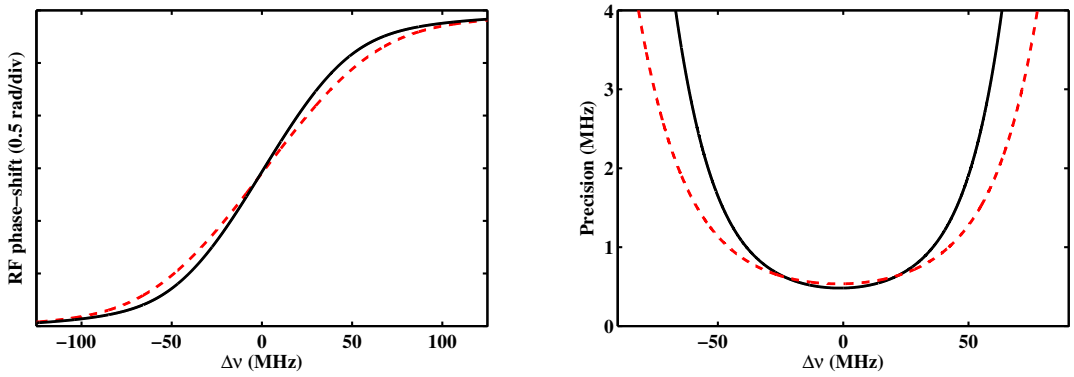

(a) (b)

Fig. 2.12. Calculated (a) RF phase-shift of the proposed technique for two Gaussian pulses of different temporal duration with a equivalent Brillouin linewidth of 90 and 100 MHz and (b) precision of both pulses for a SNR equal to 44dB.

Experimental setup and measurements

The experimental setup shown in Fig. 2.13 was assembled in order to demonstrate the capabilities of the system. The output of a laser source is divided in two optical branches with an optical coupler. In the upper branch, the optical pump pulses of 10-ns duration are formed using a Mach-Zehnder electro-optic modulator (MZ-EOM) by the RF pulse-shaping technique so as to obtain clean and leakage-free pulses [67]. After amplification in an erbium doped fiber amplifier (EDFA), the resulting pump pulses are directed via a circulator to a 160-m-long fiber. In the lower branch, the probe wave is generated with an electro-optic phase modulator driven by a 850-MHz RF signal. After interacting both sidebands with the pump pulses via SBS, the probe signal is directed to a receiver and the resultant RF signal is demodulated. Finally, the BOTDA signal is captured in a digital oscilloscope.

In order to prove experimentally that the detected phase shift is independent to amplitude changes of the BOTDA signal, several spectra were measured varying the attenuation of the

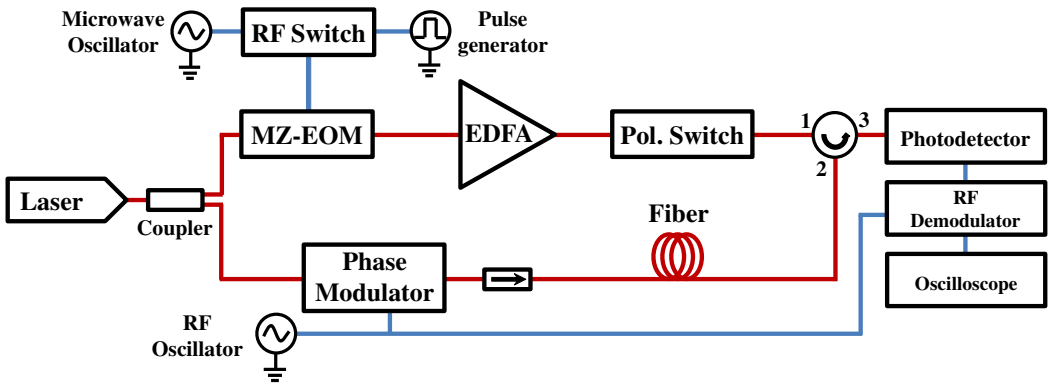

Fig. 2.13. Experimental setup of the BOTDA sensor based on PM probe wave used for dynamic sensing.

probe and pulse signals. Fig. 2.14 shows that, indeed, the detected RF phase-shift remains unaltered while the amplitude suffers severe attenuation.

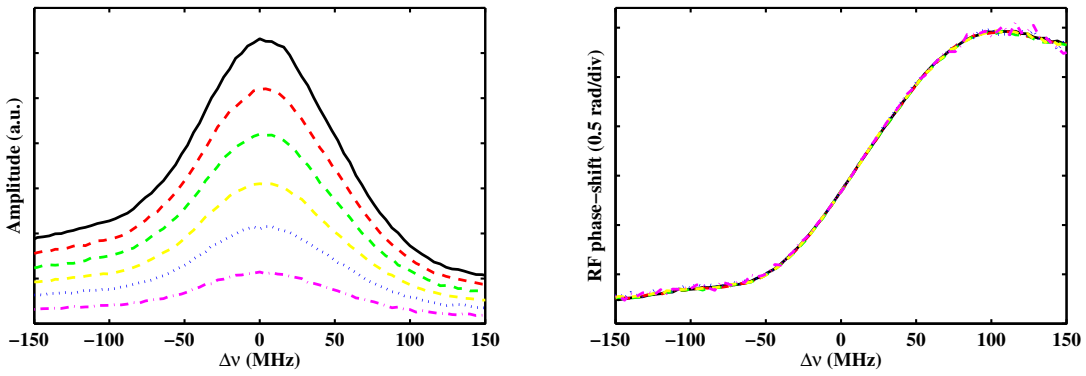

(a) (b)

Fig. 2.14. (a) Amplitude and (b) phase-shift spectra for different attenuation values of the pulse and probe signals.

In addition to this, the measurement range achieved by the phase-shift technique was measured for two different pulse durations of 9 ns and 10 ns. This is represented in Fig. 2.15(a). The measurement range achieved for a precision of 1 MHz is 76 MHz (1520 $\mu\varepsilon$) for the 10 ns pulse in contrast to 84 MHz (1680 $\mu\varepsilon$) for the 9 ns pulse. These results were derived from the measurement of twenty five successive RF phase-shift spectra using 64 averages at the oscilloscope capture. As it is shown in Fig. 2.15(b), the effective interaction spectrum is broadened by employing shorter pulses and a greater measurement range is obtained. Furthermore, the precision achieved for a given pulse duration can be enhanced by increasing the SNR of the detected signal, simply by increasing the averaging at the oscilloscope. For

instance, for a 9 ns pulse and a minimum precision of 1 MHz, the measurement range is 128 MHz (2560 $\mu\varepsilon$) when using 128 averages.

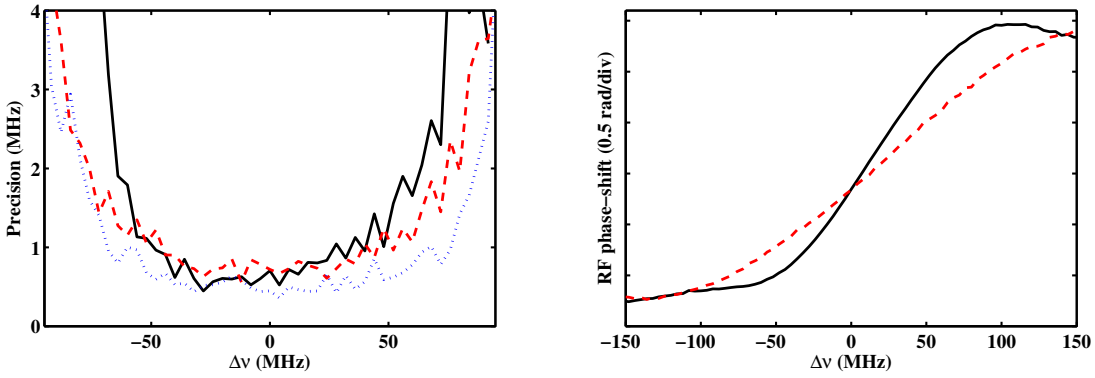

(a) (b)

Fig. 2.15. (a) BFS precision achieved for the phase-shift technique using pulses of 9 ns with 64 averages (red dashed line) and 128 averages (blue dotted line), and for pulses of 10 ns with 64 averages (black solid line). (b) RF phase-shift spectra for pulses of 9 ns (red dashed line) and 10 ns (black solid line).

Finally, a 1-meter section of the fiber was affixed by epoxy resin onto the surface of a 1-m cantilever beam. The cantilever beam was made to vibrate so that dynamic measurements of the induced strain could be performed (Fig. 2.16). The pulse duration was set to 10-ns,

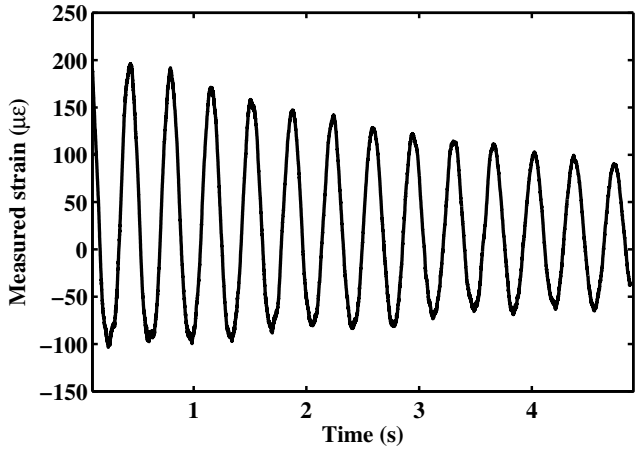

Fig. 2.16. Fast-acquisition measurement of the induced strain at the cantilever beam.

with a measurement rate of 1.66 kHz, achieving a precision of 20 $\mu\varepsilon$ with an averaging

of 64 samples. Notice that this sampling rate was limited by the available acquisition instrumentation, so that higher measurement rates maintaining the same precision should be possible.

2.3.2 Polarization diversity technique based on double orthogonal Brillouin interaction

Once the distributed Brillouin sensors was adapted to perform dynamic measurements, the next target was to further improve the acquisition time of these systems. In SA-BOTDA sensors, the measurement time is basically limited by the repetition rate of the pump pulses and its time-of-flight, which are ultimately determined by the length of the sensing fiber. In addition to this, the precision and measurement range are limited by the available SNR at reception, which may not be enough requiring an averaging process. Finally, another important issue is the required compensation of the polarization dependence of Brillouin interaction.

The polarization dependence of BOTDA is usually overcome by performing a time domain polarization scrambling of the probe wave or of the pump pulses. Other possibility is to use a polarization switch, so that two orthogonal SOPs are sequentially launched into the fiber [68]. A third approach is to implement a passive polarization scrambler using an unbalanced Mach-Zehnder interferometer [69]. Assuming that a SA-BOTDA sensor requires few averages to perform the measurement due to the deployment of optical fibers of short length and hence, high injected pump and probe powers, then the use of a polarization scrambler forces a higher averaging in the measurement than necessary, as a large number of states of polarization (SOP) must be averaged in order to reduce polarization-induced noise. Furthermore, the measurement time linearly increases with the number of averages. On the other hand, a polarization switch only doubles the acquisition time compared to an acquisition of a single trace (if the switching time is not considered), being a better option than the polarization scrambling technique although it also adds additional complexity to the system. Finally, the third approach provides an excellent polarization scrambling with no time penalty in the measurement but it's limited to sensor setups deploying single wavelength CW probe signals.

In this section, we propose an improved setup of the SA-BOTDA technique based on the use of a double orthogonal pulsed pumps. The technique is valid for SA-BOTDA sensors based on the phase-modulated probe wave, which retains the advantage of performing measurements largely immune to attenuation in the optical fiber and adds a new one: the

capability to perform polarization independent measurements throughout the fiber even if no averaging is applied.

Fundamentals

Stimulated Brillouin scattering process has its origin in the interference between two optical waves which generates a traveling longitudinal acoustic wave. This acoustic wave, in turn, couples the optical waves to each other. As the process is coherent in the optical domain, its efficiency is dependent on the relative states of polarization of the two waves involved in the process. This polarization dependence of SBS interaction can be mathematically modeled by the real factor η which determines the mixing efficiency of the counter-propagating signals [70]. In general, this mixing efficiency factor η ($0 \leq \eta \leq 1$) can be described as a function of the SOP of probe and pump signals as:

$$\eta = \frac{1}{2}\left(1 + s_{1P}s_{1S} + s_{2P}s_{2S} - s_{3P}s_{3S}\right) \tag{2.14}$$

where $\hat{S}_S = (s_{1S}, s_{2S}, s_{3S})$ and $\hat{S}_P = (s_{1P}, s_{2P}, s_{3P})$ are the normalized Stokes vectors representing the SOP of the counter-propagating probe and pump signals, respectively, at a given position of the sensing fiber. Therefore, for a differential length of fiber, SBS interaction between pump and probe waves is optimal ($\eta = 1$) when the orientation, the ellipticity and the sense of rotation of their polarization ellipses are the same when seen from one direction, as shown in Fig. 2.17(a). Conversely, no SBS interaction takes place ($\eta = 0$) when the polarization ellipses of pump and Stokes waves are similar to the first case, but with orthogonal orientation (their long axes are orthogonal to each other, see Fig. 2.17(b)) [70, 71].

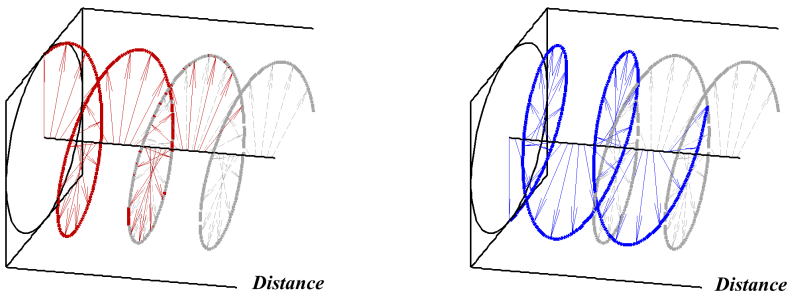

(a) (b)

Fig. 2.17. Schematic representation of probe (gray line) and pump waves (red and blue lines) for (a) equal and (b) orthogonal states of polarization.

In the most usual scenario for distributed fiber sensors, the measurement is performed over standard single-mode fiber, where the SOP of the counter-propagating waves will vary randomly and dynamically. Therefore, it is not possible to guarantee a proper alignment between them for every position of the fiber. As a result, the signal to noise ratio (SNR) of the measurement will be very low in some positions of the fiber, being zero for those where there is no Brillouin interaction. As a consequence, in Brillouin-based sensors it is necessary to apply some kind of polarization averaging or polarization diversity technique.

If we now consider the case where the state of polarization of the pump wave is orthogonal to the previous one ($\hat{S}_P$), then its normalized Stokes vector will be given by $\hat{S}_{P\perp} = (-s_{1P}, -s_{2P}, -s_{3P})$ and the mixing efficiency will yield:

$$\eta_\perp = \frac{1}{2}(1 - s_{1P}s_{1S} - s_{2P}s_{2S} + s_{3P}s_{3S}) \tag{2.15}$$

Therefore, by simply adding η and $\eta_\perp$ represented in Eq. (2.14) and (2.15), respectively, it is found that both interactions will be complementary:

$$\eta + \eta_\perp = 1 \tag{2.16}$$

Furthermore, due to the unitary nature of the fiber, the two orthogonal polarization states entering the fiber will keep their relative orthogonallity, even though the states themselves are continuously changing along the fiber [71]. As a consequence, the complementarity of the two Brillouin interactions will be guaranteed throughout the whole length of fiber, even for relatively long fibers, where the orthogonalization error induced by polarization dependent loss is still negligible [72].

In our technique, we take advantage of this property by generating two simultaneous and complementary Brillouin interactions along the sensing fiber. Fig. 2.18 schematically depicts the fundamentals of the proposed system. A single tone phase-modulated probe wave is injected into one end of the optical fiber under test, while two orthogonal pump pulses are introduced at the other end. Each sideband of the phase-modulated probe wave interacts with its respective pump pulse via stimulated Brillouin scattering. The resulting phase-modulated probe wave affected by both quadrature polarization Brillouin interactions is directed to the receiver. Finally, the detected RF electrical signal is demodulated in a synchronous demodulator so that both the amplitude and the phase-shift of the detected RF signal can be recovered [73]. As schematically shown in Fig. 2.18, the wavelengths of the pump pulses are adjusted so that each of the two orthogonal pumps interacts with one of the modulation sidebands of the phase-modulated probe wave. The aim of this double interaction is to produce a Brillouin gain over one of the sidebands, while a Brillouin loss is generated

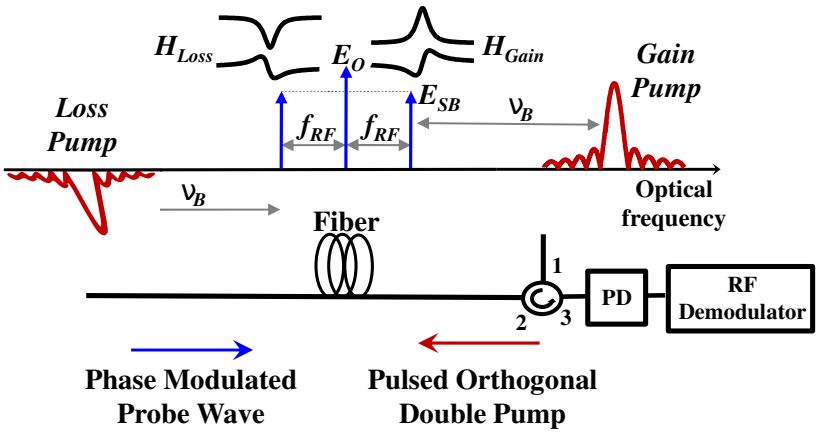

Fig. 2.18. Schematic representation of the fundamentals of the double orthogonal-pump SBS interaction, where each of the two orthogonal pump pulses (red) interacts with a different modulation sideband of the phase-modulated probe wave (blue).

over the second one. Notice that these two optical interactions of opposite sign will not cancel each other once the phase-modulated probe wave is detected, due to the fact that the two sidebands of the modulation have a phase-shift of π radians [73]. If the modulation frequency of the probe wave is much higher than the Brillouin bandwidth, we can consider that each SBS interaction only affects one sideband of the modulation, leaving the other sideband and the carrier unaffected. Then, the optical field at the input of the photodetector coming from the interaction of pump and probe at a particular location in the fiber, z, is given by the following expression:

$$\begin{aligned} E(t) = &-E_{SBi}\exp\left(-\frac{\alpha}{2}L\right)\exp\left(i2\pi\left(\nu_0 - f_{RF}\right)t\right)H_{SBS,Loss}(z,\Delta\nu) \\ &+E_{0i}\exp\left(-\frac{\alpha}{2}L\right)\exp\left(i2\pi\nu_0 t\right) \\ &+E_{SBi}\exp\left(-\frac{\alpha}{2}L\right)\exp\left(i2\pi\left(\nu_0 + f_{RF}\right)t\right)H_{SBS,Gain}(z,\Delta\nu) \end{aligned} \tag{2.17}$$

where $H_{SBS,Gain}$ and $H_{SBS,Loss}$ are, respectively, the complex Brillouin gain and loss spectra at position z defined in Eq. (2.3) and repeated here for convenience to include the mixing efficiency factor:

$$\begin{aligned} H_{SBS}(z,\Delta\nu) &= \exp\left(\eta\frac{g_0\Delta\nu_B}{\Delta\nu_B + 2i\Delta\nu}P_P(z)\Delta z\right) \\ &= \exp\left(\eta\left(\frac{g_0\Delta\nu_B^2}{\Delta\nu_B^2 + 4\Delta\nu^2}P_P(z)\Delta z - i\frac{2g_0\Delta\nu_B\Delta\nu}{\Delta\nu_B^2 + 4\Delta\nu^2}P_P(z)\Delta z\right)\right) \\ &\approx 1 + \eta\left(g_{SBS} - i\,\varphi_{SBS}\right) \end{aligned} \tag{2.18}$$

where, g_0 is the Brillouin gain ($g_0 > 0$) or loss ($g_0 < 0$) depending on the described SBS interaction. The approximation in the last term of Eq. (2.18) is obtained assuming a small gain (or loss). Note also that, G_{SBS} and φ_{SBS} represent, respectively, the Brillouin gain (or loss) factor and the Brillouin phase-shifts of each interaction shown in Fig. 2.18. Furthermore, the symmetry of both Brillouin interactions is so, that the phase-shift induced over both sidebands will be equal ($\varphi_{SBS} = \varphi_G = \varphi_L$), and the gain factor will be of identical magnitude but opposite sign ($g_{SBS} = G_G = -G_L$). In that case, the detected optical power signal at the demodulation frequency f_{RF} can be expressed as:

$$\begin{aligned} P(z,\Delta\nu)\big|_{f_{RF}} &= 2\sqrt{P_{0i}P_{SBi}}\exp(-\alpha L)\cos(2\pi f_{RF}t) \\ &\cdot[(1+\eta_G(G_G+i\varphi_G))-(1+\eta_L(G_L-i\varphi_L))] \\ &= 2\sqrt{P_{0i}P_{SBi}}\exp(-\alpha L)(\eta_G+\eta_L)(G_{SBS}+i\varphi_{SBS})\cos(2\pi f_{RF}t) \end{aligned} \tag{2.19}$$

If we now consider that both sidebands of the phase-modulated probe wave have the same SOP, then Eq. (2.16) can be applied so that η_G and η_L can be removed from the equation. Therefore, the technique removes the need for polarization scrambling, as the detected signal for any given position of the fiber will be independent of the SOP of the probe wave. As a consequence, no averaging is required to eliminate the polarization induced fluctuations. Substituting Eq. (2.18) in Eq. (2.19), we finally obtain the expression of the detected RF signal using the presented technique:

$$\begin{aligned} P(t)\big|_{f_{RF}} \approx 2\sqrt{P_{0i}P_{SBi}}\exp(-\alpha L)\frac{g_0\Delta\nu_B}{\sqrt{\Delta\nu_B^2+4\Delta\nu^2}}P_P(z)\Delta z \\ \cdot\cos\left(2\pi f_{RF}t-\arctan\left(2\frac{\Delta\nu}{\Delta\nu_B}\right)\right) \end{aligned} \tag{2.20}$$

Equation (2.20) shows that the detected RF phase-shift is independent of the particular Brillouin gain peak experienced by the probe wave and of the received optical power as shown in section 2.2. This is a key feature for dynamic measurements, as the sensor will not be susceptible to errors caused by changes in pump power or attenuation in the fiber, which are highly probable in a structure with dynamic deformations [73]. Therefore, the same technique described in section 2.3.1 can be deployed to perform dynamic measurements, but with the additional advantage of having polarization independent BOTDA traces.

Experimental setup and measurements

The experimental setup shown in Fig. 2.19 was assembled in order to demonstrate the system. The output of a 1550.5 nm laser source is divided in two optical branches with an optical

coupler. In the upper branch, the optical beam is pulsed using a semiconductor optical amplifier (SOA). This pulsed beam is directed to a Mach-Zehnder electro-optic modulator driven by a microwave signal of 9.6 GHz and biased in minimum transmission, so that two pulsed sidebands are generated, while the optical carrier is suppressed. In order to

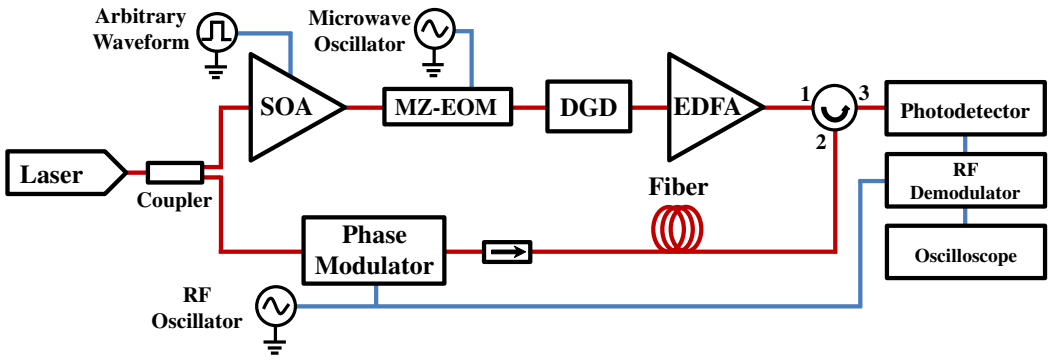

Fig. 2.19. Experimental setup for the polarization diversity BOTDA sensor based on a phase-modulated probe wave, a double orthogonal pump and RF demodulation.

orthogonalize the SOP of the two pulsed sidebands of the optical double-sideband with suppressed-carrier (ODSB-SC) modulation, an all optical, passive and simple technique is implemented. This is performed by the use of a differential group delay (DGD) module, which provides a group delay between two linear orthogonally polarized waves. The technique is schematically described in Fig. 2.20. The linearly polarized light coming from the MZ-EOM is launched into the birefringent material at 45º or 135º with the axis of the DGD module. This feature can be provided by the manufacturer, so that the connection of the DGD module to the output of a MZ-EOM with polarization maintaining fiber is straightforward, requiring no additional polarization control. After going through the DGD module, the differential phase-shift suffered by the light travelling through the two principal axis of the DGD depends on its wavelength (λ):

$$\theta(\lambda) = \frac{2\pi L(n_e - n_o)}{\lambda} \tag{2.21}$$

where L is the length of the DGD module, and n_e and n_o are, respectively, the extraordinary and ordinary refraction indexes of the DGD module. Therefore, depending on the wavelength of the incident beam, the birefringent material provides different polarization states at its output [74]. Notice that if the wavelengths of two waves are tuned in such a way that the difference between the relative phase-shifts suffered by them is made equal to π, their SOP will be orthogonal at the output of the DGD.

$$\Delta\theta = 2\pi \cdot \Delta f \cdot \Delta\tau = \pi \tag{2.22}$$

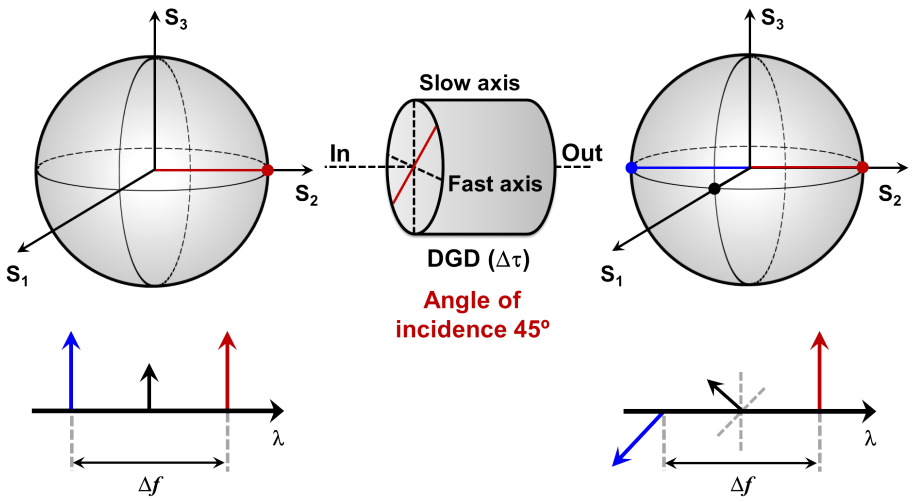

Fig. 2.20. Schematic representation of the procedure deployed to orthogonalize the sidebands of the optical modulation at the output of the MZ-EOM. The optical carrier and the modulation sidebands have the same SOP when they impinge the DGD module, but the differential delay suffered by each of them makes the two modulation sidebands orthogonal.

where $\Delta\tau$ is the differential group delay introduced by birefringence and Δf is the frequency difference between both waves. As a result, in order to obtain linear orthogonal polarizations between both sidebands of the ODSB-SC modulation, the $\Delta\tau$ needed is $1/(4\,f_\mu)$, where f_μ is the frequency of the microwave signal driving the MZ-EOM. In this way, the two pump waves are made orthogonal by simply inserting in the setup an inexpensive, passive and easy to deploy component. In our experiment, a DGD module with $\Delta\tau$=26 ps was used, so that the two pulsed sidebands of the modulation, separated by 19.2 GHz, were made orthogonal.

In order to verify the orthogonallity of the generated pump pulses, a polarization controller and a polarization beam splitter (PBS) where inserted after the DGD module in the experimental setup. Fig. 2.21 shows the spectra at the two outputs of the PBS, measured in an optical spectrum analyzer (OSA), when the SOP of one of the sidebands at the input of the PBS is aligned with one of its principal axis. A sideband suppression of more than 30 dB is observed, showing an excellent orthogonallity between both sidebands. The modulation was not pulsed during this measurement so that the spectrum could be properly acquired in the OSA. Once the double orthogonal pump is generated, this is amplified by an erbium doped fiber amplifier, and the resulting pump pulses are directed via a circulator to a 930 m long fiber. In the lower branch of the setup in Fig. (2.19), the probe wave is generated with an electro-optic phase modulator driven by a 1.3 GHz RF signal. The modulation frequency is chosen so that the upper sideband of this modulation interacts via SBS with the lower sideband of the ODSB-SC modulated pump pulse, while the lower sideband of the phase

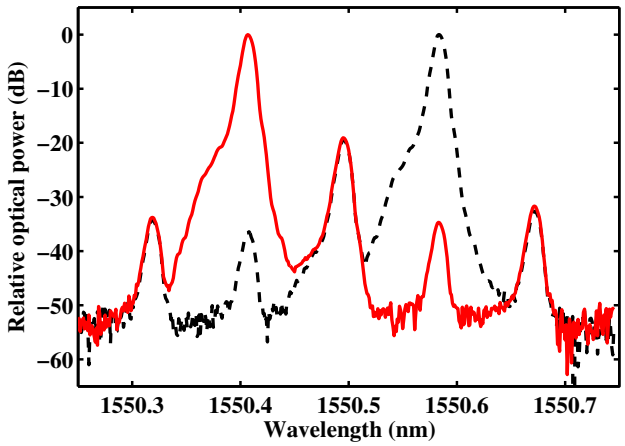

Fig. 2.21. Measured spectra at the outputs of a PBS inserted after the DGD module, when the state of polarization of one of the sidebands of the modulation is aligned with the principal axis of the PBS (red-solid line and black-dashed line).

modulation is affected by the higher frequency pulsed pump. After interacting with the orthogonal pump pulses via SBS, the probe signal is directed to a receiver and the resultant RF signal is demodulated. Finally, the BOTDA signal is captured in a digital oscilloscope. The BOTDA trace captured in the oscilloscope is depicted in Fig. 2.22(a), showing negligible polarization dependence, as compared with a conventional BOTDA trace (Fig. (2.22(b))). The trace in Fig. 2.22(b) was obtained by removing the DGD module from the setup. Both traces have been acquired using a 128 averaging rate, but deploying no further technique to compensate the polarization dependence of SBS interaction.

In order to perform dynamic measurements, a 1-meter section at the end of the 930-m fiber was affixed by epoxy resin onto the surface of a 1 m cantilever beam. The cantilever beam was made to vibrate so that dynamic distributed measurements of the induced strain along the fiber could be performed. The pulse duration was set to 10 ns to obtain 1-m spatial resolution. Moreover, a BOTDA trace was captured every 12 μs and 128 averages were used, achieving a 651 Hz measurement rate. Fig. 2.23 shows the measured strain in the final locations of the fiber when the cantilever beam is made to vibrate. The distributed measurement is also demonstrated, as only the section of the fiber attached to the cantilever beam is suffering strain, while the adjacent sections of fiber remain steady. The estimated uncertainty was 2 MHz for a 145 MHz (2900 $\mu\varepsilon$) measurement range measured using the guidelines given in [73]. These parameters can be enhanced by increasing the SNR parameter of the sensor or reducing its phase noise [75].

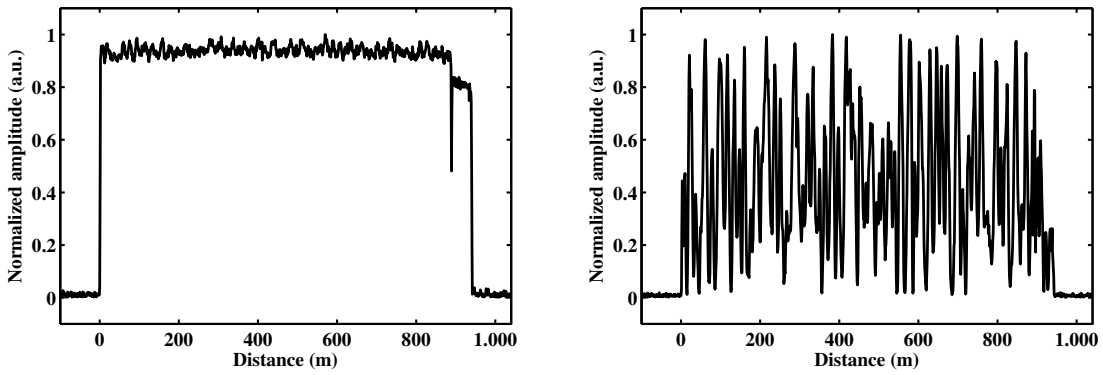

(a) (b)

Fig. 2.22. Measured BOTDA trace (a) when the polarization diversity technique is implemented and (b) when the DGD module is removed from the setup.

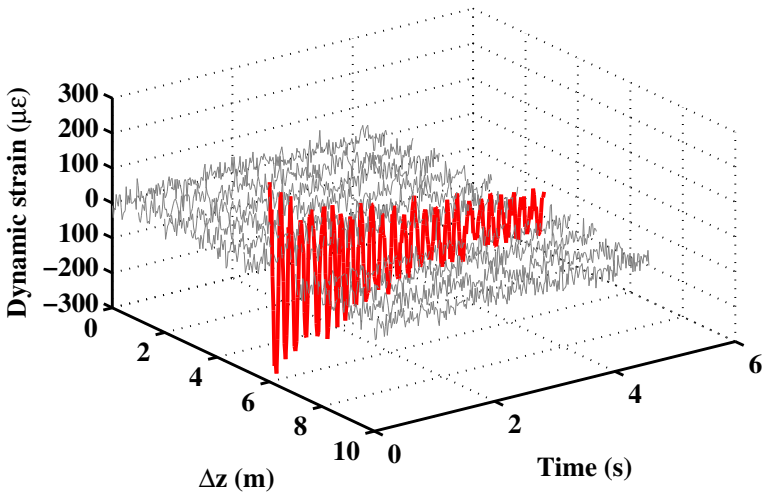

Fig. 2.23. Fast-acquisition polarization-compensated measurement of the strain induced at the last locations of the fiber (grey traces), where the cantilever beam (red-solid line) is made to vibrate.

2.4 Long-range measurements using BOTDA sensors

Brillouin optical time-domain analysis sensors are bound to become a fundamental tool for monitoring in a number of structures ranging from oil and gas pipelines to electric power. This wide variety of applications is stimulating a very important research effort into these sensors. One of the main trends is the development of long-range BOTDA sensors, where the ultimate distance is constrained by several effects:

- **Non-local effects:** as discussed in section 1.5.1, they limit the maximum probe power injected into the fiber in order to avoid distortion of the measured Brillouin spectra at the end of the fiber, which may induce to BFS errors [19]. Consequently, the optical power reaching the receiver is limited, degrading the performance of the sensor.
- **Modulation instability:** limits the maximum pump power injected into the fiber to avoid excessive depletion of the pulsed wave and hence, a limited Brillouin gain at the end of the fiber [30] (see section 1.5.2).
- **Spatial resolution:** defines the number of resolved points along the fiber. This parameter is increased reducing the pulse duration, which leads to a limited SNR and a broadening of the measured Brillouin linewidth, as explained in section 1.5.3. Both aspects make it very difficult to precisely determine the Brillouin peak spectrum and hence, the BFS value [35].

During the following sections, the aspects described above will be studied when using a phase-modulated probe wave in BOTDA sensors.

2.4.1 Mitigation of non-local effects

In a conventional BOTDA setup, a probe wave and a pump wave are counter-propagated through an optical fiber with a frequency difference near the BFS (around 10.8 GHz for a standard single mode fiber). As a result, the pump pulse generates a local Brillouin gain or loss (depending on the sensor's configuration) in the probe wave, whose magnitude depends on the pump pulse power. The spectrum of this interaction, and hence the BFS, can be measured by scanning the frequency difference between the two waves as the probe wave is detected. However, the pump pulse is also affected by SBS interaction, either being slightly amplified (loss configuration) or attenuated (gain mode) at each location of the fiber. Therefore, as the pulse propagates along the fiber, this energy transfer is accumulated and can significantly modify the pulse power, as it is schematically depicted in Fig. 2.24. More specifically, this amplification of the pump pulse power changes with the frequency difference

between the two waves. Therefore, the gain or loss spectrum is scanned with different pump pulse powers, which can distort the recovered spectrum, particularly at the final locations of the fiber (z ≈ L). This is a non-local effect as the measurement at a particular location is affected by Brillouin interaction at all the preceding locations along the fiber.

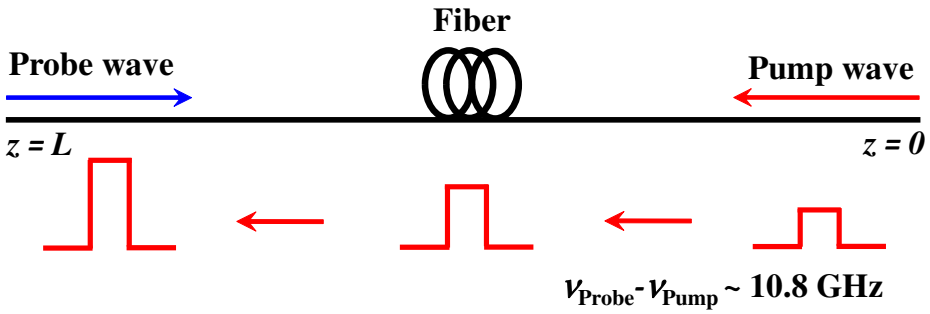

Fig. 2.24. Schematic representation of the amplification of the pump pulse along its propagation at a conventional loss based BOTDA sensor.

This fact is a major restriction for long-range sensing distances because, as the probe wave optical power increases to achieve larger monitoring distances, the energy transfer between the pump pulse and the probe wave is greater at each location of the fiber and hence, non-local effects become more detrimental [19].

The most popular solution to reduce this effect is to employ a balanced Brillouin interaction between a pulse wave and equally frequency spaced probe waves. As a consequence, the pump pulse suffers the same gain and loss at the frequency of maximum interaction [24]. However, the use of balanced BOTDA sensor limits the use of other possible configurations to create other techniques more advanced. Therefore, it is necessary to study other approaches, where the power of a single probe component can be increased without being affected by the generation of frequency-dependent pump power variations.

During this section, the advantage of using a phase-modulated probe wave in BOTDA sensor regarding non-local effects is presented. As in the previous section, the system benefits from the special features of the RF phase-shift in relation to tolerance to variations of the Brillouin gain. Therefore, the proposed technique allows to increase the probe power and hence, enhance the amplitude of the detected signal at the receiver.

Fundamentals

In contrast to conventional BOTDA sensors, we propose a configuration scheme based on the RF phase-shift used for dynamic sensing [73] (shown in the previous section 2.3.1). The difference with respect to the configuration proposed in section 2.3.1 is the suppression of

one pulsed sideband to avoid depletion of the pulses due to four wave mixing. As shown in Fig. 2.25, the upper optical frequency pulse has been removed in order to implement a loss-based BOTDA sensor although the technique equally applies to a gain configuration.

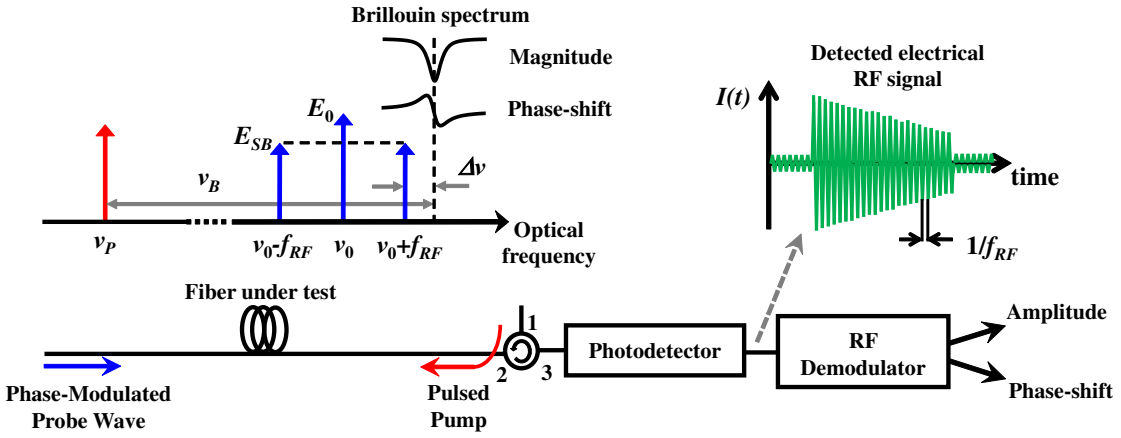

Fig. 2.25. Schematic representation of SBS interaction and the received RF signal.

Considering that SBS interaction only affects the first sideband of the modulation, the optical field at the input of the photodetector coming from the interaction between the pump and probe waves at a particular location in the fiber, z, is given by the following expression:

$$\begin{aligned} E(t)\big|_{rx} = &-E_{SBi}\exp\left(-\frac{\alpha}{2}L\right)\exp\left(i2\pi\left(\nu_0 - f_{RF}\right)t\right) \\ &+E_0\exp\left(-\frac{\alpha}{2}L\right)\exp\left(i2\pi\nu_0 t\right) \\ &+E_{SB}\exp\left(-\frac{\alpha}{2}L\right)\exp\left(i2\pi\left(\nu_0 + f_{RF}\right)t\right)H_{SBS}\left(z,\Delta\nu\right) \end{aligned} \tag{2.23}$$

where H_{SBS} is the complex Brillouin loss spectrum at position z (see Eq. (2.3)).

The resultant RF signal after detection of the optical field in Eq. (2.23) can be described as:

$$\begin{aligned} P(t)\big|_{f_{RF}} = &\,2\sqrt{P_{0i}P_{SBi}}\exp\left(-\alpha L\right)\frac{g_0\Delta\nu_B}{\sqrt{\Delta\nu_B^2+\Delta\nu^2}} \\ &\cdot\cos\left(2\pi f_{RF}\,t - \arctan\left(2\frac{\Delta\nu}{\Delta\nu_B}\right)\right) \end{aligned} \tag{2.24}$$

Notice in Eq. (2.24) that the detected RF phase-shift remains independent of the pump pulse power. This feature, which has already been discussed in the context of dynamic measurements, has major implications regarding the tolerance of the technique to non-local effects, as the measurements of the RF phase-shift are not going to be affected by frequency dependent changes of the pump pulse power.

In order to study theoretically the potential of the technique, we consider the worst-case scenario for non-local effects. This arises when a long sensing fiber with a uniform BFS profile is followed by a short section at the far end of the fiber, where the BFS is shifted from the rest of the fiber by $\Delta\nu_B/3$ [19]. As the pump pulse propagates along the fiber, it is amplified by the energy transferred from the probe wave. This amplification of the pump pulse has a direct dependence on the injected probe power into the fiber and the properties of the fiber itself, but not on the injected pump pulse power [19]. As shown in section 1.5.1 for a gain-based BOTDA configuration, the change of the pump power due to Brillouin interaction is useful to estimate the maximum BFS error. Here, the gain factor can be analogously calculated for a loss-based BOTDA configuration by:

$$d = \exp\left(\frac{g_0}{A_{eff}} P_{Si} L_{eff}\right) - 1 \tag{2.25}$$

In order to present general results independent of the particular parameters of a system, we consider the effects of different gain factors at the end of the long fiber section ($L > L_{eff}$). These are shown in Fig. 2.26, where gain factors from 0% (no change of the pump pulse power) to a maximum amplification of 171.8% have been represented. Notice that the pump pulse amplification depends on the frequency difference between pump pulse and probe waves ($\Delta\nu$), following a Lorentzian profile corresponding to SBS interaction. As

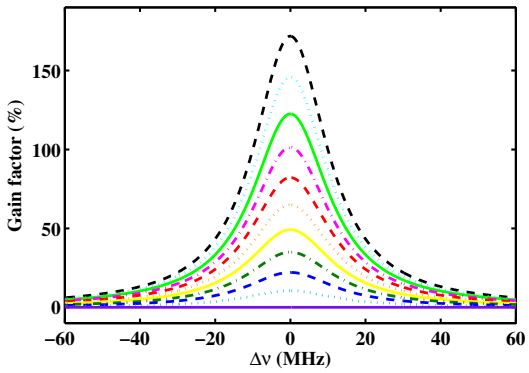

Fig. 2.26. Gain factor as a function of the frequency difference between pump and probe waves, for several probe wave optical powers. A Brillouin interaction with a linewidth equal to 30 MHz has been assumed.

a consequence, at the last positions of the fiber, the Brillouin spectrum will be scanned deploying a frequency dependent pump pulse power, resulting in a distorted Brillouin spectrum. This is depicted in Fig. 2.27(a), where the recovered Brillouin loss spectra at a conventional BOTDA sensor have been calculated considering the frequency dependent

pump pulses of Fig. 2.26. Arbitrary units are used in the figure, as the focus here is on highlighting the general trends of this effect. As it is shown, the distortion of the measured Brillouin spectrum leads to a systematic error in the measurement of the BFS (Δ_{BFS}). This biasing effect of the peak at the recovered Brillouin loss spectrum can be explained by the increment of the pump pulse power at those frequencies, which generates a higher Brillouin interaction that reduces to a greater extent the magnitude of the probe wave at that location. In contrast to the conventional BOTDA sensors, if the same conditions are applied to the proposed technique, the recovered RF phase-shift spectra remain unaltered to changes of the pump pulse power. This is highlighted in Fig. 2.27(b), where the calculated RF phase-shift spectra are superposed independently of the injected probe power. Consequently, larger probe wave power than in conventional BOTDA sensors can be injected into the optical fiber, because the limitation due to non-local effects is mostly removed. This enables a rise in SNR, which could enhance the system performance. Notice that the magnitude of this enhancement depends on the actual noise sources at the particular receiver deployed. For instance, for ideal shot noise limited performance, the SNR improvement would be directly proportional to the increment in the detected power. Moreover, this SNR increment adds to that already provided by the heterodyne detection deployed in our technique [45]. Therefore, our system enhances the SNR due to two factors: the possibility to inject large probe wave optical powers into the fiber and the demodulation technique.

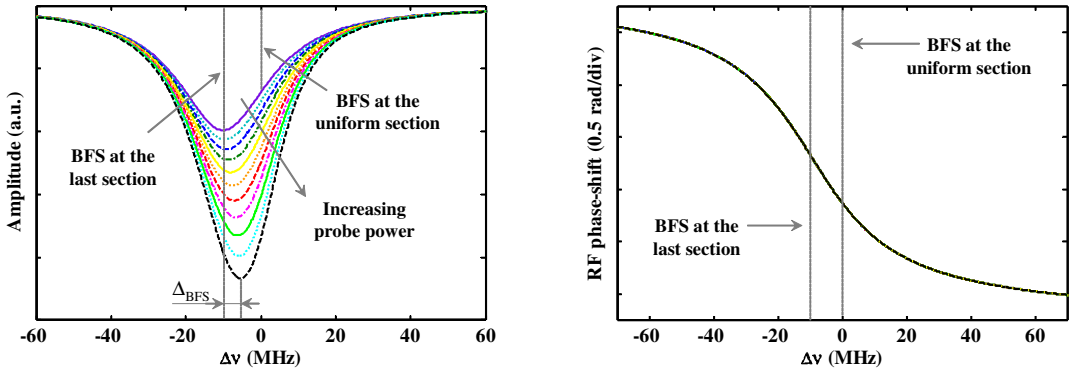

(a) (b)

Fig. 2.27. Calculated (a) amplitude spectra for a conventional loss-based BOTDA and (b) RF phase-shift spectra of the proposed technique for different probe wave powers, at the last section of the fiber.

Experimental setup and measurements

The experimental setup assembled to validate the capabilities of the system is depicted in Fig. 2.28. The setup is very similar to the one shown in section 2.3.1. The only differences reside on the incorporation of a fiber Bragg grating to remove one of the double sidebands of the pump wave and the setting of the pulse duration to 50 ns that is a typical duration for long-range systems based on differential pulse-width pair BOTDA [35]. Measurements were performed over a 20 km long standard single mode fiber, whose last 200 m (the closer to the probe wave input) were introduced in a climatic chamber while the rest of it was maintained at room temperature. The peak pump power was 20.5 dBm.

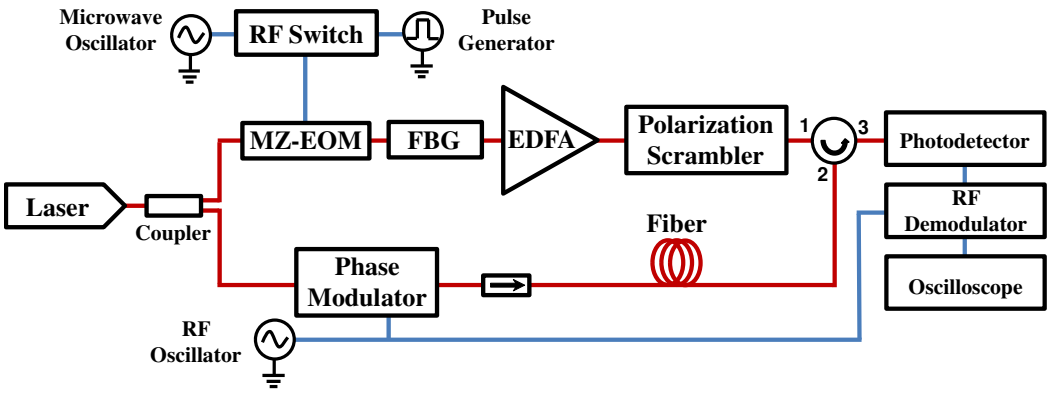

Fig. 2.28. Experimental setup for the BOTDA sensor based on phase-modulated probe wave and RF demodulation.

In order to determine the amplification suffered by the pump pulse during its propagation through the optical fiber, the pump pulse power was measured for several probe wave powers at the end of the fiber for $\Delta\nu = 0$ MHz. This is depicted in Fig. 2.29(a), where the measured pulse power is doubled for the largest probe wave optical power in relation to the pump pulse only affected by the attenuation of the fiber. In addition, the experimental pump gain factor was calculated as a function of the frequency difference between the pump and probe waves as shown in Fig. 2.29(b). Notice the frequency dependent nature of this amplification as the probe power is increased.

This energy transfer from the probe wave to the pulsed pump is clearly reflected in the amplitude of the BOTDA trace in Fig. 2.30. The amplitude of the BOTDA trace depends on the pulse power, which is being amplified through its propagation along the fiber. This amplification compensates the attenuation of the fiber (0.2 dB/km) giving rise to an almost flat BOTDA trace.

In addition, in order to create a propitious scenario for the emergence of non-local effects, the temperature of the fiber section placed at the climatic chamber was shifted from that of

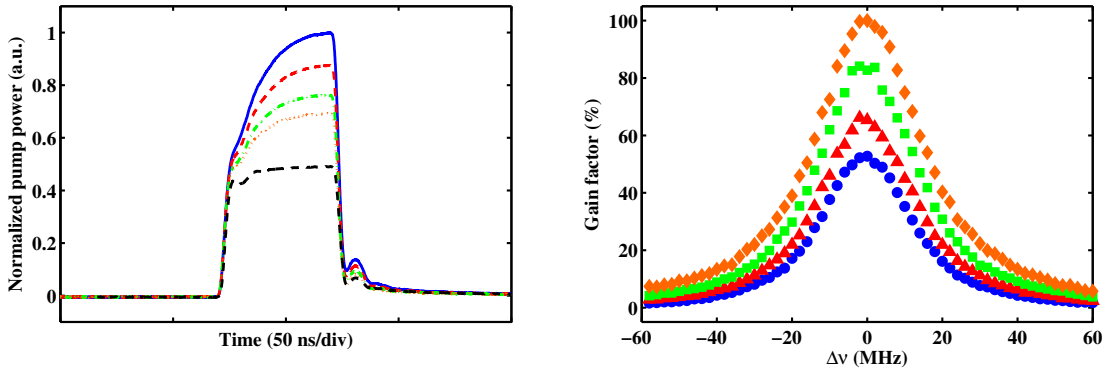

(a) (b)

Fig. 2.29. (a) Measured pulses for different probe wave optical powers (blue solid line 0.67mW, red long dashed line 0.56mW, green short dashed line 0.47mW and orange dashed dot line 0.37mW) and without Brillouin interaction (black dashed dot dot line). (b) Experimental calculated gain factor at the end of the fiber for several probe wave powers (blue circle symbol 0.67mW, red triangle symbol 0.56mW, green square symbol 0.47mW and orange diamond symbol 0.37mW).

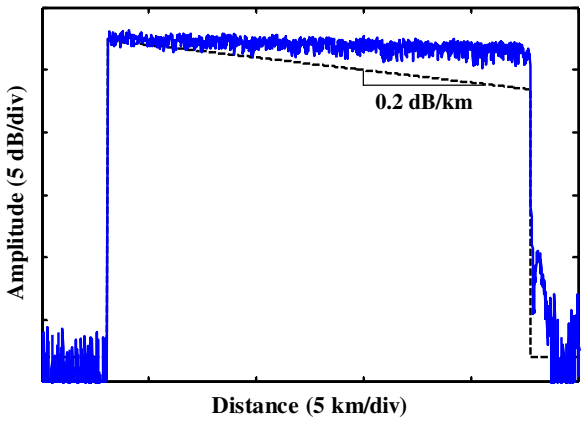

Fig. 2.30. Measured amplitude of a BOTDA trace at $\Delta\nu = 0$ MHz (blue solid line) and theoretical BOTDA trace not affected by pump wave amplification (black dashed line).

the rest of the fiber [19]. In this situation, measurements of the RF phase-shift and amplitude spectra were performed at the heated section, injecting different probe wave powers into the optical fiber. As it is depicted in Fig. 2.31(a), the RF phase-shift spectra remain largely independent of probe power in contrast to the amplitude spectra in Fig. 2.31(b), which are clearly distorted by non-local effects as the probe wave power increases.

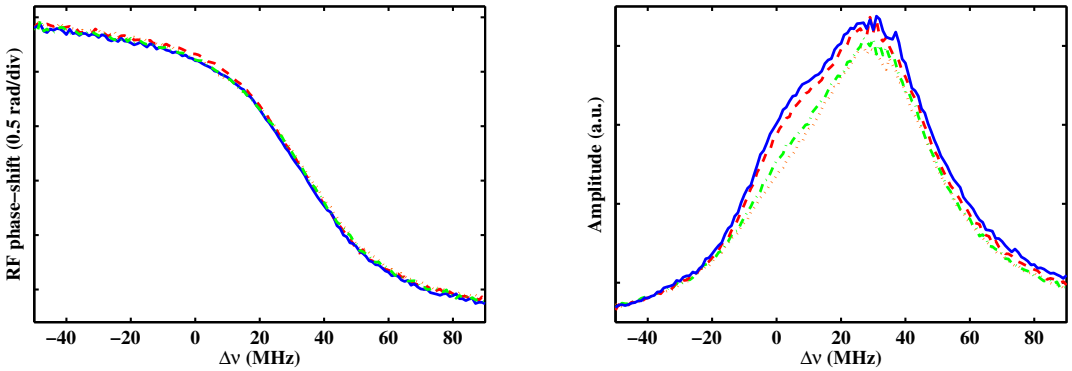

(a) (b)

Fig. 2.31. Measured (a) RF phase-shift spectra and (b) amplitude spectra for different optical powers of the probe wave (blue solid line 0.67mW, red long dashed line 0.56mW, green short dashed line 0.47mW and orange dashed dot line 0.37mW) at the heated section with a 30ºC temperature difference from the rest of the fiber.

Finally, the temperature of the climatic chamber was modified in order to evaluate the performance of the technique for temperature measurements. These measurements were performed setting the probe wave power to a level high enough to induce a large frequency dependent amplification to the pump pulse. The spectra measured at the heated section of the fiber are depicted in Fig. 2.32. As it is shown, the RF phase-shift spectra are shifted in frequency as the temperature is risen. However, their shape remains unaltered in contrast to the amplitude spectra, which suffer the detrimental impact of non-local effects. Furthermore, as it is shown in the inset, there is a good agreement between the changes of temperature at the climatic chamber (5^oC per measurement) and the frequency shift of the RF phase-shift spectra. In addition, the BFS corresponding to the RF phase-shift and the amplitude spectra were obtained by performing a mathematical fit based on Eq. (2.24). This is depicted in Fig. 2.33, where the linear regression performed to the BFS data obtained from the RF phase-shift spectra shows a clear linear relation with temperature, in contrast to the data obtained from the amplitude spectra.

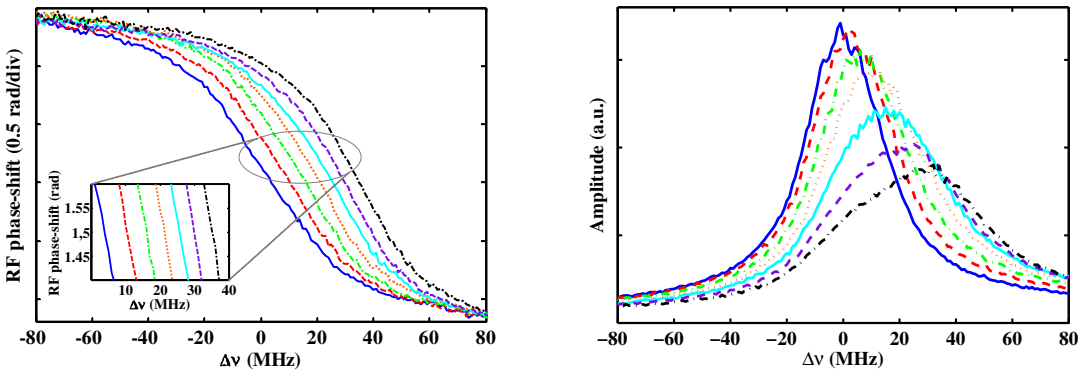

(a) (b)

Fig. 2.32. Measured (a) RF phase-shift spectra and (b) amplitude spectra injecting a 0.67mW probe wave power into the fiber for different temperatures at the climatic chamber from 24C (blue solid line) to 54C (black short-long dashed line) in 5C steps.

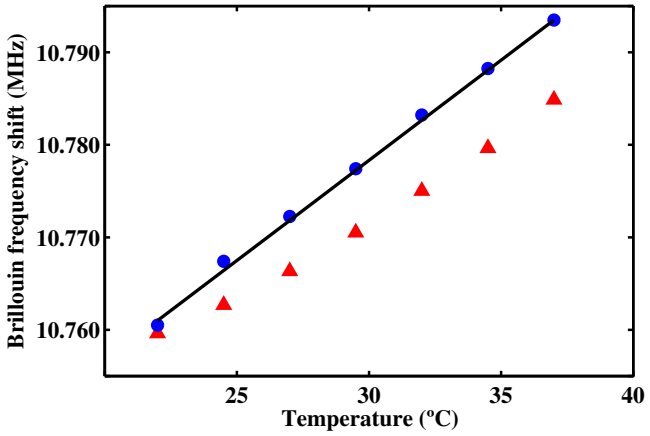

Fig. 2.33. BFS measurement given by the amplitude spectra (red triangle symbol) and by the RF phase-shift spectra (blue circle symbol). The linear regression to the BFS data obtained from the RF phase-shift (black solid line) gives a 1.08ºC/MHz coefficient.

2.4.2 Differential pulse-width pair technique for phasorial BOTDA traces

The improvement of the spatial resolution in BOTDA sensor has been deeply researched in order to increase the number of resolved points along the optical fiber. The spatial resolution is directly related to the pump pulse length. However, as shown in section 1.5.3, decreasing the temporal duration of the pump pulses to enhance the spatial resolution has a negative impact on the Brillouin frequency shift (BFS) measurement precision because it leads to broadening of the measured Brillouin linewidth [35]. There are different proposals to overcome this limitation [35, 76, 77]. However, one of the most effective and easy to deploy in long-range BOTDA sensors is the differential pulse width pair (DPP) technique [35], which is based on the subtraction of the time domain Brillouin signals measured by sequentially injecting two pump pulses with slightly different pulse durations. This enhances the spatial resolution of the measurement, which is given by the pulse-width difference, and simultaneously preserves the BFS precision, as the Brillouin linewidth is defined by the comparatively long duration of the individual pulses.

In this section, we introduce a novel phasorial differential pulse-width pair (PDPP) technique for BOTDA sensors whose supplied output is a phasorial signal (amplitude and phase-shift). The technique performs a full phasorial subtraction of the responses to two sequential pump pulses with differential duration, which allows to enhance the spatial resolution while keeping the Brillouin linewidth of long pulse durations. Specifically, the phasorial subtraction technique is applied to a BOTDA sensor with phase modulation, which has demonstrated to perform correct measurements under the influence of non-local effects (see section 2.4.1) [78]. Moreover, the differential signal keeps the same properties regarding non-local effects. In addition, the influence of chromatic dispersion in modulated probe waves is analyzed, specifically for the case of phase modulation.

Fundamentals

As shown previously in section 2.4.1, BOTDA sensors based on phase-modulated probe wave are tolerant to non-local effects. This feature along with the improvement on the detected SNR (see section 2.2) make this technique as a very interesting tool to perform long-range measurements. Nevertheless, when long-range distances are the objective of these sensors, an extra phase-shift term (ϕ) caused by chromatic dispersion has to be considered at the

optical field reaching the receiver. This extra-term modifies Eq. (2.23) yielding:

$$\begin{aligned} E(t)\big|_{rx} = & -E_{SBi}\exp\left(-\frac{\alpha}{2}L\right)\exp\left(i2\pi\left(\nu_0 - f_{RF}\right)t\right)\exp\left(-i\phi\right) \\ & + E_{0i}\exp\left(-\frac{\alpha}{2}L\right)\exp\left(i2\pi\nu_0 t\right) \\ & + E_{SBi}\exp\left(-\frac{\alpha}{2}L\right)\exp\left(i2\pi\left(\nu_0 + f_{RF}\right)t\right)H_{SBS}\left(z,\Delta\nu\right)\exp\left(-i\phi\right) \end{aligned} \tag{2.26}$$

The resulting modulated wave is detected, giving rise to an RF signal (amplitude and phase-shift) that can be expressed for a given location of a long sensing fiber, z, as:

$$\begin{aligned} P(t)\big|_{f_{RF}} = & 2\sqrt{P_{0i}P_{SBi}}\exp\left(-\alpha L\right)\cos\left(\phi\right)\frac{g_0\Delta\nu_B}{\sqrt{\Delta\nu_B^2+\Delta\nu^2}} \\ & \cdot\cos\left(2\pi f_{RF}\,t - \arctan\left(2\frac{\Delta\nu}{\Delta\nu_B}\right)\right) \\ & + 2\sqrt{P_{0i}P_{SBi}}\exp\left(-\alpha L\right)\sin\left(\phi\right)\exp\left(\frac{g_0}{A_{eff}}\frac{\Delta\nu_B^2}{\Delta\nu_B^2+4\Delta\nu^2}P_P\left(z\right)\Delta z\right) \\ & \cdot\cos\left(2\pi f_{RF}\,t + \frac{g_0}{A_{eff}}\frac{2\Delta\nu_B\Delta\nu}{\Delta\nu_B^2+4\Delta\nu^2}P_P\left(z\right)\Delta z - \frac{\pi}{2}\right) \\ & + 2\sqrt{P_{0i}P_{SBi}}\exp\left(-\alpha L\right)\sin\left(\phi\right)\cos\left(2\pi f_{RF}\,t - \frac{\pi}{2}\right) \end{aligned} \tag{2.27}$$

where ϕ is the relative phase difference between carrier and sidebands caused by chromatic dispersion at the fiber [79]:

$$\phi = \frac{L\pi cDf_{RF}^2}{\nu_0^2} \tag{2.28}$$

where L is the length of the fiber, c is the velocity of light in free space, D is the fiber dispersion parameter, ν_0 is the optical frequency of the carrier and f_{RF} is the modulation frequency. Eq. (2.27) incorporates the well-known effect of phase to intensity modulation conversion through chromatic dispersion in long fibers [79]. This is clearly shown in Eq. (2.27), where the first term on the right hand side is the detected phasor originated by SBS interaction with a phase-modulated probe wave (see Eq. (2.11) in section 2.2), the second term is that originated using an intensity-modulated probe wave (see Eq. (2.6) in section 2.1) and the third term corresponds to the beating signal between the lower-sideband and the carrier for an intensity-modulated wave. Therefore, the detected spectra for both the amplitude and the phase-shift are a combination of the PM and AM modulations, whose contribution to the detected RF signal depends on ϕ. Considering that we have small chromatic dispersion or that it is compensated making $\phi = 0$, the detected RF signal is then given by the first term of

Eq. (2.27), whose RF phase-shift signal has no dependence with the particular local Brillouin gain associated to the SBS process, as previously shown in section 2.4.1.

The signal represented in Eq. (2.27) is deployed in a novel PDPP scheme where instead of simply subtracting two consecutive time domain BOTDA traces to obtain the differential amplitude signal, we perform a full phasor subtraction of the complex responses (amplitude and phase-shift) obtained by sequentially injecting two pulses with different duration. This process is illustrated in Fig.2.34 that schematically depicts the measurement at location z_0 of a fiber section that has a given BFS (BFS_1) followed by a short section with a different BFS (BFS_2). A first pulse with a spatial length of u is injected in the fiber, yielding, for the

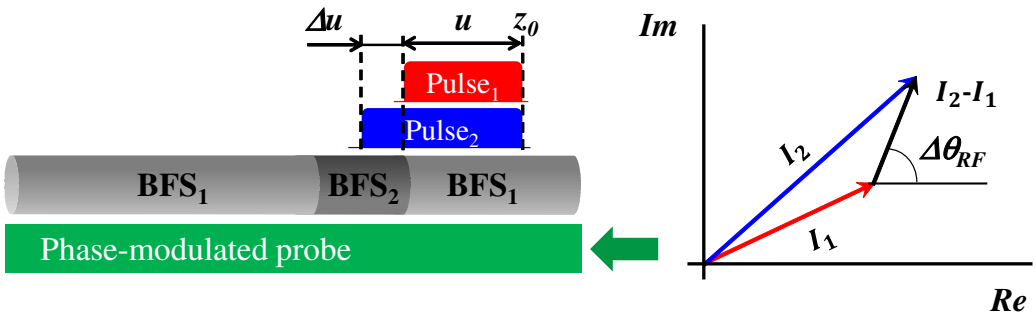

Fig. 2.34. Schematic representation of SBS interaction and the received RF signal using the PDPP technique.

measurement at location z_0, an RF signal represented by phasor I_1. This resultant RF signal is affected by the integrated Brillouin gain and phase-shift (characterized by BFS_1) experienced by the probe wave over the length covered by this first pulse. Then, a second pump pulse of differential duration (Δu) is injected and the RF signal measured for the same location will be affected by the complex Brillouin spectra of both consecutive fiber sections (characterized by BFS_1 and BFS_2), leading to a change in the amplitude and phase-shift of a second phasor I_2 that represents this second RF signal. Finally, the two phasors are subtracted to obtain the differential RF signal, which corresponds to the Brillouin interaction in the differential length Δu (characterized by BFS_2). Therefore, enhanced spatial resolution is obtained. Moreover, the RF phase-shift, $\Delta\theta_{RF}$, of this differential signal retains the tolerance to non-local effects.

The scenario described above has been analyzed by numerically solving the coupled ordinary differential equation system that gives the evolution of the optical fields of the probe

E_S and pump waves, E_P, along the fiber [17]:

$$\frac{d}{dz}E_P(z) = \left[-\frac{g_0}{2}\frac{i\Delta\nu_B}{i\Delta\nu_B + 2\Delta\nu}|E_S|^2 - \frac{\alpha}{2}\right]E_P \tag{2.29a}$$

$$\frac{d}{dz}E_S(z) = \left[-\frac{g_0}{2}\frac{i\Delta\nu_B}{i\Delta\nu_B - 2\Delta\nu}|E_P|^2 + \frac{\alpha}{2}\right]E_S \tag{2.29b}$$

where α is the fiber attenuation. The solution of these equations gives the optical field of the upper sideband of the modulated wave, while the carrier and lower sideband are assumed to only attenuate along its propagation. Moreover, the calculations are simplified assuming steady-state conditions for long pulse lengths of 5 m and 6 m.

Figure 2.35(a) shows the RF amplitude and phase-shift spectra at position, z_0, for each pump pulse and the resulting differential RF spectra. Notice that the calculated spectra using a 6 m pulse length clearly display the combined response to the two consecutive fiber sections with different BFS, while the amplitude and phase-shift of the differential phasor signal just retains the response to the second section (BFS_2), as expected. Therefore, the proposed technique presents an enhanced spatial resolution and BFS accuracy in RF magnitude and phase-shift measurements.

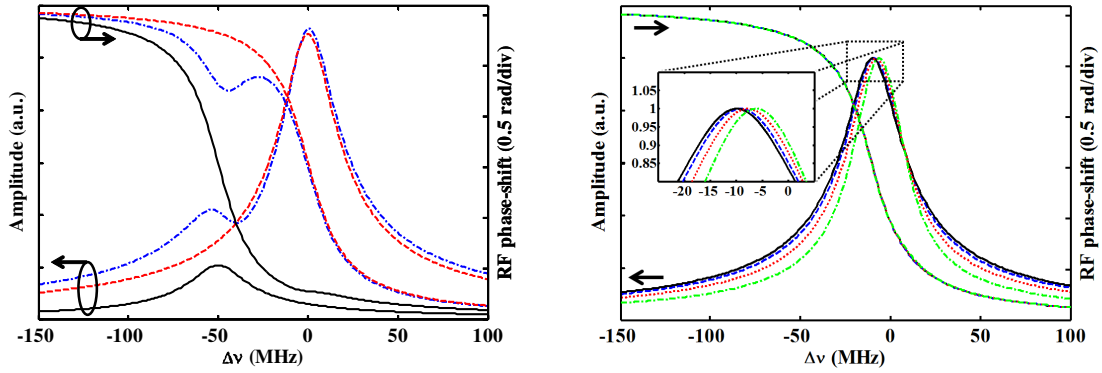

(a) (b)

Fig. 2.35. (a) Calculated magnitude and RF phase-shift spectra for 5 m (red dashed line), 6 m (blue dot dashed line) pulse lengths and the differential RF spectra (black solid line) for a BFS difference of 50 MHz between sections. (b) Calculated magnitude and RF phase-shift spectra for a BFS difference of 10 MHz and different injected probe powers: 20 μW (black solid line), 45 μW (blue dashed line), 100 μW (red dotted line) and 200 μW (green dot dashed line). Simulations parameters are $g_0 = -1.5 \cdot 10^{-11}$m/W, $\Delta\nu_B = 30$ MHz, $L = 30$ km, effective area is $7.18 \cdot 10^{-11}$m^2 and the injected optical pump power is 100 mW.

Furthermore, it has also been found that the differential RF phase-shift signal keeps the same properties regarding non-local effects than the individual responses to each pulse. Figure 2.35(b) presents the calculated differential RF spectra for several probe powers considering the worst case situation for non-local effects, which occurs when the BFS_2 has a frequency difference of $\Delta_{\nu_B}/3$ with the rest of a uniform BFS fiber [19]. In these simulations, the peak of the magnitude spectra are clearly biased from the real BFS measurement for increasing probe power, meanwhile the differential RF phase-shift spectra remain unaltered. A loss-based BOTDA is assumed in these calculations, but the distortion induced to the measured spectra is independent of the sensor's configuration (loss or gain), the only difference resides in the direction of the Brillouin spectrum biasing.

Experimental setup and measurements

The experimental setup sketched in Fig. 2.36 was assembled in order to evaluate the potential of the technique. The light from a distributed feedback (DFB) laser diode at 1560 nm is coupled into two optical branches. In the upper branch, a double-sideband suppressed-carrier modulation is generated using a Mach-Zehnder electro-optic modulator driven by a microwave tone whose frequency is tuned around 9.5 GHz. The resultant signal is pulsed using a semiconductor optical amplifier and then amplified by an erbium-doped fiber amplifier. The lower-sideband of the pulsed signal is selected using a narrowband fiber Bragg grating (FBG) obtaining the desired pump wave. Its state of polarization is randomized with a polarization scrambler to reduce polarization-mismatching induced fluctuations on the signal, before being launched into the sensing fiber via a circulator. In the lower branch, a probe wave is generated with an electro-optic phase modulator driven by a 1.3 GHz RF signal. Once the probe wave has interacted with the pump pulse via SBS, the chromatic dispersion phase-shift is corrected using a dispersion compensating module (DCM) prior to signal detection. Finally, the resultant RF signal is demodulated and captured in a digital oscilloscope. The deployed RF demodulator's bandwidth is 220 MHz, so that changes faster than 10 ns in the demodulated signal can be resolved (1 m resolution). For higher spatial resolutions, the needed bandwidth should be adjusted to $1.5/\tau$, where τ is the pulse duration [80]. Note that for the low f_{RF} used in this setup, the sensing fiber length needed to completely convert the phase modulation into an intensity modulation is around 2000 km. For the deployed 50 km long fiber, chromatic dispersion only induces a slight phase-shift at the sidebands, which has no real impact in the measurements because the second term in Eq. (2.27) becomes merely a DC baseline. The DCM was simply used to reduce this DC in order to fully exploit the dynamic range of the RF demodulator and oscilloscope.

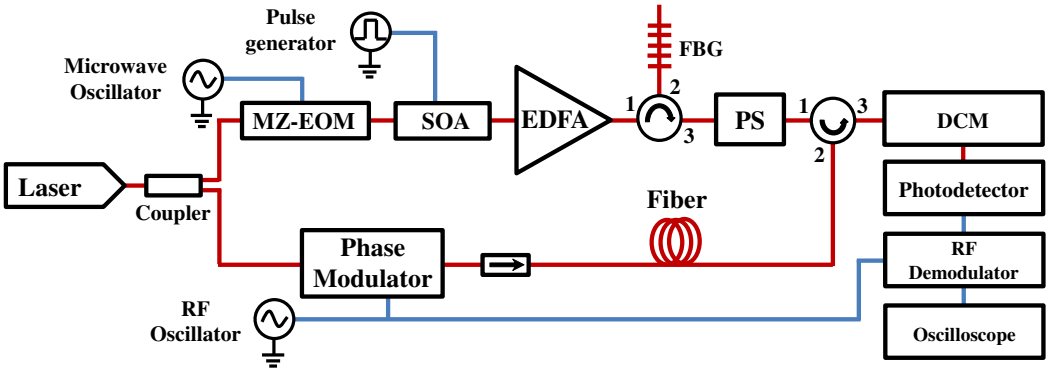

Fig. 2.36. Experimental setup for the PDPP-BOTDA sensor based on phase-modulated probe wave and RF demodulation.

In order to evaluate the detrimental impact of non-local effects in long-range measurements, the probe wave power is set to a value, 0.54 mW, that clearly outreaches the maximum power (45 μW) for which the pump power modifies by a factor of 17% (see Eq. (2.25)). This huge optical power results in amplification of the pump pulse power due to the energy transfer from the probe wave to the pump pulse in a loss-based BOTDA sensor. Figure 2.37(a) shows this effect, where the optical power of the pump pulse is amplified to more than double its original value (a factor of 115%) for the frequency difference between both waves that matches the average BFS of the optical fiber (set as $\Delta\nu = 0$). This value largely exceeds the maximum tolerable factor (17%), which induces, as described in section 1.5.1, a measurement error of 1 MHz at the worst case scenario, i.e. when a long fiber with a uniform BFS is followed by a small section at the end of the fiber with a BFS change [19]. Such scenario was simulated by inserting a 13 m length section at the end of the fiber in a climatic chamber at 61°C. Figure 2.37(b) depicts the amplitude and RF phase-shift spectra for that section, using 50-ns pump pulses for two measurements performed by swapping the fiber input ends of pump and probe waves, which is an effective method to observe the influence of non-local effects [23]. Notice that when the hot-spot is located at the probe end of the fiber, the amplitude spectrum is distorted and there is a biasing effect that introduces a measurement error. In contrast to the amplitude spectra, the shape of the RF phase-shift spectra remains unaltered for both measurements.

A similar experiment was performed but, this time, deploying the full-phasor subtraction of the time-domain BOTDA traces measured by sequentially injecting two pump pulses of 50 and 60 ns. The experimental results shown in Fig. 2.38(a), match those obtained using 50-ns pulses, apart from the expected reduction of SNR due to the enhanced spatial resolution.

The precision achieved in the BFS measurements based on RF phase-shift was 1.3 MHz (1.3ºC/26 $\mu\varepsilon$) at the worst-contrast position. Finally, in order to demonstrate the spatial

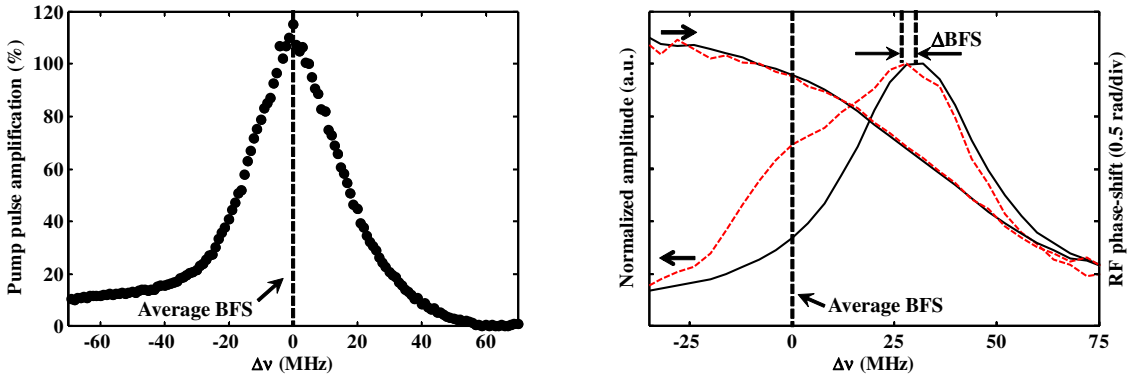

(a) (b)

Fig. 2.37. (a) Measured pump pulse amplification at the end of the fiber. (b) Measured amplitude and RF phase-shift spectra at the hot spot section when that section is located at the probe input (red-dashed line) or at the pump input (black-solid line).

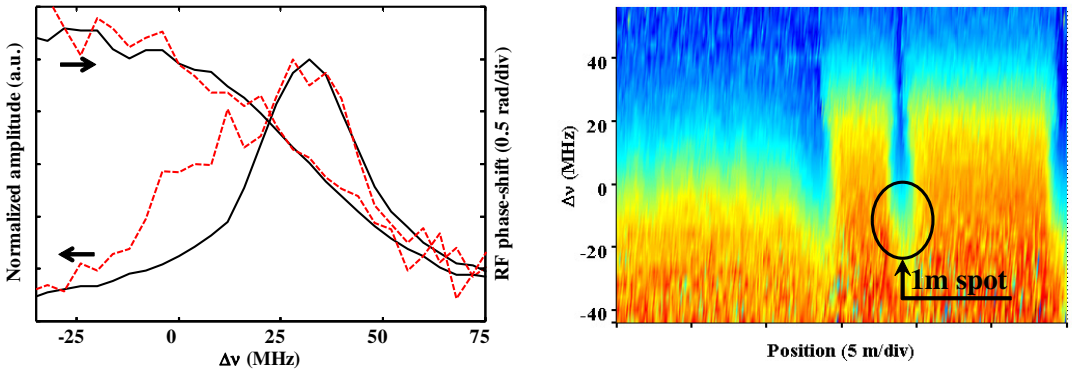

(a) (b)

Fig. 2.38. (a) Differential amplitude and RF phase-shift spectra at the hot-spot section, when that section is located at the probe input (red-dashed line) or at the pump input (black-solid line). (b) Differential RF phase-shift distribution.

resolution enhancement, one meter was extracted from the final section located at the climatic chamber and placed at room temperature in a loose state. Figure 2.38(b) depicts the color coded RF phase-shift distribution along the final section of the fiber. At the location corresponding to the room temperature one-meter section, a shift from $\Delta\nu \approx$30 MHz to $\approx$-5 MHz, which fits the temperature change for that section, is clearly appreciable.

2.4.3 Mitigation of modulation instability by using orthogonal pump pulses

In long-range BOTDA sensors, optimizing the system actually requires launching high probe power (as shown previously) but also high pump powers into the sensing fiber to provide a sufficient SNR on the measurements at the far end of the fiber. However, increasing the input power above a critical level excites undesired nonlinear effects such as modulation instability and stimulated Raman scattering (SRS), which deplete the pump and reduce the maximum sensing range of the system [28, 81]. Compared to SRS, MI shows a lower threshold and thus imposes a more restrictive limitation to the maximum pump power in BOTDA schemes [28]. As a consequence, MI has been further studied.

Recently, the influence of the background noise level has been analyzed. It seeds the apparition of MI, depleting faster the pulse power when the noise level is high [31]. Consequently, a narrow bandwidth filter is required to remove the amplified spontaneous emission coming from the EDFA and hence, increment the length of the sensing fiber. Furthermore, different techniques based on multi-wavelength pulses have been recently proposed to extend the measurement range [82], to provide high spatial resolution [77] or to enable fast dynamic sensing [56]. However, it has been identified in all these cases that nonlinear cross Kerr-effect interactions between the different spectral lines would take place if high-power pulses are simultaneously launched into the sensing fiber, leading to severe distortions of the measured time-domain traces [56, 82].

In this section, an effective method to reduce the pump power depletion in systems with two pulses is presented. The technique relies on the use of orthogonal-polarized pulses at different wavelengths, which has theoretically and experimentally demonstrated to mitigate the impact of Kerr nonlinearities in comparison to the use of a single pump or parallel pump. Although the improvement is significant, the technique is still limited by nonlinear-cross interactions that obey a Manakov model [83, 84].

This work was done in collaboration with the research Group for Fibre Optics of the École Polytechnique Fédérale de Lausanne led by Prof. Luc Thévenaz.

Fundamentals

The limitations imposed by modulation instability in standard BOTDA systems have been investigated thoroughly using the scalar nonlinear Schrödinger equation (NLSE) [81]. To take into account the interaction between orthogonally-polarized pumps, the scalar analysis of MI needs to be extended to its vector counterpart, where the vector NLSE (VNLSE) governs the polarization components of the lightwave. The form of the VNLSE depends on the birefringence characteristics of the fiber. Conventional single-mode fibers are categorized as randomly varying birefringent fibers, meaning that their birefringence changes randomly over a length scale of around 10 m in both value and axes [83]. The random fluctuations in the degree of modal birefringence and the orientation of birefringence axes force the Stokes vector to sweep the entire surface of the Poincaré sphere over a approximately 1 km length scale. For optical fibers longer than this length scale, averaging the VNLSE over the Poincaré sphere leads to the following coupled nonlinear Schrödinger equations referred to as the Manakov system for the two orthogonal polarization components $u(z,t)$ and $v(z,t)$ [83, 84]:

$$\frac{\partial u}{\partial z} + i\frac{\beta_2}{2}\frac{\partial^2 u}{\partial t^2}\frac{\alpha}{2}u = i\gamma\left(|u|^2 + |v|^2\right)u \tag{2.30a}$$

$$\frac{\partial v}{\partial z} + i\frac{\beta_2}{2}\frac{\partial^2 v}{\partial t^2}\frac{\alpha}{2}v = i\gamma\left(|u|^2 + |v|^2\right)v \tag{2.30b}$$

where α is the fiber attenuation and $\beta_2 < 0$ is the group-velocity dispersion (GVD) coefficient. Note that to take into account the randomness of polarization [83], the nonlinear coefficient γ is obtained by multiplying the linearly-polarized Kerr nonlinearity by the factor 8/9. It is evident from the right-hand side of Eq. (2.30) that both polarization components ($u(z,t)$ and $v(z,t)$) contribute equally to the nonlinear phase modulation of the optical waves. Therefore, under the same total power conditions, the MI spectral bands originated by a single pump and a double orthogonal pump scheme are the same. However, since in the latter case the total power is split into two polarizations at different wavelengths, the peak power and thus the MI gain turn out to be reduced.

To verify the above-described situation, a numerical analysis of Eq. (2.30) has been carried out using the split-step Fourier method for solving the VNLSE and a Monte Carlo simulation for considering the background noise as a seeding signal for the onset of MI. Fig. 2.39(a) depicts the MI gain spectrum originated in a 25 km-long standard SMF with a total input pump power of 250 mW, under three different scenarios: the standard single pulse case at zero-frequency detuning (blue curve) is compared with the use of two pulses at around 10 GHz having parallel (green curve) and orthogonal (red curve) states of polarization. It

should be noticed that the pumps lines are removed from the plots for the sake of visibility. It is possible to observe that while the MI gain in the single pump case is higher than the one of the orthogonal polarizations, an efficient four-wave mixing (FWM) process dominates the interaction between the pulses with parallel polarizations. Fig. 2.39(b) shows the evolution of the total pump power along the fiber for the three scenarios (note that the fiber attenuation has been compensated for a better visualization). While the single pump power is substantially depleted by MI (about 70-80% of depletion), the case of parallel pumps suffers from strong FWM, leading to abrupt pump power oscillations along the fiber. On the other hand, it is interesting to observe the behavior of the double orthogonal pumps, which shows a considerable improvement in terms of MI pump depletion compared to the standard single pump configuration, but also offers a significant suppression of FWM when compared to the parallel pumps. Note also that the hypothetical case of orthogonal polarizations with only scalar MI is plotted for comparison.

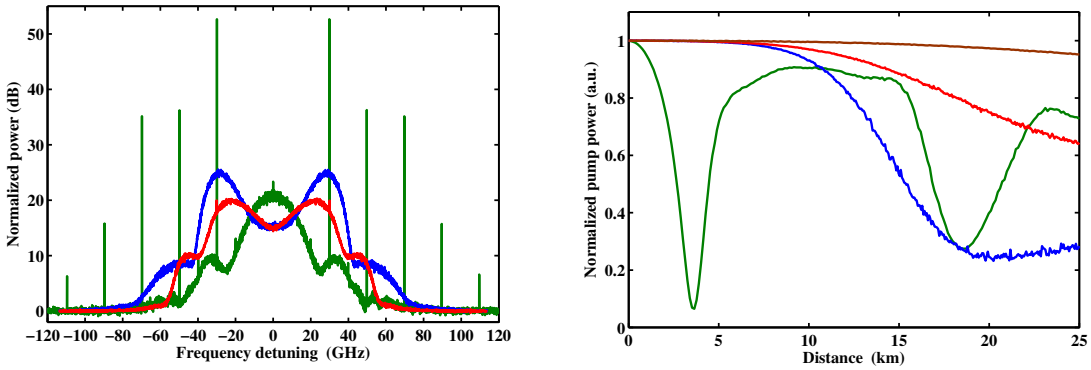

(a) (b)

Fig. 2.39. (a) MI gain spectrum and (b) longitudinal pump power evolution along the fiber, for a 25 km-long SMF with $\alpha = 0.2$ dB/km, $\gamma = 1.8$ W^{-}1/km and $\beta_2 = -22$ ps^2/km, in three different pump scenarios: single-wavelength pump (blue curves), two parallel pumps (green curves), and two orthogonal pumps (red curves). The frequency spacing between pumps is 20 GHz, the noise power spectral density is -118 dBm/Hz, and total power is 250 mW. In (b) the hypothetical case of two orthogonal polarizations with scalar MI is also depicted (brown curve).

Experimental setup and results

Fig. 2.40 depicts the experimental setup assembled to demonstrate the reduction of Kerr nonlinearities by using orthogonal pump pulses in BOTDA sensors. The output of a laser source is divided in two optical branches with an optical coupler. In the upper branch,

optical pump pulses are shaped using a Mach-Zehnder electro-optic modulator driven by a 9.55 GHz pulsed microwave signal and biased in minimum transmission. This way, two pulsed optical sidebands are generated, while the optical carrier is highly suppressed. This optical signal goes through a polarization controller (PC), a differential group delay module and a programmable optical filter (POF) shown inside a dashed box in Fig. 2.40. These optical components actually allow setting the three-above mentioned scenarios for the study of MI, i.e. orthogonal pump pulses, parallel pulses and single pulse. The polarization controller allows the linearly-polarized light at the output of the MZ-EOM to be properly aligned into the DGD module. This birefringent material generates a wavelength-dependent phase-shift difference between its axes given by $\Delta\theta = 2\pi \cdot \Delta f \cdot \Delta\tau$, where $\Delta\tau$ is the differential group delay introduced by birefringence in the DGD module and Δf is the frequency spacing between the optical waves, as shown in section 2.3.2 [85]. Therefore, depending on the wavelength difference and the incident angle, the birefringent material can provide different polarization states at its output (see section 2.3.2 for a detailed explanation). On the one hand, two orthogonally-polarized pulses can be obtained if the incident angle into the birefringent material is set to 45° and $\Delta\theta = \pi$. In our setup, this last condition is easily fulfilled by choosing a DGD module with $\Delta\tau = 26$ ps. On the other hand, the generation of pulses with parallel polarizations only requires to adjust the incident angle to one of the principal axes of the DGD module. Finally, for a standard single-wavelength pulse, the programmable optical filter is adjusted to select only one of the sidebands. Once the desired pump signal is generated, this is amplified by an erbium doped fiber amplifier, whose amplified spontaneous emission noise is filtered out by a 1-nm optical filter.

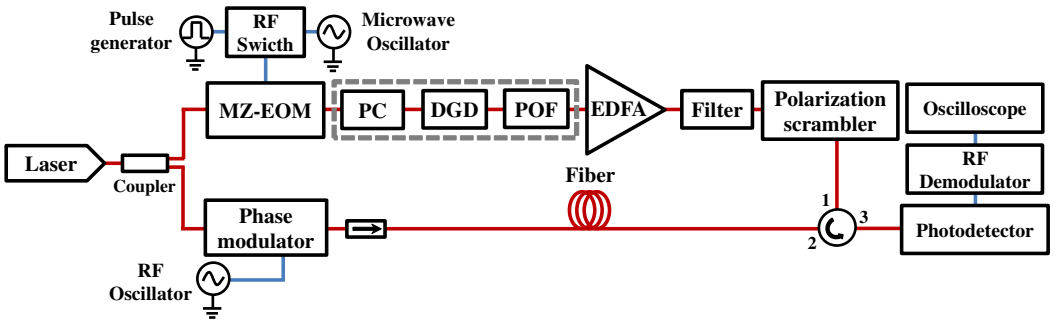

Fig. 2.40. Experimental BOTDA sensor using the orthogonal pump pulses.

In the lower branch, the probe wave is generated with an electro-optic phase modulator driven by a 1.3 GHz RF signal. This modulation frequency is chosen so that the upper (lower) sideband of the phase modulation interacts with the lower (higher) pulsed sideband, so that a cross interaction between the different sidebands occurs. After interacting via stimulated Brillouin scattering, the probe signal is directed to a photodetector, where the

resulting RF signal is then demodulated [85]. Finally, the BOTDA signal is captured in a digital oscilloscope.

Fig. 2.41 shows the measured and simulated time-domain traces obtained in a BOTDA sensor using: a single pulse, parallel pulses and orthogonally-polarized pulses for a total input power of 300 mW. As it is evident from the figure, the numerical simulations of the coupled nonlinear Schrödinger equations (2.30) follows accurately the experimental results demonstrating the validity of the model. Fig. 2.41(a) compares the single-pump BOTDA with the double parallel pumps. This clearly shows more than 50% pump depletion at the end of the fiber in both scenarios when compared to the undepleted exponential decay. The deep power oscillation for the parallel pumps at 5 km distance confirms that the FWM between parallel pumps dominates the sensor response. As a comparison, Fig. 2.41(b) shows the trace evolution obtained with orthogonal polarizations and single pulse for the same power as in Fig. 2.41(a). Clear differences in the pump power evolution can be observed, especially in the last 10 km of fiber, where the power of the single pump is depleted by approximately 50% as a result of scalar MI, while the total power in the two orthogonal pulses is only depleted by 12% due to vector MI. This represents a $\sim$3 dB improvement in the sensor response at the end of the fiber, enabling a sensing range extension of $\sim$7.5 km while maintaining the same SNR. It is interesting to remark that another advantage of using orthogonal polarizations is the mitigation of FWM [84]. In addition, small differences in the polarization fading should be observed between the traces depicted in Fig. 2.41(a); however this is only caused by the polarization diversity method used in each scheme. Thus, while a polarization scrambler is required in the cases of single and parallel pulses, the use of orthogonal pulses does not require additional polarization scrambling since it ensures two complementary Brillouin interactions taking place at each position of the sensing fiber [85].

In order to evaluate the performance improvement provided by the use of orthogonal pulses, the measured depletion ratio at the end of the fiber is compared with the single pulse case for different input pump powers. As shown in Fig. 2.42, the depletion ratio using a single pulse is clearly much higher than when using orthogonally-polarized pulses. For instance, tolerating a depletion ratio of $\sim$15%, the input pump power can be increased from about 220 mW to 320 mW using pulses with orthogonal polarizations, representing a 1.5-fold improvement in the input pump power supported by the sensor before inducing distortions in the time-domain traces. Under a pump power of 320 mW, the depletion ratio grows from 15% using orthogonal polarization up to 53% using the single pulse, which also reaffirms the advantage of using pulses with orthogonal polarizations.

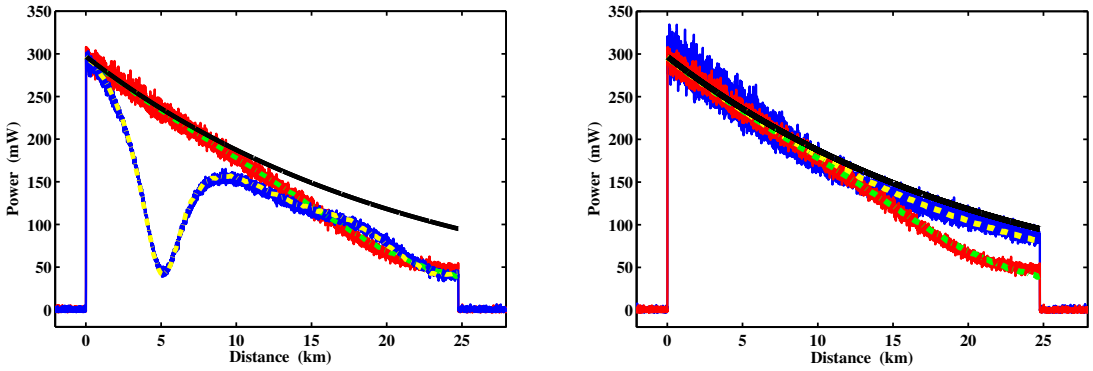

(a) (b)

Fig. 2.41. Measured (continuous line) and simulated (dashed line) time-domain Brillouin traces in a 25-km SMF for an input power of 300 mW for three cases: (a) single pump (red solid line and green dashed line) and parallel pulses (blue solid line and yellow dashed line), and (b) single pump (red solid line and green dashed line) and double orthogonal pumps (blue solid line and yellow dashed line). The parameters used to solve Eq. (2.30) are: $\alpha = 0.2$ dB/km, $\gamma = 1.0$ W^{-1}/km and $\beta_2 = -23$ ps^2/km. The frequency difference between pumps is 19.1 GHz and the noise power spectral density is -109 dBm/Hz.

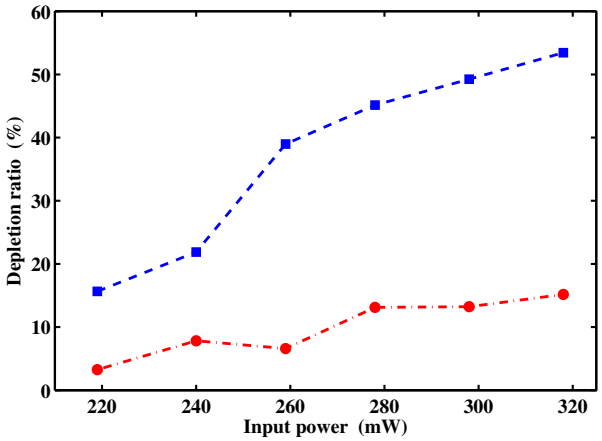

Fig. 2.42. Measured pump depletion versus total input power at 25 km distance, for two cases: single pump (squares), and double orthogonal pumps (circles).

2.5 Conclusions

During this chapter, different solutions based on BOTDA sensors using phase-modulated probe wave and heterodyne detection have been proposed and demonstrated, solving some of the fundamental limitations in dynamic and long-range measurements.

In the first place, a novel dynamic Brillouin sensor based on the slope-assisted technique using the detected RF phase-shift spectrum was introduced. The technique has demonstrated to be largely immune to variations of the Brillouin peak gain, attenuation on the fiber, or changes in the power of the pump pulses that may be produced by mechanical stress induced losses. This is an important advantage regarding other techniques based on the detected amplitude, which misreads the measured temperature/strain due to changes of the amplitude not connected with variations of the BFS.

Furthermore, the application of the RF phase-shift as the tool to translate variations of the phase-shit into changes of the BFS has other benefits. The shape of the RF phase-shift spectrum approximately covers both skirts of the Brillouin gain spectrum. This means that, in identical noise conditions, the measurement range of the phase-shift is larger since the technique based on the amplitude only uses one of the skirts. In addition, the technique deploys a self-heterodyne detection, which has previously demonstrated to increment the detected amplitude and hence, enhance the precision. Therefore, the measurement range of the system for a certain precision can be simply increased by incrementing the power of the carrier of the phase modulation.

Moreover, the BOTDA sensor based on phase modulation of the probe wave is perfectly applicable to the use of double orthogonal pump pulses without loosing any of the features described above. The proposed polarization diversity technique relies on the fact that for any given location of the fiber, both Brillouin interactions remain complementary, so that their sum is always equal to a single Brillouin interaction with aligned SOP for probe and pump waves. Therefore, the technique removes the need for polarization scrambling or for any other polarization compensating technique performing polarization independent measurements throughout the fiber even if no averaging is applied. This feature allows to reduce the measurement time of dynamic sensors.

A theoretical model has been developed and the capabilities of these schemes have been experimentally demonstrated, performing a fast dynamic distributed strain measurement in a cantilever beam with high measurement range and precision. For this case, the performance is similar to the state of the art in dynamic sensors in terms of measurement rate, spatial resolution, precision or length of fiber. Besides, the practical implementation of the double orthogonal pump, relies on the use of a DGD module, which is an inexpensive optical component that can be introduced in the setup without requiring any polarization control.

This makes it very robust to environmental changes, so that it can be considered as a solution for commercial sensors. However, when practical applications are considered, the optical fiber may be made by sections with different BFSs. In this case, dynamic slope-assisted BOTDA sensors cannot be deployed even if the dynamic strain changes are small, due to their limited measurement range. This limitation can be overcome by deploying a probe wave that varies its frequency along the fiber in order to fit the Brillouin profile. This technique is compatible with the SA-BOTDA based on phase-modulation so that the advantages of both can be combined.

The proposed technique has been also applied in long-range measurements. Firstly, the technique allows to inject a higher probe power due to the tolerance of the detected RF phase-shift spectrum to changes of the pump power. While in a conventional setup, the maximum probe power is limited to -14 dBm for long fibers (> 20 km), the proposed technique has demonstrated to be able to inject around -3 dBm of probe power for a 50 km fiber without deleterious influence of non-local effects on the measured shape of the RF phase-shift spectrum. In addition, the injected probe power is comparable to the maximum probe power injected in the BOTDA sensor using double-sideband probe wave [26]. Consequently, it would be interesting to combine both techniques to further increase the input probe power.

In addition, the proposed technique has been successfully combined with the differential pulse-width pair technique. The use of the DPP technique has been extended to BOTDA sensors with phasorial signals, obtaining not only the BGS with high spatial and spectral resolution but also a phase-shift spectrum with the same characteristics. Furthermore, the differential RF phase-shift spectrum measured using the phasorial DPP technique keeps the same properties regarding the tolerance to non-local effects than the original RF phase-shift spectrum. An experimental proof-of-concept has been performed with a 50-km long fiber to validate the unaltered phase-shift spectra in presence of non-local effects. Moreover, a 1-m section has been detected by using the RF phase-shift of the differential Brillouin signal.

Finally, the modulation instability effect has been theoretically and experimentally mitigated by using pulses with orthogonal states of polarization at different wavelengths. The results indicate that Kerr nonlinearities between orthogonally-polarized pulses are not completely nulled, and the maximum pump power allowed by a BOTDA system is in this case determined by the Manakov model for the Kerr effect. However, the MI threshold for pulses with orthogonal polarizations states is higher than for conventional single-pulse schemes. Furthermore, the proposed technique not only mitigates the impact of modulation instability, but also the four-wave mixing occurring in systems using pumps with parallel polarization.

In conclusion, BOTDA sensors with phase-modulated probe wave and orthogonal Brillouin interactions are a promising tool able to enhance the monitoring distances, as they

allow to increment the power of both waves involved in the stimulated Brillouin scattering effect. Moreover, they also provide an efficient mechanism for dynamic measurements.

Chapter 3

Modulation of the probe wave wavelength in BOTDA sensors

The extension of the monitoring distance in Brillouin optical time-domain analisys (BOTDA) sensors has been one of the fundamental research topics since the first sensor was assembled in 1990 [12, 13]. One of the main solutions to improve the sensing range is the reception of a powerful probe wave to increase the signal-to-noise ratio (SNR) of the detected electrical signal. However, this requires to inject an optical probe power that is large enough to excite other detrimental effects for the operation of the sensor, such as, the so-called non-local effects (NLE) or noise transferred to the probe wave when its power reaches the Brillouin theshold of the fiber. Both effects manifest for lower probe powers when the deployed optical fiber presents a uniform Brillouin frequency shift (BFS) distribution. This is the typical case unless the sensing fiber is previously designed with fiber sections of different properties, e.g. using different fibers or periodically stressing some sections of the same fiber. However, in some cases, the fiber is already attached to the structure and hence, there is not possibility to replace or modify it. Furthermore, the modification of their properties is a cumbersome procedure that should be done during the installation process of the fiber, increasing the cost of the solution. Therefore, it would be very interesting to be able of modifying the profile of the Brillouin frequency shift as the user requires in order to improve the performance of the sensor.

During this chapter, a novel technique for BOTDA sensors is introduced. The solution is based on the modulation of the optical frequency of the probe wave, so that the effective Brillouin interaction induced by the pulsed wave is equivalent to that of an optical fiber with a virtual BFS profile, configurable by the user, instead of the real BFS profile of the fiber. This solution has been developed to mitigate non-local effects and noise added to the probe

signal by amplified spontaneous Brillouin scattering components. The basic principle of the technique has been implemented by two different approaches:

- Wavelength modulation of the optical source of a BOTDA sensor, which is a valid implementation method for most configurations used in BOTDA sensors.
- Frequency modulation of the optical probe wave, which can be applied to balanced BOTDA sensors to suppress the effect of non-local effects (first and second order) even when using probe powers higher than the Brillouin threshold of the fiber.

3.1 Introduction

One of the main limitations to increase the probe power in BOTDA sensors is given by the apparition of non-local effects (see section 1.5.1). These effects arise from the continuous Brillouin interaction of the probe signal with the pulsed pump wave that considerably modifies its peak power along its propagation. Moreover, as the pump power variation is generated by Brillouin transfer, it also has a frequency dependence related to the Brillouin frequency shift of the entire fiber. The worst-case scenario takes place when the distribution of the Brillouin frequency shift is uniform and hence, the amplitude of the pulsed wave as a function of the frequency detuning acquires a Lorentzian shape whose peak matches the BFS. Recalling that the measured Brillouin gain has a linear dependence with the pump power, if the BFS at a certain location is slightly shifted from the uniform part of the fiber, then the measured Brillouin spectrum can be distorted and hence, the determination of the BFS would not be accurate. The maximum error induced by this non-local effect can be quantified as a function of the probe power level. It is found that a -14 dBm probe power could generates a 1-MHz BFS error (1 °C or 20 $\mu\varepsilon$) in a long-range BOTDA system [86].

For BOTDA systems using a double-sideband configuration, non-local effects should be negligible whenever the probe power is lower than the Brillouin threshold of the fiber [19]. However, another study found out the apparition of a second order non-local effect capable of distorting the measured Brillouin spectrum without reaching the Brillouin threshold of the fiber [26]. This effect is generated by a pulse spectrum distortion taking place when the frequency of both probe waves differs from the BFS of the fiber and hence, the Brillouin gain and loss spectra are not overlapped on the pulse spectrum to be compensated [26]. Consequently, this effect occurs when the Brillouin spectrum is scanned, generating a 1-MHz BFS error when the probe power reaches a level of -3 dBm [26].

Furthermore, even though non-local effects were completely overcome, another limit for the probe power would remain: the Brillouin threshold of the fiber. This threshold defines

the maximum power that can be launched into the sensing fiber before the amplification of thermally-induced spontaneous Brillouin scattering (SpBS) leads to depletion of the probe wave and addition of noise to the detected signal.

In the following section, the fundamentals of the generation of virtual BFS will be explained to mitigate both effects: non-local effects and noise induced by SpBS.

3.2 Fundamentals of the BOTDA sensor based on source wavelength modulation

The principle of the proposed technique is schematically depicted in Fig. 3.1.

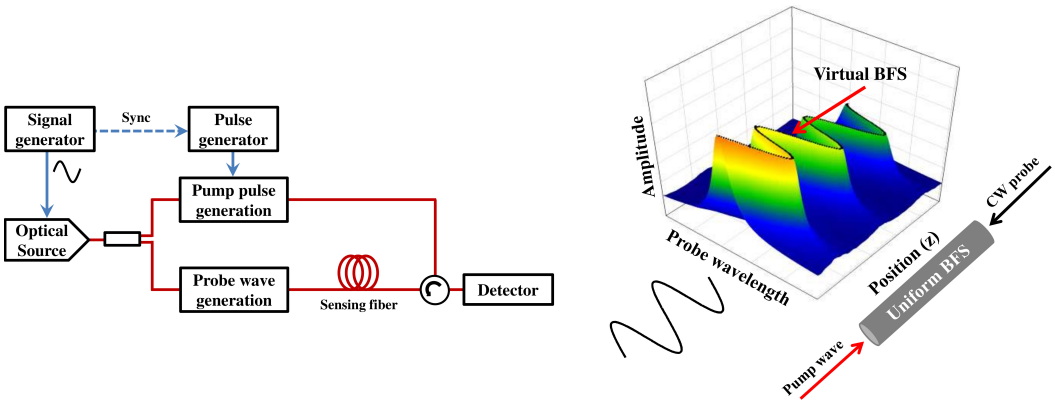

Fig. 3.1. Fundamentals of the laser wavelength dithering technique for virtual BFS synthesis.

This figure describes a conventional BOTDA setup based on a single source, although the technique is also applicable to double-laser setups. The laser source is divided in two branches. As it is well-known, a basic BOTDA setup requires the generation of a pump pulse and a CW probe that have a controlled frequency difference, which should be tunable around the Brillouin frequency shift of the deployed fiber. In Fig. 3.1, the upper branch is used to generate the pump pulses by pulsing the laser source signal and the lower branch is used to generate the probe wave. Depending on the particular type of BOTDA setup deployed, the frequency translation of the laser source signal required to have the tunable wavelength difference between pump and probe that is needed for Brillouin interaction may be performed either in the upper or lower branch, typically by the sideband generation technique, i.e. using modulation in the microwave range to generate sidebands of the narrow laser source.

The only difference to a conventional BOTDA resides on the addition of a frequency modulation of the optical source using a low frequency periodic wave that is synchronized to

the pulse generator. This is performed using a small current modulation that modifies the instantaneous optical frequency of the optical source through the semiconductor laser's chirp (mostly adiabatic or thermal, depending on the modulation frequency [87]). Furthermore, the frequency modulation shape is directly translated to a synthesized virtual BFS profile along the fiber as it is explained below. A sinusoidal wave is depicted in the figure as an example, but any other modulation shapes are possible.

In the upper branch, a synchronism signal activates the temporal switching of the modulated optical wave providing a pump pulsed signal, whose frequency depends on the fixed propagation delay between the optical source and the optical switch. Then, this pump pulse is directed into the sensing fiber to interact with the probe wave via stimulated Brillouin scattering (SBS). However, in contrast to conventional BOTDA sensors, the frequency of the probe wave varies along the optical fiber according to the frequency modulation applied to the optical source. As a consequence, the pump pulse meets a probe wave of different frequency at each location of the fiber. The resulting Brillouin interaction between both waves will be given by the detuning from the center of the Brillouin spectrum at each position of the fiber:

$$\Delta\nu(z) = \nu_P - \nu_S(z) + BFS(z) \tag{3.1}$$

where ν_P is the pump pulse frequency and ν_S is the probe wave frequency at position z. Note that the last expression points out that it is equivalent to have an actual variation in BFS due to the fiber characteristics than to have that same variation in ν_S. Therefore, a virtual BFS profile is synthesized by the probe frequency modulation.

This synthesized virtual BFS profile can be used, for instance, to compensate non-local effects or increase the Brillouin threshold of the fiber and hence, reducing the noise at the detected probe wave. The presented technique relies on the same idea that methods that use an optical fiber made of fiber segments with different characteristic BFS [40]. The advantage is that there is no need to modify the fiber type along the route, which is a cumbersome process. On the contrary, the system can use any optical fiber already installed and create a virtual BFS profile along the fiber by using source wavelength modulation.

3.2.1 Theoretical study of non-local effects using wavelength modulation

As mentioned in section 1.5.1, when a uniform fiber is employed, non-local effects manifest as a frequency dependent variation of the peak pulse power that follows a Lorentzian profile [19]. This is caused by the continuous Brillouin interaction between pump and probe waves. However, using our technique we can ameliorate this problem because, even in

the worst-case scenario, the frequency difference of pump and probe waves varies along the sensing fiber, effectively synthesizing a virtual BFS. As a consequence of this position dependency, the energy transfer principally occurs at those locations where $\Delta\nu = 0$, i.e. where the difference between probe and pump frequencies coincides with the natural BFS of the fiber (see Eq. (3.1)). Therefore, there is less frequency dependence of the pulse power and hence, less non-local effects and measurement error.

In order to theoretically study the compensation of non-local effects using the virtual BFS synthesis, we performed numerical simulations of the depletion factor of the pump power for the worst-case scenario (uniform BFS) and for different virtual BFSs. This factor is defined as [19]:

$$d = \frac{|P_{P,SBS} - P_{P0}|}{P_{P0}} \tag{3.2}$$

where $P_{P,SBS}$ and P_{P0} are the pump powers with and without Brillouin interaction, respectively. Note that the last expression is equally defined for gain or loss based BOTDA configurations, even though the pump pulses are amplified using the latter one. However, both systems lead to an equally distorted Brillouin spectrum [86]. As shown in section 1.5.1, the pump power under Brillouin interaction can be simply calculated from the basic model that governs Brillouin interaction [88] assuming small gain condition:

$$\begin{aligned} P_P(z) &= P_P(0)\exp(-\alpha z) \\ &\cdot \exp\left(-\frac{P_S(L)\exp(-\alpha L)}{A_{eff}}\int_0^z \frac{g_0}{1+\left[2\Delta\nu(z)/\Delta\nu_B\right]^2}\exp(\alpha z)\,\mathrm{d}z\right) \end{aligned} \tag{3.3}$$

where P_P and P_S is the pump and probe powers at location z, respectively, L is the fiber length, A_{eff} is the effective area of the fiber, α is the attenuation of the optical fiber, g_0 is the local gain and $\Delta\nu_B$ is the Brillouin linewidth.

Figure 3.2(a) depicts the depletion factor of the pump power for the different simulated scenarios of synthesized BFS and uniform BFS represented in Fig. 3.2(b).

As it is shown, if the sensing fiber has a uniform BFS (10.8 GHz), the frequency dependence of pump power shows a Lorentzian profile, whose peak matches the BFS. Note that for this pump power profile, the maximum depletion factor tolerated for a 1-MHz in BFS accuracy is 17% [19]. In this case, this value reaches a 30% change and the maximum error induced in the BFS measurement is around 2 MHz. This depletion of the pump power can be reduced by synthetizing a virtual BFS. For instance, using a square wave, we could simulate a sensing fiber with two equally-long segments, but different BFS values as shown in Fig. 3.2(b). Therefore, the energy transfer to the pump wave takes place at two frequencies instead of one, reducing the depletion. Note in Fig. 3.2(a) that a higher depletion takes place at

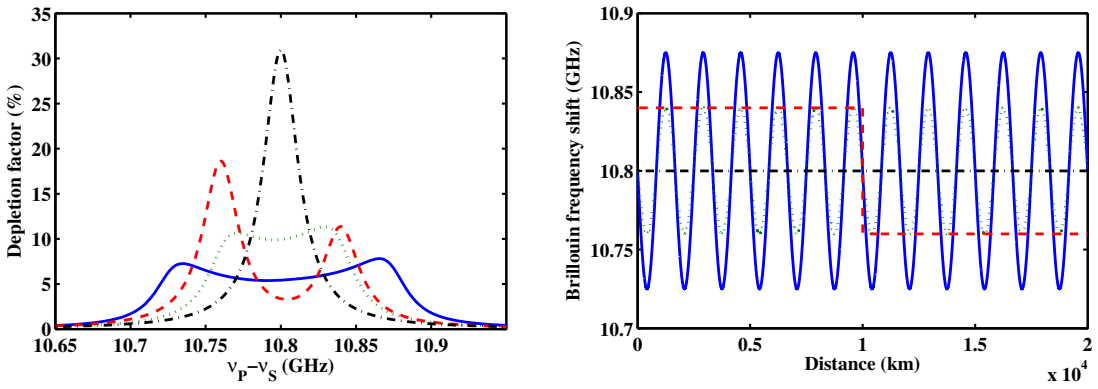

(a) (b)

Fig. 3.2. (a) Calculated depletion factor of pump power using (b) different BFS distributions: a uniform BFS fiber (black-dot-dashed line), a virtual BFS based on two fiber segments (red-long-dashed line) and two sinusoidal virtual BFSs with a frequency modulation of 80 MHz (green-short-dashed line) and 150 MHz (blue-solid line) with 12 cycles along the fiber. Simulation's parameters are: $g_0 = 1.1 \cdot 10^{-11}$m/W, $\Delta\nu_B = 30$ MHz, $L = 20$ km, effective area is $8 \cdot 10^{-11}$ m^2 and the injected optical pump and probe powers are 100 mW and 150μW, respectively.

the synthesized BFS that is located closer to the probe wave input as the Brillouin interaction is larger at that location. Another possibility is to synthesize a frequency modulation that varies continuously along the fiber, for example, a sinusoidal virtual BFS, which spreads the energy transfer into a larger frequency range than the square modulation. As it is shown in Fig. 3.2(b), we have simulated two sinusoidal virtual BFSs with different frequency range. The one with lower modulation index clearly reduces the depletion as the Brillouin energy transfer has been spread into an 80-MHz frequency range, as it is shown in Fig. 3.2(a). In this case, the depletion factor has been reduced from 18% to 12% comparing to the square modulation, but it is still appreciable that one of the peaks is slightly higher than the other. This asymmetry is again due to the distribution of the probe power, which is larger at the semi-cycle of BFS variation that coincides with the last kilometer of the sensing fiber. The last scenario presented in Fig. 3.2(a) is the sinusoidal virtual BFS with higher modulation index, which gets better results, bringing the depletion factor below 10% and ensuring a good performance in the BOTDA sensor. This result is due to the spreading of the interaction into a larger frequency range (150 MHz).

However, the modulation index or the number of cycles in the BFS can not be increased indefinitely. Both parameters determine how rapidly varies the frequency of the probe wave in time domain, so that during the pulse-probe interaction, the frequency difference between

both signals must be lower than the precision of the system to avoid a loss of the measurement contrast.

Note that the scenarios mentioned above are only examples that reveal the working principle of the technique and any other virtual BFS profiles can be implemented to reduce even more this detrimental effect.

3.2.2 Increment of the Brillouin threshold using wavelength modulation

Another advantage of using virtual BFS profiles is the reduction of the Brillouin induced noise in the detected signal. This effect arises from the injection of high power components into the optical fiber, which can pump SBS amplification of thermally induced SpBS waves, in a process that leads to the onset of the so-called Brillouin threshold [89]. This threshold establishes a maximum power that can be injected in a fiber before significant power begins to be reflected back and the launched signal is depleted. Moreover, it has been found that noise is added to the signal as it approaches the Brillouin threshold power [89, 90]. This is an important problem for all types of BOTDA sensors, but particularly for those that deploy a modulated probe wave that tends to have a strong carrier [45, 91, 92]. In these setups, the Brillouin noise induced into the optical carrier is transferred to the detected RF signal when the injected carrier power approaches the Brillouin threshold, compromising its SNR performance.

The Brillouin threshold can be increased and the Brillouin induced detection noise reduced by implementing the virtual BFS technique. Again, the idea is to mimic those approaches that seek to increase the SBS threshold by using fiber links with a variation of BFS along their length [93], but synthesizing a virtual SBS profile instead of implementing a real one. We have numerically studied the Brillouin threshold increment when a virtual BFS is synthesized. This was accomplished by solving the numerical model based on the coupled intensity equations presented in section 1.3.3 (see Eq. (1.29)). This simulates that the thermally induced SpBS waves can be interpreted as a low power component injected at one end of the fiber [94]. Figure 3.3 shows the backscattered and transmitted power resulting from gradually increasing the launched optical power for the worst-case scenario (a uniform BFS) and for a sinusoidal virtual BFS. Note that using the proposed technique, the Brillouin threshold rapidly increases from 7 mW to 44 mW (defined as the launched power at which the reflected power becomes 1% of the input power [95]). As a consequence, higher power can be injected into the fiber, enhancing the SNR value in detection.

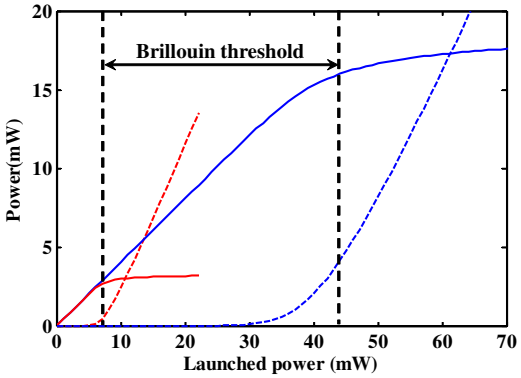

Fig. 3.3. Calculated reflected (dashed-line) and transmitted (solid-line) power using a uniform BFS fiber (red line) and a sinusoidal virtual BFS of 150 MHz frequency modulation and 12 cycles (blue line). Simulation parameters are: $g_0 = 1.1 \cdot 10^{-11}$m/W, $\Delta\nu_B = 30$ MHz, $L = 20$ km, effective area is $8 \cdot 10^{-11}$ m^2 and the optical power injected to simulate SpBS waves is 7 nW.

3.3 Experimental setup and measurements

The BOTDA configuration used to demonstrate the potential of the technique is based on a phase-modulated probe wave and RF demodulation [78, 92]. This setup was chosen to simultaneously show the compensation of non-local effects and the reduction of Brillouin induced noise generated by the injection of a high optical carrier power. Figure 3.4 sketches the deployed experimental setup. As it was indicated before, the setup is modified to add a function generator, which is synchronized to the pulse generator, to directly modulate a 1560-nm high power distributed feedback laser (DFB) laser. The light from this modulated wavelength laser is coupled into two optical branches. In the upper branch, a double sideband suppressed carrier modulation is deployed with a Mach Zehnder electro-optic modulator (MZ-EOM) and then is pulsed using a semiconductor optical amplifier (SOA). The temporal switching provides a pulsed signal with a frequency given by the time delay between the DFB and the SOA switch. This signal is amplified by an erbium-doped fiber amplifier (EDFA) and the upper-sideband of the pulsed signal is filtered by a narrowband fiber Bragg grating (FBG). Then, a polarization scrambler (PS) is used to reduce polarization induced fluctuations in the signal before launching the pulses into the sensing fiber via a circulator. In the lower branch, a probe wave is generated with an electro-optic phase modulator driven by a 1.3-GHz RF signal. Once the probe wave has interacted with the pump pulse via SBS, it is photodetected and the resultant RF signal is demodulated and captured in a digital oscilloscope. A 20-km standard single-mode fiber was deployed as sensing fiber.

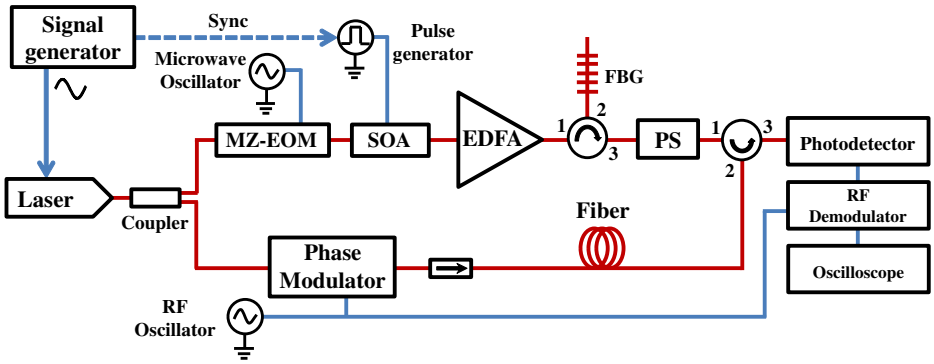

Fig. 3.4. Experimental setup for the BOTDA sensor based on virtual BFS synthesis technique.

Figure 3.5 compares the distribution of the measured Brillouin spectra along the fiber after and before applying the frequency modulation to the optical source. In the former case,

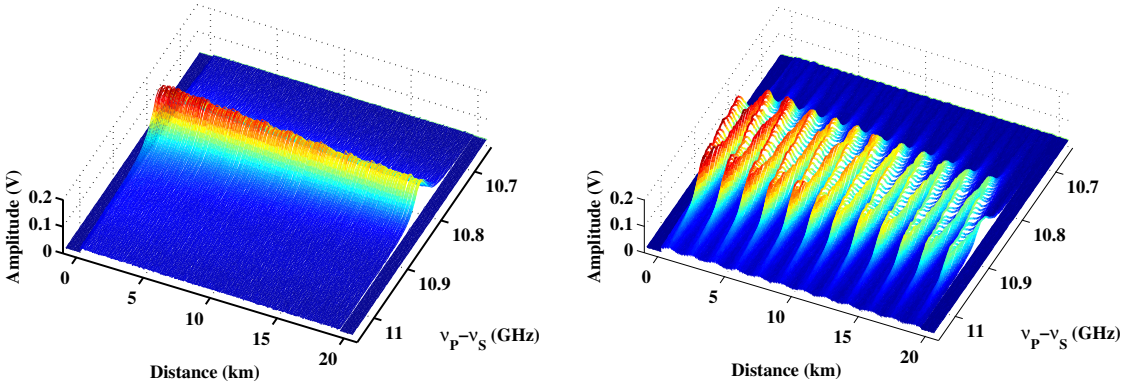

Fig. 3.5. (a) Experimental distribution of Brillouin spectra along the fiber for a conventional BOTDA measurement and (b) for a sinusoidal synthesized BFS distribution after applying modulation to the optical source (ν_{S0} is the optical carrier frequency, when no modulation is applied to the laser source).

the output of the signal generator was chosen to be a sinusoidal signal of frequency 60 KHz and amplitude of 200 mV, which yields a frequency modulated probe wave of 6 cycles for the 20-km long fiber and a maximum 150-MHz frequency shift, respectively. Notice that with this modulation, a sinusoidal virtual BFS distribution that mimics the frequency modulation is synthesized. Other spectral profiles could be easily implemented, for instance, a frequency modulation using a square wave with 5 kHz frequency would lead to a BFS profile equivalent to that of two concatenated 10 km fiber segments with different characteristic BFS value.

Furthermore, as the frequency modulation of the probe wave is known, the technique also offers the possibility to recover the natural BFS profile of the fiber by simply using Eq. (3.1).

Notice that the number of cycles shown in Fig. 3.5(b) is doubled when it is compared with the total number of cycles of the probe wave along the fiber. This is due to the counter-propagation of both waves, which gives rise to the following relation between the frequency of the modulated signal (f_{mod}) and the number of cycles of the BFS (N_{BFS}):

$$N_{BFS} = \frac{2nL f_{mod}}{c} \tag{3.4}$$

where c is the light's velocity, n is the refractive index and L is the length of the fiber. Note also that direct modulation of the laser generates a small sinusoidal variation of the amplitude of the measured Brillouin spectra along the fiber, which has no implications on the sensor performance.

In order to study the potential of the system regarding non-local effects, the probe power was set to a value high enough (0.34 mW) to induce a significant frequency dependence on the pump power. The deployed BOTDA sensor was set in a loss-based configuration and hence, the pump pulses were amplified during their propagation. Figure 3.6(a) compares the amplification factor of the pump power using the conventional technique and after applying the frequency modulation to the laser source. Notice that the technique brings the gain factor below the 17% required to ensure less that 1°C measurement error in the worst-case scenario, which is given by the deployment of a long optical fiber with a uniform BFS followed by a final section with a different BFS [19]. This scenario was simulated by inserting the last meters of the optical fiber into a climatic chamber at 50°C. Figure 3.6(b) shows the measured Brillouin spectra at the heated section before and after synthetizing a virtual BFS. Notice that the measured spectrum using the conventional technique is clearly distorted by the transfer function induced by the pump power frequency dependence, which clearly biases its peak. On the other hand, the Brillouin spectrum is perfectly recovered using the virtual BFS technique, as expected, since the pump power does not present this frequency dependence. Note that the frequency difference between the virtual BFS profile and the natural BFS profile of the fiber has been corrected in order to compare both spectra.

Another set of experiments was performed to highlight the potential to reduce Brillouin induced noise and increase the Brillouin threshold. The power of the injected carrier was gradually increased without applying the frequency modulation until the appearance of Brillouin noise at around 5 mW. Then, the carrier power was raised to 9 mW and Brillouin spectrum measurements were performed turning on and off the frequency modulation (Fig. 3.7). As it is shown, the Brillouin noise induced in the RF signal leads to a noisy spectrum, while the

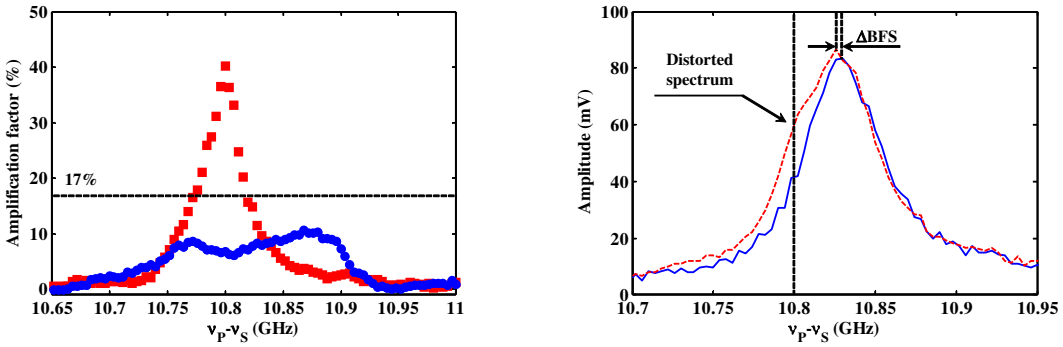

(a) (b)

Fig. 3.6. (a) Measured gain factor of the pump power as a function of the frequency separation between pump and probe waves after (blue circles) and before (red squares) the source wavelength modulation is turned on. (b) Measured Brillouin spectra using the conventional technique (red-dashed line) and using the sinusoidal synthesized BFS distribution (blue-solid line).

presented technique greatly reduces the noise in the trace. The SNR enhancement between both measurements was quantified to be 10.17 dB, which was measured by computing the standard deviation of the detected noise.

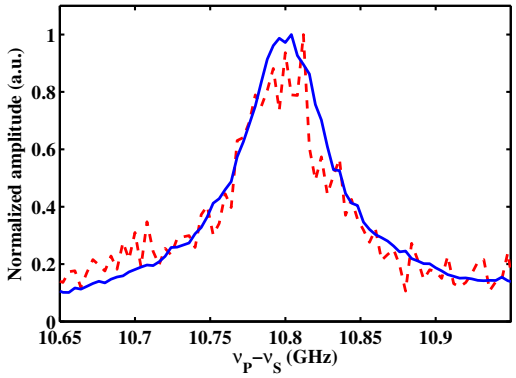

Fig. 3.7. Measured Brillouin spectra turning on (blue-solid line) and off (red-dashed line) the wavelength modulation applied to the laser source.

Note that the measured Brillouin spectrum using the presented technique deploys an optical carrier power that outreaches the Brillouin threshold of the used sensing fiber, which was experimentally measured as 7.9 mW. We would also like to remark that the optical power injected into the fiber was limited by the available power and hence, a higher optical carrier

power could be deployed to enhance even more the achieved SNR. Furthermore, the probe power was set to 0.236 mW to also compensate non-local effects.

Finally, the BOTDA sensor with BFS synthesis was used for temperature measurements, obtaining for the particular experimental conditions used, 1-m resolution and around 1°C uncertainty at the end of the fiber (worst-case).

3.3.1 Discussion

The presented technique allows to enhance the performance of most BOTDA configurations, as it only requires to include a signal generator to modulate the optical source of the sensor. Basically, the improvement comes from the increment of the injected probe power from -14 dBm to -4.6 dBm, which has been experimentally proved to provide an error smaller than the precision of the sensor. Consequently, higher optical probe powers could be injected into the fiber.

Furthermore, it must be mentioned that the use of this technique has a fundamental drawback regarding the conventional technique: the number of scanned frequencies increases considerably and hence, it also increments the measurement time of the system. This is caused by the virtual BFS synthesized at the fiber, which is no longer uniform for the purpose of the Brillouin interaction and hence, the system must scan more frequency points. In order to give an example, it is widely accepted that a fiber with a uniform BFS distribution can be measured using 150 points frequency-separated with a step of 1 MHz. If the peak frequency variation of the probe wave is 75 MHz, then the proposed technique must scan 300 points with 1 MHz of frequency step to retrieve exactly the same information than in the previous case. As a consequence, the number of points and the measurement time is doubled at the expense of a considerable enhancement of the system performance.

During the following sections, an evolution of the proposed technique will be introduced to completely suppress non-local effects, even when probe powers higher than the Brillouin threshold of the fiber are used. Moreover, the drawback mentioned about the measurement time is removed thanks to a different way to scan the Brillouin spectrum.

3.4 Optical frequency modulation in dual-sideband probe BOTDA systems

The use of a dual-probe-sideband BOTDA sensor has been the most popular method to compensate non-local effects since 2009 [24]. This technique, also known as balanced BOTDA sensor due to the complementary Brillouin interaction taking place at the pulse, deploys two

probe waves equally spectrally-shifted from the pulse, such that, the energy that the pulse transfers to the lower optical frequency probe is compensated by that transferred from the upper optical frequency probe to the pulse [19]. Therefore, this system should be very likely limited by the onset of amplified spontaneous Brillouin emission [19]. However, it has been recently shown that the probe power that can be deployed in such dual-probe-sideband setup is rather limited (around -3dBm), because non-local effects are compensated only to first order and there is an additional distortion of the pump pulse spectra that is brought by the combined gain and loss spectra generated by the two probe waves [26].

Therefore, the limitation to BOTDAs coming from non-local effects is yet to be resolved. Furthermore, even though non-local effects were completely overcome, the limit for the probe power would remain at the Brillouin threshold of the fiber. This threshold defines the maximum power that can be launched into the sensing fiber before the amplification of thermally-induced spontaneous Brillouin scattering (SpBS) leads to depletion of the probe wave and addition of noise to the detected signal [89, 90].

During the following sections, a method to greatly increase the probe power that can be deployed in BOTDA sensors will be introduced, overcoming previous non-local effect limits and even the Brillouin threshold limit. The technique is based on the working principle described at the previous section 3.2, but deploying an electrical frequency modulation of the probe waves in a dual-probe BOTDA setup instead of modulating the wavelength of the laser source used to generate the optical waves needed in a self-heterodyne BOTDA setup. Moreover, in the previous work the pulse depletion was not compensated but simply made flatter in terms of its frequency dependence so as to avoid BFS measurement errors [96]. Finally, this technique avoids the need to sweep the frequency of the probe waves by changing the microwave frequency applied to the modulator used to generate those waves. Instead, the Brillouin gain spectra is characterized by changing the delay between the pump pulse and the probe wave optical frequency modulation.

3.4.1 Fundamentals of the technique

Fig. 3.8 shows the fundamentals of the technique by depicting the spectra of the various optical waves involved. A BOTDA setup with two probe waves counter-propagating to the pump pulse is assumed. As it is highlighted in the figure, the optical frequency of the probe waves is modulated in the time domain. Moreover, this FM signal is synchronized to the pump pulses so that a sequence of pulses experiences the same frequency of the probe waves at any given location. Therefore, as explained in section 3.2, the modulation of the optical frequency of the probe waves leads to a variation of the Brillouin interaction frequency along the fiber that follows the same profile of this modulation.

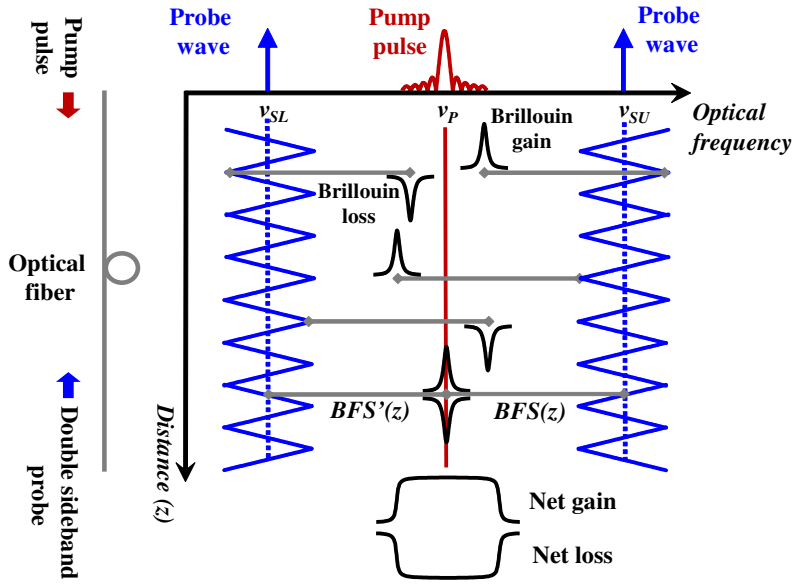

Fig. 3.8. Fundamentals of the technique: details of the Brillouin interaction on the pump pulse.

This has important implications for the Brillouin interaction generated by both probe waves onto the pump pulse, as it is schematically depicted in Fig. 3.8. The modulation of the optical frequency of the probe waves makes the Brillouin interaction induced by them upon the optical pulse to spread over a large frequency range. At the same time, the Brillouin gain interaction integrated along all the fiber generates a flat wideband total gain spectrum that does not distort the pulse spectrum, provided that an adequate shape is chosen for the frequency modulation. Similarly, the integrated Brillouin loss interaction along the fiber provides a complementary spectrum. Using Eq. (3.3) and including the effect generated by the other probe wave, the optical frequency response of both interactions at the end of the fiber is given by:

$$H_{B-SBS} = \exp\left[-\frac{P_S(L)\,\mathrm{e}^{-\alpha L}}{A_{eff}}\int_0^L\left(\frac{g_0}{1+\left(\frac{2\Delta\nu_G(z)}{\Delta\nu_B}\right)^2}-\frac{g_0}{1+\left(\frac{2\Delta\nu_L(z)}{\Delta\nu_B}\right)^2}\right)\mathrm{e}^{\alpha z}\,\mathrm{d}z\right] \tag{3.5}$$

where $\Delta\nu_L$ and $\Delta\nu_G$ are the detuning of the Brillouin loss and gain spectra respectively, from the pump pulse at a particular location (z), which can be expressed as:

$$\Delta\nu_L(z) = \nu_{SL}(z) - \nu_P + BFS(z) \tag{3.6}$$

$$\Delta\nu_G(z) = \nu_P - \nu_{SU}(z) + BFS(z) \tag{3.7}$$

where ν_P, ν_{SL} and ν_{SU} are the optical frequencies of the pump pulse, the lower-frequency probe sideband and the upper-frequency probe sideband, respectively. Both probe waves generate a net gain and loss that are cancelled giving rise to a flat frequency response over the frequency band of the pulse and hence, completely overcoming non-local effects. As shown in Fig. 3.8, a triangular modulation of the probe wave frequency is assumed. However, other modulation shapes are possible to optimize the objective of having the flattest possible total gain and depletion spectra so that no distortion is introduced to the pulse. Finally, it is worth to remark that the net gain and loss spectra are equivalent even if the evolution of the frequency probe along the fiber differs for the upper and lower sidebands as shown in Fig. 3.8. This is actually true for a large enough number of cycles of the probe wave along the fiber.

In detection, just one of the probe waves is detected, typically the lower-frequency one, while the other is filtered out. In order to measure the Brillouin spectra experienced by the retained probe wave at any given location, it is necessary to scan the frequency of the probe wave at that location. In a conventional BOTDA this is done by sweeping the frequency of the probe wave. However, when the frequency sweep is done, the resultant gain and loss spectra do not overlap during all the scanning, as shown in Fig. 3.9. This effect may generate a frequency distortion of the pulse spectrum and hence, a distortion of the measured Brillouin spectrum for that frequency detuning.

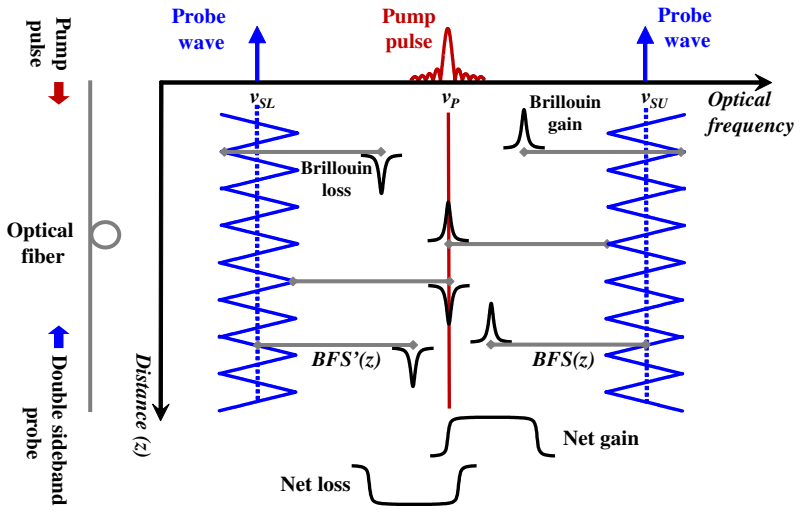

Fig. 3.9. Problematic of the frequency sweeping in BOTDA schemes.

Our system can perform the frequency sweeping in a much simpler way and without displacing the net gain and loss spectra by sequentially changing the relative delay between the pump pulse and the FM probe wave. The frequency detuning at a certain location z can

be expressed for a given relative delay $(\Delta\tau)$ between probe and pulse signals as:

$$\Delta\nu_L(z,\Delta\tau_P) = \nu_{SL,0} + \Delta\nu_{mod}\,\Lambda\left(2\pi f_{mod} z\frac{2n}{c} + 2\pi f_{mod}\Delta\tau_P\right) - \nu_P + BFS(z) \tag{3.8}$$

where $\nu_{SL,0}$ is the average probe frequency, $\Delta\nu_{mod}$ is the frequency deviation, Λ denotes a triangle function, f_{mod} is the frequency of the triangle signal and $\Delta\tau_P$ is the relative temporal delay between the pulse and probe wave. If the latter parameter is modified, e.g. delaying the generation of the pump pulse, then the detuning frequency of both waves varies scanning another point of the Brillouin spectrum, as it is schematically depicted in Fig. 3.10. The relation between the delay time and the FM signal defines the frequency step of the BOTDA sensor.

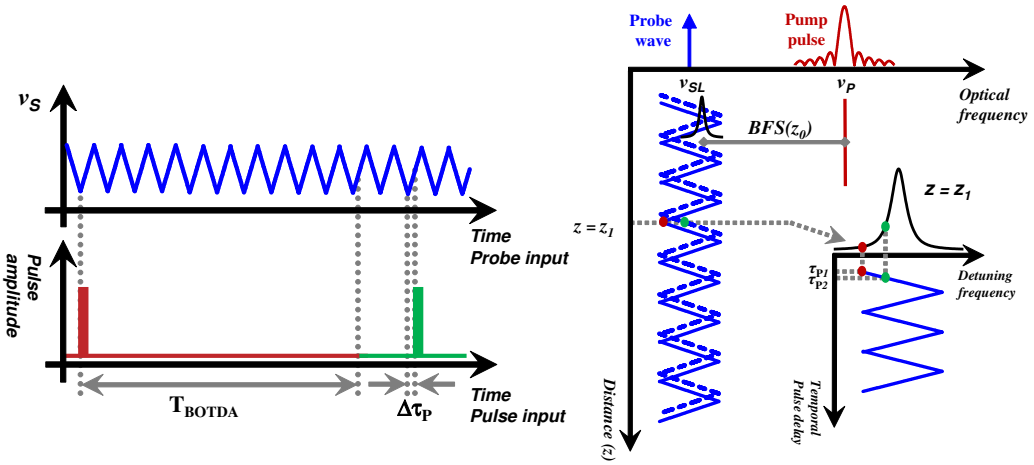

Fig. 3.10. Sweeping method based on changing the relative temporal delay between probe and pump waves.

Finally, the raw data extracted from the whole process requires a post-processing to compensate the frequency shift of the probe wave. This post-processing needs to know the probe frequency along the fiber for a given delay between pump and probe waves. This is accomplished by measuring the length of the fiber and the optical path difference between the pump and the probe branches. These parameters allows calculating the phase term of the frequency modulated signal when the pump pulse is injected into the fiber and hence, it is possible to update Eq. (3.8) to directly calculate the frequency detuning for the assembled BOTDA system.

3.5 Experimental setup and measurements

Fig. 3.11 depicts the assembled setup used to demonstrate our technique. The output of a laser source is divided into two branches to generate the pump and probe waves. In the upper branch, the pump signal is pulsed using a semiconductor optical amplifier (SOA). Then, the pulse power is boosted to a peak of 140 mW using a erbium doped fiber amplifier (EDFA) and its polarization state is randomized using a polarization scrambler (PS) before being launched into 50 km of standard singlemode fiber (SMF).

In the lower branch, a double-sideband probe wave is generated using a Mach-Zehnder electrooptic modulator (MZ-EOM) driven by an arbitrary waveform generator (AWG) and biased at the minimum transmission point of its transfer curve. The AWG provides a FM microwave signal whose instantaneous frequency varies around the average BFS of the fiber following a triangular shape. This induces an identical modulation of the optical frequency of the probe waves. The microwave signal was designed to have a carrier frequency of 10.8 GHz and a peak frequency deviation of 75 MHz. The modulation frequency was 40 kHz, which yields a total of 24 cycles of triangular variation of the local probe frequency along the 50-km long sensing fiber.

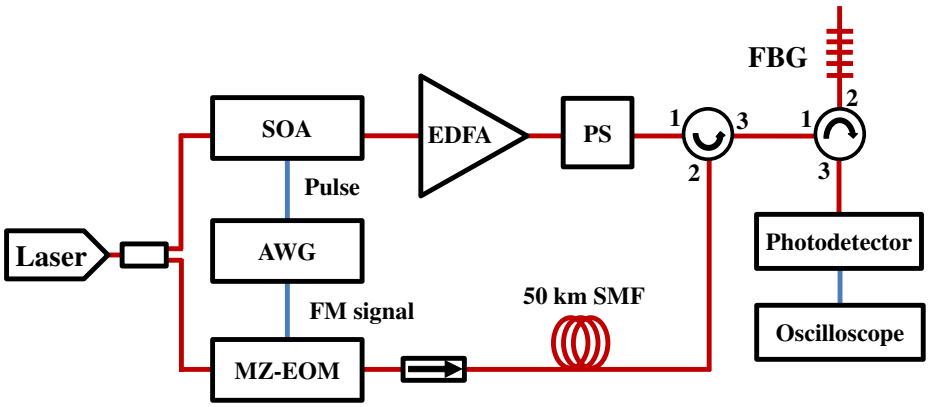

Fig. 3.11. Experimental setup.

When the Brillouin interaction provided by such FM modulated probe waves is integrated along the fiber, it gives Brillouin gain and loss spectra with a bandwidth of around 150 MHz, which is more than enough to avoid distortion in 10-ns pulses for 1-m resolution. Shorter pulses can be accommodated simply by increasing the peak frequency deviation. In the particular proof-of-concept experiments described in this paper 50-ns pulses are deployed.

Finally, after Brillouin interaction of these probe signals with the pump pulse, they are directed to a fiber Bragg grating (FBG) to filter out the upper sideband. The remaining probe wave is detected, captured in a digital oscilloscope and processed in a computer.

We started our experiments by confirming that, indeed, in the conventional dual-probe BOTDA there is a serious problem with non-local effects as the probe power is increased. This was done by simply switching off the FM modulation on the AWG so that it generated tunable CW microwave tones, and sweeping the optical frequency of the probe waves to scan the Brillouin spectra along the fiber.

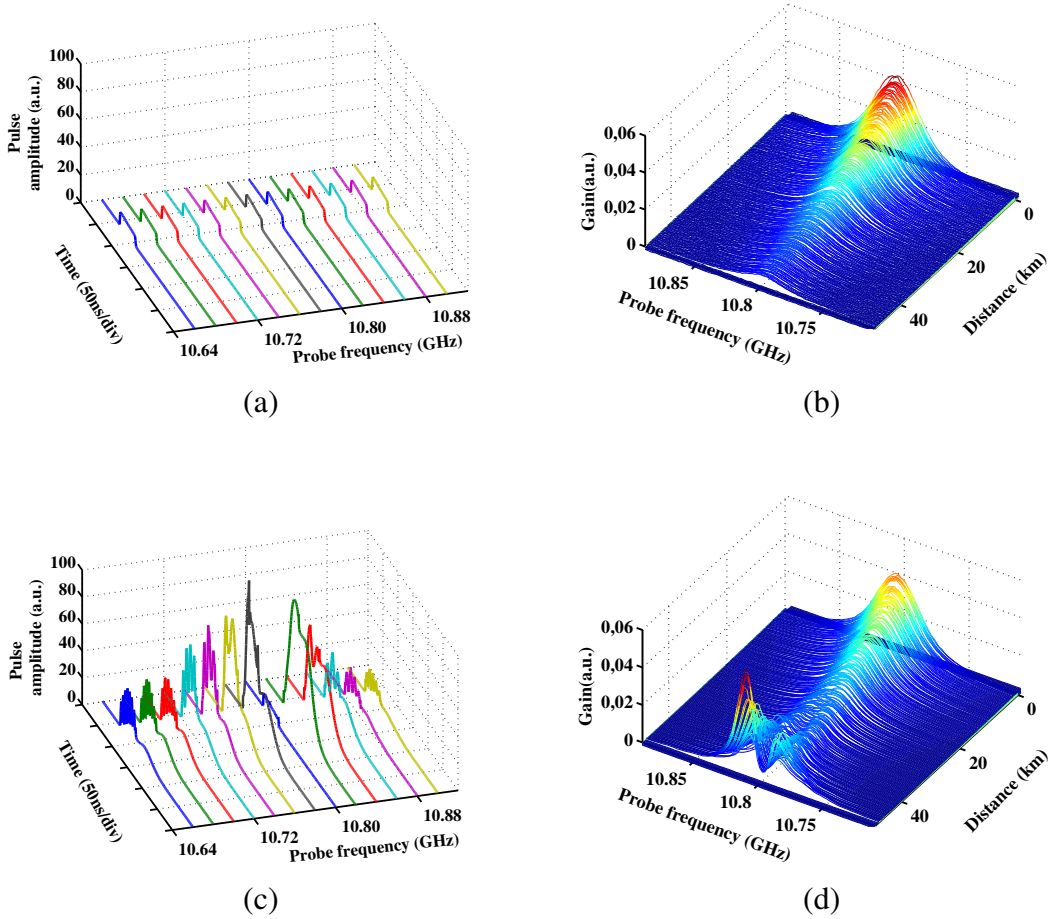

Fig. 3.12. Pulses at the output of the fiber and measured Brillouin spectra for a conventional dual-probe BOTDA in two cases for probe wave powers of -6 dBm (a)(b) and 5 dBm (c)(d).

Fig. 3.12 (a) and (c) shows the pulses that were measured at the output of the fiber as the microwave frequency was swept to measure the Brillouin spectra for two cases with low probe power (-6 dBm) and with high probe power (5 dBm). Notice that, when the probe power is low, non-local effects are negligible so the pulse remains constant and undistorted for all the probe's optical frequencies. However, when the probe power is increased the pulses are greatly distorted depending on the probe frequency. This distortion has been previously reported in the literature, but the effect was found to be rather mild due to the deployment of

lower probe powers than the one used here [26]. However, it can be seen that the distortion is much more pronounced as the probe wave power is increased. In Fig. 3.12 (c), it can be seen that the gain and depletion induced by both probe waves upon the pulse compensate just when the microwave frequency coincides with the average BFS of the fiber (around 10.8 GHz). However, for small departures of the microwave frequency from that value, the pulse gets distorted as its spectral components get differential amplification or depletion [26]. This makes the pulse peak power to greatly increase around the BFS frequency. There is also increased temporal duration of the pulses at those frequencies.

The distortion of the pulses has an strong impact on the measured Brillouin spectra along the fiber. Fig. 3.12 (b) and (d) shows a 3D view of the Brillouin spectra measured for the two cases considered before. It is clearly appreciated that for larger probe powers at the far away locations of the fiber, where the pulse arrives with great distortion, the measured spectra is also greatly distorted. Note that in Fig. 3.12 (d) the spectra at the end of the fiber has two peaks around the mean BFS of the fiber that correspond to the probe frequencies at which the pulse was shown to be amplified in Fig. 3.12 (c).

A more detailed view of the spectra at the end of the fiber is highlighted in Fig. 3.13. It shows how the spectra is affected by the distortion of the pulse spectra due to non-local effects when the probe power is increased. This spectra has lost his Lorentzian shape and two peaks have appeared around his center due to the amplification of the pulse at that frequencies.

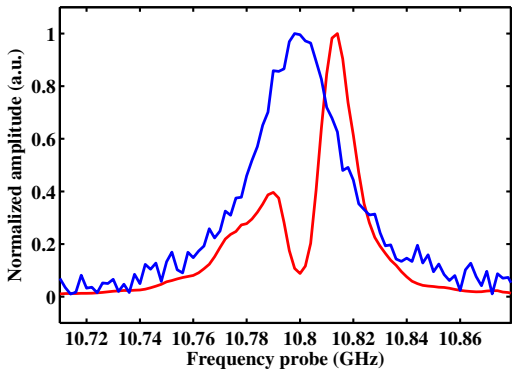

Fig. 3.13. Measured Brillouin spectra at the end of the fiber for -6 dBm (blue line) and 5 dBm (red line) probe power.

In contrast to the conventional technique, Fig. 3.14 depicts measurements with our technique with FM modulation of the probe waves. Fig. 3.14 (a) depicts the pulses measured at the output of the fiber with an without probe wave applied. Notice that the pulse shape remains almost identical for both cases with negligible distortion and just some added noise,

which is attributed to SpBS amplified by the probe waves. Also note that the deployed probe power is larger than for previous measurements, i.e., ~8dBm, which, to our knowledge, is the largest probe power ever demonstrated in a long-range BOTDA sensor without errors induced by non-local effects. The raw measurement data obtained as the delay between the pulse and the FM modulation is depicted in Fig. 3.14 (b) and (c). Note that in contrast to Fig. 3.5(b), it does not follow a triangle shape due to the new sweeping method. This raw data is post-processed to compensate the frequency shift in the measurement introduced by FM modulation of the probe wave along the fiber, resulting in the measurement of the well-behaved spectra in Fig. 3.14 (d). The spectra are completely normal, not suffering any distortion at the end of the fiber.

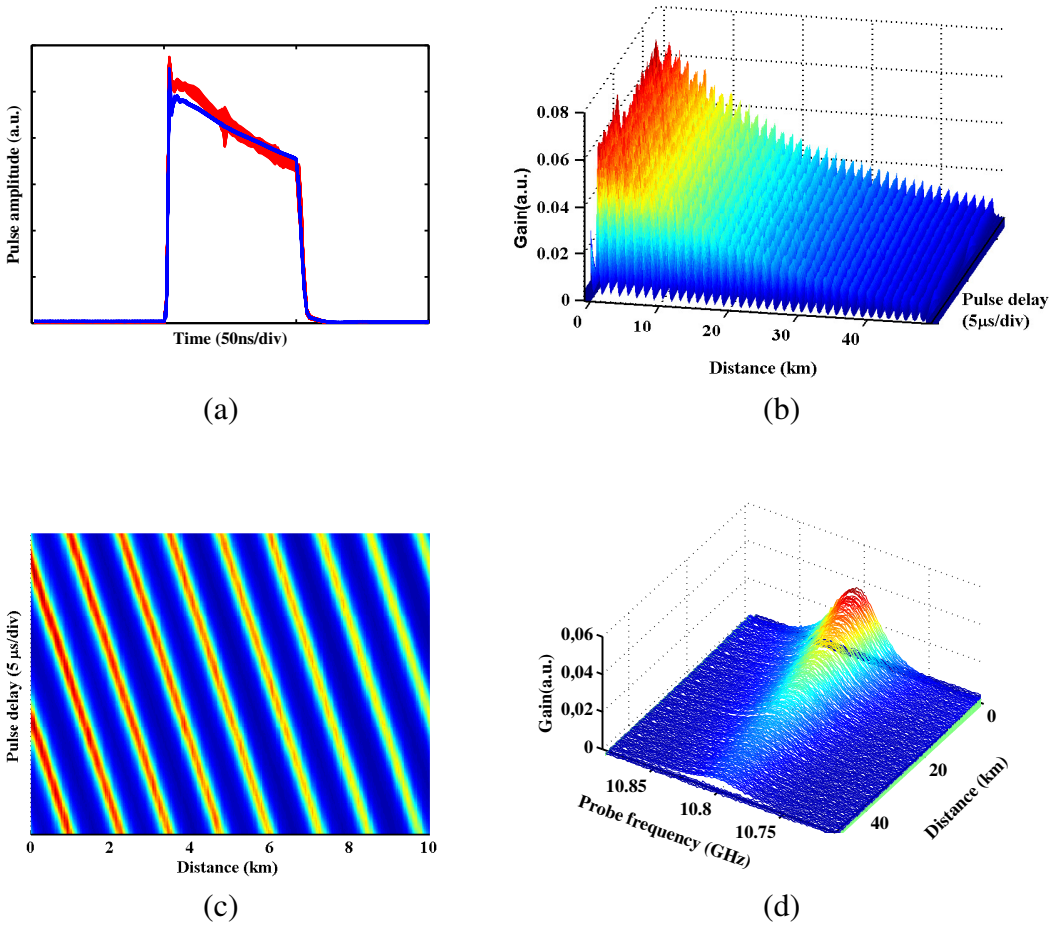

Fig. 3.14. (a) Pulses at the output of the fiber in two cases for probe wave power of 8-dBm (red line) and without probe power (blue line), (b) raw measurement data for the FM dual-probe BOTDA with 8-dBm probe power, (c) a top view of the raw data and (d) the measured Brillouin spectra.

Fig. 3.15 compares the spectra measured at the output of the fiber for our FM technique with low and high power of the probe wave. It can be seen that, indeed, the larger power measurement is not distorted at all. The only difference between the measurements is that the higher power one is less noisy, as it was expected, due to higher probe wave reaching the receiver. Specifically, the SNR increment is 3 dB higher. Although this improvement is significant by itself, it is just a sample of what can be achieved with our technique because in these experimental results the optical power reaching the detector was attenuated to ~-13dBm when using 8 dBm of probe power to prevent saturation of the deployed receiver.

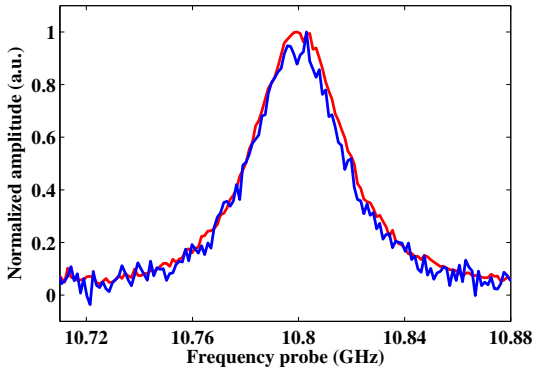

Fig. 3.15. Measured Brillouin spectra at the end of the fiber for -6-dBm (blue line) and 8-dBm (red line) probe power with the FM dual-probe BOTDA system.

Moreover, there is no systematic error in the BFS measurement with our technique when the probe power is increased. This is confirmed by Fig. 3.16 that displays the BFS measured for the conventional dual-probe BOTDA and for our system for different powers of the probe wave. Notice that, as it was explained before, there is a large systematic measurement error as the probe power is increased for the conventional dual-probe BOTDA, while for our system the BFS measurement remains error-free even for larger probe power.

Finally, it must be pointed out that our FM BOTDA setup was operating with a probe power above the Brillouin threshold, which was measured to be 6-dBm for the deployed sensing fiber. This is made possible by a side effect of the FM modulation, which has been previously shown to increase the effective Brillouin threshold (see section 3.2.2). In order to properly measure the Brillouin threshold, the probe power at the input of the fiber was gradually increased while the rms noise of the detected electrical signal was measured. This was accomplished using a constant optical power at the input of the photoreceiver, ensuring that the rest of noise sources are equal for each measurement. As it is shown in Fig. 3.17, in the conventional dual probe system there was a larger than six times increment in rms noise

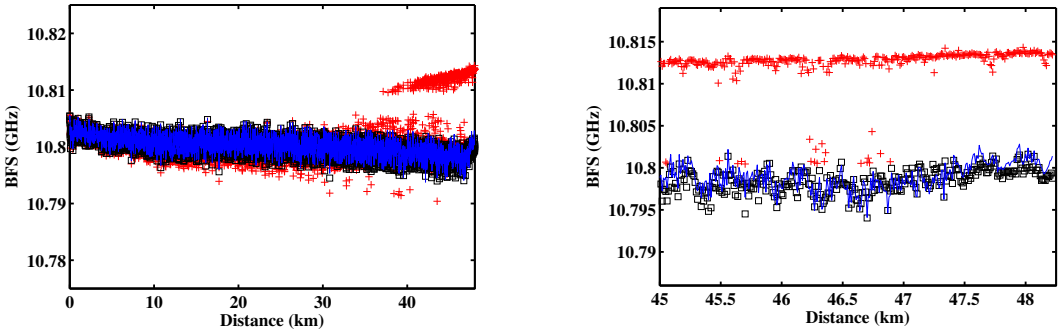

(a) (b)

Fig. 3.16. Comparison of measured BFS for the FM technique with 8 dBm probe power (black squares) and for the conventional dual probe with 5 dBm (red crosses) and -6-dBm (blue solid line) probe power for (a) all the fiber and (b) in the last kilometers.

as the probe power was increased from 6-dBm to 8-dBm, whereas with the FM technique the noise lever remains stable.

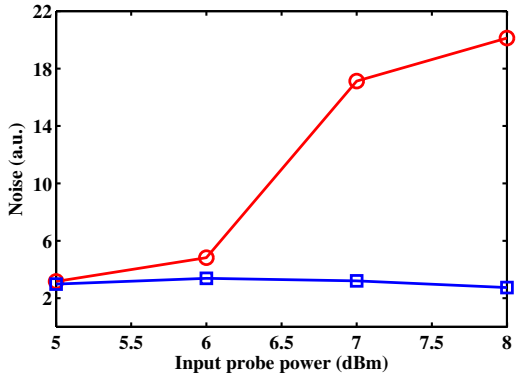

Fig. 3.17. Comparison of measured rms noise at the detector for different probe power injected in the fiber using the conventional dual proble system (red line with circles) and the FM technique (blue line with squares).

3.6 Conclusions

During these chapter a new concept for BOTDA sensors based on the synthesis of a virtual BFS profile along the sensing fiber has been proposed and verified. The technique relies on the wavelength modulation of an optical source using a periodic signal that is synchronized

to the pulse generator. Due to the simplicity of the technique, it is perfectly applicable to the vast majority of BOTDA sensor setups. The technique has been theoretically studied and proof-of-concept experiments have been performed to demonstrate the generation of this virtual BFS profile and its application to solving two of the fundamental problems presented in long-range BOTDA sensors: non-local effects and Brillouin induced noise.

In the case of standard BOTDA sensors, i.e a pump wave interacting with a probe wave, the technique has experimentally demonstrated to increase the maximum injected probe power from -14 dBm to -4.6 dBm ensuring that non-local effects generate a maximum of 1-MHz error at the BFS estimation in a very long fiber $L \geq L_{eff} \simeq 22$ km. This means a 9.4 dB improvement in SNR by using this technique assuming that the noise level is equal for both received powers at the photoreceiver. Moreover, for the particular experimental case shown in section 3.3, the probe power could be increased 1.3 dB to reach a depletion factor of 0.17. This predicted probe power (-3.27 dBm) is close to the power limit of dual-sideband probe BOTDA, which is one of the best techniques to reduce non-local effects.

On the other hand, when the technique is applied to BOTDA systems deploying a modulated probe wave and RF detection, the technique also increases the tolerance to non-local effects but also allows to increase the amplitude of the detected RF signal and reduce the Brillouin induced noise generated by the optical carrier of the probe wave. For the particular case study described in section 3.2, the optical power injected into the fiber can be increased from 7 mW to 44 mW. Recalling that the SNR in these systems is directly proportional to the power of the optical carrier, then the SNR can be enhanced by a factor ~8 dB. Moreover, the noise induced by Brillouin transfer rapidly increases in the detected signal, when the optical power is higher than the Brillouin threshold. As shown in section 3.3, the carrier power was set to 9 mW, which is only 1.1 mW higher than the Brillouin threshold. However, a SNR deterioration of 10.14 dB was observed when turning off the modulation confirming the potential of the technique to reduce Brillouin noise.

Moreover, the technique has been evolved for dual-probe-sideband BOTDA sensors. The solution is based on deploying FM modulation of the probe waves being able to completely cancel the non-local effects using two complementary gain and loss wideband spectra at the frequency band of the pulse spectrum. Consequently, both spectra avoid a variation of the pulse power due to Brillouin transfer. Furthermore, the technique allows scanning the Brillouin distribution of the fiber without modifying the average frequency of both probe waves but simply delaying the pump signal regarding the probe wave. This has major implications for the avoidance of non-local effects because there is not a frequency shift of the net gain and loss spectra or an amplitude change in their shape that could distort the pump spectrum along the sweeping process.

Furthermore, the frequency modulation of the probe wave reduces the Brillouin induced noise in the detected signal when the probe power reaches the Brillouin threshold of the fiber. The experiments have demonstrated that this method permits much larger power injected in the sensing fiber that was previously possible, opening the way to substantial enhancement in the performance of BOTDA sensors. This will come in the form of enhanced SNR in the detectors at the end of the fiber as more optical power reaches them, which in turn leads to enhanced sensor performance in terms of precision or measurement time.

In addition, when the new sweeping method is used, the frequency deviation generated by the probe frequency modulation is also the frequency range scanned by the sensor to retrieve the BFS distribution, as shown in section 3.4.1. The frequency deviation is set to properly accommodate the pulse spectrum, which could have a bandwidth around 100 MHz for a typical spatial resolution of 1 m. Consequently, the number of frequency points scanned by this technique is equal to the standard technique solving one the fundamental problems of the virtual BFS technique.

Finally, it is worth comparing the presented solution with another technique presented to solve second order non-local effects [97]. The latter modifies the frequency sweep method by shifting the frequency of the probe wave in the same direction instead of opposite directions as it is done in the conventional technique. This gives rise to a complementary Brillouin interaction when both probe waves are frequency-shifted from the pulse by the average BFS of the fiber. The only difference with the technique presented in these sections is the frequency modulation of the probe wave, which spreads the energy transfer into a larger frequency range. This gives the opportunity to increase the probe power above the Brillouin threshold but most importantly it also reduces the distortion on the pump spectrum when non-uniforms fibers are deployed.

Chapter 4

BOTDA sensor assisted by Brillouin distributed amplification of pump pulses

Brillouin optical time-domain analysis (BOTDA) sensor technology has evolved during the last years to such an extent that it has become a powerful commercial tool to monitor temperature and strain over large structures (around 50 km). These measurements are of great value for diverse field applications such as ensuring the structural health of oil and gas pipelines or assessing the operating conditions of high voltage transmission lines, all of which have a common need for large monitoring distances. However, structures with distances longer than 50 km requiring high spatial resolution (one meter or less) need to deploy more than one sensing unit to secure the whole asset integrity, doubling the cost of the sensing application.

In this chapter, a BOTDA sensor that deploys a distributed Brillouin amplifier (DBA) is presented. The technique is based on injecting a DBA pump at the probe input that generates amplification of the pump pulses where it is more needed, i.e. at the last kilometers of the fiber. Moreover, the DBA pump is frequency modulated along the fiber to equally amplify all the frequency components of the optical pulse spectrum, and hence, avoiding any possible distortion induced to the pulsed wave by the amplification. Furthermore, the deployment of a DBA does not introduce any significant noise to the probe wave due to the inherent directionality of the Brillouin gain. Finally, a differential pulse-width pair (DPP) measurement is deployed to avoid measurement errors due to the interplay between the self-phase modulation (SPM) effect and the changes in the temporal shape of the pulses induced by the transient behaviour of Brillouin gain.

4.1 Introduction

As shown in section 1.4.4, when the probe wave and pulsed signal counter-propagate along an optical fiber, the optical probe power is locally modified due to the interaction with the pulsed wave through stimulated Brillouin scattering (SBS). This variation of the optical probe power can be expressed as [18]:

$$\Delta P_S(z) = \frac{g_0}{A_{eff}} P_{Pi} \exp(-\alpha z) P_{Si} \exp(-\alpha L) \Delta z \tag{4.1}$$

where P_{Si} and P_{Pi} are the input optical probe and pump power, respectively, g_0 is the local gain coefficient, A_{eff} is the effective area of the fiber, α is the attenuation of the optical fiber, L is the fiber's length and Δz is the spatial resolution. Assuming that the input optical powers are optimized to avoid any non-linear effect such as modulation instability [30] or non-local effects [19], and that the spatial resolution is fixed, then the measured response depends only on the characteristics of the fiber such as the Brillouin coefficient gain or its attenuation factor, which is scaled by the length of the fiber. The latter defines how much the probe power attenuates (αL) before being detected at the receiver, while the variation of the probe power (due to Brillouin gain) exponentially drops as the pump pulse propagates along the fiber (αz). As a consequence, the signal-to-noise ratio (SNR) of the detected Brillouin gain becomes too small at distant locations from the pulse input to provide measurements with the required accuracy. This reduction of SNR can be compensated to some degree by the use of signal averaging, but at the cost of increasing the measurement time, which becomes impractically large. The obvious solution is to amplify either the probe wave to compensate the losses generated by the sensing fiber or the pump wave to increase the Brillouin gain experienced by the probe wave. Both solutions have been demonstrated by the use of erbium-doped fiber amplifiers (EDFA) as pulse repeaters along the fiber length [40, 98]. Fig. 4.1 shows an example of this kind of system deploying repeaters, in which each circulator extracts from the sensing fiber either the pump or the probe waves to be independently amplified, and then both waves are injected again to the sensing fiber to follow their propagation through the fiber. A maximum length of around 150 km has been successfully monitored using this mid-way amplification [40]. However, distant EDFAs need to be powered, whereas an all-passive sensing network is much more attractive and practical.

A more elegant solution is to use distributed Raman amplification (DRA) by injecting a Raman pump in the sensing fiber. This can provide amplification not only to the pump pulse but also to the probe wave by using a bidirectional DRA pump configuration, as shown in Fig. 4.2 [42, 99]. This kind of BOTDA sensor assisted by DRA has experimentally demonstrated to be able to monitor distances around 100 km with 0.5 m of spatial resolution [42].

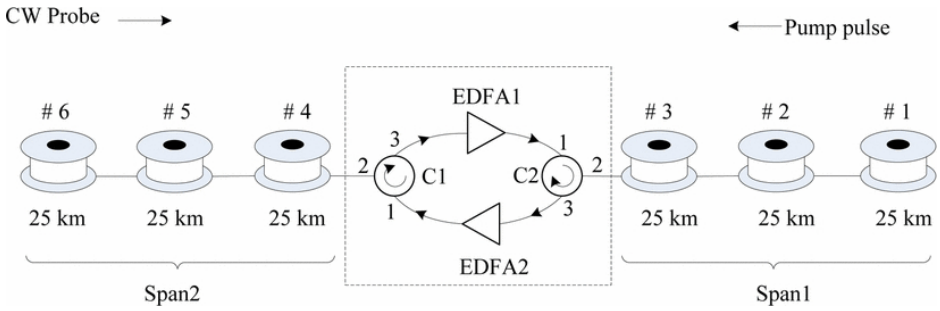

Fig. 4.1. Layout of the sensing fibers and in-line EDFAs. ©2012, IEEE [40].

However, the deployment of Raman amplification requires the use of very high power (of the order of hundreds of milliwatts) in the fiber, which can become an eye-safety concern in the installation and operation of real systems. In addition, the tens-of-nanometers bandwidth of a DRA is wasted just to amplify narrowband signals, such as the probe or the pulse waves. Finally, using DRA, the relative intensity noise (RIN) of the Raman pump laser is translated to the detected probe signal, significantly degrading the accuracy of the sensor [100].

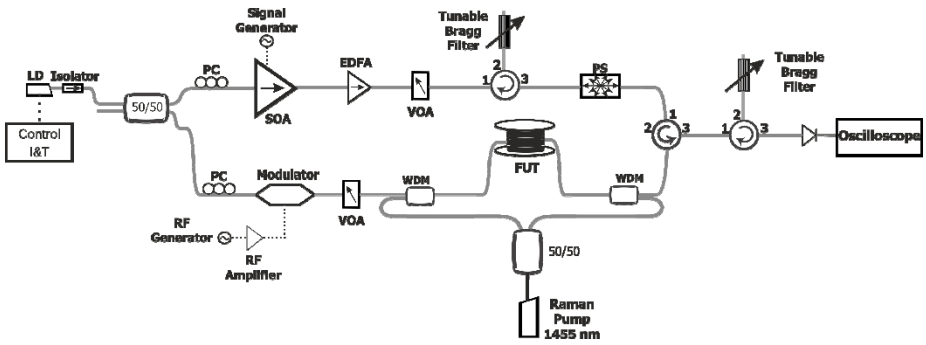

Fig. 4.2. BOTDA sensor assisted by Raman amplification. ©2013 Optical Society of America [42].

4.2 Fundamentals of DBA-assisted BOTDA sensor

Figure 4.3 schematically highlights the fundamentals of the technique depicting the various optical waves involved in the DBA-assisted BOTDA and their spectra. As shown in the figure, two Brillouin interactions co-exist in the sensing fiber. The first one is for sensing purposes, where the conventional BOTDA interaction between a CW probe wave and a counter-propagating pump pulse provides a distributed measurement of the Brillouin frequency shift (BFS) in the fiber, which is directly related to temperature or strain. The second interaction, between the DBA pump wave and the pump pulse, is deployed to amplify

the power of the latter as it propagates through the fiber. This requires that the DBA pump wave is offset from the pump pulse by an optical frequency difference that is around the mean BFS of the sensing fiber. However, the Brillouin gain spectrum generated by a CW DBA pump would be very narrow, just the intrinsic Brillouin linewidth (aprox. 30 MHz), which would severely distort the pump pulse spectrum. Therefore, there is a need to increase the

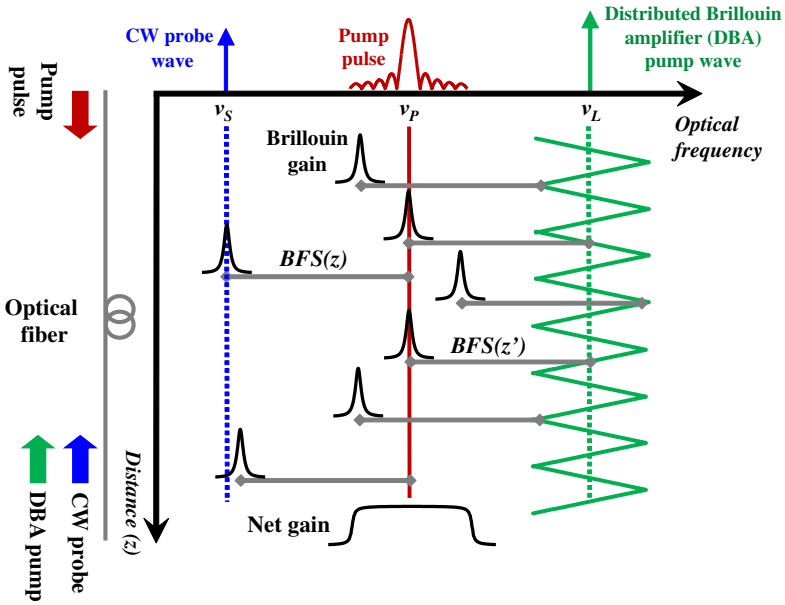

Fig. 4.3. Fundamentals of the technique, showing the spectra of the optical waves present in the fiber for a DBA-assisted BOTDA.

DBA bandwidth beyond the natural Brillouin linewidth to properly amplify all optical spectral components of the pump pulse so as to avoid distortion. This increment can be obtained by modulating the wavelength of the DBA pump wave, as it is schematically depicted in Fig. 4.3. This makes the center wavelength of the Brillouin gain spectra experienced by the pump pulses to vary along the fiber as it meets the counter-propagating wavelength-modulated DBA pump wavefront, so that the pulse experiences a broad total integrated gain spectrum. The wavelength modulation of the DBA pump is additionally synchronized to the injection of the pump pulses in the fiber, so that successive pump pulses experience the same gain at the same location; thus making the gain stable and avoiding the addition of noise to the BOTDA signal. Furthermore, the net gain can be made to have a flat frequency response with a judicious choice of wavelength modulation shape and frequency [101].

The theoretical model for the interaction of the three waves depicted in Fig. 4.3 is based on the solutions of the steady-state coupled wave equations that define the evolution of their power along the fiber [88]:

$$\frac{dP_P}{dz} = [g_B(\Delta\nu_{DBA})P_L - g_B(\Delta\nu)P_S]\frac{P_P}{A_{eff}} - \alpha P_P \tag{4.2a}$$

$$\frac{dP_S}{dz} = -\frac{g_B(\Delta\nu)}{A_{eff}}P_P P_S + \alpha P_S \tag{4.2b}$$

$$\frac{dP_L}{dz} = \frac{g_B(\Delta\nu_{DBA})}{A_{eff}}P_P P_L + \alpha P_L \tag{4.2c}$$

where P_S, P_P and P_L are the optical powers of probe, BOTDA's pump pulse and DBA pump wave, respectively, at each position z of the fiber, A_{eff} is the effective core area, and g_B is the Brillouin gain spectrum, which depends either on $\Delta\nu$ or $\Delta\nu_{DBA}$, the detuning of the pump pulse and probe wave wavelengths or the pump pulse and DBA pump wavelengths, respectively, from the center of the Brillouin gain spectrum. As in a conventional BOTDA sensor, it can be noticed that the pump pulse power is depleted by the Brillouin gain transferred to the probe wave and by the optical attenuation. However, in the present technique it also receives an additional energy transfer from the DBA pump wave, that is going to compensate its attenuation. This model assumes pulses that are longer than the acoustic phonon lifetime (10 ns).

Furthermore, the model needs to take into account the wavelength modulation of the DBA pump, which makes the pump pulses experience a position-dependent Brillouin gain generated by the DBA pump, as it is depicted in Fig. 4.3. Synchronization of the DBA wavelength modulation and the pulses means that the detuning of the pump pulse wavelength from the center of the Brillouin gain spectrum, $\Delta\nu_{DBA}$, at each position along the fiber is given by:

$$\Delta\nu_{DBA}(z) = \nu_P - \nu_L(z) + BFS(z) \tag{4.3}$$

where ν_P is the wavelength of the pump pulses and ν_L is the local wavelength of the DBA pump. Note that the latter changes due to the wavelength modulation introduced to the DBA pump and, as a consequence, a distribution of the Brillouin spectra that follows the wavelength variations in ν_L is created (see section 3.2) [96]. The latter is factually correct when the deployed sensing fiber presents an approximate uniform BFS distribution. Although this is the typical case, it could be possible that the BFS of the fiber would vary considerably not being fully uniform. In this case, the wavelength modulation applied to the DBA laser could be adapted to compensate this effect.

The theoretical model in Eqs. (4.2) can be easily solved either directly, through numerical integration, or analytically with some preliminary simplifications. For instance, Eq. (4.2c) can be simplified by neglecting the depletion induced by the short pump pulse on the DBA

pump. Similarly, Eq. (4.2a) can be solved taking into account that the Brillouin gain provided to the probe by the pump pulse is very small. With these approximations, the pump pulse power along the fiber is found to be:

$$P_P(z) = P_P(0)\exp\left[\int_0^z \frac{g_B(\Delta\nu_{DBA})}{A_eff} P_L(L)\exp(-\alpha(L-z))\,dz\right] \cdot \exp\left[-\frac{g_B(\Delta\nu)}{A_eff} P_S(L)\exp(-\alpha L)\frac{(\exp(\alpha z)-1)}{\alpha}\right]\exp[-\alpha z] \quad (4.4)$$

The first exponential term is the gain provided by the DBA pump and the second is just the pump pulse depletion due to the energy transferred to the probe assuming nearly uniform BFS along the fiber.

Figure 4.4(a) depicts the calculated local Brillouin spectrum that is experienced by the pump pulses at each location of a 50-km fiber for a triangular modulation of the DBA pump with a frequency of 80 kHz and a peak frequency deviation of 125 MHz. A zoom of the z axis showing just the last 5 km of the fiber is used in Fig. 4.4(a) to highlight that the profile of the detuning of the Brillouin spectrum along the fiber indeed follows the same triangular profile of the DBA pump modulation.

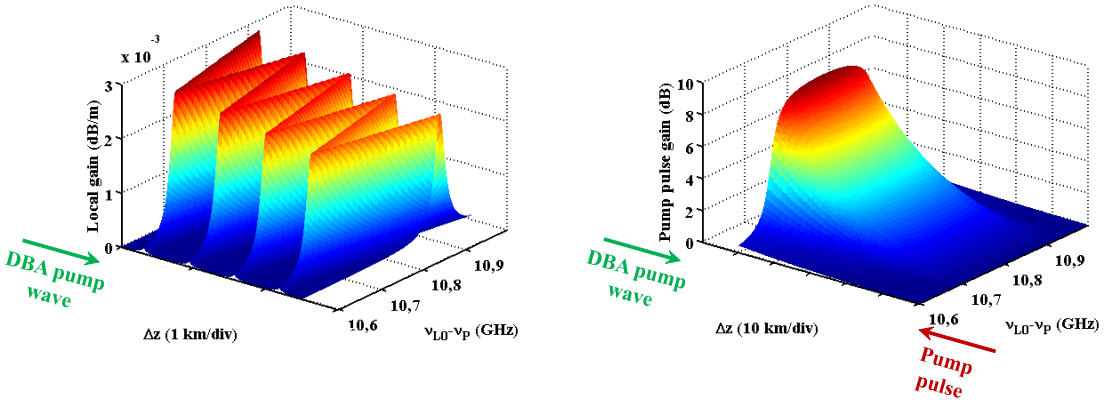

(a) (b)

Fig. 4.4. (a) Local Brillouin gain experienced by the pump pulses at each location of the fiber and (b) total gain experienced by the pulses in their propagation for each location of the fiber. ν_{L0} is the wavelength of the DBA pump wave when no modulation is applied. Simulation parameters are: Brillouin gain $1.1 \cdot 10^{-11}$m/W, Brillouin linewidth 30MHz, effective area is $8 \cdot 10^{-11}$ m^2 and the injected optical pump pulse and DBA pump are 100mW and 4.7mW, respectively.

The local gain shown in the previous figure is accumulated by the pump pulse during its propagation through the fiber, giving rise to the total gain depicted in Fig. 4.4(b). This can

be easily calculated using Eq. (4.4) as the result of the integration of the position dependent gain provided by the Brillouin spectrum at each z. As shown in Fig. 4.4(b), the DBA has a flat frequency response over the pulse bandwidth avoiding any spectral distortion of the pump pulse. This feature depends mainly on the choice of the wavelength modulation shape and the frequency of the modulation, i.e. the number of cycles of the DBA modulation wavelength along the fiber. For this particular case, a triangular shape provides a convenient flat response [101], whose bandwidth can be simply set by the peak frequency deviation parameter. However, the chosen frequency of the triangular shape must be high enough to avoid different gain contributions for any frequency component of the pulse spectrum during its propagation. This effect is shown in Fig. 4.5(a), where the accumulated gain experienced by the pump pulse is depicted using a triangular modulation of the DBA pump with a frequency of 20 kHz and a peak frequency deviation of 125 MHz. As it is shown, a different total gain is accumulated by the pulse spectrum at different locations of the fiber, which may induce distortion to the pulse wave and hence, to the measured Brillouin spectrum. Figure 4.5(b) shows the total gain accumulated by the pulsed signal at the end of the fiber when the frequency of the triangular modulation is increased. As shown, for frequencies higher than 80 kHz, no effect is observed at the shape of the DBA and hence, there is no need to increase more the frequency, which would be upper-limited by the temporal interaction between the pulse and DBA pump waves.

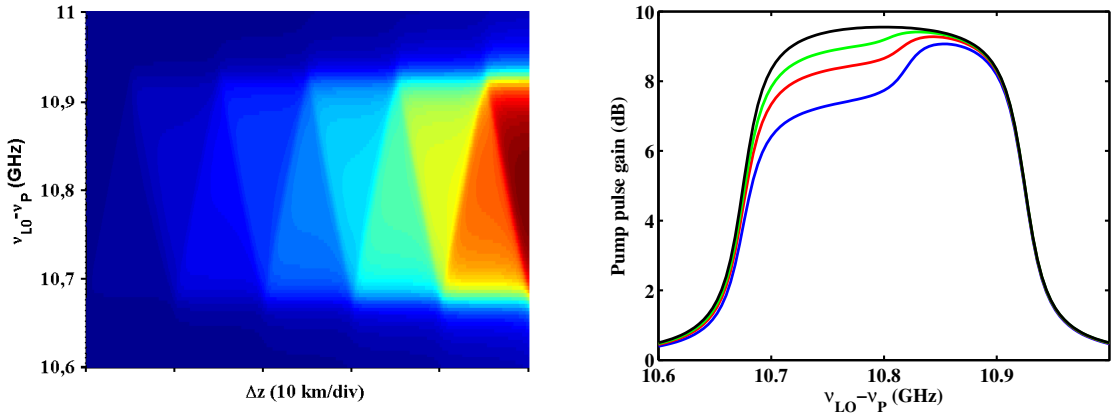

(a) (b)

Fig. 4.5. Variation of the total gain accumulated by the pump pulse due to the frequency value of the wavelength modulation (a) along the fiber for a triangular wavelength modulation with a frequency of 20 kHz and a peak frequency deviation of 125 MHz and (b) at the pulse input using the same wavelength modulation but varying the frequency of the modulation: 20 kHz (blue line), 40 kHz (red line), 80 kHz (green line) and 160kHz (black line). Simulation parameters are the same shown at the caption of Fig. 4.4.

Finally, notice that even if the DBA pump and the CW probe waves do not directly interact, the pump pulse amplification induced by the DBA is also appreciated in the Brillouin gain suffered by the probe wave as shown Fig. 4.6. This has been calculated using the theoretical model in Eqs. (4.2) assuming the preliminary simplifications previously discussed and generating the DBA depicted in Fig. 4.4(b).

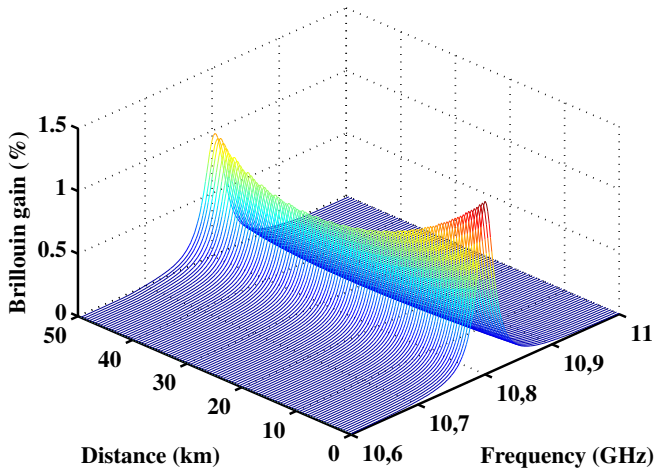

Fig. 4.6. Distribution of the Brillouin spectra using the DBA-assisted technique. Simulation parameter are the same shown at the caption of Fig. 4.4 and the probe power is 150μW.

4.3 Experimental setup

Figure 4.7 schematically depicts the assembled setup to demonstrate the potential of the technique. It is based on the conventional BOTDA sensor that derives the pump and probe waves from a single laser. However, the method is perfectly applicable to BOTDA schemes using other configurations, such as those based on using two separated lasers to generate pump and probe waves [40]. In this particular case, the pump pulse is obtained by using a semiconductor optical amplifier (SOA). Then, it is amplified using an EDFA and filtered to remove amplified spontaneous emission noise. The peak pulse power injected into the fiber was 22.4 dBm. In the probe branch, a Mach-Zehnder electro-optic modulator (MZ-EOM) was driven by a microwave synthesizer and biased at minimum transmission to generate a double-sideband suppressed carrier signal. This provides a double probe wave, which has been shown to greatly compensate non-local effects [19]. Each of these probe waves is launched into the fiber with a power of -8 dBm. Then, a polarization switch is used, as it is

customary in BOTDA setups, to eliminate the polarization-dependent response of Brillouin interaction. Before detecting the optical signal, the double probe wave was filtered out to operate in gain mode and the resulting component was pre-amplified by an EDFA. The deployed fiber was a 50-km spool of standard single mode fiber.

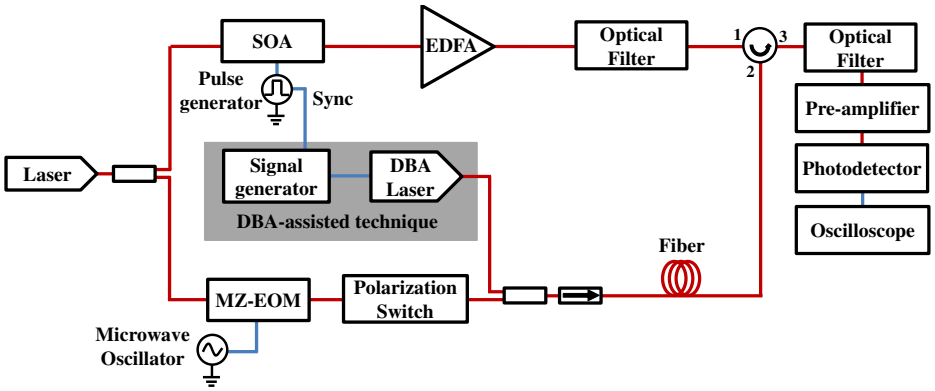

Fig. 4.7. Experimental setup for the DBA-assisted BOTDA sensor.

The only addition to upgrade the conventional BOTDA technique into a DBA-assisted BOTDA sensor is highlighted in Fig. 4.7. It requires the incorporation of an additional laser (DBA laser) whose output is coupled into the sensing fiber, and a signal generator to wavelength-modulate the DBA laser and synchronize the pump pulses. Note that the optical filter used to retain just one of the received probe sidebands, also filters out the remaining of the DBA laser power. The pump power for the DBA injected in the fiber was 4.7 mW. Moreover, the current of the DBA pump laser wavelength was modulated with a triangular electrical signal with a frequency of 80 KHz and an amplitude adjusted to obtain a peak optical frequency deviation of 125 MHz. Note that the latter value is large enough to accommodate short pulse durations of 10 ns and to avoid also any variation of the gain induced by the DBA to the pump pulses due to a frequency drift between the deployed lasers. The resultant wavelength modulation was not perfectly triangular, but was slightly deformed due to the characteristics of the laser chirp [101]. This could be improved employing well-known methods to linearize the chirp response [101], but this was not necessary for the experiments outlined here.

Figure 4.8 compares the distribution of the Brillouin gain spectra measured along the fiber using the conventional BOTDA technique, i.e. when the DBA is turned off, see Fig. 4.8(a), and when is turned on to become a DBA-assisted BOTDA, see Fig. 4.8(b). As it is shown in Fig. 4.8(a), the measured amplitude of the Brillouin spectra exponentially decays due to the progressive attenuation of the pump pulse as it propagates through the fiber. In contrast, when the DBA is on, the amplitude of the spectra initially decays but starts to recover by

mid-span. This is due to the gain generated by the DBA pump wave starting to kick-in. The latter is injected at the opposite end to the pump pulse input and the gain that it generates is proportional to its power. Therefore, the pump pulses find amplification where they need it most: at the final segment of the fiber where they have experienced more attenuation.

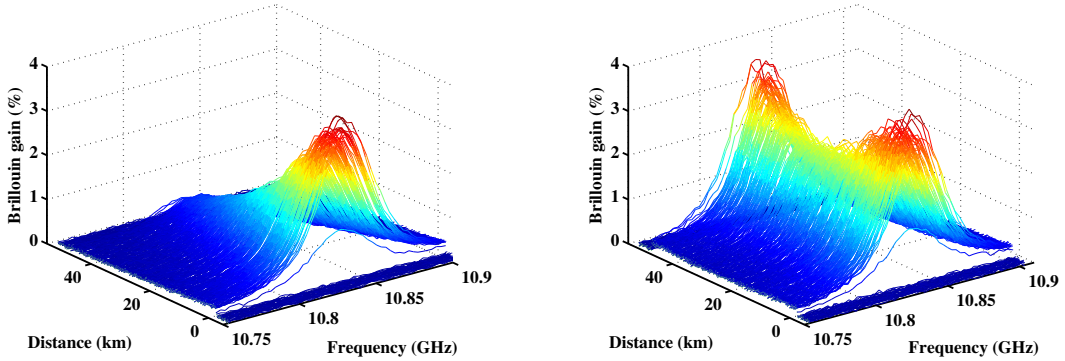

(a) (b)

Fig. 4.8. Measured distribution of the Brillouin spectra when the DBA is turned (a) off and (b) on for 55-ns pulses.

The net gain provided by the DBA can be simply determined by the pump pulse power at the end of the fiber, i.e. once it has interacted with the probe and the DBA pump waves. Note, that the double probe wave configuration allows to avoid the detrimental impact of non-local effects and, hence, the pump pulse power measured at the end of the fiber is only affected by the gain transferred by the DBA and the attenuation of the fiber. Figure 4.9 compares the pump pulse switching on and off the DBA pump for pulses of 40-ns and 55-ns. The difference between both measurements reflects a 9.2 dB increment of the pump pulse power using the DBA technique, enough to compensate the 50-km fiber attenuation. Note that the shape of the pump pulse, when the DBA is not active, is determined by the transient response of the SOA. However, when the DBA is on, the leading edge of the pulse is modified due to the grow caused by the excitation time of the acoustic wave. Note also in Fig. 4.9 that no significant temporal delay is observed between the pulses captured when the DBA is turned on or off (pulses were measured using an external trigger). However, it must be mentioned that higher DBA pump powers could induce not only amplification but a slow light effect onto the pump pulse, which would affect the spatial resolution of these systems [102].

However, this amplification of the pump pulse does not only occur at the final section of the fiber but during its time-flight. This effect is even more apparent in Fig. 4.10, where two BOTDA traces are compared in logarithmic scale. Therefore, using the conventional BOTDA technique, the detected Brillouin signal falls with a linear slope (in logarithmic units) given

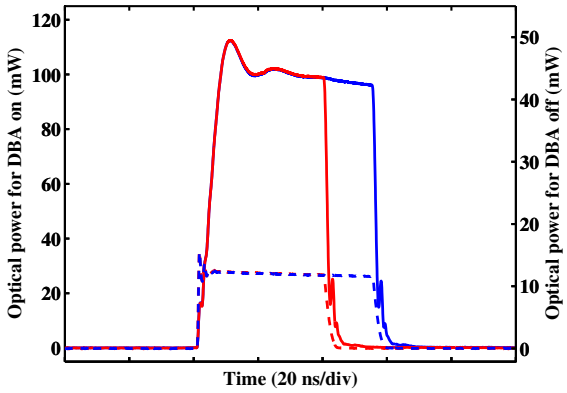

Fig. 4.9. Optical power of pump pulses at the output of the fiber. Two pulses of 40 ns (red) and 55 ns (blue) are depicted at the output of the fiber with the DBA turned off (dashed line, right vertical axis) and on (solid line, left vertical axis).

by the attenuation coefficient of the fiber (0.184 dB/km). As a consequence, the detected signal falls by 9.2 dB at 50-km. Considering that the detected SNR is proportional to the square of the detected amplitude, the SNR degradation at the end of the fiber, compared to the start, is double the value in decibels of the extra attenuation of the pulse, i.e., 18.4 dB. In contrast, using the DBA-technique, the worst attenuation of the detected signal is experienced for this particular scenario at the mid-span of the fiber. At that location, the experienced attenuation is 2.95 dB and hence, the maximum SNR degradation is 5.9 dB.

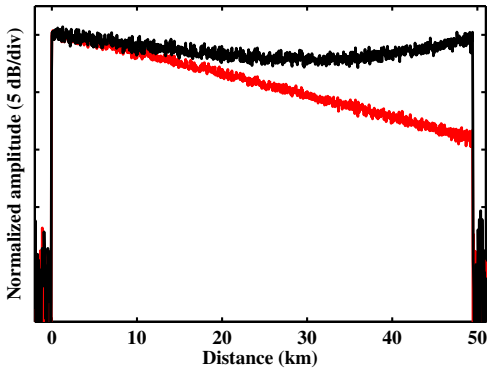

Fig. 4.10. Measured BOTDA traces when the DBA is switched off (red-dotted line) and on (black-solid line).

Nonetheless, the most significant improvement obtained with the presented technique is observed at the final section of the fiber, where the conventional BOTDA technique obtains the worst results. Figure 4.11(a) compares the measured Brillouin spectra at the first and

final sections of the fiber, using both techniques: the conventional in Fig. 4.11(a) and the DBA-assisted BOTDA in Fig. 4.11(b). With the DBA off, the measured amplitude at the last km gets into the noise floor and hence, the measurement of the BFS cannot be determined with accuracy. In contrast, using the presented technique, the measured Brillouin gain at the final section is similar in amplitude to that measured at the first km.

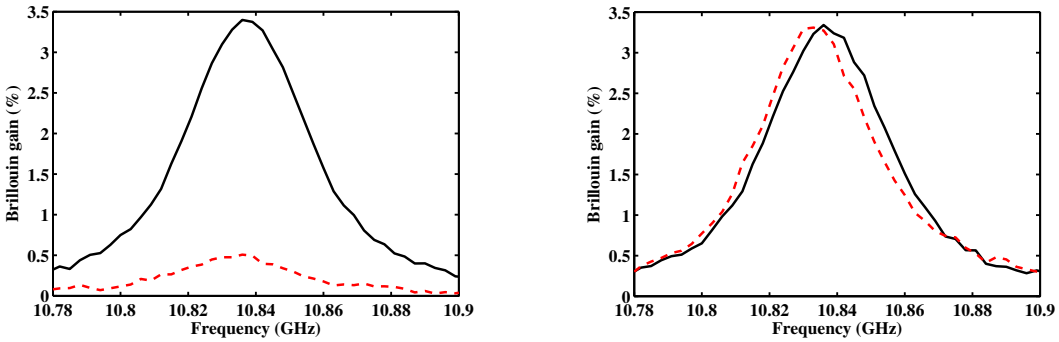

(a) (b)

Fig. 4.11. Measured Brillouin spectra at the first (black-solid line) and final (red-dashed line) section using (a) the conventional BOTDA technique and (b) the DBA-assisted technique.

Furthermore, if we compare the measured spectra at the first and last sections with the DBA on, it is clear that there is no noticeable degradation of the SNR between both measurements, as both have almost the same amplitude and noise level. This is confirmed in Fig. 4.12, where the evolution of the SNR was calculated for both the conventional and the DBA-assisted BOTDA. As shown in the figure, once the pump pulse is amplified by the DBA, the SNR grows, instead of linearly decaying along the fiber as it happens in the conventional system. Moreover, note that the measured SNR at the start of the fiber is identical turning on and off the DBA (both measurements were performed with the same averaging number (4096) to properly compare the results). As a consequence, it can be concluded that the use of the DBA does not lead to any significant SNR penalty.

Measurements of BFS for different duration pulses with the DBA turned on and off are displayed in Fig. 4.13(a). Note that, towards the end of the fiber, the BFS for the shorter pulses deviates from that measured with the conventional BOTDA. The shorter the pulse, the larger the deviation. This effect is attributed to the interplay between the temporal shape changes in the pulse brought by the distributed Brillouin amplification and the self-phase modulation effect. Stimulated Brillouin scattering is a dynamic phenomena that depends on the interaction of a pump and Stokes waves via an acoustic wave. The DBA pump is present at a certain location in the fiber and an acoustic wave is created and starts to grow

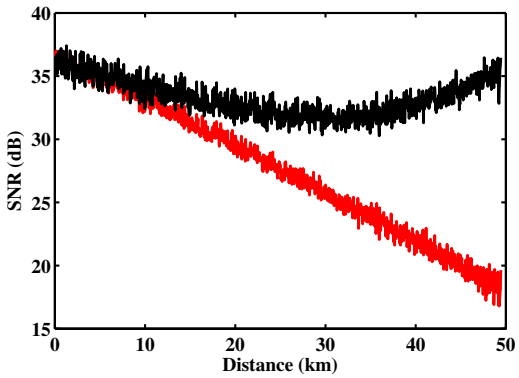

Fig. 4.12. SNR evolution for the DBA-assisted technique (black-solid line) and the conventional BOTDA sensor (red-dotted line).

exponentially when the pump pulse arrives, then it reaches an steady state (if the pulse is long enough) and, finally, the gain is abruptly cut-off as the pulse leaves [103]. This alters the shape of the pulse as it is amplified along the fiber and makes it asymmetrical in time. Then, SPM comes into play generating an optical phase modulation that has been shown to increase the Brillouin gain linewidth when using symmetric pulses with large rise-time [33]. In our case, with an asymmetrical pulse, SPM leads to a down-shift of the instantaneous frequency of the pulse that translates into an apparent up-shift of the measured BFS. This effect is more pronounced for shorter duration pulses because the change in shape of the pulse takes place during the acoustic wave growth, which is of the order of the acoustic phonon lifetime. Moreover, further evidence on the role of SPM was confirmed by repeating the measurements with a reduced pulse power and observing that, in this case, the BFS profile matches that of the conventional BOTDA.

We have devised a solution to compensate the BFS error due to SPM by deploying DPP measurements, i.e. substracting the BOTDA traces for pulses of different duration [35], which are longer than the acoustic phonon lifetime. This takes advantage of the fact that temporal asymmetry in the pulses due to the transient behavior of the Brillouin amplification takes place at the start of the pulses during the acoustic wave growth. Furthermore, for pulses longer than the acoustic phonon lifetime, the pulse reaches quasi-steady state Brillouin amplification. Therefore, DPP measurements with two long pulses are not affected by SPM-induced shift in optical frequency and error in BFS. This was confirmed by experimental measurements of the BFS profile for DPP (purple), which is superimposed to that of the conventional BOTDA in Fig. 4.13(b). In addition, the measured Brillouin spectra using DBA amplification for a 15-ns pulse duration and the differential Brillouin spectrum using DDP of pulses 40/55-ns

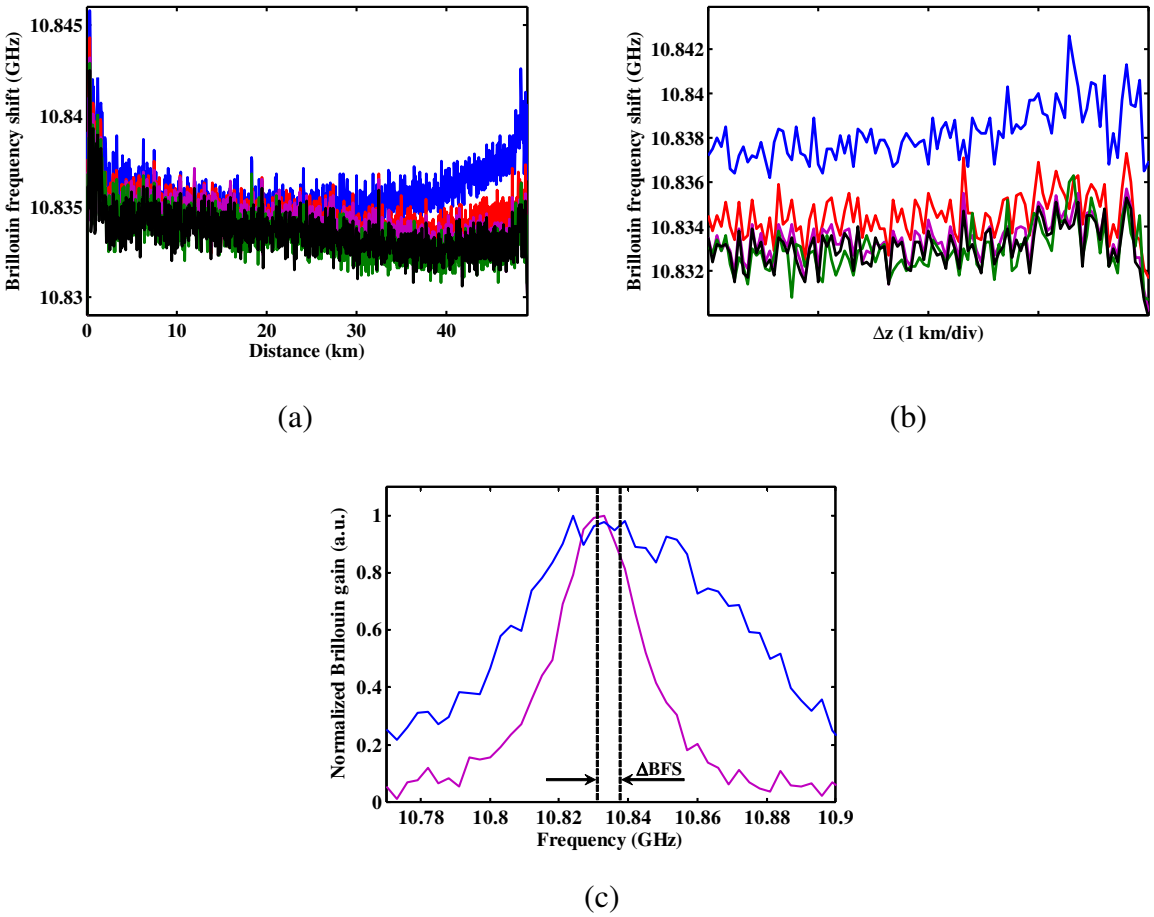

Fig. 4.13. BFS distribution measured (a) along the whole lenght of fiber and (b) at the last kilometers, using DBA for 15-ns (blue), 30-ns (red) and 40-ns (black) pulses and DPP of 40/55-ns (purple), and without DBA amplification for 40-ns pulses (green). Brillouin gain spectra (c) measured at the last kilometers using DBA for 15-ns (blue) and DPP of 40/55-ns (purple).

duration are shown in Fig. Fig. 4.13(c). Note that the frequency shift of the Brillouin peak is effectively corrected and no asymmetrical shape is observed at the differential Brillouin spectrum.

Finally, Fig. 4.14 compares the measured DPP gain spectra at the input and output of the fiber. As it was expected, the amplitude of both spectra is similar (no normalization is used in the figure) as fiber attenuation has been compensated by DBA. Furthermore, the noise in both measurements was also found to have the same standard deviation as the noise detected without DBA. Just to visually compare them, the detection noise without DBA is also shown in Fig. 4.14.

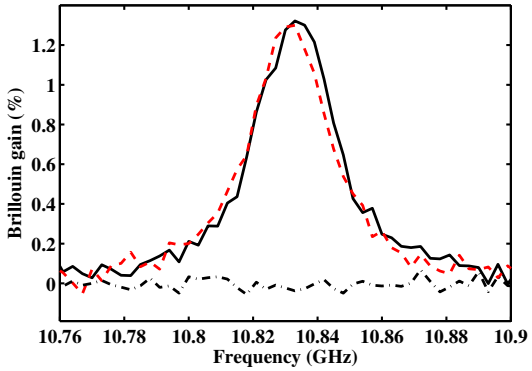

Fig. 4.14. Brillouin gain spectra at the input (solid-black line) and output (medium-dashed red line) of the fiber link, for the DBA-assisted BOTDA deploying DPP using 40-ns and 55-ns pulses. Detection noise (long-dashed black) without DBA.

4.4 Conclusions

During this chapter, distributed Brillouin amplification of the pump pulses in BOTDA sensors has been proven as a powerful tool to extend the measurement range of these sensors.

While in a conventional BOTDA sensor the maximum gain at a distant location is limited by the input pump pulse power, and hence by modulation instability, using a DBA the pulse wave can be powered up along its propagation reaching longer distances.

The generation of the DBA is done by wavelength-modulating an optical signal (DBA pump) that interacts with the pulse along the fiber. As shown during section 4.2, the determined parameters (frequency or peak frequency deviation) of the modulation as well as the kind of signal used to wavelength modulate the source are crucial to obtain a convenient DBA for BOTDA sensors. The main factors, that must be considered, are:

- The signal used for the wavelength modulation determines the spectral response of the DBA, which must be flat to properly amplify all the spectral components of the pulsed wave. A triangular modulation has been shown, previously at the literature, to accomplish this target.

- The peak frequency deviation determines the gain's bandwidth. This parameter must be higher than the spectrum of the optical signal to be amplified. For instance, using 10 ns pulse duration, the bandwidth must be higher than 100 MHz.

- The frequency or number of cycles of the DBA pump along the fiber determines the flatness of the gain experienced by the pulse wave at each location of the fiber. Low frequencies induce abrupt variations, while high frequencies generate smooth variations of the gain at each cycle of the wavelength modulation.

Furthermore, the use of a DBA does not add any significant noise to the measurement. This is a remarkable result, specially compared to the use of Raman distributed amplification, which has the drawback of adding significant noise to the measurements. This feature can be explained by taking into account that Brillouin distributed amplification, despite having a large noise figure, only amplifies the pulses that counter-propagate with the DBA pump, but it has no effect on the probe wave.

In addition, it has been experimentally shown that the variation of the temporal shape of the pump pulse due to distributed Brillouin amplification along with self-phase modulation brings a BFS deviation effect. This error at the measurement has been solved by using differential pulse-width pair technique, which removes the transient response generated by the growth of the acoustic wave at the leading edge of the pulsed signal.

Finally, the technique has been experimentally demonstrated in a 50-km fiber to provide full compensation of the attenuation of the fiber at the most distant location of the fiber.

Chapter 5

Sources of noise in BOTDA sensors

During the last years, remarkable progress has been done in the field of distributed Brillouin sensing, specially, in Brillouin optical time domain analyzers (BOTDA), where the spatial resolution has been improved from meters to centimeters scale and the monitoring distance extended from 30 km to 150 km using smart and advanced techniques. Nevertheless, the ultimate performance of the BOTDA technique based on double-sideband probe wave has hardly exceeded 50 km of monitoring range with 1-m resolution and a precision lower than 1 MHz, constituting an insurmountable barrier for this conventional sensor. Although this technique allows to inject a high optical probe power due to the tolerance to non-local effects of this configuration, the ultimate restriction is imposed by the signal-to-noise ratio (SNR) parameter, which can not be indefinitely improved by increasing the sensor's response, i.e. the detected signal. At this point, it is time to analyze the different noise sources existing in BOTDA sensors to find a way of ultimately improve their performance.

This chapter starts with a brief overview of the different parameters affecting the temperature or strain uncertainty, focusing on the signal-to-noise ratio parameter. In addition, the different noise sources existing in BOTDA sensors are theoretically and experimentally analyzed. Finally, the study gives some guidelines regarding the relevance of some noise sources depending on the monitoring range of the system.

This work was done in collaboration with the Group for Fibre Optics at the École Polytechnique Fédérale de Lausanne led by Prof. Luc Thévenaz.

5.1 Introduction

In Brillouin distributed time-domain sensing, the Brillouin spectra distribution is determined by measuring the probe power variation as a function of the distance for successive frequency detuning between probe and pump waves. Sorting the different measurements as a function

of the frequency detuning, the Brillouin spectrum at each location of the fiber can be reconstructed, as shown in Fig. 5.1. The peak of this resonance determines the Brillouin frequency shift (BFS), which is automatically estimated using a fitting procedure.

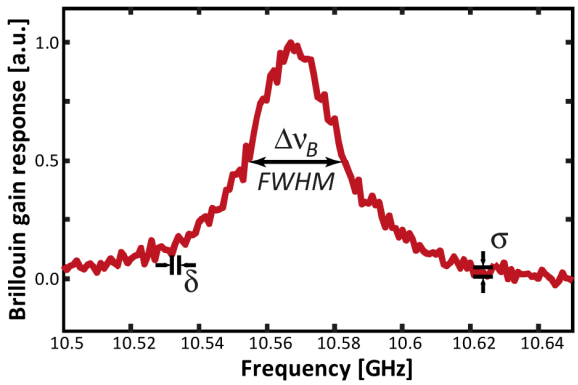

Fig. 5.1. Normalized Brillouin spectrum and decisive parameters for the BFS estimation error: (σ) is the noise in the signal, $(\Delta\nu_B)$ is the Brillouin linewidth and (δ) is the frequency step. ©2013 Optical Society of America [18].

The BFS estimation error using a least-square parabolic fitting is [18]:

$$\sigma_{BFS}(z) = \sqrt{\frac{1}{SNR(z)} \frac{3\delta\Delta\nu_B}{8\sqrt{2}(1-\zeta)^{3/2}}} \tag{5.1}$$

Note that $\sigma_{BFS}(z)$ depends on the features of the Brillouin spectrum shown in Fig. 5.1, i.e. the frequency step δ, the Brillouin linewidth $\Delta\nu_B$, the noise at the measured amplitude and consequently, the SNR at the local position z. Another parameter involved in the fitting procedure is the number of points, which is given by all the points above of a fraction of the peak level (ζ), e.g. $\zeta = 0.5$ means that the quadratic fitting is performed taking into account only the data points within the Brillouin linewidth [18].

It is worth noticing that Eq. (5.1) shows a strict proportionally relation between the frequency error and the SNR parameter, which becomes the key parameter that defines the ultimate performance of the system. This ratio is given by the squared sensor's response (see Eq. (4.1)) and the noise variance $\left(\sigma_{I_s}^2\right)$ at the system [45, 47]:

$$SNR(z) = \frac{\Delta I_s^2(z)}{\sigma_{I_s}^2} = \frac{R_D^2 \left(\frac{g_{SBS}(z)}{A_{eff}} P_{Pi} e^{-\alpha z} P_{Si} e^{-\alpha L} \Delta z\right)^2}{\sigma_T^2 + \sigma_s^2 + \sigma_I^2 + \sigma_{DRS}^2 + \sigma_{FBG}^2 + \sigma_{SBS}^2 + \sigma_{SpBS-Probe}^2} \tag{5.2}$$

where P_{Si} and P_{Pi} are the input probe and pump powers, respectively, R_D is the responsivity of the photoreceiver, L is the length of the fiber, A_{eff} is the effective area of the optical fiber, Δz

is the spatial resolution, $g_{SBS}(z)$ is the Brillouin spectrum at location, z and σ_T^2, σ_s^2, σ_I^2 are the variances of the thermal, shot noises and the relative intensity noise (RIN) of the laser source noise sources, respectively, which are defined here as the classical contributions of noise studied in BOTDA sensors [45]. The other components σ_{DRS}^2, σ_{FBG}^2, σ_{SBS}^2 and $\sigma_{SpBS-Probe}^2$ are the double Rayleigh scattering noise generated by the probe wave, the phase-to-intensity noise generated at the fiber Bragg grating (FBG), the phase-to-intensity noise conversion in stimulated Brillouin scattering (SBS) and the spontaneous Brillouin scattering-probe beating noise, respectively, that will be described along this chapter. Note that, when all the input optical powers are optimized to maximize the optical response, the only feasible way to improve the SNR is minimizing the noise signal, which is typically performed by increasing the number of averages that is directly related with the frequency error as:

$$\sigma_{BFS}^N = \frac{\sigma_{BFS}^1}{\sqrt{N_{AV}}} \tag{5.3}$$

where the indexes 1 and N represent the number of averages (N_{AV}) used to obtain σ_{BFS} . As shown in Fig. 5.2, the frequency error tends to zero when the number of averages is increased. However, the measurement time becomes impractically large, immediately discarding this option. A more elegant solution is to study the different noise sources and design innovative techniques to decrease their impact on the detected BOTDA signal.

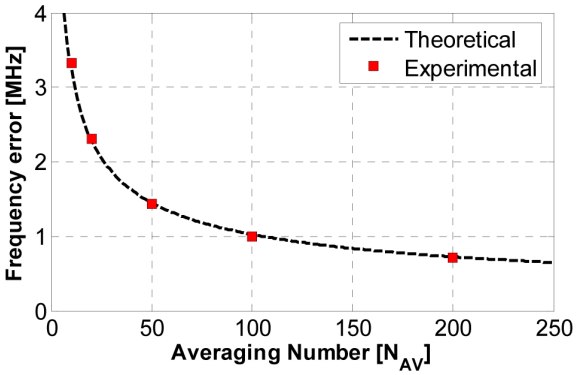

Fig. 5.2. Evolution of the estimated BFS error as a function of the number of averages. ©2013 Optical Society of America [18].

5.2 Classical noise sources

As mentioned previously, the classical noise sources being studied in BOTDA sensors are the thermal, shot noise sources and RIN coming from the laser source. These noise sources

have been thoroughly studied due to their importance in optical communications systems and hence, its influence on the performance of the system is well-known [2] and are already taken into consideration when modelling the SNR of the BOTDA systems [45, 47]. During this section, a description is given along with the influence of this noise sources and the different approaches deployed to reduce their detrimental effect on different BOTDA systems.

5.2.1 Thermal and shot noise

The thermal noise and shot noise are the two fundamental noise sources responsible for current fluctuations of the detected optical signal in all optical receivers. In response to a constant optical power applied to a photoreceiver, the generated current can be written as [2]:

$$I(t) = I_{rx} + i_T(t) + i_s(t) \tag{5.4}$$

where $I_{rx} = P_{rx}R_D$ is the average current being R_D the photoreceiver's responsivity and P_{rx} is the received optical power; $i_T(t)$ and $i_s(t)$ are the thermal and shot noises, respectively.

The thermal noise is caused by random thermal motion of electrons in a resistor, which manifest even in the absence of optical signal. Mathematically, thermal noise can be modelled as a stationary Gaussian random process with a spectral density that is frequency independent up to 1 THz and a constant value of $2k_BT/R_L$ being k_B the Boltzmann constant, T is the absolute temperature and R_L is the load resistor. The variance of the thermal noise can be obtained through the integration of the spectral density $S_T(f)$ in the receiver's bandwidth yielding [2]:

$$\sigma_T^2 = \int_{-\infty}^{+\infty} S_T(f)\,\mathrm{d}f = \frac{4k_BT}{R_L}\Delta f \tag{5.5}$$

where Δf is the effective noise bandwidth of the receiver, which is defined as the bandwidth of an ideal spectral response with same average noise power and amplitude than the receiver spectral response $(H_{rx}(f))$ [75]:

$$\Delta f = \frac{\int_0^{\infty} |H_{rx}(f)|^2 \mathrm{d}f}{|H_{rx}(f)|^2_{max}} \tag{5.6}$$

Note that the result obtained in Eq. (5.5) includes only the thermal noise generated in a load resistor. However, a receiver contains many other electrical devices, such as electrical amplifiers, that may add additional noise affecting in the experimental value measured at the photoreceiver.

Shot noise is a manifestation of the fact that an electric current consists of a stream of electrons that are generated at random times. Mathematically, shot noise is a stationary

random process with Poisson statistics, whose spectral density is a white noise with value qR_DP_{rx} being q the electron charge. As in the case of thermal noise, the variance of shot noise can be derived as [2].

$$\sigma_s^2 = \int_{-\infty}^{+\infty} S_s(f)\,\mathrm{d}f = 2qR_D P_{rx}\Delta f \tag{5.7}$$

Analyzing both equations (5.5) and (5.7), it can be clearly observed that both noise sources could only be reduced by modifying the receiver's circuitry or the bandwidth required to detect the optical signal. The latter depends on the spatial resolution of the technique, which is given by the temporal pulse width of the pulse activating the measuring process in classical time-domain techniques. Therefore, the detection stage must offer a sufficient bandwidth to resolve a point change over a distance given by the pulse width (T_P). A traditional relationship from signal theory fixes the minimum bandwidth necessary to resolve the pulse as $BW = 1.5/T_P$, so that a 1-m spatial resolution requires at least a 150 MHz bandwidth in the detection stage [80]. This bandwidth can be reduced by using optical sampling techniques, which demonstrated to be capable of decreasing the required bandwidth in BOTDA systems from 125 MHz to 100 kHz [80].

5.2.2 Relative intensity noise of the optical transmitter

The output of a semiconductor laser exhibits fluctuations in its intensity, phase, and frequency even when the laser is biased at a constant current with negligible current fluctuations. The two fundamental noise mechanisms are spontaneous emission and electron-hole recombination (shot noise). Noise in semiconductor lasers is dominated by spontaneous emission. Each spontaneously emitted photon adds to the coherent field (established by stimulated emission) a small field component whose phase is random, and thus perturbs both amplitude and phase in a random manner. Intensity fluctuations lead to a limited signal-to-noise ratio, whereas phase fluctuations lead to a finite spectral linewidth when semiconductor lasers are operated at a constant current [2].

In the context of intensity noise of a laser (power fluctuations), it is common to specify the power fluctuations as a random process given by:

$$P(t) = \bar{P}\left[1 + \frac{\Delta P}{\bar{P}}\right] \tag{5.8}$$

where $\bar{P}$ is the averaged power and ΔP represents the power fluctuations. The last term of Eq. (5.8) represents the relative intensity noise, which can be employed to calculate the

power fluctuations at the output of the receiver as:

$$\sigma_I^2 = R_D^2 \bar{P}^2 \mathrm{RIN} \Delta f \tag{5.9}$$

It is interesting to remark that the variance coming from any relative intensity noise has a quadratic dependence with the optical power unlike the shot contribution that has a linear dependence (see Eq. (5.7)). As a consequence, the influence of relative intensity noise may be more detrimental for high probe power and must be carefully studied.

Recently, a numerical study evaluated the impact on the system performance caused by the presence of relative intensity noise [47]. As depicted in Fig. 5.3, the maximum sensing distance achieved by the standard BOTDA technique could be considerably increased up to 100 km when reducing this kind of noise. Furthermore, considering that the BOTDA sensor based on double-sideband probe wave is limited to 50 km of sensing range with 1-meter resolution securing 1 MHz, then the detected signal should have a RIN level higher than -115 dB/Hz. Recalling that a standard RIN value for a current laser source is lower than -150 dB/Hz, there is a huge difference between the predicted value and the previous value, so that other noise sources must be present in the system.

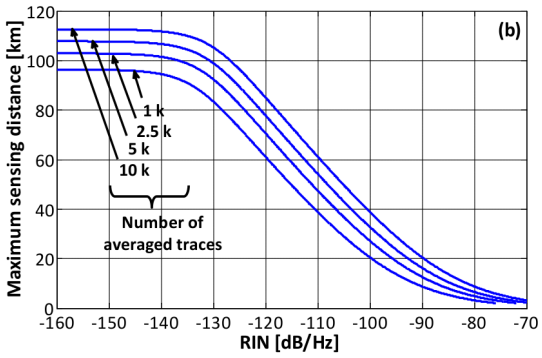

Fig. 5.3. Maximum sensing distance that secures 1 MHz with 1-m spatial resolution as a function of the averaging number and RIN. A certain value of shot and thermal noise is included [47].

In order to mitigate any common-mode noise in the probe signal path, such as laser intensity noise or modulator drifts, a balanced detection technique can be deployed in a BOTDA sensor [104]. As shown in Fig. 5.4, the presented technique is based on the BOTDA setup using double-sideband probe wave, in which both probe waves balance the Brillouin interaction experienced by the pulse pump. Instead of filtering one of the probe waves and detecting the optical probe signal, the technique filters both probe waves and they are introduced to the inputs of a balanced detector. As a consequence, the Brillouin gain and loss

are subtracted doubling the measurement amplitude as shown in Fig. 5.5(a). This increment in SNR is translated into a better determination of the BFS, as shown in Fig. 5.5(b).

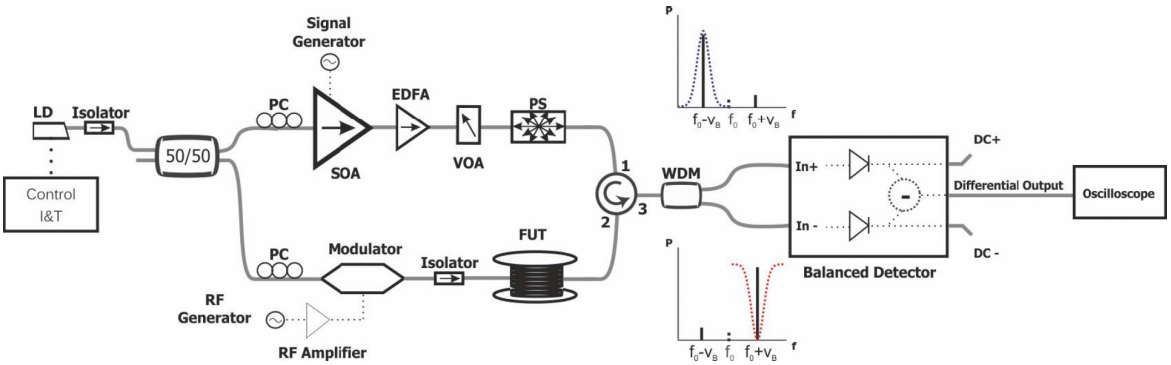

Fig. 5.4. Experimental BOTDA sensor using balanced detection system. LD: Laser Diode; PC: Polarization controller; EDFA: Erbium Doped Fiber Amplifier; RF: Radio-frequency generator; VOA: Variable Optical Attenuator; PS: Polarization Scrambler; WDM: Wavelength Division Multiplexer. ©2014, IEEE [104].

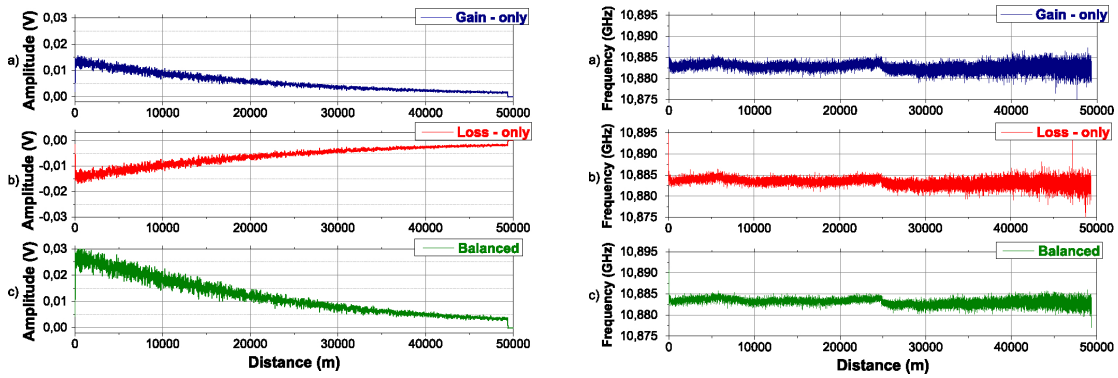

(a) (b)

Fig. 5.5. (a) Measured amplitude detecting the gain signal, loss signal and gain/loss signals in a balanced detector. (b) Brillouin frequency shift distribution for the different cases: gain, loss and balanced detection. ©2014, IEEE [104].

Another technique suffering from RIN is the Raman-assisted BOTDA sensor, which deploys distributed Raman amplification to achieve ~100 km sensing distances with sub-meter spatial resolution [42]. Although this technique differs from the standard sensor, it is worth mentioning how the technique presented below is capable of reduce RIN coming from Raman laser source [50]. As shown in Fig. 5.6(a), the noise power spectral density (PSD) considerably increases regarding the conventional technique when Raman amplification is turned on. Furthermore, the noise at the frequency operation of the standard technique (i.e.

from DC to 200 MHz) is ~15 dB larger than at frequencies higher than 500 MHz. This frequency dependence can be beneficial to reduce the noise intensity if the detected probe wave is moved to higher frequencies using a modulated probe wave, e.g. as the one shown in Fig. 5.6(b). As in the case of the standard technique, both probe waves interact with the pump pulse via stimulated Brillouin scattering, but once the optical signal is detected, a beating signal at frequency f_{RF} containing the Brillouin signal is detected at the output of the receiver. The value of f_{RF} is set to be higher than 500 MHz and hence, the noise at the system is reduced obtaining a better performance [50].

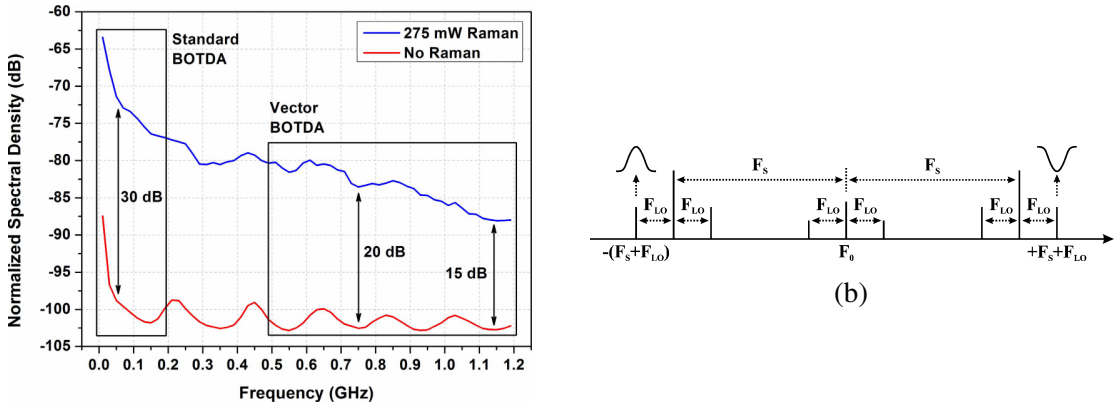

Fig. 5.6. (a) Noise power spectral density when Raman amplification is turned on (blue line) and off (red line). (b) Brillouin interaction between modulated probe wave and pump pulse. ©2014, IEEE [50].

As previously discussed, another way to reduce common-noises in the detected probe wave is to deploy a balanced detector. When Raman amplification is used in the standard

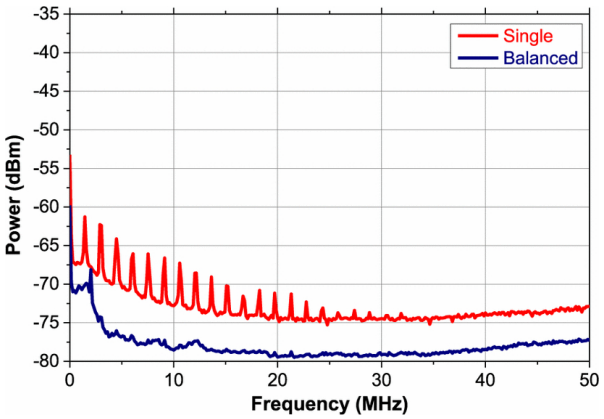

Fig. 5.7. Noise power spectral density using the standard technique with (blue line) and without (red line) balanced detection. ©2014, IEEE [49].

sensor, the RIN caused by Raman is transferred equally to both probe waves and hence, the RIN is subtracted reducing around 10 dB the amplitude of all the frequencies components of the PSD, as shown in Fig. 5.7 [49].

5.3 Additional noise sources in BOTDA sensors

This section focuses on the apparition of other noise sources, whose contribution may be greater (depending on the scenario) than the classical noise sources described in the previous section and had not been previously considered in the estimation of the SNR parameter of BOTDA sensors. Some of them are simply generated by the transmission of the optical signal through the fiber or filtering process, while others require the Brillouin interaction to show up.

5.3.1 Double Rayleigh scattering generated by the probe wave

In BOTDA sensors, the optical fiber is not only used as the sensing element, but also as a transmission medium to receive the probe signal back once it has interacted via SBS. This twofold nature makes possible that some noise sources existing in fiber optic transmission systems are also present in BOTDA sensors. Such is the case of double Rayleigh scattering (DRS), a fundamental noise source in optical communications systems [105, 106]. Double Rayleigh scattering corresponds to a multi-path interference of the doubly scattered signal with the original transmitted signal that converts signal phase noise into intensity noise [107]. In the case of BOTDA sensors, the probe wave propagates through the optical fiber undergoing Rayleigh scattering twice as shown in Fig. 5.8.

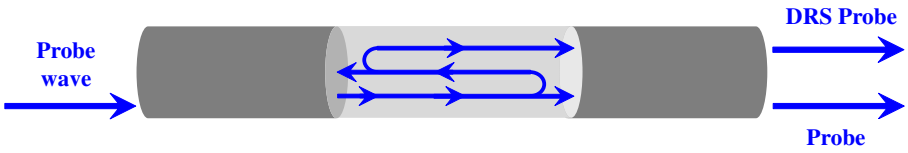

Fig. 5.8. Double Rayleigh scattering generated by the probe wave.

Due to the double reflection caused by Rayleigh scattering, another optical field (denominated here as DRS probe signal) co-propagates with the probe wave along the fiber. This DRS probe field can be expressed as a fraction of the transmitted probe field but delayed on time:

$$\Delta E_{DRS}(t,z_2,z_1,L) = E_S\left(t-2\frac{z_2-z_1}{v_g},L\right)\mathrm{e}^{(-\alpha/2+j\beta)2(z_2-z_1)}\,\Delta\rho_{DRS}(z_2)\,\Delta\rho_{DRS}(z_1) \quad (5.10)$$

where t is the temporal variable, L is the fiber's length, E_S is the complex amplitude of the probe field, υ_g is the velocity group, α is the attenuation coefficient, β is the propagation constant and $\Delta\rho_{DRS}$ is the fraction of the scattered field due to Rayleigh scattering at the local position z_1 and z_2.

By dividing the optical fiber into differential sections, then it is possible to define a Rayleigh backscattering coefficient [108]:

$$\rho_{DRS}(z) = \lim_{\Delta z \to 0} \frac{\Delta\rho_{DRS}(z)}{\Delta z} \tag{5.11}$$

Using Eq. (5.11), the total DRS probe field at the end of the fiber can be obtained by integrating Eq. (5.10):

$$E_{DRS}(t,L) = \int_0^L \int_0^{z_2} E_S\left(t - 2\frac{z_2 - z_1}{\upsilon}, L\right) \mathrm{e}^{(-\alpha/2 + j\beta)2(z_2 - z_1)} \rho_{DRS}(z_2)\, \rho_{DRS}(z_1)\, \mathrm{d}z_1 \mathrm{d}z_2 \tag{5.12}$$

Note that this equation calculates not only the DRS field coming from two reflections at z_1 and z_2 but the DRS field generated along all the optical fiber [107].

Finally, the probe field and the probe DRS field achieve the end of the fiber and are tipically directed to a FBG in order to filter out one of the probe sidebands, as shown in Fig. 5.13. Unfortunately, the probe DRS components propagate in the same band as the useful probe signal and thus, cannot be eliminated by filtering. Therefore, the total intensity at the output of the receiver can be expressed as:

$$\begin{aligned} I(t) &= [E_S(t,L) + E_{DRS}(t,L)]\,[E_S(t,L) + E_{DRS}(t,L)]^* \\ &= |E_S(t,L)|^2 + |E_{DRS}(t,L)|^2 + 2\mathbb{R}\left[E_S(t,L)\, E_{DRS}^*(t,L)\right] \end{aligned} \tag{5.13}$$

where * denotes complex conjugate and $\mathbb{R}$ is the real part. The first term in Eq. 5.13 is the detected probe wave, the second term is the DRS intensity and the third term is the intensity generated by the DRS probe signal beating with the probe wave. As the magnitude of the second term is negligible compared to the third term, then the DRS noise intensity is given by [107]:

$$I_{DRS}(t) = 2\mathbb{R}\left[E_S(t,L)\, E_{DRS}^*(t,L)\right] \tag{5.14}$$

Calculating the time-average autocorrelation function of the DRS noise intensity and applying the Fourier transform, it is possible to find the DRS noise power spectral density [107, 109]:

$$P_{DRS}(f) = \frac{10}{9} R_{Rb}^2 \left(2\alpha L + \mathrm{e}^{-2\alpha L} - 1\right) \mathscr{F}\langle |R_{E_S}(\tau)|^2 \rangle \tag{5.15}$$

where the constant takes into account the fiber birefringence, R_{Rb} is the Rayleigh backscattering coefficient, $\mathscr{F}$ denotes Fourier transform and $\langle |R_{E_P}(\tau)|^2 \rangle$ is the magnitude square of the autocorrelation function of the probe field. Note that the DRS noise power spectral density is simply related to the autocorrelation function of the transmitted probe field, which is generated using an unmodulated optical source. For this particular case, the DRS noise spectrum assumes the original line shape of the optical source with a spectral width that is double that of the laser [105]. Assuming that the line shape of the optical source has a Lorentzian profile, then the variance of double Rayleigh scattering generated by the probe wave can be expressed as:

$$\sigma_{DRS}^2 = 3\frac{10}{9}R_{Rb}^2\left(2\alpha L + \mathrm{e}^{-2\alpha L} - 1\right)R_D^2 P_S^2 \tag{5.16}$$

5.3.2 Phase-to-intensity noise conversion in FBG

Conventional BOTDA sensors use narrowband fiber Bragg gratings to select the probe signal to be detected. Unfortunately, the reflection band of FBGs is temperature dependent, and therefore, it can likely shift during operating conditions. If the probe signal is tuned at the top of a flat FBG, there should be no significant noise added to the probe. However, when the probe optical frequency lies on the slope of the FBG, the laser phase noise is converted into intensity noise as depicted in Fig. 5.9. The amplitude of this noise depends directly on

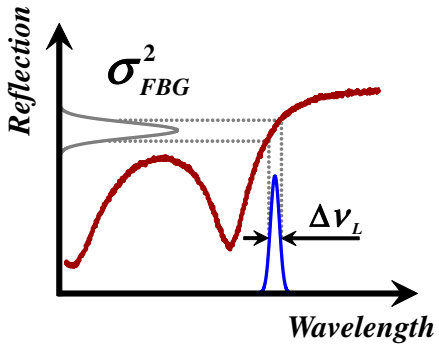

Fig. 5.9. Laser phase noise converted into intensity noise due to the spectral shape of the FBG.

the linewidth of the laser source and the spectral shape of the FBG as [110]:

$$\sigma_{FBG}^2(\lambda) = \left(\frac{\mathrm{d}R(\lambda)}{\mathrm{d}\lambda}\Delta\nu_{LS}\right)R_D^2 P_{ref}^2 \tag{5.17}$$

where $R(\lambda)$ is the reflectivity FBG spectrum, $\Delta\nu_{LS}$ is the linewidth of the laser source and P_{ref} is the reflected optical power.

5.3.3 Phase to intensity noise conversion in SBS process

The sources of noise presented so far consider only the propagation of the probe along the system. Nevertheless, when pump pulses travel in the fiber, other new sources of noise appear in the detected BOTDA trace. One of them could be the Rayleigh scattering originated by the pump. However, this can be easily eliminated using suitable optical filtering. In addition, the pump RIN can be generally neglected owing to the low cut-off frequency of the pump-probe RIN transfer in the SBS process [111]. More important are: i) the noise generated by phase-to-intensity noise conversion in the SBS process, and ii) the noise resulting from the pump-induced spontaneous Brillouin scattering (SpBS) beating with the probe at the receiver.

Recently, it has been numerically and experimentally demonstrated that insufficient coherence of the laser sources used in stimulated Brillouin amplification setups not only leads to a reduce gain but also to fluctuations of the gain [112]. Fig. 5.10 depicts the probability function distribution of the signal output power for (a) probe wave with phase noise and (b) pump wave with phase noise for 3 different linewidths. As it is shown, the presence of phase noise on either input wave reduces the average Brillouin gain and makes the signal output power noisy. However, both cases differ in several aspects, while the mean gain penalty is larger for phase noise pump, the fluctuations are greater for phase noise probe [112]. This study was done for counter-propagating continuous waves (CW), where the acoustic wave is permanently excited experiencing the variations generated by the laser phase noise. Along this section, the influence of phase laser noise is analyzed specifically for the BOTDA sensors, where a pulse wave meets a CW signal.

In standard BOTDA schemes, a pulsed pump and a probe wave interfere through electrostriction generating an acoustic wave, which transfers energy from the pulse to the probe signal or vice versa. The acoustic decay time of approximately 6 ns makes the Brillouin effect a narrowband process, demanding optical sources with linewidths much narrower than the Brillouin bandwidth (~30 MHz) [6]. Recalling that the linewidth of a laser $(\Delta\nu_{LS})$, as well as its coherence time $(\tau_c = 1/(\pi\Delta\nu_{LS}))$, are statistical average measures related to the noisy character of laser phase, then insufficient coherence may not only lead to reduced energy transfer in the SBS process but also to fluctuations of the gain/loss of the probe signal. These fluctuations induce intensity noise in the detected signal caused by the laser phase noise and hence, it detrimentally affects the system performance [112].

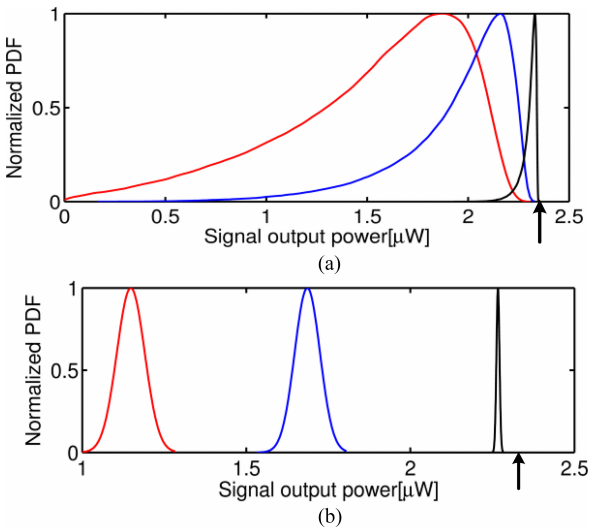

Fig. 5.10. Probability distribution function of the signal output power for (a) phase noise probe and (b) phase noise pump using a linewidth of 318 kHz (black line), 3.18 MHz (blue line) and 7.95 MHz (red line). The upward arrows point to the value of the signal output power in the absence of phase noise. ©2015, IEEE [112].

Generally, the lasers deployed in BOTDA sensors have a linewidth of ~1 MHz or even less. It gives rise to a coherence time of ~318 ns or even higher, which is much larger than the activation time of the acoustic wave generated by the pump pulses (tipically from 10 ns to 50 ns). As a consequence, the influence of phase noise laser is negligible during the short activation time of the acoustic wave.

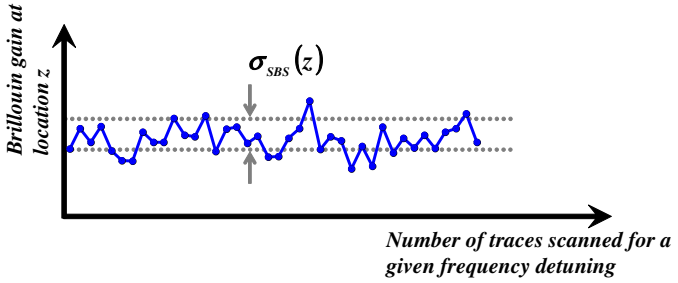

Fig. 5.11. Variation of the detected Brillouin signal at a given position due to laser phase noise.

However, a large number of traces is typically averaged to increase the SNR of the measurements. During the acquisition of the different traces, the relative phase difference between pulse and probe varies at a certain location of the fiber due to laser phase noise. This can be interpreted as a variation of the instantaneous frequency difference between pulse and

probe wave. Consequently, the Brillouin gain/loss of the probe signal fluctuates at a given fiber position for each trace acquisition, as shown in Fig. 5.11. Assuming that the sensor response is relatively smooth around the mean value of the frequency detuning between probe and pump waves, the variance of the sensor response can be expressed as [113]:

$$\sigma^2_{\Delta P_S} = \sigma^2_{\Delta\nu}\left(\left.\frac{\mathrm{d}\Delta P_S}{\mathrm{d}\Delta\nu}\right|_{\overline{\Delta\nu}}\right)^2 \tag{5.18}$$

where $\sigma^2_{\Delta\nu}$ is the variance of the frequency detuning $\Delta\nu$ between probe and pump waves and $\overline{\Delta\nu}$ denotes the mean value of the frequency detuning. Note that both signals, the pump and probe waves, are typically generated through the same laser source and hence, experience the same laser phase noise. Consequently, the variance of the frequency detuning can be expressed as:

$$\sigma^2_{\Delta\nu} = \sigma^2_{\nu_P} + \sigma^2_{\nu_S} - 2\mathrm{Cov}(\nu_P, \nu_S) = 2\Delta\nu^2_{LS} \tag{5.19}$$

where σ_{ν_P} and σ_{ν_S} are the instantaneous frequency deviation of pump and probe signal, respectively and $\Delta\nu_{LS}$ is the linewidth of the laser source. Note that in Eq. (5.19), it has been assumed that probe and pump are uncorrelated, which is true for sensing fibers equal to, or larger than twice the coherence length of the fiber [114, 115].

Using Eq. (5.18) and Eq. (5.19), the standard deviation of the gain or loss fluctuations caused by phase-to-intensity noise conversion in SBS process can be expressed as:

$$\sigma^2_{SBS}(z) = R^2_D \frac{\sigma^2_{\Delta P_S}}{P^2_{Si}\,\mathrm{e}^{-2\alpha L}} = 2\Delta\nu^2_{LS} R^2_D \left(P_{Pi}\,\mathrm{e}^{-\alpha z}\,\Delta z\,\frac{\mathrm{d}g_{SBS}(\Delta\nu)}{\mathrm{d}\Delta\nu}\right)^2 \tag{5.20}$$

where P_{Si} and P_{Pi} are the input power of probe and pump waves, respectively, α is the fiber's attenuation, L is the fiber's length, Δz is the spatial resolution and $g_{SBS}(\Delta\nu)$ is the Brillouin spectrum at a given pump-probe detuning $\Delta\nu$ and R_D is the responsivity of the photoreceiver that converts the fluctuations of the optical power into intensity variations.

5.3.4 Spontaneous Brillouin scattering-probe beating noise

As shown in Fig. 5.12, when the pump pulse propagates in the fiber, spontaneous Brillouin scattering is generated at a frequency that depends on the local Brillouin frequency shift of each fiber's location. Since the FBG is tuned to select the probe signal, which scans the Brillouin spectrum, then the SpBS components are also in the reflection band of the FBG.

Consequently, the total optical field reaching the photoreceiver can be expressed as:

$$E(t) = E_S\,\mathrm{e}^{(2\pi\nu_S t+\phi_S)} + E_{SpBS}\,\mathrm{e}^{\left(2\pi(\nu_P-\nu_B)t+\phi_{SpBS}\right)} \tag{5.21}$$

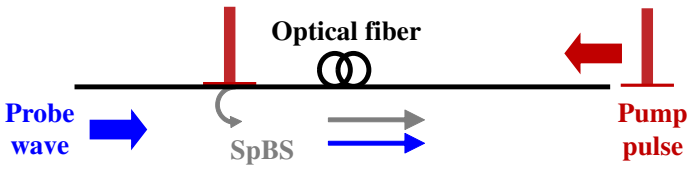

Fig. 5.12. Spontaneous Brillouin scattering components generated by the pump pulse and co-propagating with the probe wave.

where E_S and E_{SpBS} are the amplitude of the probe wave and SpBS components, respectively, ν_S and ν_P are the optical frequency of probe and pump waves, ϕ_S and ϕ_{SpBS} are the phases of the probe wave and SpBS and ν_B is Brillouin frequency shift of the fiber.

At the output of the photoreceiver, the total intensity is given by the detected probe wave, the noise intensity coming from SpBS components and a noise intensity, much higher than the previous one, generated by SpBS beating with the probe wave, which can be written as:

$$I(t)\big|_{SpBS-Probe} = 2E_S E_{SpBS}\cos(2\pi\Delta\nu t + \Delta\Phi) \tag{5.22}$$

where $\Delta\nu = \Delta\nu_P - \Delta\nu_S + \nu_B(z)$ is the frequency detuning between probe and the peak frequency of the Brillouin spectrum at a certain location z and $\Delta\Phi$ is the phase difference between probe and SpBS, which is a random variable with uniform distribution between $-\pi$ and π. This is a stationary random process, whose autocorrelation function is [75]:

$$R(\tau) = 2P_S P_{SpBS}\cos(2\pi\Delta\nu\tau) \tag{5.23}$$

where P_S is the probe power at the receiver and P_{SpBS} is the SpBS power, which is given by [1]:

$$P_{SpBS} = \frac{1}{2}S\alpha_B P_P \Delta z \tag{5.24}$$

where S is the backscatter capture fraction, α_B is the Brillouin scattering coefficient, P_P is the peak pump power and Δz is the spatial resolution.

As the expression shown in Eq. (5.22) is a random process with zero mean, the variance of the SpBS-probe beating noise can be calculated as:

$$\sigma^2_{SpBS-Probe} = R(0) = R_D^2 P_S P_P S\alpha_B \Delta_z \tag{5.25}$$

5.4 Specific SNR parameter for BOTDA sensors

Once the different noise sources existing in a BOTDA sensor have been considered and theoretically calculated, then it is possible to update Eq. (5.2) to provide a more complete SNR parameter, yielding:

$$SNR(z) = \frac{\Delta I_s^2(z)}{\sigma_{I_s}^2} = \frac{R_D^2 \left(\frac{g_B(z)}{A_{eff}} P_{pump,i} \mathrm{e}^{-\alpha z} P_{probe,i} \mathrm{e}^{-\alpha L} \Delta z \right)^2}{\sigma_T^2 + \sigma_s^2 + \sigma_I^2 + \sigma_{DRS}^2 + \sigma_{FBG}^2 + \sigma_{SBS}^2 + \sigma_{SpBS-Probe}^2} \tag{5.26}$$

being each contribution of the denominator:

$$\sigma_T^2 = \frac{4k_B T}{R_L} \Delta f \tag{5.27}$$

$$\sigma_s^2 = 2qR_D P_S \Delta f \tag{5.28}$$

$$\sigma_I^2 = R_D^2 P_S^2 \mathrm{RIN} \Delta f \tag{5.29}$$

$$\sigma_{DRS}^2 = 3\frac{10}{9} R_{Rb}^2 \left(2\alpha L + \mathrm{e}^{-2\alpha L} - 1 \right) R_D^2 P_S^2 \tag{5.30}$$

$$\sigma_{FBG}^2 = \left(\frac{\mathrm{d}R(\lambda)}{\mathrm{d}\lambda} \Delta \nu_{LS} \right) R_D^2 P_S^2 \tag{5.31}$$

$$\sigma_{SBS}^2 = 2\Delta \nu_{LS}^2 R_D^2 \left(P_{Pi} \mathrm{e}^{-\alpha z} P_{Si} \mathrm{e}^{-\alpha L} \Delta z \frac{\mathrm{d}g_B(\Delta \nu)}{\mathrm{d}\Delta \nu} \right)^2 \tag{5.32}$$

$$\sigma_{SpBS-Probe}^2 = R_D^2 P_S P_P S \alpha_B \Delta_z \tag{5.33}$$

Note that the final expression only depends on the probe and pump power injected into the fiber, the sensing distance and characteristics of the deployed components to assemble the BOTDA sensor.

5.5 Experimental setup for the study of noise sources

Many possible BOTDA configurations exist in the literature [67, 116]. Although the working principle is pretty similar between them, the BOTDA sensor based on double-probe wave is one of the most representative sensors that the scientific community has used to develop other more advanced techniques [42, 117–119]. In addition to its simplicity and good performance, the balanced Brillouin interaction taking place between both sidebands and pulse reduces the pump depletion allowing to inject higher probe power than other configurations based on a single Brillouin interaction at the fiber [19, 24]. As a consequence, the probe power reaching

the receiver is high enough to have a good SNR at the measurements. For these reasons, this sensor was selected to study the different noise sources. Nevertheless, the information gathered in this chapter should be perfectly applicable for any kind of BOTDA sensor.

As it is shown in Fig. 5.13, this sensor deploys a laser source, whose output is divided into two branches using an optical coupler. In the upper branch, the light is pulsed using a semiconductor optical amplifier (SOA) and then, the peak power is boosted using an erbium doped fiber amplifier (EDFA) to stimulate the Brillouin scattering effect in the fiber. In the lower branch, a tunable-frequency probe is generated using the modulation sidebands obtained by driving a Mach-Zehnder electro-optic modulator (MZ-EOM) with the signal from a microwave generator that outputs frequencies close to the Brillouin frequency shift of the sensing fiber. During the probe wave propagation, it interacts with the pump pulse experiencing locally a gain or loss (depending on the configuration of the sensor) that can be analyzed by recording the probe power in the time domain by using a direct detection of the optical field at the photoreceiver. The choice of the configuration of the sensor is simply made by selecting the upper frequency sideband (loss configuration) or the lower sideband (gain configuration) with an optical filter.

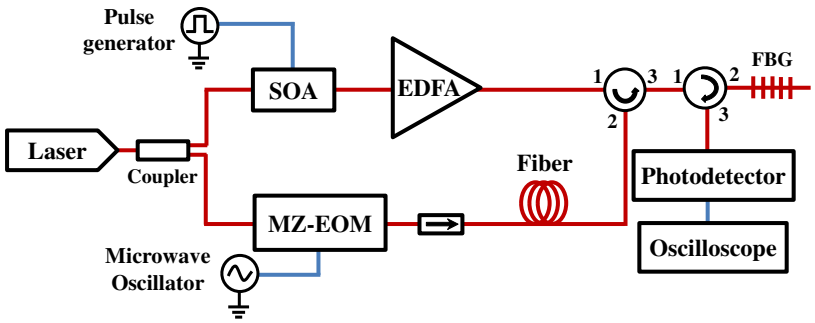

Fig. 5.13. Experimental setup assembled for the noise sources study.

For this study, a 125 MHz photoreceiver with a high trans-impedance amplifier was used to have a representative condition and an optimized SNR. Furthermore, the impact of the laser phase noise was analyzed using two lasers: a distributed feedback (DFB) laser of 1.6 MHz linewidth and an external cavity (EC) laser of 20 kHz linewidth. Finally, the effect introduced by the fiber's length was also studied, which was varied from a few meters up to several tens of km.

5.5.1 Experimental measurements

In order to provide a better understanding of the kind of noise sources existing in BOTDA sensors, the accumulated noise along the probe path was measured at the different points

labeled as A-D in Fig. 5.14, with no pump pulse propagating in the fiber. This was accomplished by using an electrical spectrum analyzer (ESA) connected to a 125-MHz photodetector, whose input power was set to -18 dBm for each measurement, ensuring a known shot noise level.

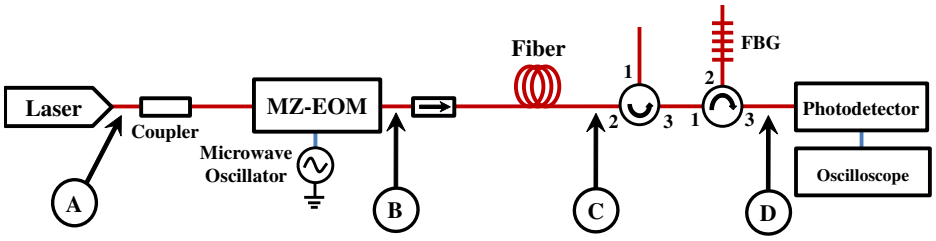

Fig. 5.14. Noise sources located along the probe wave propagation.

Fig. 5.15 shows the electrical power spectral density at the different points of the setup. The black curve is the thermal noise of the detector (equivalent to a noise amplitude σ_{th} = 890 μV). The green curve is the PSD measured when detecting the laser output, i.e. at point A in Fig 5.14. As it will be described below, it was verified that this spectrum corresponds mainly to the shot noise contribution (σ_s= 464.4 μV) added to the thermal noise, and the laser RIN (< 150 dB/Hz) has no observable effect on the measurements. To evaluate the noise introduced by the generation of the double-sideband probe, the PSD at the EOM output has been measured (point B in Fig. 5.14). Results indicate that the PSD at point B is the

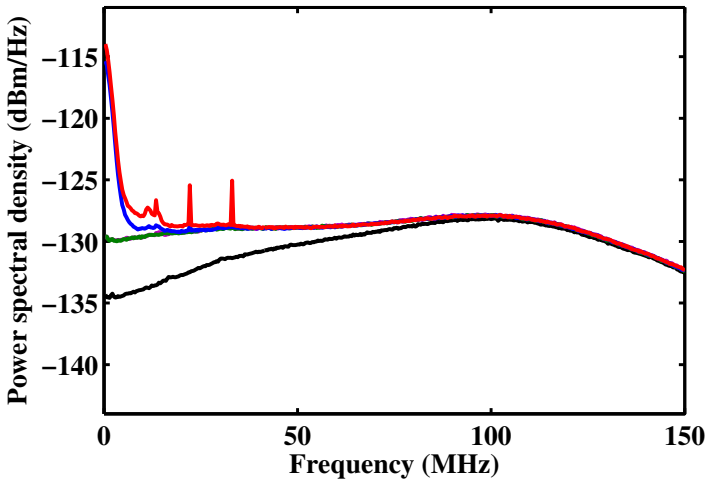

Fig. 5.15. PSD measured at different points in the system. Black and green curves are the thermal and shot noise of the detector; blue and red curves are the PSD after the fiber and after the FBG.

same as the one at point A, proving that no significant noise is added by the modulation. Then, the noise PSD measured at the sensing fiber output (point C) shows that low frequency components increase significantly (blue curve) and its amplitude varies with the fiber's length. As it was explained before in section 5.3.1, this is due to phase-to-intensity noise conversion due to double Rayleigh scattering of the probe. Finally, the red curve shows the noise PSD at point D, which includes the phase-to-intensity noise conversion taking place in the FBG located before the receiver. Note that a peak at 33 MHz is shown in some curves, but this is related to a component introduced by the laser driver, and has no relevance for the study.

Characterization of shot noise and RIN from the laser source

In order to experimentally calculate the shot noise amplitude, the output of the laser source was connected using an optical attenuator to the 125-MHz photoreceiver. Then, the optical power injected into the receiver was increased, while the variance was measured at the oscilloscope. As shown in Fig. 5.16, the variance of this noise starts to linearly increase with the detected optical power around the CW saturation power of the receiver (~-16 dBm). Referring to Eq. (5.7), this linear dependence is the clearest evidence to identify this noise as shot noise and not relative intensity noise of the laser source, which has a quadratic dependence with the detected power (see Eq. (5.9)). As a consequence, the influence of RIN caused by the laser source, which is characterized as <150dB/Hz in the data sheet, results negligible when it is compared to the thermal or shot noises.

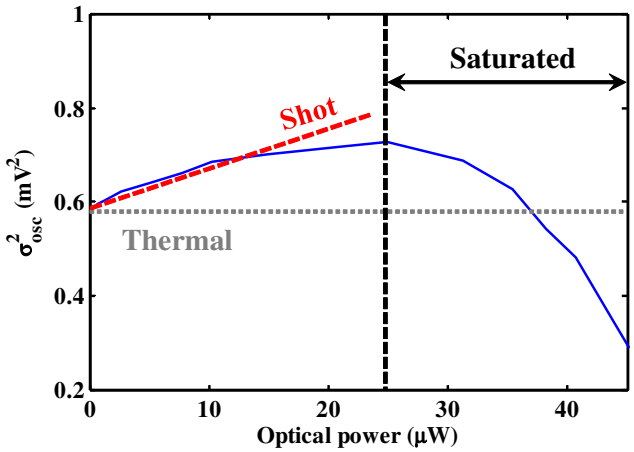

Fig. 5.16. Measured variance at the oscilloscope varying the optical power injected into the receiver.

Validation of double Rayleigh scattering generated by the probe wave

In order to demonstrate that the noise induced in the fiber (shown previously in Fig. 5.15) is caused by DRS probe components beating with the probe signal, the measured DRS noise PSDs were compared with the respective theoretical PSD obtained by Eq. (5.15), for standard single-mode fibers of different lengths. As shown in Fig. 5.17, theoretical and experimental curves, both obtained with a DFB laser, show a good agreement, demonstrating that the noise induced in the fiber is essentially due to probe DRS. Furthermore, as it was mentioned previously, the shape of the experimental DRS noise spectrum adopt the line shape of the laser source, which was previously determined (see the appendix A) to provide a better accuracy between the experimental results and the theoretical model.

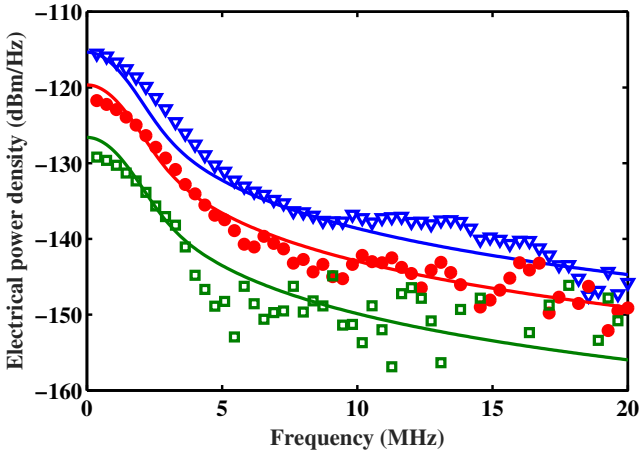

Fig. 5.17. Numerical (symbols) and experimental (solid line) spectral power density of the DRS probe wave for a 10-km (green), 25-km (red) and 50-km (blue) fiber lengths using a DFB laser.

In contrast to other fiber non-linearities, the DRS power does not depend on the fiber effective length, but grows linearly with distance. This behavior actually makes the DRS-induced noise to be very important in long-range BOTDA sensing, becoming one of the dominating sources of noise. This is especially critical in sensors that use a leading fiber to propagate the probe to a remote location, since this signal has to propagate along a fiber two-fold longer than the actual sensing fiber [120].

Finally, in order to analyze the effects of the laser phase noise, the DRS-induced noise measured after a 25-km long fiber with a DFB laser and an EC laser (having the same power) are compared in Fig. 5.18. Although the PSD narrows for the EC laser, the spectral components within the laser linewidth become stronger, leading to the same total noise amplitude: σ_{DRS} =247.2 μV for the DFB laser and σ_{DRS} =249.2 μV for the EC laser.

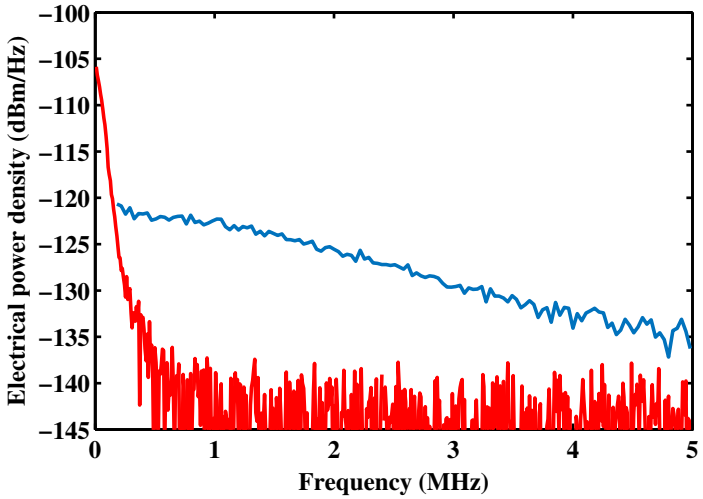

Fig. 5.18. Spectral power density of the probe DRS and its effect of the laser linewidth (1.6 MHz vs 20 kHz, blue and red lines, respectively).

Phase-to-intensity noise in the FBG as a function of the wavelength

The experimental results obtained for the phase-to-intensity noise conversion in the FBG were obtained by connecting the laser source to the receiver using a FBG in reflection. Then, the standard deviation of the photodetector voltage was measured as a function of wavelength within the FBG reflection band. While Fig. 5.19 (a) depicts the spectrum of the top region of the FBG reflection, Fig. 5.19 (b) shows the FBG-induced noise amplitude. It can be seen that

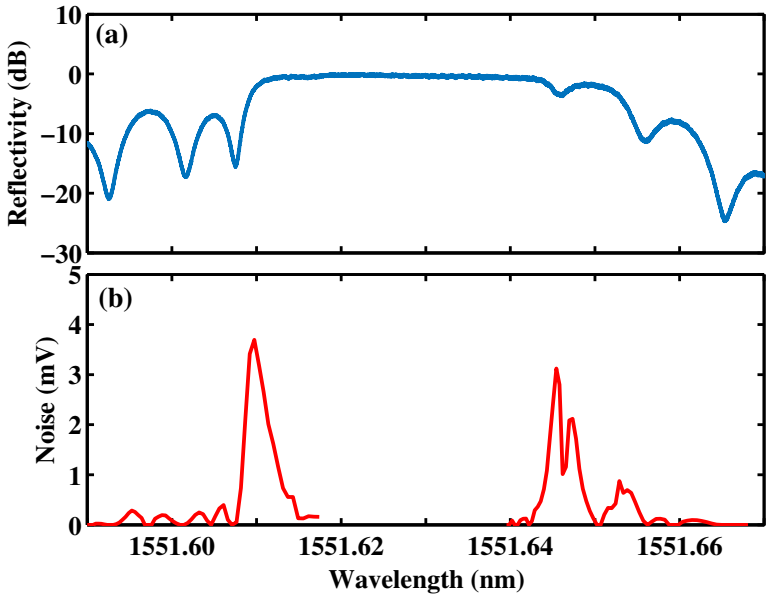

Fig. 5.19. Measured (a) FBG reflectivity and (b) FBG-induced noise amplitude.

this noise increases in the slopes of the FBG reflection spectrum (up to $\sigma_{FBG} = 3.5\ mV$ in this case[1]). However, in a well-tuned condition the FBG-induced noise should be expected to be lower than the other noise levels reported in this chapter.

Characterization of phase-to-intensity noise in SBS process

The measurement of this noise source requires to counter-propagate the pump and probe waves to stimulate the Brillouin scattering effect. The amount of energy transfer produced by this interaction depends on the relative polarization state between both waves and hence, it can change during the measurement time. Note also that this variations on the detected signal induced by polarization fluctuations in a standard SMF highly depends on the polarization diversity method (polarization scrambler, switch...) and can be simply minimized by a proper control of the input pump and probe polarization states. In order to obtain a reliable characterization of this noise source, and to fully mitigate the effect of polarization fluctuations inside the sensing fiber, a 90 m-long polarization-maintaining fiber has been used for the measurements shown in this section.

Fig. 5.20(a) compares the measured noise as a function of the frequency detuning using a DFB laser and the theoretical noise amplitude obtained by Eq. (5.20), for pulses of 10 ns and 70 ns (for a fair comparison, the pump power has been adjusted to have the same Brillouin gain in the two cases). Note that, at the Brillouin peak frequency (zero detuning), a minimum noise level is induced due to the zero gradient of the Brillouin spectrum. However, a maximum phase-to-intensity conversion occurs at the BGS full-width half-maximum (100 MHz and 35 MHz for the 10 ns and 70 ns pulse, respectively), where the BGS slope is maximum. Note that this effect has major implications for the dynamic-BOTDA sensors based on the slope-assisted technique [51], as the frequency of the probe wave is tuned into the skirt of the detected Brillouin spectrum, where the influence of phase-to-intensity noise conversion due to SBS process reaches its maximum value.

Furthermore, it is worth noticing that the minimum noise amplitude matches the level measured with the EC laser (black dashed line). Due to the reduced linewidth of the EC laser, the SBS-induced phase-to-intensity noise conversion is negligible; and therefore the noise level shown in the figure corresponds the SpBS beating with the probe at the receiver, as it will be described in the next section.

Finally, Fig. 5.20(b) shows the top-view of the 3D map of the detected noise versus distance and frequency detuning. Note that, at 30 m from one of the fiber inputs, the SBS-induced noise amplitude vanishes as a result of the high phase correlation between pump and probe at this position. This point actually corresponds to the fiber's location at

[1] optical power at the photoreceiver was maintained to ensure a known shot noise level

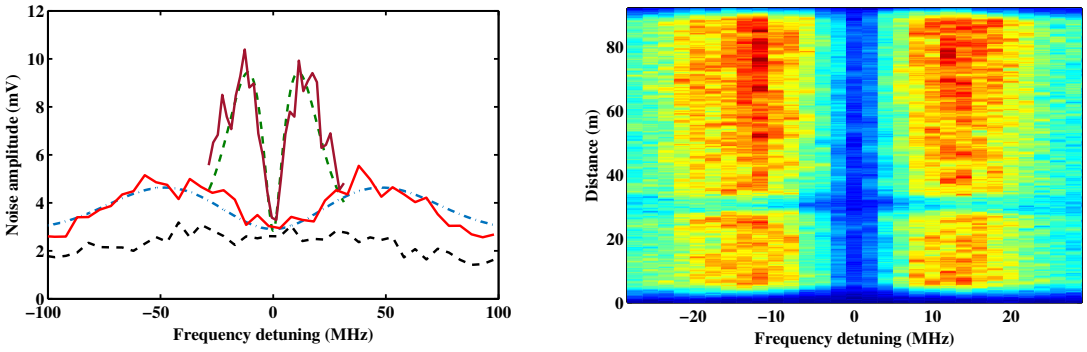

(a) (b)

Fig. 5.20. SBS-induced noise for a DFB laser. (a) Experimental (continuous line) and theoretical (dashed line) noise amplitude at the end of the fiber are compared for 10 ns (red and blue lines) and 70 ns pump pulses (purple and green lines). The black dashed line is the noise measured with an EC laser. (b) Topview of 3D noise map distance vs. frequency detuning for a 70 ns pump pulse.

which pump and probe have propagated the same distance from the laser, so that their phases are perfectly correlated. Note that from that point, the amplitude noise increases in both directions of propagation, until it reaches its maximum value when pump and probe signals become again uncorrelated.

Characterization of SpBS-probe beating noise

In order to analyze the effect of SpBS-probe beating noise when frequency sweeping the probe wave, the PSDs were measured for a detuning ranging from 0 MHz up to 140 MHz, with 10 MHz steps, when using an EC laser (Fig. 5.21(a)) and a DFB laser (Fig. 5.21(b)). Note that, as depicted in Eq. (5.22), the frequency content of the beating noise shifts towards higher frequencies when the detuning increases. Since measurements in Fig. 5.21 are obtained while pump and probe counter-propagate and interact through SBS, the PSDs also include the effect of phase noise on the SBS process. Thus, while Fig. 5.21(a) shows essentially the SpBS-probe beating noise with negligible SBS-induced noise; Fig. 5.21(b) shows that the level obtained with the DFB laser at zero-detuning (blue curve having the maximum at zero frequency) is lower than the noise measured in the slope of the Brillouin spectrum, following the same behaviour described in Fig. 5.20(a). The SpBS beating noise is evaluated by integrating each curve (removing the contribution of the SBS induced noise and the spectral response of the receiver), giving an average frequency independent amplitude $\sigma_{SpBS-Probe} =$ 2.5 mV, which agrees with the black dashed line in Fig. 5.20(a).

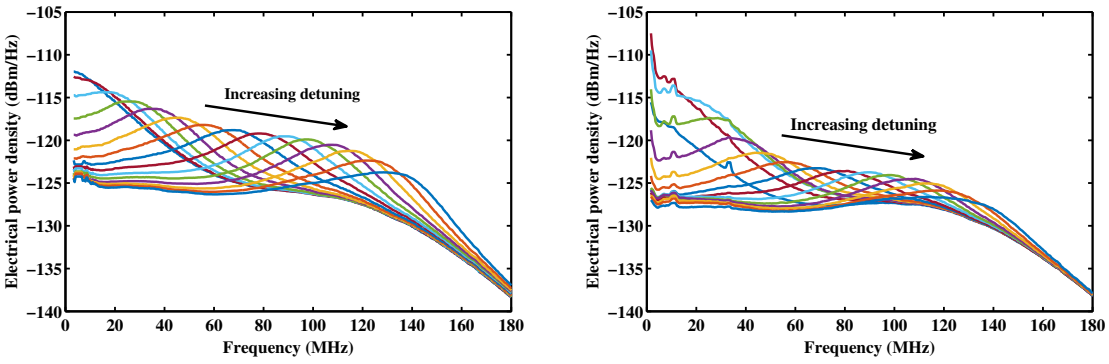

(a) (b)

Fig. 5.21. PSD of beating between probe and pump-induced SpBS. For (a) an EC and (b) a DFB laser. Measurements for different detuning, with 10 MHz steps.

5.6 Conclusions

The different noise sources existing in BOTDA sensors have been analyzed and modeled. Results point out that under optimized receiver conditions, i.e. having a high trans-impedance to improve the SNR, the dominating noise is highly dependent on the sensing range of the system. Thus, in short distance scenarios (less than about 15 km), where the Brillouin gain is relatively high and the pump power has not been highly attenuated (< 3 dB loss), the phase-to-intensity noise conversion in the SBS process and the SpBS-probe beating noise are the dominating sources of noise in the system. When the sensing range increases, the Brillouin gain experienced by the probe wave and the SpBS components backscattered from the far end of the fiber are reduced due to the fiber attenuation, and hence, thermal noise could have a dominating contribution. However, the DRS-induced noise also plays an important role since it increases linearly with the fiber length and can become the dominating source of noise at very long sensing ranges (> 50-70 km), especially if an additional leading fiber is used to propagate the probe wave to a very remote location (thus doubling both the probe propagation length and the DRS-induced noise). It is also important to mention that in dynamic sensing, based for instance on a slope-assisted BOTDA scheme based on the amplitude spectrum, where the probe wave is tuned to the wings of the Brillouin gain spectrum, the SBS-induced phase-to-intensity noise conversion increases considerably and therefore it may induce a significant degradation of the SNR and sensor performance.

Chapter 6

Conclusions and open lines

6.1 Conclusions

In a summarized way, this section brings together all the conclusions derived at each chapter of this thesis dissertation, whose main objective is to develop advanced techniques to improve the performance of Brillouin optical time-domain analysis (BOTDA) sensors overcoming the existing limitations. Conclusions are presented associating them to each of the factors limiting the performance of BOTDA sensors, binding all the proposed configurations together when a limitation has been tackled following different approaches:

Measurement time: two solutions have been proposed to reduce it. The first one is a slope-assisted BOTDA (SA-BOTDA) sensor based on a phase-modulated probe wave. This configuration allows, as the conventional SA-BOTDA based on the amplitude, to dynamically acquire the temperature or strain profile of the fiber. However, the proposed configuration, unlike the systems based on the amplitude, allows to avoid measurement errors induced by variations of the attenuation of the optical fiber. This characteristic is provided by the tolerance of the detected RF phase-shift spectrum to changes of the local Brillouin coefficient that was experimentally proven by attenuating the pump pulse around without suffering any change in the detected RF phase-shift spectra. The deployment of this spectrum, instead of the conventional one, also allows to enlarge the useful monitoring range by a factor of two as it covers both slopes of the Brillouin gain spectrum. Furthermore, this technique deploys a a self-heterodyne detection that allows to increase the signal-to-noise ratio (SNR) of the system. Consequently, it enhances the precision and the measurement range of the system or reduce the measurement time by means of the required number of averages.

The second solution is based on the implementation of a polarization diversity technique that deploys two orthogonal pump pulses. The solution is deployed again on a BOTDA sensor based on a phase-modulated probe wave, in which two orthogonal Brillouin interactions take

place at the two first sideband of this modulation. This provides complementary Brillouin signals at each sideband, which are constructively added at the receiver due to the phase difference between both sidebands. Consequently, there are not fluctuations in the detected signal caused by polarization mismatching between the probe and the pump waves, being able to retrieve the complete information of the BOTDA trace using a single acquisition of it.

Non-local effects: three different solutions have been implemented to alleviate the probe power limitations in BOTDA sensor. The first one is based on the BOTDA sensor using a phase-modulated probe wave. In this case, the tolerance of the detected RF phase-shift spectrum to variations of the local Brillouin gain translates to a tolerance to changes of the pump pulse power. Consequently, the measured spectrum is not distorted in the presence of frequency-dependent variations of the pump power caused by non-local effects. The maximum probe power experimentally proved is -3 dBm, which supposes a 11 dB improvement compared to the conventional BOTDA sensors.

The second solution is based on the variation of the optical frequency of the probe wave along its propagation through the optical fiber, which makes the pulse to meet a different probe frequency at each location of the fiber. This effect reduces the accumulated Brillouin depletion suffered by the pulsed wave along the fiber. The experimental verification of this technique was demonstrated with a probe power of -3 dBm obtaining measurements with no observable impact of non-local effects. Moreover, this approach is valid for any configuration of a BOTDA sensor and can be extended to other configurations such as the balanced BOTDA sensor based on a double-sideband probe wave. This is the case for the third solution proposed in this thesis, in which the optical frequencies of both probe waves in a double sideband setup are changed along the optical fiber. One of the probe waves generates an accumulated Brillouin gain transfer over the pulse spectrum that compensates with the Brillouin loss generated by the other probe wave, so that variations of the pump signal caused by Brillouin interaction become negligible. Furthermore, the net Brillouin gain or loss transfer experienced by the pulsed signal is flat over the pulse spectrum with a bandwidth that avoids any spectral distortion of the pulse spectrum. Moreover, the Brillouin gain or loss spectrum is scanned by changing the relative temporal delay between pulse and probe waves, so that, at a given location of the fiber, the pulse meets another frequency of the probe wave, effectively scanning the Brillouin gain spectrum. This novel frequency swept allows to measure the Brillouin spectrum avoiding a frequency displacement of the net Brillouin gain or loss transfer generated over the pulse spectrum, so that both interactions are always canceled. This solution has been experimentally proven with a probe power of 8 dBm.

Amplification of spontaneous Brillouin scattering generated by the probe wave: This limitation had not been considered prior to the work done in this thesis since the probe power had been first limited by non-local effects. However, this limitation is important in different scenarios, such as long-range systems deploying a leading fiber to transmit the probe wave to a remote location, BOTDA sensors based on self-heterodyne detection where a powerful local oscillator co-propagates with the probe wave or BOTDA sensors in which the non-local effects limitation has been overcome.

The solution proposed in this thesis is based on the frequency modulation of the signals deployed in the scenarios mentioned above, so that the effective Brillouin interaction is broaden and the maximum power injected into the fiber can be increased. In the particular case of the BOTDA sensor based on a double sideband setup, the configuration not only allows to mitigate non-local effects, as mentioned before, but also permits to increase the probe power above the spontaneous Brillouin scattering (SpBS) threshold.

The technique has been also proposed on a BOTDA sensor based on a self-heterodyne detection. In this case, using a phase-modulated probe wave, whose carrier represents the local oscillator of the system. The power of this component is also limited by this effect and hence, deploying the dithering on this component, its optical power was increased, considerably increasing the intensity of the detected signal.

More important is the reduction of the detected noise transferred to the probe wave when the power of the local oscillator reaches the SpBS threshold.

Modulation instability: a solution based on pump pulses with orthogonal polarization states at different wavelengths has been proposed to increase the maximum pump power injected in BOTDA sensors. The deployed configuration is the BOTDA sensor using phase modulation of the probe wave, in which the first sidebands of the modulation interact with a pump pulse with different polarization state. The technique removes the onset of four-wave mixing as both pulses have orthogonal polarizations and it also allows to inject a larger pump power than the modulation instability (MI) threshold as the power is split at different pump wavelengths. Consequently, the effect of modulation instability is alleviated.

Spatial resolution: a solution for BOTDA sensor measuring phasorial signals, i.e. amplitude and phase-shift, has been proposed in this thesis. The idea is based on the differential pulse-width pair technique in which the Brillouin response of two consecutive pump pulses is subtracted. In this case, a full phasorial subtraction is performed, so that, the advantages obtained with the amplitude signal, such as high spatial resolution and narrow linewidth of the measured spectra, are also obtained with the detected phase-shift signal. The employed pulse durations were 50 and 60 ns, obtaining a spatial resolution of 1 m. However, the technique is valid for any pulse-width difference.

Sensing range: a solution based on the implementation of a distributed Brillouin amplifier (DBA) in a BOTDA sensor has been presented. This allows to increase the power of the pump pulses during their propagation along the fiber. Consequently, the Brillouin gain interaction increases at the last kilometers of the sensing fiber. The technique has been experimentally demonstrated in a 50-km fiber length providing full compensation of the fiber attenuation. Moreover, the deployment of a DBA does not induce an observable penalty on the signal-to-noise ratio of the detected measurements.

Signal-to-noise ratio: a study of the different noise sources affecting the BOTDA sensor was performed during the thesis work. The study indicates that the noise source ultimately limiting the sensor performance depends basically on the fiber length and the input pump and probe powers. Thus, while phase-to-intensity noise conversion induced by stimulated Brillouin scattering can have a dominant effect at short distances, a combination of sources determines the noise floor in long-range sensing, basically dominated by double Rayleigh scattering generated by the probe wave. The results obtained were contrasted by analytical and experimental results.

6.2 Open lines

The resultant open lines coming from the work performed during this thesis are presented on the following paragraphs:

Measurement time: The SA-BOTDA sensor based on phase-modulated probe wave assumes small Brillouin gain condition. As a consequence, the equation representing the RF phase-shift shows immunity to variations of the local Brillouin coefficient. However, when the gain is not small enough, the RF phase-shift spectrum may slightly change its spectral shape, inducing an error on the dynamic measurement. This effect must be considered and studied to limit the maximum gain that this system can afford without error.

Another issue of this system is the available measurement range. Although the system doubles its value regarding the SA-BOTDA sensor based on the amplitude using a single pump pulse. It may be necessary to increase its value for real applications, such as monitoring the vibrations on the blades of wind turbines. Consequently, new methods to extend the measurement range would be very useful to enhance the system performance. In addition to this point, the system could be updated to deploy a synthesized and adaptable probe wave to always work on the slope of the measured spectrum when the sensing fibers has not a uniform Brillouin frequency shift (BFS).

Finally, the evolved system using the new polarization diversity technique based on double orthogonal pump pulses assumes that the BFS between the pump pulses and the probe

waves is equal. However, there exists around 1 MHz difference that may induce an error on the detected BFS. For example, for a given location of the fiber in which the probe waves have the same state of polarization (SOP) than one pump pulse, the Brillouin transfer would be given only by that interaction, however the SOP of the probe waves may change along time and consequently be aligned with the other pulsed signal, inducing an error of approximately 1 MHz. This issue may be solved by deploying a dual parallel Mach-Zehnder electro-optic modulator that outputs a double sideband signal in which the frequency difference between the optical carrier and the sidebands differs 1 MHz. Consequently, the frequency error caused by the BFS dependence on the pump frequency may be corrected.

Non-local effects: In systems based on phase-modulated probe wave, the pulsed wave is amplified or depleted by a narrowband signal given by the characteristics of stimulated Brillouin scattering. This amplification or depletion process may induce a spectral distortion of the pulsed signal, which may affect the measured Brillouin spectrum. This effect should be carefully studied when short pump pulses are used to retrieve the measured Brillouin signal, since they have a larger bandwidth than the natural Brillouin spectrum. Moreover, as the small gain condition typically applied in BOTDA sensors has been also employed for this study, it would be very interesting to determine the maximum Brillouin amplification that the system can tolerate.

In BOTDA sensors using frequency modulation of the probe wave (the single probe wave case), the pump power evolution when sweeping the frequency difference is not longer a Lorentzian shape for uniform BFS fibers. Consequently, the equations developed in [19] that provide the frequency error for a given depletion/amplification factor are no longer valid, since the frequency-dependence pump power acquires a different shape due to the frequency modulation. This shape may affect less the distortion of the measured spectra since it is designed to be approximately flat during the frequency sweep. Therefore, a large probe power could be injected into the optical fiber that the power experimentally verified in this thesis. This effect should be studied to evaluate the maximum performance that can be obtained with this system.

Finally, the BOTDA sensor using a frequency modulation of both probe waves (balanced BOTDA sensor) has been demonstrated with a fiber length of 50 km. For this range, the SNR improvement that this technique can provide is not fully exploited since the received optical probe power saturates the high-transimpedance receiver and hence, the optical power must be attenuated before being detected. An interesting point will be to increase the sensing range using this technology to experimentally demonstrate its potential.

Modulation instability: the degree of orthogonality between the two pump pulses with different wavelengths that are used to increase the MI threshold must be studied for

long-range systems. In this case, the orthogonality between both waves may be lost during their propagation and hence, four-wave mixing could play an important role, drastically reducing the useful length of the sensing fiber. Therefore, this effect should be considered in future implementations using this technique.

Sensing range: the amplification to the pump pulse provided by a DBA pump wave is obtained from a different laser source that the one used to generate the pump pulse and probe wave. Consequently, the stability of the sensing system could be affected due to frequency drifts between both lasers during time. It would be interesting to present a DBA-assisted BOTDA sensor using only one laser source to generate the three waves required in this technique. Furthermore, the gain provided by the DBA pump wave is adjusted with a polarization controller at the output of the laser source. Due to the variation of the polarization, the gain could be considerably modified along time. This effect should be fixed by studying the influence of introducing a polarization scrambler at the output of the DBA laser source that averages the gain provided to the pulsed signal.

Another interesting point is the influence of the amplification of the pulsed signal on the deviation of the Brillouin frequency shift of the fiber due to self-phase modulation (SPM). As it is shown in chapter 4, this can be solved by using long pulses and differential pulse-width pair technique since the problem comes from the gradual amplification of the pump pulse caused by the acoustic wave growth. However, it would be interesting to further study this effect in order to provide a more elegant solution. Moreover, this effect may be also detrimental for BOTDA systems that can tolerate amplification or depletion caused by non-local effects, since the effect caused by the acoustic growth is equivalent.

Signal-to-noise ratio: the analysis presented for BOTDA sensors does not include the introduction of an erbium-doped fiber amplifier, typically used to amplify the low power probe signal before being detected. The introduction of this device could increase the noise level not only by the amplified spontaneous emission but also by its beating with the other noise sources identified during this work. Therefore, it would be an interesting contribution to extend this study in order to basically cover all the different scenarios used in BOTDA systems.

Furthermore, it would be remarkable to analyze the effect of phase-to-intensity noise conversion in SBS process for SA-BOTDA sensors based on the amplitude and the RF phase-shift. The SA-BOTDA sensor based on the amplitude set the probe frequency at the skirt of the Brillouin spectrum in which this noise takes its highest values. On the contrary, the SA-BOTDA sensor based on the RF phase-shift sets the probe frequency at the exact location of the BFS in which the noise is minimum. This could be another advantage of using this kind of system.

Finally, considering the work done by our research group on the development of BOTDA sensors based on phase-modulated probe wave and RF demodulation, the extension of the SNR study to this kind of system would be of great interest to properly compare it with the conventional BOTDA sensors.

Bibliography

[1] R. W. Boyd. *Nonlinear Optics*. Academic Press, 2008.

[2] G. P. Agrawal. *Fiber-Optic Communication Systems*. John Wiley & Sons, 2002.

[3] L. Thévenaz. *Advanced Fiber Optics*. EFPL Press, 2011.

[4] M. J. Damzen, V. Vlad, A. Mocofanescu, and V. Babin. *Stimulated Brillouin scattering: Fundamentals and Applications*. Bristol and Philadelphia, 2003.

[5] W. Zou, Z. He, and K. Hotate. Investigation of strain and temperature dependences of Brillouin frequency shifts in GeO2-doped optical fibers. *Journal of Lightwave Technology*, 26(13):1854–1861, 2008.

[6] M. Niklès, L. Thévenaz, and P. A. Robert. Brillouin gain spectrum characterization in single-mode optical fibers. *Journal of Lightwave Technology*, 15(10):1842–1851, 1997.

[7] K. Hotate. Measurement of Brillouin gain spectrum distribution along an optical fiber using a correlation-based technique-proposal, experiment and simulation. *IEICE Transactions on Electronics*, E83-C(3):405–411, 2000.

[8] K. Y. Song, Z. He, and K. Hotate. Distributed strain measurement with millimeter-order spatial resolution based on Brillouin optical correlation domain analysis. *Optics Letters*, 31(17):2526–2528, 2006.

[9] K. Y. Song and K. Hotate. Brillouin optical correlation domain analysis in linear configuration. *IEEE Photonics Technology Letters*, 20(24):2150–2152, 2008.

[10] D. Garus, T. Gogolla, K. Krebber, and F. Schliep. Distributed sensing technique based on Brillouin optical-fiber frequency-domain analysis. *Optics Letters*, 21(17):1402–1404, 1996.

[11] R. Bernini, A. Minardo, and L. Zeni. Distributed sensing at Centimeter-Scale spatial resolution by BOFDA: Measurements and signal processing. *IEEE Photonics Journal*, 4(1):48–56, 2012.

[12] T. Kurashima, T. Horiguchi, and M. Tateda. Distributed-temperature sensing using stimulated Brillouin scattering in optical silica fibers. *Optics Letters*, 18(15):1038–1040, 1990.

[13] T. Horiguchi, T. Kurashima, and M. Tateda. Nondestructive measurement of optical fiber tensile strain distribution based on Brillouin spectroscopy. *IEICE*, J73-B-I(2):144–152, 1990.

[14] M. Iten and A. M. Puzrin. BOTDA road-embedded strain sensing system for landslide boundary localization. In *Proceedings of SPIE*, volume 7293, 2009.

[15] M. Iten and A. M. Puzrin. Monitoring of stress distribution along a ground anchor using BOTDA. In *Proceedings of SPIE*, volume 7647, 2010.

[16] A. Minardo, G. Porcaro, D. Giannetta, R. Bernini, and L. Zeni. Real-time monitoring of railway traffic using slope-assisted Brillouin distributed sensors. *Applied Optics*, 52(16):3770–3776, 2013.

[17] C. L. Tang. Saturation and spectral characteristics of the Stokes emission in the stimulated Brillouin process. *Journal of Applied Physics*, 37(8):2945–2955, 1966.

[18] M. A. Soto and L. Thévenaz. Modeling and evaluating the performance of Brillouin distributed optical fiber sensors. *Optics Express*, 21(25):31347–31366, 2013.

[19] L. Thévenaz, S. Foaleng-Mafang, and J. Lin. Effect of pulse depletion in a Brillouin optical time-domain analysis system. *Optics Express*, 21(12):14017–14035, 2013.

[20] T. Horiguchi, K. Shimizu, T. Kurashima, M. Tateda, and Y. Koyamada. Development of a distributed sensing technique using Brillouin scattering. *Journal of Lightwave Technology*, 13(7):1296–1302, 1995.

[21] R. Bernini, A. Minardo, and L. Zeni. Reconstruction technique for stimulated Brillouin scattering distributed fiber-optic sensors. *Optical Engineering*, 41(9):2186–2194, 2002.

[22] A. Zornoza, A. Minardo, R. Bernini, A. Loayssa, and L. Zeni. Pulsing the probe wave to reduce nonlocal effects in Brillouin optical time-domain analysis (BOTDA) sensors. *IEEE Sensors Journal*, 11(4):1067–1068, 2011.

[23] Y. Dong, L. Chen, and X. Bao. System optimization of a long-range Brillouin-loss-based distributed fiber sensor. *Applied Optics*, 49(27):5020–5025, 2010.

[24] A. Minardo, R. Bernini, and L. Zeni. A simple technique for reducing pump depletion in long-range distributed Brillouin fiber. *IEEE Sensors Journal*, 9(6):633–634, 2009.

[25] R. Bernini, A. Minardo, and L. Zeni. Long-range distributed Brillouin fiber sensors by use of an unbalanced double sideband probe. *Optics Express*, 19(24):23845–23856, 2011.

[26] A. Domínguez-López, X. Angulo-Vinuesa, A. López-Gil, S. Martín-López, and M. González-Herráez. Non-local effects in dual-probe-sideband Brillouin optical time domain analysis. *Optics Express*, 23(8):10341–10352, 2015.

[27] D. Alasia, M. González-Herráez, L. Abrardi, S. Martín-López, and L. Thévenaz. Detrimental effect of modulation instability on distributed optical fibre sensors using stimulated Brillouin scattering. In *Proceedings of SPIE*, volume 5855, 2005.

[28] S. Foaleng-Mafang and L. Thévenaz. Impact of Raman scattering and modulation instability on the performances of Brillouin sensors. In *Proceedings of SPIE*, volume 7753, 2011.

[29] M. N. Alahbabi, Y. T. Cho, T. P. Newson, P. C. Wait, and A. H. Hartog. Influence of modulation instability on distributed optical fiber sensors based on spontaneous Brillouin scattering. *Journal of the Optical Society of America B: Optical Physics*, 21(6):1156–1160, 2004.

[30] M. Alem, M. A. Soto, and L. Thévenaz. Analytical model and experimental verification of the critical power for modulation instability in optical fibers. *Optics Express*, 23(23):29514–29532, 2015.

[31] M. A. Soto, M. Alem, W. Chen, and L. Thévenaz. Mitigating modulation instability in Brillouin distributed fibre sensors. In *Proceedings of SPIE*, volume 8794, 2013.

[32] Y. Dong and X. Bao. High spatial resolution and long-distance BOTDA using differential Brillouin gain in a dispersion shifted fiber. volume 7503, 2009.

[33] S. Foaleng-Mafang, F. Rodríguez-Barrios, S. Martín-López, M. González-Herráez, and L. Thévenaz. Detrimental effect of self-phase modulation on the performance of Brillouin distributed fiber sensors. *Optics Letters*, 36(2):97–99, 2011.

[34] D. Cotter. Stimulated Brillouin scattering in monomode optical fiber. *Journal of Optical Communications*, 4(1):10–19, 1983.

[35] W. Li, X. Bao, Y. Li, and L. Chen. Differential pulse-width pair BOTDA for high spatial resolution sensing. *Optics Express*, 16(26):21616–21625, 2008.

[36] X. Bao, A. Brown, M. DeMerchant, and J. Smith. Characterization of the Brillouin-loss spectrum of single-mode fibers by use of very short (<10-ns) pulses. *Optics Letters*, 24(8):510–512, 1999.

[37] A.W. Brown, B.G. Colpitts, and K. Brown. Distributed sensor based on dark-pulse Brillouin scattering. *IEEE Photonics Technology Letters*, 17(7):1501–1503, 2005.

[38] K. Kishida and C. Li. Pulse Pre-Pump-BOTDA technology for new generation of distributed strain measuring system. In *Structural Health Monitoring and Intelligent Infrastructure - Proceedings of the 2nd International Conference on Structural Health Monitoring of Intelligent Infrastructure, SHMII 2005*, volume 1, 2006.

[39] S. Foaleng-Mafang, M. Tur, J. C. Beugnot, and L. Thévenaz. High spatial and spectral resolution long-range sensing using Brillouin echoes. *Journal of Lightwave Technology*, 28(20):2993–3003, 2010.

[40] Y. Dong, L. Chen, and X. Bao. Extending the sensing range of Brillouin optical time-domain analysis combining frequency-division multiplexing and in-line EDFAs. *Journal of Lightwave Technology*, 30(8):1161–1167, 2012.

[41] Z. Yang, M. A. Soto, and L. Thévenaz. Increasing robustness of bipolar pulse coding in Brillouin distributed fiber sensors. *Opt. Express*, 24(1):586–597, 2016.

[42] X. Angulo-Vinuesa, S. Martín-López, P. Corredera, and M. González-Herráez. Raman-assisted Brillouin optical time-domain analysis with sub-meter resolution over 100 km. *Optics Express*, 20(11):12147–12154, 2012.

[43] S. Martín-López, M. Alcón-Camas, F. Rodríguez, P. Corredera, J. D. Ania-Castañon, L. Thévenaz, and M. González-Herráez. Brillouin optical time-domain analysis assisted by second-order raman amplification. *Optics Express*, 18(18):18769–18778, 2010.

[44] M. A. Soto, G. Bolognini, F. Di Pasquale, and L. Thévenaz. Simplex-coded BOTDA fiber sensor with 1 m spatial resolution over a 50 km range. *Optics Letters*, 35(2):259–261, 2010.

[45] A. Zornoza, M. Sagues, and A. Loayssa. Self-heterodyne detection for SNR improvement and distributed phase-shift measurements in BOTDA. *Journal of Lightwave Technology*, 30(8):1066–1072, 2012.

[46] M. A. Soto, M. Taki, G. Bolognini, and F. Di Pasquale. Simplex-coded BOTDA sensor over 120-km SMF with 1-m spatial resolution assisted by optimized bidirectional Raman amplification. *IEEE Photonics Technology Letters*, 24(20):1823–1826, 2012.

[47] M. A. Soto and L. Thévenaz. Towards 1'000'000 resolved points in a distributed optical fibre sensor. In *Proceedings of SPIE*, volume 9157, 2014.

[48] F. Rodríguez-Barrios, S. Martín-López, A. Carrasco-Sanz, P. Corredera, J.D. Ania-Castañón, L. Thévenaz, and M. González-Herraáez. Distributed Brillouin fiber sensor assisted by first-order Raman amplification. *Journal of Lightwave Technology*, 28(15):2162–2172, 2010.

[49] A. Domínguez-López, A. López-Gil, S. Martín-López, and M. González-Herráez. Strong cancellation of RIN transfer in a Raman-assisted BOTDA using balanced detection. *IEEE Photonics Technology Letters*, 26(18):1817–1820, 2014.

[50] X. Angulo-Vinuesa, D. Bacquet, S. Martín-López, P. Corredera, P. Szriftgiser, and M. González-Herráez. Relative intensity noise transfer reduction in Raman-assisted BOTDA systems. *IEEE Photonics Technology Letters*, 26(3):271–274, 2014.

[51] R. Bernini, A. Minardo, and L. Zeni. Dynamic strain measurement in optical fibers by stimulated Brillouin scattering. *Optics Letters*, 34(17):2613–2615, 2009.

[52] Y. Peled, A. Motil, L. Yaron, and M. Tur. Slope-assisted fast distributed sensing in optical fibers with arbitrary Brillouin profile. *Optics Express*, 19(21):19845–19854, 2011.

[53] Y. Peled. *Strain sensors and optical comunication in optical fibers using the Brillouin effect*. Thesis dissertation from Tel-Aviv University, 2014.

[54] A. Motil, O. Danon, Y. Peled, and M. Tur. Pump-power-independent double slope-assisted distributed and fast Brillouin fiber-optic sensor. *IEEE Photonics Technology Letters*, 26(8):797–800, 2014.

[55] Y. Peled, A. Motil, and M. Tur. Fast Brillouin optical time domain analysis for dynamic sensing. *Optics Express*, 20(8):8584–8591, 2012.

[56] A. Voskoboinik, O. F. Yilmaz, A. W. Willner, and M. Tur. Sweep-free distributed Brillouin time-domain analyzer (SF-BOTDA). *Optics Express*, 19(26):B842–B847, 2011.

[57] M. González-Herráez, K. Y. Song, and L. Thévenaz. Arbitrary-bandwidth Brillouin slow light in optical fibers. *Optics Express*, 14(4):1395–1400, 2006.

[58] K. Y. Song, M. Kishi, Z. He, and K. Hotate. High-repetition-rate distributed Brillouin sensor based on optical correlation-domain analysis with differential frequency modulation. *Optics Letters*, 36(11):2062–2064, 2011.

[59] Y. Peled, A. Motil, L. Yaron, and M. Tur. Distributed and dynamical Brillouin sensing in optical fibers. In *Proceedings of SPIE*, volume 7753, 2011.

[60] A. Voskoboinik, J. Wang, B. Shamee, S. R. Nuccio, L. Zhang, M. Chitgarha, A. E. Willner, and M. Tur. SBS-based fiber optical sensing using frequency-domain simultaneous tone interrogation. *Journal of Lightwave Technology*, 29(11):1729–1735, 2011.

[61] P. Chaube, B. G. Colpitts, D. Jagannathan, and A. W. Brown. Distributed fiber-optic sensor for dynamic strain measurement. *IEEE Sensors Journal*, 8(7):1067–1072, 2008.

[62] A. Voskoboinik, D. Rogawski, H. Huang, Y. Peled, A. E. Willner, and M. Tur. Frequency-domain analysis of dynamically applied strain using sweep-free Brillouin time domain analyzer and sloped-assisted FBG sensing. *Optics Express*, 20(26):B581–B586, 2012.

[63] K. Tsuji, H. Noda, and N. Onodera. Sweep-free Brillouin optical time domain analysis using two individual laser sources. *Optical Review*, 19(6):381–387, 2012.

[64] Qingsong C., S. Pamukcu, X. Wen, and M. Pervizpour. Truly distributed fiber vibration sensor using pulse base BOTDA with wide dynamic range. *IEEE Photonics Technology Letters*, 23(24):1887–1889, 2011.

[65] A. Motil, R. Hadar, I. Sovran, and M. Tur. Gain dependence of the linewidth of Brillouin amplification in optical fibers. *Optics Express*, 22(22):27535–27541, 2014.

[66] J. Humlíček, E. Schmidt, L. Bočánek, R. Svehla, and K. Ploog. Exciton line shapes of GaAs/AlAs multiple quantum wells. *Physical Review B*, 48(8):5241–5248, 1993.

[67] A. Zornoza, D. Olier, M. Sagues, and A. Loayssa. Brillouin distributed sensor using RF shaping of pump pulses. *Measurement Science and Technology*, 21(9), 2010.

[68] K. Hotate, K. Abe, and K. Y. Song. Suppression of signal fluctuation in Brillouin optical correlation domain analysis system using polarization diversity scheme. *IEEE Photonics Technology Letters*, 18(24):2653–2655, 2006.

[69] S. Díaz, S. Foaleng-Mafang, M. López-Amo, and L. Thévenaz. High performance Brillouin distributed fibre sensor. In *Proceedings of SPIE*, volume 6619, 2007.

[70] M. O. van Deventer and A. J. Boot. Polarization properties of stimulated Brillouin scattering in single-mode fibers. *Journal of Lightwave Technology*, 12(4):585–590, 1994.

[71] A. Zadok, E. Zilka, A. Eyal, L. Thévenaz, and M. Tur. Vector analysis of stimulated Brillouin scattering amplification in standard single-mode fibers. *Optics Express*, 16(26):21692–21707, 2008.

[72] G. D. VanWiggeren and R. Roy. Transmission of linearly polarized light through a single-mode fiber with random fluctuations of birefringence. *Applied Optics*, 38(18):3888–3892, 1999.

[73] J. Urricelqui, A. Zornoza, M. Sagues, and A. Loayssa. Dynamic BOTDA measurements based on Brillouin phase-shift and RF demodulation. *Optics Express*, 20(24):26942–26949, 2012.

[74] J. P. Gordon and H. Kogelnik. PMD fundamentals: Polarization mode dispersion in optical fibers. *Proceedings of the National Academy of Sciences of the United States of America*, 97(9):4541–4550, 2000.

[75] A. B. Carlson, P. B. Crilly, and J. Rutledge. *Communication Systems: An Introduction to Signals and Noise in Electrical Communication*. McGraw-Hill Series in Electrical Engineering, 2001.

[76] K. Y. Song, S. Chin, N. Primerov, and L. Thévenaz. Time-domain distributed fiber sensor with 1 cm spatial resolution based on Brillouin dynamic grating. *Journal of Lightwave Technology*, 28(14):2062–2067, 2010.

[77] A. Motil, O. Danon, Y. Peled, and M. Tur. High spatial resolution BOTDA using simultaneously launched gain and loss pump pulses. In *Proceedings of SPIE*, volume 8794, 2013.

[78] J. Urricelqui, M. Sagues, and A. Loayssa. BOTDA measurements tolerant to non-local effects by using a phase-modulated probe wave and RF demodulation. *Optics Express*, 21(14):17186–17194, 2013.

[79] A. R. Chraplyvy, R. W. Tkach, L. L. Buhl, and R. C. Alferness. Phase modulation to amplitude modulation conversion of CW laser light in optical fibres. *Electronics Letters*, 22(8):409–411, 1986.

[80] S. Foaleng-Mafang, J. C. Beugnot, and L. Thévenaz. Optical sampling technique applied to high resolution distributed fibre sensors. In *Proceedings of SPIE*, volume 7503, 2009.

[81] M. Alem, M. A. Soto, and L. Thévenaz. Modelling the depletion length induced by modulation instability in distributed optical fibre sensors. In *Proceedings of SPIE*, volume 9157, 2014.

[82] M. A. Soto, A. L. Ricchiuti, L. Zhang, D. Barrera, S. Sales, and L. Thévenaz. Time and frequency pump-probe multiplexing to enhance the signal response of Brillouin optical time-domain analyzers. *Optics Express*, 22(23):28584–28595, 2014.

[83] P. K. A. Wai and C. R. Menyuk. Polarization mode dispersion, decorrelation, and diffusion in optical fibers with randomly varying birefringence. *Journal of Lightwave Technology*, 14(2):148–157, 1996.

[84] B. Kibler, B. Frisquet, P. Morin, J. Fatome, F. Baronio, M. Conforti, G. Millot, and S. Wabnitz. Observation of Manakov polarization modulation instability in the normal dispersion regime of randomly birefringent telecom optical fiber. In *European Conference on Optical Communication, ECOC*, 2014.

[85] J. Urricelqui, F. Lopez-Fernandino, M. Sagues, and A. Loayssa. Polarization diversity scheme for BOTDA sensors based on a double orthogonal pump interaction. *Journal of Lightwave Technology*, 33(12):2633–2638, 2015.

[86] L. Thévenaz, S. Foaleng-Mafang, and J. Lin. Impact of pump depletion on the determination of the Brillouin gain frequency in distributed fiber sensors. In *Proceedings of SPIE*, volume 7753, 2011.

[87] H. Shalom, A. Zadok, M. Tur, P. J. Legg, W. D. Cornwell, and I. Andonovic. On the various time constants of wavelength changes of a DFB laser under direct modulation. *IEEE Journal of Quantum Electronics*, 34(10):1816–1822, 1998.

[88] X. Bao, J. Dhliwayo, N. Heron, D. J. Webb, and D. A. Jackson. Experimental and theoretical studies on a distributed temperature sensor based on Brillouin scattering. *Journal of Lightwave Technology*, 13(7):1340–1348, 1995.

[89] A. David and M. Horowitz. Low-frequency transmitted intensity noise induced by stimulated Brillouin scattering in optical fibers. *Optics Express*, 19(12):11792–11803, 2011.

[90] T. Shimizu, K. Nakajima, K. Shiraki, K. Ieda, and I. Sankawa. Evaluation methods and requirements for the stimulated Brillouin scattering threshold in a single-mode fiber. *Optical Fiber Technology*, 14(1):10–15, 2008.

[91] P. Szriftgiser, M. Dossou, and D. Bacquet. Vector Brillouin optical time-domain analyzer for high-order acoustic modes. *Optics Letters*, 35(22):3850–3852, 2010.

[92] J. Urricelqui, M. Sagues, and A. Loayssa. Phasorial differential pulse-width pair technique for long-range Brillouin optical time-domain analysis sensors. *Optics Express*, 22(14):17403–17408, 2014.

[93] K. Shiraki, M. Ohashi, and M. Tateda. SBS threshold of a fiber with a Brillouin frequency shift distribution. *Journal of Lightwave Technology*, 14(1):50–57, 1996.

[94] L. Chen and X. Bao. Analytical and numerical solutions for steady state stimulated Brillouin scattering in a single-mode fiber. *Optics Communications*, 152(1-3):65–70, 1998.

[95] P. Bayvel and P. M. Radmore. Solutions of the SBS equations in single mode optical fibres and implications for fibre transmission systems. *Electronics Letters*, 26(3):434–436, 1990.

[96] J. Urricelqui, M. Sagues, and A. Loayssa. Synthesis of Brillouin frequency shift profiles to compensate non-local effects and Brillouin induced noise in BOTDA sensors. *Optics Express*, 22(15):18195–18202, 2014.

[97] A. Domínguez-López, Z. Yang, M. A. Soto, X. Angulo-Vinuesa, S. Martín-López, L. Thévenaz, and M. González-Herráez. Reaching the ultimate performance limit given by non-local effects in BOTDA sensors. In *Proceedings of SPIE*, volume 9634, 2015.

[98] F. Gyger, E. Rochat, S. Chin, M. Niklès, and L. Thévenaz. Extending the sensing range of Brillouin optical time-domain analysis up to 325 km combining four optical repeaters. In *Proceedings of SPIE*, volume 9157, 2014.

[99] M. Fernández-Vallejo, D. Olier, A. Zornoza, R. A. Pérez-Herrera, S. Díaz, C. Elosua, C. Bariain, A. Loayssa, and M. López-Amo. 46-km-long Raman amplified hybrid double-bus network with point and distributed Brillouin sensors. *IEEE Sensors Journal*, 12(1):184–188, 2012.

[100] X. Angulo-Vinuesa, S. Martín-López, J. Nuño, P. Corredera, J. D. Ania-Castañón, L. Thévenaz, and M. González-Herráez. Raman-assisted Brillouin distributed temperature sensor over 100 km featuring 2 m resolution and 1.2 °c uncertainty. *Journal of Lightwave Technology*, 30(8):1060–1065, 2012.

[101] A. Zadok, A. Eyal, and M. Tur. Gigahertz-wide optically reconfigurable filters using stimulated Brillouin scattering. *Journal of Lightwave Technology*, 25(8):2168–2174, 2007.

[102] L. Zou, X. Bao, S. Yang, L. Chen, and F. Ravet. Effect of Brillouin slow light on distributed Brillouin fiber sensors. *Optics Letters*, 31(18):2698–2700, 2006.

[103] J. C. Beugnot, M. Tur, S. Foaleng-Mafang, and L. Thévenaz. Distributed Brillouin sensing with sub-meter spatial resolution: Modeling and processing. *Optics Express*, 19(8):7381–7397, 2011.

[104] A. Domínguez-López, A. López-Gil, S. Martín-López, and M. González-Herráez. Signal-to-noise ratio improvement in BOTDA using balanced detection. *IEEE Photonics Technology Letters*, 26(4):338–341, 2014.

[105] A. F. Judy. Intensity noise from fiber Rayleigh backscatter and mechanical splices. In *Proceedings of SPIE*, volume 9157, 2014.

[106] J. L. Gimlett, J. Young, R. E. Spicer, and N. K. Cheung. Degradations in Gbit/s DFB laser transmission systems due to phase-to-intensity noise conversion by multiple reflection points. *Electronics Letters*, 24(7):406–408, 1988.

[107] P. Wan and J. Conradi. Impact of double Rayleigh backscatter noise on digital and analog fiber systems. *Journal of Lightwave Technology*, 14(3):288–297, 1996.

[108] P. Gysel and R. K. Staubli. Statistical properties of Rayleigh backscattering in single-mode fibers. *Journal of Lightwave Technology*, 8(4):561–567, 1990.

[109] M. Nazarathy, W. V. Sorin, D. M. Baney, and S. A. Newton. Spectral analysis of optical mixing measurements. *Journal of Lightwave Technology*, 7(7):1083–1096, 1989.

[110] Q. Liu, T. Tokunaga, and Z. He. Realization of nano static strain sensing with fiber Bragg gratings interrogated by narrow linewidth tunable lasers. *Optics Express*, 19(21):20214–20223, 2011.

[111] J. Zhou, J. Chen, Y. Jaouën, L. Yi, X. Li, H. Petit, and P. Gallion. A new frequency model for pump-to-signal RIN transfer in Brillouin fiber amplifiers. *IEEE Photonics Technology Letters*, 19(13):978–980, 2007.

[112] O. Shlomovits, T. Langer, and M. Tur. The effect of source phase noise on stimulated Brillouin amplification. *Journal of Lightwave Technology*, 33(12):2639–2645, 2015.

[113] S. Bottacchi. *Noise and Signal Interference in Optical Fiber Transmission Systems: An Optimum Design Approach*. WILEY, 2009.

[114] B. Moslehi. Analysis of optical phase noise in fiber-optic systems employing a laser source with arbitrary coherence time. *Journal of Lightwave Technology*, 4(9):1334–1351, 1986.

[115] M. Tur, B. Moslehi, and J. W. Goodman. Theory of laser phase noise in recirculating fiber-optic delay lines. *Journal of Lightwave Technology*, 3(1):20–31, 1985.

[116] L. Thévenaz, S. Le Floch, D. Alasia, and J. Troger. Novel schemes for optical signal generation using laser injection locking with application to Brillouin sensing. *Measurement Science and Technology*, 15(8):1519–1524, 2004.

[117] Z. Yang, M. A. Soto, and L. Thévenaz. 200 km fiber-loop Brillouin distributed fiber sensor using bipolar Golay codes and a three-tone probe. In *Proceedings of SPIE*, volume 9634, 2015.

[118] Javier Urricelqui, Mikel Sagues, and Alayn Loayssa. Brillouin optical time-domain analysis sensor assisted by Brillouin distributed amplification of pump pulses. *Optics Express*, 23(23):30448–30458, 2015.

[119] R. Ruiz-Lombera, J. Urricelqui, M. Sagues, J. Mirapeix, J.M. López-Higuera, and A. Loayssa. Overcoming nonlocal effects and Brillouin threshold limitations in Brillouin optical time-domain sensors. *IEEE Photonics Journal*, 7(6):1–9, 2015.

[120] M. A. Soto, X. Angulo-Vinuesa, S. Martín-López, S. Chin, J. D. Ania-Castañón, P. Corredera, E. Rochat, M. González-Herráez, and L. Thévenaz. Extending the real remoteness of long-range Brillouin optical time-domain fiber analyzers. *Journal of Lightwave Technology*, 32(1):152–162, 2014.

[121] S. Ryu and S. Yamamoto. Measurement of direct frequency modulation characteristics of DFB-LD by delayed self-homodyne technique. *Electronics Letters*, 22(20):1052–1054, 1986.

Appendix A

Determination of the laser source spectral shape

The setup assembled to retrieve the spectral shape of the laser source is the one shown in Fig. A.1.

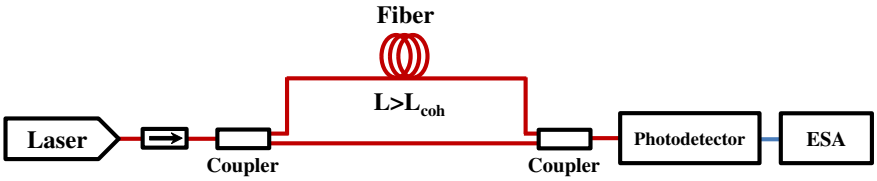

Fig. A.1. Self-delayed homodyne detection system.

This setup is based on the delayed self-homodyne measurement technique, which is typically deployed to measure the linewidth of a laser source [121]. The light of a DFB source passes an optical isolator and then is divided into two optical branches by an optical splitter. Each optical signal propagates trough a different length of fiber and they are combined again using an optical coupler. Then, the optical signal is detected with a photodiode, which is connected to an ESA, where the AC signal is measured. Note that for an accurate determination of the spectral shape it is crucial to get both signals uncorrelated. This is accomplished by choosing a fiber with a length greater than the coherence length of the deployed DFB ($L_{coh} = 2\pi v_g/\Delta\nu_{LS}$, where υ_g is the group velocity of the fiber and $\Delta\nu_{LS}$ is the linewidth of the laser source).

The electrical spectrum measured in the ESA is supposed to be a Lorentzian profile with twofold the linewidth of the laser. However, this result is only retrieved if an ideal current source drives the laser source and only under absolutely stable environmental conditions. When these conditions are not fulfilled, the Lorentzian shape of the laser source is affected

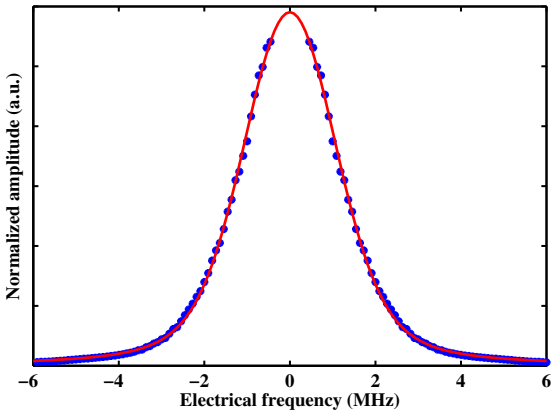

Fig. A.2. Measured spectral shape using the delayed self-homodyne detection system and Voigt fitting curve.

by a Gaussian profile that stems from the noise of the current source and fluctuations of temperature and pressure in the laboratory. As a consequence, the measured spectral shape is a Voigt profile (combination of a Gaussian shape with a Lorentzian profile) that reflects the actual linewidth when running the DFB under particular environmental conditions, using standard laser drivers. Figure A.2 shows the measured power spectral density and the fitting curve using a Voigt profile. The linewidth of the Lorentzian, Gaussian and Voigt profiles obtained by the fitting procedure are 0.4498, 1.0540, 1.3710 MHz, respectively, which matches well with the data provided by the manufacturer of the laser source.

Appendix B

List of publications

International journals

1. **J. Urricelqui**, A. Zornoza, M. Sagues, and A. Loayssa. Dynamic BOTDA measurements based on Brillouin phase-shift and RF demodulation. *Optics Express*, 20(24):26942-26949, 2012.

2. **J. Urricelqui**, M. Sagues, and A. Loayssa. BOTDA measurements tolerant to non-local effects by using a phase-modulated probe wave and RF demodulation. *Optics Express*, 21(14):17186-17194, 2013.

3. **J. Urricelqui**, M. Sagues, and A. Loayssa. Phasorial differential pulse-width pair technique for long-range Brillouin optical time-domain analysis sensors. *Optics Express*, 22(14):17403-17408, 2014.

4. **J. Urricelqui**, M. Sagues, and A. Loayssa. Synthesis of Brillouin frequency shift profiles to compensate non-local effects and Brillouin induced noise in BOTDA sensors. *Optics Express*, 22(15):18195-18202, 2014.

5. **J. Urricelqui**, F. López-Fernandino, M. Sagues, and A. Loayssa. Polarization diversity scheme for BOTDA sensors based on a double orthogonal pump interaction. *Journal of Lightwave Technology*, 33(12):2633-2638, 2015.

6. **J. Urricelqui**, M. Sagues, and A. Loayssa. Brillouin optical time-domain analysis sensor assisted by Brillouin distributed amplification of pump pulses. *Optics Express*, 23(23):30448-30458, 2015.

7. R. Ruiz-Lombera, **J. Urricelqui**, M. Sagues, J. Mirapeix, J. M. López-Higuera, and A. Loayssa. Overcoming nonlocal effects and Brillouin threshold limitations in Brillouin optical time-domain sensors. *IEEE Photonics Journal*, 7(6):1-9, 2015.

Conference proceedings

1. **J. Urricelqui**, A. Zornoza, M. Sagues, and A. Loayssa. Dynamic BOTDA measurements using Brillouin phase-shift. *Proceedings of SPIE*, volume 8421, 2012.

2. **J. Urricelqui**, M. Sagues, and A. Loayssa. Phase-shift based BOTDA measurements tolerant to non-local effects. *Proceedings of SPIE*, volume 8794, 2013.

3. **J. Urricelqui**, J. Mariñelarena, M. Sagues, and A. Loayssa. Phasorial DPP-BOTDA sensor tolerant to non-local effects. *Proceedings of SPIE*, volume 9157, 2014.

4. **J. Urricelqui**, F. López-Fernandino, M. Sagues, and A. Loayssa. Polarization diversity for Brillouin distributed fiber sensors based on a double orthogonal pump. *Proceedings of SPIE*, volume 9157, 2014.

5. **J. Urricelqui**, M. Sagues, and A. Loayssa. Synthesis of virtual Brillouin frequency shift profiles in BOTDA sensors using optical source dithering. *Proceedings of SPIE*, volume 9157, 2014.

6. **J. Urricelqui**, M. Sagues, and A. Loayssa. Brillouin distributed sensing assisted by Brillouin amplification of pump pulses. *Proceedings of IEEE Sensors*, pages 1776-1779, 2014.

7. **J. Urricelqui**, M. Sagues, and A. Loayssa. Brilloun optical time-domain analysis sensor assisted by a Brillouin distributed amplifier. *Proceedings of SPIE*, volume 9634, 2015.

8. **J. Urricelqui**, M. Alem, M. Sagues, L. Thévenaz, A. Loayssa, and M. A. Soto. Mitigation of modulation instability in Brillouin distributed fiber sensors by using orthogonal polarization pulses. *Proceedings of SPIE*, volume 9634, 2015.

9. **J. Urricelqui**, M. A. Soto, and L. Thévenaz. Sources of noise in Brillouin optical time-domain analyzers. *Proceedings of SPIE*, volume 9634, 2015.

10. **J. Urricelqui**, R. Ruiz-Lombera, M. Sagues, J. Mirapeix, J. M. López-Higuera, and A. Loayssa. Overcoming non-local effects and Brillouin threshold limitations in Brillouin distributed sensors. *Proceedings of SPIE*, volume 9634, 2015.

11. H. Iribas, **J. Urricelqui**, M. Sagues, and A. Loayssa. Enhanced tolerance to pulse extinction ratio in Brillouin optical time domain analysis sensors by dithering of the optical source. *Proceedings of SPIE*, volume 9634, 2015.

12. H. Iribas, **J. Urricelqui**, J. Mariñelarena, M. Sagues, and A. Loayssa. Simplified Brillouin sensor for structural health monitoring applications based on passive optical filtering. *Proceedings of SPIE*, volume 9634, 2015.

Patents

1. ES 201430832 - Spanish patent application. Sensor de medida de la distribución de magnitudes físicas en una fibra óptica y procedimiento de medida asociado. Inventors: A. Loayssa, M. Sagues, and **J. Urricelqui**.